

NASA Technical Memorandum 85833

100% REPRODUCED BY OPTICAL SCANNING
2013 RELEASE UNDER E.O. 14176

NASA-TM-85833 19840021828

HEAT TRANSFER AND OIL FLOW STUDIES ON A SINGLE-STAGE-TO-ORBIT CONTROL-CONFIGURED WINGED ENTRY VEHICLE

V. T. HELMS III and P. F. BRADLEY

JUNE 1984

LIBRARY COPY

JUN 27 1984

LANGLEY RESEARCH CENTER
LIBRARY, NASA
HAMPTON, VIRGINIA



National Aeronautics and
Space Administration

Langley Research Center
Hampton, Virginia 23665

HEAT TRANSFER AND OIL FLOW STUDIES ON A
SINGLE-STAGE-TO-ORBIT CONTROL-CONFIGURED WINGED ENTRY VEHICLE

Vernon T. Helms III and Pamela F. Bradley

NASA Langley Research Center

Hampton, Virginia 23665

SUMMARY

Results are presented for heat transfer and surface flow visualization tests conducted on a 0.006-scale model of an advanced winged entry configuration which is a proposed single-stage-to-orbit control-configured vehicle (CCV). The data were taken at angles of attack up to 40° at a free-stream Mach number of 10. The model's heating environment and the associated surface flow patterns are characterized as a function of angle of attack and Reynolds number. A detailed discussion of surface flow patterns and their interpretation in terms of three-dimensional flow-field structures for each test condition is given in order to aid analysis of the magnitude and distribution of heating. Shock interference effects resulting from the bow-shock/wing-shock interaction and from the wing-shock formation that left clearly visible streaks in the oil flow patterns were also found to produce high localized heating rates on the wing lower surface at low to moderate angles of attack. The effect of this phenomenon decreased with increasing incidence. Most of the model's leeward fuselage was influenced by a wake-type flow and thus received very little heating. There were few significant differences in overall patterns of heating and surface flow directions over the Reynolds number range used in these tests.

INTRODUCTION

Technological advances since the inception of the Space Shuttle have made the more efficient single-stage-to-orbit concept a viable candidate for a future space transport. The purpose of the present investigation is to provide a basic understanding of flow phenomena and the resulting thermal environment at simulated entry conditions for one such configuration that has been studied at the Langley Research Center (ref. 1). The test data presented here were obtained in the Langley 31-Inch Mach Tunnel at angles of attack from 0° to 40° and Reynolds numbers of 0.5×10^6 , 1.0×10^6 , and 2.0×10^6 . Heating on the windward surface, side fuselage and leeward surfaces of the model was measured using phase change paint. Corresponding surface flow patterns were visualized by oil flow. A close relationship between oil flow patterns and phase change heating contours was observed on many areas of the model. Details of this relationship are given for each test condition.

N84-29897

SYMBOLS

cs	centistoke
h	local heat transfer coefficient
h_0	stagnation point heat transfer coefficient on a 0.305 meter radius sphere in the free stream
K	degrees kelvin
M	Mach number
Re_∞	Reynolds number based on free stream conditions and model length
t	run time

APPARATUS AND METHODTunnel

These tests were conducted in the Langley 31-Inch Mach 10 Tunnel operated in a blow-down mode. A description of this facility and its calibration is given in references 2 and 3.

Models and Test Conditions

Three 0.006-scale CCV models made of a Styccast resin and one model made of aluminum were used to obtain the heating and flow visualization data for this study. The CCV configuration is shown in figure 1. Thermophysical properties of the Styccast were measured from samples cast at the same time as the corresponding models. Tests were conducted at free-stream Reynolds numbers based on model length of 2.0×10^6 , 1.0×10^6 , and 0.5×10^6 . The angles of attack were 0° , 10° , 20° , 30° , 35° , and 40° . The total temperature was 1006K.

Test Methods

Heat-transfer data were obtained using the phase change paint technique as documented in reference 4. The data were recorded on 35-mm motion picture film at the rate of 10 frames per second. Two of the Styccast models used in these tests were black while the third Styccast model was red. It was found that photographing the red model with color film provided better melt line contrast than using black and white film with either the red or black models. Three separate wind-tunnel runs for each test condition were necessary to acquire data on the windward surface, side fuselage and leeward surface of the model. The phase change paint temperature was varied from 311K to 367K depending on which model surface was viewed. Run times were limited

Oil flow studies were conducted using the aluminum model coated with high temperature black paint. The painted surface was buffed lightly with No. 600 grit sandpaper and water to provide a smooth finish. The oil is a mixture of Liquitex Artist Oil Color (Zinc Everwhite) and Dow Corning 200 Fluid silicone liquid. Mixtures using fluids with viscosities of 10, 50, 100, 200, and 350 centistokes (cs) were applied to different parts of the model. For example, the 10 cs oil was used in the low shear leeward fuselage and wing separated regions, 50 and 100 cs oils were generally applied to the leeward wing attached flow area and side fuselage, and the 200 and 350 cs oils were used almost exclusively on the high shear windward surface. A light-to-moderate base coat of 10 cs fluid was brushed onto the low shear areas of the model to act as a lubricant for the oil mixtures. Droplets of the oil mixture were applied to the model by rapidly stroking the end of a small, stiff, oil-laden brush with the forefinger to produce a thick array of white spots on the black surface. This procedure usually allowed satisfactory surface flow visualization to be obtained on most areas of the model during the same run. The model was removed from the wind-tunnel test section after each run to photograph the oil flow patterns.

DATA REDUCTION

The phase change paint data presented here were reduced to a demensionless ratio of heat transfer coefficients, h/h_0 , using the semi-infinite slab method of reference 4 and a laminar recovery factor of 0.9. The quantity h_0 is the stagnation point value on a scaled 0.305 meter radius sphere in the free stream. The technique discussed in reference 4 is applicable to all areas on the fuselage. However, its assumption of a thick body at constant temperature can be violated on thin sections such as the wings and vertical tail. Reference 5 provides a method of computing correction factors for the semi-infinite slab heating calculations that accounts for the effect of thin model segments. A general assessment was made of correction factors required for different areas on the wing and vertical tail rather than making detailed calculations of corrected heating rate distributions.

The correction factors given below should be multiplied by the semi-infinite slab wing and vertical tail heating values presented in the diagrams of phase change paint contours discussed later in this report. The thermal diffusion time, which depends on material properties and thickness, and the phase change paint melt time are the key parameters used to determine the correction factors. Windward surface melting usually occurred earlier than on the wing's leeside for a given spanwise and chordwise location. This resulted in the wing's windward surface correction factor having a minimum value of 0.9 near the thin trailing edge where the thermal diffusion time is approximately one second. No correction is needed elsewhere on the wing's lower surface due to shorter melt times and to thermal diffusion times which range up to 9 seconds over the forward and central areas. The leeward surface melt times over the forward wing areas are predominately similar to those on the windward side, thus resulting in a reduction of the semi-infinite slab heating rates of only a few percent. However, substantial wing leeside correction factors are required in the general vicinity of the trailing edge

due to a combination of short thermal diffusion times and long melt times. The precise correction factor for a given point near the trailing edge depends on melt time and the nature of both windward and leeward surface local heating contours. An average factor of 0.5 will generally yield corrected heating data that are within ± 10 percent of true value. Phase change melting on the vertical tail was generally concentrated near the leading and trailing edges with similar melt times at both locations. The thermal diffusion time close to the tail's leading edge is one second while that near the extremely thin trailing edge is around one-tenth second. By assuming symmetrical heating patterns on the vertical tail, a correction factor of approximately 0.8 was calculated for areas near the leading edge while a factor of roughly 0.25 must be used for trailing edge data.

RESULTS AND DISCUSSION

Diagrams showing the phase change paint heating contours and photographs of the corresponding oil flow patterns are presented together in figures 2 through 20. The data are in order of increasing incidence beginning at $\alpha = 0^\circ$. Test results are subdivided at each angle of attack for $Re_\infty = 2.0 \times 10^6$, 1.0×10^6 , and 0.5×10^6 in that sequence. This outline was followed primarily because a nearly complete set of phase change data were obtained only at the high Reynolds number. Representative heating data were measured for $Re_\infty = 1.0 \times 10^6$ and 0.5×10^6 only at $\alpha = 20^\circ$ and 35° . Small portions of the model not shown in some of the phase change diagrams were hidden from view by wind-tunnel apparatus. Oil flow patterns are available for all three Reynolds numbers throughout the angle of attack range.

Heat Transfer and Oil Flow Data at 0° Angle of Attack

Bottom View.— Heat-transfer data and oil flow patterns at $\alpha = 0^\circ$ and $Re_\infty = 2.0 \times 10^6$ are presented in figure 2. Surface flow patterns shown in figure 2(a) correspond to the heating contours in figure 2(b). The oil flow reveals strongly inboard flow over a large portion of the lower fuselage. There is a strip of flow along the symmetry plane which is caused by a pair of vortices. The vortex system forms near the nose as a result of the interaction of flow which has been turned in a streamwise direction on and near the centerline with inboard flow originating farther downstream along the chine. The phase change diagram for this test condition shows that significant heating on the bottom surface of the fuselage occurred only near the nose and the chines. The lowest measured value of h/h_0 is 0.0188. A paint with a lower melting temperature should produce additional heating contours associated with the central vortex impingement at heating levels less than the minimum measured value stated above.

Surface flow on the wings varies from large inboard angles on the inner portions to nearly streamwise directions on the outer areas. The abrupt inboard flow from the wing leading edge junction with the fuselage is caused by flow compression and formation of the wing shock. Of special interest is the set of streaks in the surface flow patterns near each wing tip and also

near the wing-body junction. The wing tip streaks appear to originate from the same point on the wing leading edge and are a result of the bow-shock/wing-shock interaction. These features produce high heating as evidenced by the "streak" patterns in the phase change contours of figure 2(b) at the same locations on the wing. There is also a slender region of relatively high heating along the line where the wing and fuselage join. It is noted that this corresponds to the inside edge of the diffuse white pattern of inboard flow which runs parallel to the model's axis where the wing and body blend together. A similar, but smaller feature, lies a short distance outboard and both are apparently associated with the formation of the wing shock. A more detailed discussion on the nature of these interference effects will be given in the following section for data taken at $\alpha = 10^\circ$ and $Re_\infty = 2.0 \times 10^6$ where the patterns are more fully developed. It will be shown that the wing patterns in figure 2(a) are caused by vortices which are generated by shock interactions.

Oil flow patterns at $\alpha = 0^\circ$ for $Re_\infty = 1.0 \times 10^6$ and 0.5×10^6 are presented in figures 3 and 4, respectively. Windward surface features at $Re_\infty = 1.0 \times 10^6$ in figure 3(a) are very much like those at $Re_\infty = 2.0 \times 10^6$. The only notable difference is that formation of the bottom centerline vortex occurs at slightly larger values of x/L for the low Reynolds number. There is little indication of a windward symmetry plane vortex at $Re_\infty = 0.5 \times 10^6$ in figure 4(a) until reaching an axial location near that of the wing-body junction. Also, shock interference patterns on the wing are not imprinted as clearly in the oil flow as they are for the high Reynolds number test conditions.

Side View.- One of the dominant features on the side of the model is the vortex impingement above the wing. This is illustrated for $Re_\infty = 2.0 \times 10^6$ in figure 2(c). The impingement line, with the accompanying feather-like surface flow pattern, remains close to the wing at $\alpha = 0^\circ$ and is nearly parallel to the free stream. This is also evident in the corresponding phase change contour of highest heating shown in figure 2(d) where $h/h_0 = 0.0320$. Flow compression takes place at the forward wing-body junction, and it is intensified due to the lower surface of the wing root being located above the fuselage. The compression produces a shock wave which influences surface flow on the side fuselage just ahead of the wing.

The vertical tail is subjected to some rather complex flow even at this low angle of attack. Figure 2(c) shows that flow is in a streamwise direction at the top of the tail. Closer to the fuselage, flow initially turns downward and then curves back up in response to a plume of base flow rising from the lower areas of the vertical tail. Part of the base flow plume can be seen turning forward into a separated region on top of the fuselage while the remainder turns aft and trails off into the wake. Figure 2(d) indicates that those areas on the tail affected by base flow have heating rates lower than $h/h_0 = 0.0189$, whereas the uniform flow on the upper portion of the tail corresponds to significantly higher heating.

Another characteristic of the surface flow at $\alpha = 0^\circ$ which can be observed in the side oil flow photo is the predominately downward flow direction close to the nose on the side of the fuselage. Remnants of this trend can be detected back to axial locations beyond that of the canopy. This flow is turned under the fuselage and produces the inboard patterns on the bottom of the model illustrated in figure 2(a). Moreover, tracing the side oil flow patterns forward shows that their source is on, or in close proximity to, the model's upper centerline very near the nose. Heating at mid-fuselage locations decreases in a nearly longitudinal fashion corresponding to the general direction of surface flow patterns at those stations.

Figure 3(b) shows a side oil flow photograph for $Re_\infty = 1.0 \times 10^6$. Figure 4(b) contains side view results for the test at $Re_\infty = 0.5 \times 10^6$. Both sets of patterns are virtually identical to the oil flow obtained at $Re_\infty = 2.0 \times 10^6$.

Top View.- Flow interactions around the canopy dominate the top view oil flow patterns for $Re_\infty = 2.0 \times 10^6$ in figure 2(e). A flow impingement occurs on the side of the superstructure ahead of the canopy, as can also be seen in figure 2(c). A prominent separation line originates at the apex of the fuselage superstructure and curves outboard to the side fuselage upper corner where it dissipates near $x/L = 0.75$. The curvature of surface flow just ahead of the primary separation line results from pressure propagating upstream through the boundary layer. There are three distinct zones of flow between the separation line and the superstructure on each side of the model. The two innermost zones are caused by two pairs of vortices generated at the forward end of the superstructure. These vortex pairs border on a common separation line, and their flow becomes predominately parallel to the model's axis near $x/L = 0.6$. Similar flow patterns were observed on yawed pointed half-cones on flat plates in reference 6. A second separation line dividing the third and outermost zone from the second vortex pair described above is most clearly seen on the left side of the model beginning near $x/L = 0.5$. This zone appears to contain nearly parallel surface patterns and has its origins in outboard flow emanating from the second vortex pair at locations close to the canopy. The middle and outer patterns blend together near $x/L = 0.80$ where streamwise flow directions prevail. The inner vortex pair continues aft until reaching a base-influenced separated region, which will be discussed below. The inboard flow component of this vortex washes against the side of the superstructure where it separates along a curved line upon meeting streamwise flow from the canopy impingement. Figure 2(f) is a closeup of the canopy region. This photograph shows the development of the two inboard pairs of vortices as well as the outward flow from the second vortex which turns downstream to form the outermost flow pattern. Flow

separation occurs on the superstructure ahead of the canopy resulting in flow impingement on the canopy's forward face with a pair of counter-rotating vortices in the separated region. Figure 2(g) shows that no phase change melting occurred in the canopy's separated region. It also indicates that h/h_0 is greater than 0.0776 on the superstructure ahead of the canopy and in narrow strips on the upper fuselage at the location of the inboard vortex pair. The middle and outer flow patterns on the upper fuselage produced no melting of the phase change paint. Heating in these areas corresponds to h/h_0 less than 0.0208.

Another region of interest in the upper fuselage flow patterns is the separated area at the aft end of the fuselage shown in figure 2(h). Separation occurs on the superstructure and on the fuselage top surface. It is caused by the model's base flow, observed on the vertical tail in figure 2(c), moving forward onto the upper fuselage from the lower portion of the tail. Some of the flow from the superstructure and fuselage top surface combine with the base flow to form a reattachment pattern in the separated region.

Both of the lower Reynolds numbers produced upper fuselage flow patterns, shown in figures 3(c) and 4(c), similar to those at $Re_\infty = 2.0 \times 10^6$. Instead of three vortices on each side of the superstructure, the low Reynolds number test conditions generated only two such features. Both vortex systems end at the forward boundary of an aft fuselage separated region. Impingement patterns within this region for $Re_\infty = 1.0 \times 10^6$ appear to be somewhat unsymmetrical, and only traces of oil movement can be detected at $Re_\infty = 0.5 \times 10^6$ due to low shear.

Figure 2(h) also shows details on the wing's upper surface at $Re_\infty = 2.0 \times 10^6$. Attached flow covers most of the area. Close to the fuselage and along the forward portions of the wing root, there is a narrow wedge of flow separation with outboard and streamwise components of flow from the side vortex impingement. Separation occurs farther outboard at the wing's trailing edge with surface flow traveling forward as a result of base flow spilling over into the low pressure separated region. Further evidence for the bow shock impingement on the wing's leading edge can be seen near the wing tip in the form of a dark streak similar to those on the bottom of the wing shown in figure 2(a). Both the upper and lower surface streaks occupy approximately the same spanwise locations on the wing, and they also share a common origin on the wing's leading edge. Slight streamwise surface flow deflections across the leeward streak indicate that it may be caused by a swept shock above the wing. Like its lower surface counterparts, the upper surface streak produces a thin strip of locally higher heating rates as shown in figure 2(g).

The wing separated flow patterns at $Re_\infty = 1.0 \times 10^6$ in figure 3(d) are similar to those at $Re_\infty = 2.0 \times 10^6$. Due to the reduced influence of base flow, the area of the wing affected by separation at $Re_\infty = 0.5 \times 10^6$, shown in figure 4(d), is less than for the high Reynolds numbers. The

base-related flow travels in a nearly spanwise direction at the low Reynolds number instead of the generally upstream paths taken at $Re_\infty = 1.0 \times 10^6$ and 2.0×10^6 .

Heat Transfer and Oil Flow Data at 10° Angle of Attack

Bottom View - Fuselage.- Figure 5 contains the heating and surface flow data for $\alpha = 10^\circ$ and $Re_\infty = 2.0 \times 10^6$. The windward surface phase change contours in figure 5(a) display intricate heating patterns on both the fuselage and wings. Letters shown on this figure will be referred to in the discussion that follows. The corresponding oil flow photo is shown in figure 5(b). As was noted for $\alpha = 0^\circ$, the windward centerline experienced very low heating at this test condition with h/h_0 being less than 0.0198. Inwardly directed flow exists over the forward locations on the model, though it is not as strongly inboard as at $\alpha = 0^\circ$. The result is a thickening of the windward symmetry plane boundary-layer with a commensurate reduction in heating. Farther from the centerline the flow is nearly streamwise. The corresponding boundary-layer is thinner and higher heating rates prevail with increasing spanwise distance until reaching the vicinity of the triangular-shaped boundaries in the lower fuselage oil flow of figure 5(b). Centered along these boundaries are twin corridors of reduced heating, one on each side of the symmetry plane. Once again, converging flow seems to be the cause of reduced heating rates at these locations although the convergence angles are slight. The oil flow photograph shows that streamlines originating along the chine near the nose first move inward and then they turn slightly outboard at the forward position of the triangular boundaries. This surface pattern meets inboard flow on streamlines which also originate along the chine but at larger axial distances. Very small surface flow convergence angles can be detected from $x/L = 0.28$ to 0.38 . Farther down the model, flow close to the triangular boundaries becomes parallel and nearly streamwise. However, boundary-layer growth with increasing axial length may be influenced by characteristics of the initially thick upstream segment resulting from flow convergence. This perpetuates the corridors of relatively low heating shown in figure 5(a). The high heating levels outboard of the twin corridors are perhaps due to a thinning of local boundary-layers where the outwardly directed surface flow responds to a favorable pressure gradient around the model.

Bottom View - Wings.- A closeup of surface flow patterns on both wings for $\alpha = 10^\circ$ at $Re_\infty = 2.0 \times 10^6$ is shown in figure 5(c). There are two sets of streaks caused by interference effects on each wing, as for $\alpha = 0^\circ$, but the increase in angle of attack produces a more intricate set of features. It was not possible to obtain an accurate detailed heating distribution along the length of the streaks primarily because of the very rapid melting of phase change paint which occurred there, but also because of low contrast between fully melted paint in the center of a streak and

paint that was beginning to melt in the relatively high heating areas along a streak's boundary. A series of photographs showing the development of the wing streak heating pattern in a phase change paint test for $\alpha = 10^\circ$ are presented in figures 6(a) through 6(d) corresponding to run times from 0.1 sec. to 0.8 seconds. The white phase change paint becomes transparent when melted exposing the black Styccast model. This sequence illustrates the very rapid formation of these high heating rate patterns upon injection into the free stream. The streaks' initial phase change contours become established between 0.1 and 0.2 seconds. This corresponds to $h/h_0 \approx 0.17$ at forward locations on the wing. Streak phase change melting occurs on the wing trailing edge by 0.4 seconds into the run where $h/h_0 = 0.1024$. This melt time is less than the one second thermal diffusion time characteristic of trailing edge locations, thus thin section correction factors need not be considered here. Although the normalized heat-transfer coefficient could not be determined at precise locations along the streaks, the figures stated above roughly indicate a 40-percent decrease in heating rate over the entire length of these features.

It was noted earlier that these patterns are the result of the wing shock formation and interaction of the bow and wing shocks. A detailed study of shock-on-shock interactions corresponding to the wing leading edge region is given in reference 7, which elucidates shock interactions in a basically two-dimensional sense. There is very little information available concerning the transmitted effects of such interactions, or the effects of wing shock formation, on the associated heating and surface flow directions at downstream locations. Only a limited number of studies have attempted to characterize the downstream bow-shock/wing-shock interaction on a wing's lower surface. For example, it has been shown that the Type V shock interaction that is discussed in reference 7 seemed to qualitatively explain windward surface wing interference heating patterns observed on an early straight-wing shuttle configuration at high angles of attack (ref. 8). However, a different straight-wing orbiter concept (ref. 9) exhibited wing interference patterns at similar test conditions that could not be explained by any of the interactions described in reference 7. This seems to indicate that bow-shock/wing-shock interactions are quite sensitive to model geometry. The highly three-dimensional character of flow over a swept wing at angle of attack can produce a variety of windward surface interference effects. An extensive examination of these interference patterns on the CCV at $\alpha = 10^\circ$ will now be presented. The results of this discussion will serve as a basis for analysis of changes in the wing's windward flow field for test conditions at higher angles of attack that will be presented later.

Inboard Interference Heating and Oil Flow Patterns on Wing.-
 Interference patterns that will be discussed here are identified in the oil flow photograph of the left wing for $Re_\infty = 2.0 \times 10^6$ shown in figure 5(d). The innermost set of interference patterns will be considered first. A vortex caused by the wing-shock formation, feature A, is evident just outboard of the wing-body junction. Impingement occurs along the boundary between the strongly inboard surface directions and an adjacent segment of parallel and streamwise flow labeled B. The region in the immediate vicinity of the impingement is represented by the strip of high

of figure 5(a). The parallel flow produces the lower heating level in the next outboard zone labeled B. The high heating rates in zone C seem to be related to a series of dark streaks (C) in the oil flow pattern. The streaks are aligned with the leading edge area that is affected by formation of the wing shock. It is suggested that these features are embedded vortices within the boundary layer. This was the conclusion drawn in other studies where identical oil flow structures were observed. Note that flow directions between the dark streaks differ from the directions of the streaks themselves. Cones at low incidence can form these patterns due to cross flow instabilities (ref. 10). Corresponding striations in oil flow and in phase change paint tests on the windward surface of a delta wing shuttle orbiter configuration can be seen to be a result of shock interactions (refs. 11 and 12). Perhaps both of these factors affect the CCV oil flow. The embedded vortex phenomena is not well understood. It occurs in both laminar and turbulent flow on a wide assortment of model geometries. It has been noted that vorticity production is enhanced in highly three-dimensional flows with strong pressure gradients (ref. 13). These circumstances exist in the windward flow field around swept wings, particularly in the presence of shock interactions as demonstrated in reference 11 and by the surface patterns in figure 5(d). The feature labeled E, which will be discussed below, in the oil flow photograph forms the outer boundary of a relatively unperturbed triangular-shaped area of surface flow, D, near the wing's leading edge. The inner boundary is defined by, and includes the embedded vortices shown at, forward wing locations in figure 5(d). This area is coincident with the wedge-like contours of high heating outlining region D in the phase change diagram.

Outboard Interference Heating and Oil Flow Patterns on Wing.- All outboard interference oil flow patterns beginning with item E in figure 5(d) are induced by the bow-shock/wing-shock interaction. The line E, where surface flow begins a sudden outboard expansion, is thought to be caused by local flow similar to that of a Type VI shock interaction described in reference 7. This type of interaction occurs when the intersecting shock meets the body shock at a shallow angle, as is the case for the CCV's bow-shock and wing-shock both along the wing's leading edge and as would be viewed in a cross-sectional plane at downstream locations. This type of interaction produces an outboard expansion and a shear layer. Since the outboard surface flow patterns extend up to the wing's leading edge, it appears that a Type VI interaction may be affecting the stagnation line flow. However, a conclusive statement cannot be made due to a lack of schlieren capability in the facility in which these tests were run. It is postulated that the three-dimensional bow-shock/wing-shock interaction continues to produce an outboard expansion at downstream locations corresponding to the outward turning of flow along line E. It has been shown that the expansion of a Type VI interaction generates lower heating at outboard locations. (Refs. 14 and 15). This general trend is indicated in the spanwise phase change data near position E in figure 5(a). The large axial component of flow at these downstream locations in the wing's windward flow field away from the model may result in the effects of the shear layer being smeared out and

greatly weakened before reaching the surface, as there is no indication of anything other than flow expansion in the oil flow at large chordwise distances close to line E. Similarly, the stagnation-line shear layer will probably lose its identity as it moves outward while resulting flow will take as it then spreads traversing the leading edge radius. It cannot be predicted what form the resulting flow will take as it then spreads outward and downstream over the wing's lower surface. However, the flow patterns F and G appear to be caused by the transmitted effects of the dispersed stagnation-line shear layer. Figure 5(a) shows that the central region of flow segment F is associated with high heating rates. Its structure appears to be similar to the vortex impingement pattern A discussed earlier. The inner portion of this feature contains inboard flow which borders sharply against the parallel and streamwise directions of the outer portion. The lowest heating on the wing's windward surface is near the trailing edge at midspan and is situated at the confluence of inward flow from segment F with the outboard flow from expansion line E, which suggests a thickening of the local boundary-layer. The oil flow features identified as G are embedded vortices like those on the outside edge of interference patterns emanating from the wing-shock formation. Both the inboard and outboard sets of embedded vortices are inclined at approximately the same angle with respect to the model's axis, but system G produces significantly lower heating. This is probably due to the different local properties within the two vortex systems, which could be related to differences in spanwise and normal pressure gradients associated with the wing- and bow-shock interaction and with formation of the wing shock. It is also noted that the initiation of both sets of embedded vortices takes place downstream of the disturbances along the wing's leading edge which precipitate the interference patterns. This reflects the evolution of conditions necessary for embedded vorticity as a function of local boundary-layer cross-flow instabilities which develop in response to the effects of wing leading-edge sweep and curvature (ref. 16).

Side View.- The 10° angle of attack side oil flow patterns for $Re_\infty = 2.0 \times 10^6$ are shown in figure 5(e). Flow from the windward surface sweeps sharply upward and separates near the side fuselage top corner. Corresponding heating rates shown in figure 5(f) decrease to a minimum measured value of $h/h_0 = 0.0193$. Effects of the wing shock can be seen in the oil flow just ahead of the wing root and also along a line trailing downstream. The feather-shaped vortex impingement pattern above the wing is inclined upward with respect to the model's axis by approximately 10° . The phase change contours in figure 5(f) indicate that maximum heating, with h/h_0 greater than 0.0284, occurs far downstream of the impingement line's origin. This is a result of higher pressures farther outboard on the wing's leading edge which go into the shear layer that lifts off of the wing's leeward surface and subsequently strikes the side fuselage at downstream locations. A similar effect on side fuselage impingement heating has been noted for the Space Shuttle Orbiter (ref. 17).

A much larger region on the vertical tail is affected by base flow than at $\alpha = 0^\circ$. Figure 5(e) shows that base flow moves upward and forward over the lower half of the tail causing flow separation near the leading edge close to the superstructure. There is an area of attached flow above

the separation line which curves aft to the tail's trailing edge. Melting of the phase change paint occurred only on the attached leading edge as indicated in figure 5(f). The extreme upper aft portion of the vertical tail was hidden from view by wind-tunnel fixtures.

Side view oil flow patterns at the lower Reynolds numbers are shown in figures 7(b) and 8(b). These surface directions are nearly indistinguishable from those for $Re_{\infty} = 2.0 \times 10^6$. Decreasing Reynolds number corresponds to lower shear on the vertical tail and upper fuselage areas and, consequently, less oil movement occurred at these test conditions.

Top View.— The leeward surface oil flow patterns and phase change contours for $\alpha = 10^\circ$ at $Re_{\infty} = 2.0 \times 10^6$ are presented in figures 5(g) and 5(h), respectively. Figure 5(g) shows that there was practically no development of oil flow patterns over the aft portion of the fuselage. Strong asymmetries are present in surface flow patterns over the high shear areas behind the canopy. Heating at these locations is very low with h/h_0 much less than 0.0124. The separation line originating at the apex of the superstructure remains on the upper surface until reaching axial locations near the wing where separation moves around the corner to the uppermost portion of the side fuselage. This can also be seen in figure 5(e). It is apparently caused by a change in the nature of side fuselage flow above the wing which allows the low pressure leeside flows to expand farther outboard. Figure 5(i) is a closeup of the nose and canopy surface flow patterns. Flow on the nose converges near the top centerline and then becomes nearly parallel to the model's axis. As for $\alpha = 0^\circ$, there is prominent surface flow curvature just ahead of the separation line. Two vortex pairs are located on either side of the superstructure. Figure 5(h) indicates that only the inner vortex system produces any significant heating, in this case on parts of the fuselage upper surface and the lower areas on the superstructure. Vortex impingement on the side of the superstructure ahead of the canopy results in converging flow on the leeward centerline ahead of the canopy causing lower heating there. Flow separates ahead of the canopy followed by reattachment on the canopy's forward face where h/h_0 is greater than 0.0527. There is again a pair of counterrotating vortices within the separated region corresponding to very low heating.

Trends in upper fuselage flow patterns similar to those described above were also observed at the lower Reynolds numbers. Those results are given in figures 7(c) and 8(c). At both $Re_{\infty} = 1.0 \times 10^6$ and 0.5×10^6 there is only one reattachment on the upper fuselage beside the superstructure. Figures 5(g) and 7(c) illustrate a variety of flow patterns on the upper fuselage and superstructure downstream of the canopy which may be caused by circulation associated with the wake created by the model's very wide cross-sectional geometry. Shear in this area at $Re_{\infty} = 0.5 \times 10^6$ was too low to cause any significant oil movement.

The oil flow photograph in figure 5(j) shows the 10° angle-of-attack wing leeside flow patterns at $Re_\infty = 2.0 \times 10^6$. The separated region is larger than at $\alpha = 0^\circ$. It is still dominated by reversed flow, some of which originates near the base of the model and moves upstream in S-shaped paths. There are indications of the development of an impingement line slightly ahead of and parallel to the wing's trailing edge. The source of flow causing the trailing edge impingement is unknown. However, it may be speculated that flow lifting off from the wing's upper surface, either from within the separated region or from the aft boundary of leading edge attached flow, may become reattached farther downstream at discrete points or along lines. Another possibility is that fluid from the windward flow field expands around the wing's trailing edge and reattaches to the leeside surface. Some of the surface flow from the impingement travels upstream and outboard meeting the primary separation line while the remainder moves aft over the trailing edge. Also, the slender forward area of the separated region close to the fuselage contains outboard and streamwise flow directions from the vortex which is generated by the side fuselage shear layer impingement.

The wing tip contains a small pocket of reversed flow which expands forward from the trailing edge forming a separation line and then radiates flow both outboard and inboard. Without information on the complete three-dimensional flow-field structure in the vicinity of this pattern, it is difficult to determine with any certainty just how it is formed. This feature appears to be similar to a three-dimensional bubble type separation like that described in reference 18. Also on the wing tip is a set of curved flow patterns which may develop in response to the shedding of a wing-tip vortex.

The attached flow region on the wing's upper surface contains two linear features. They originate near the same location on the wing's leading edge as do the outboard set of streaks on the windward surface and are thus related to the bow-shock/wing-shock interaction. Figure 5(j) shows that flow turns perceptibly in a streamwise direction along the inner flow pattern. This indicates the presence of a swept shock above the wing which interacts with the attached-flow boundary-layer. In the vicinity of the outer feature, flow traveling outboard and downstream merges along a separation line while surface directions of slightly smaller spanwise locations are turned in a streamwise direction. It is concluded that the outer flow pattern is caused by shock-induced separation resulting in vortex impingement. Figure 5(h) shows that both the swept shock-boundary layer interaction and the vortex impingement produce locally enhanced heating levels.

Low Reynolds number surface flow on the wing leeside is shown in figures 7(d) and 8(d). The same basic patterns exist in the separated region at all three free-stream conditions used in these tests. The separated region is smallest at the lowest Reynolds number. Vortex impingement in the attached flow zone generated by the leading edge shock interaction is obvious at both $Re_\infty = 1.0 \times 10^6$ and 0.5×10^6 . However, a swept shock just inboard of this feature observed at the high Reynolds number is more difficult to detect for these two cases.

Heat Transfer and Oil Flow Data at 20° Angle of Attack

Bottom View.- The heat transfer and oil flow data for $\alpha = 20^\circ$ and $Re_\infty = 2.0 \times 10^6$ are presented in figure 9. Windward surface phase change contours on the forward fuselage in figure 9(a) display trends of decreased heating down the length of the model and increased heating near the edge. The oil flow photograph in figure 9(b) shows basically streamwise flow in the vicinity of the windward centerline indicating steady growth of the boundary layer. Sharply curved outboard patterns near the edge correspond to a thinning of the boundary layer and higher heating.

Figure 9(b) also contains two sets of interference streaks in surface flow on the wings that are similar to those in figure 5(b) for $\alpha = 10^\circ$, except that the wing tip embedded vortices are much less prominent. The outer set of streaks, resulting from the wing- and bow-shock interaction, can be traced to a point that is approximately 5 percent of the wing span farther outboard on the leading edge than at $\alpha = 10^\circ$. The line of outboard flow expansion caused by three-dimensional interaction of the bow-shock and wing-shock (feature E in figure 5(d)) slants more inboard than at the lower angle of attack as it approaches the wing's trailing edge. This is caused by an increase in the wing-shock layer thickness with increasing angle of attack which moves the line of intersection with the bow-shock inboard at larger axial distances, as illustrated in reference 19. This effect is very noticeable in the oil flow photographs at higher incidence that will be presented later. In general, phase change paint contours on the wings are similar to those for $\alpha = 10^\circ$ in figure 5(a). However, at $\alpha = 20^\circ$, the entire wing area is exposed to heating rates that are generally higher than at $\alpha = 10^\circ$.

Oil flow and phase change results at $\alpha = 20^\circ$ for $Re_\infty = 1.0 \times 10^6$ and 0.5×10^6 are shown in figures 10 and 11, respectively. Windward surface oil flow patterns in figures 10(a) and 11(a) at both Reynolds numbers appear to be similar to those for $Re_\infty = 2.0 \times 10^6$, except that there is no clear indication of the inboard set of embedded vortices (corresponding to feature C in figure 5(d)). Phase change contours in figures 10(b) and 11(b) exhibit strips of high interference-related heating caused by the vortex impingement near the wing-body junction, by the high pressure flow on the forward section of the wing just inboard of the bow-shock/wing-shock expansion line, and by the wing-tip impingement. However, the oil flow pattern of the wing-tip impingement becomes less conspicuous with decreasing Reynolds number.

Side View.- Side fuselage oil flow patterns for $Re_\infty = 2.0 \times 10^6$ are shown in figure 9(c). Surface flow directions along the side fuselage are steeply inclined in response to the higher angle of attack. Inclination of the impingement line above the wing stands at 20° , equal to the angle of attack, with respect to the model's axis. Phase change measurements in figure 9(d) show that peak heating of h/h_0 greater than 0.0237 on the impingement line again occurs downstream of its origin. There is very little movement of oil on the vertical tail indicating low shear and low

heating. A large portion of the tail is probably influenced by a mixture of low density flows from the separated upper fuselage area and from the base region. However, the tail's leading edge still receives moderate heating rates.

The side view oil flow patterns and heating contours at the lower Reynolds numbers are shown in figures 10(c) and 11(c) and in figures 10(d) and 11(d), respectively. A comparison of this data with that obtained at $Re_{\infty} = 2.0 \times 10^6$ shows that the side fuselage impingement heating rates become smaller with decreasing Reynolds numbers. The only observable difference in the surface flow is less movement of oil on the upper fuselage and vertical tail with decreasing Reynolds number due to lower shear.

Top View.- The overall top view of surface flow patterns for $Re_{\infty} = 2.0 \times 10^6$ in figure 9(e) shows that there is a somewhat greater degree of flow separation on the fuselage upper surface than at $\alpha = 10^\circ$ for the same free-stream conditions. The extent of the relatively high shear region has moved noticeably forward and closer to the canopy. Flow asymmetries are still present on the canopy. Figure 9(f) is a closeup of the nose and canopy region. There has been a change in character of flow along the top centerline on the nose. At lower angles of attack, surface flow converged on the top centerline traveling inboard. Between $\alpha = 10^\circ$ and $\alpha = 20^\circ$, a pair of counterrotating vortices developed above the nose. The vortex pair causes flow impingement along the leeward symmetry plane beginning near $x/L = 0.08$ as evidenced by outboard flow over the upper surface of the nose. The lines of primary flow separation now extend far forward of the superstructure's apex. The vortices also overrun the forward end of the superstructure as well as the canopy, causing flow impingement where converging flow and flow separation existed at low incidence. The twin vortex system observed on the fuselage upper surface beside the superstructure at $\alpha = 10^\circ$ no longer exists. Figure 9(g) shows that the new flow geometry produces its own distinctive pattern of heating on the upper surface. The highest heating on the forward face of the canopy is for h/h_0 greater than 0.0290 with the remainder of significant heating concentrated along the top centerline at more forward locations.

The state of development of the nose vortex pair is a function of free stream conditions. Impingement begins farther downstream at lower Reynolds numbers. Figure 10(e) shows that for $Re_{\infty} = 1.0 \times 10^6$ the nose vortex becomes fully developed at $x/L = 0.09$, whereas impingement is delayed until reaching $x/L = 0.13$ for $Re_{\infty} = 0.5 \times 10^6$, in figure 11(e). The phase change contours in figures 10(f) and 11(f) also indicate progressively lower heating rates on the upper nose and canopy as Reynolds number decreases, with maximum heating corresponding to $h/h_0 > 0.0134$ and $h/h_0 > 0.0126$ in these two figures, respectively.

Phase change contours on the wing's upper surface for $Re_{\infty} = 2.0 \times 10^6$ in figure 9(g) include streaks of locally higher heating on the outboard portion of the wing. The location of these features corresponds

to a pair of streaks emanating from the bow-shock impingement on the wing's leading edge shown in figure 9(h). The nature of the streaks appear to be the same as for those at $\alpha = 10^\circ$. The outboard vortex impingement produces much higher heating than the inboard swept shock which seems to be weaker than for $\alpha = 10^\circ$.

Surface flow patterns in the wing's separated region become more complex with increasing angle of attack. The size of the separated region in figure 9(h) is approximately the same as for $\alpha = 10^\circ$ at $Re_\infty = 2.0 \times 10^6$. The outboard and streamwise vortex-generated flow in the forward end of the separated zone meets the reversed flow supplied by the model's base region which streams forward close to the fuselage. This forward moving flow then swirls outboard toward the primary separation line and is joined by another component of reversed flow which originates along an impingement line that is parallel and very close to the wing's trailing edge. These two flows combine to produce a circulation pattern centrally located in the separated region where flow lifts off of the upper surface. The shape of the aft portion of the wing's primary separation line is greatly distorted due to the effects of these flow patterns. The inboard direction of flow from this trailing edge impingement line is opposed by outwardly directed flow originating along a short impingement line near the body flap which may result from base flow effects. Some of the reversed flow from the trailing edge impingement line near the 60-percent span station turns outboard as it moves forward. In response to adjoining attached flow directions, it next turns aft and then inboard, thereby forming another circulation pattern where flow lifts off of the surface. Closer to the wing tip, flow from the trailing edge impingement line moves outboard, and some of it expands forward resulting in a small pocket of reversed flow on the wing's outboard aft corner. Also prominent are the highly curved surface directions associated with the shedding of a wing-tip vortex.

Figures 10(g) and 11(g) show that only a single impingement influences the wing separated region at $Re_\infty = 1.0 \times 10^6$ and 0.5×10^6 . The patterns at both of these test conditions are similar. Flow impingement occurs near the wing's trailing edge close to the fuselage. Reversed and outboard flow radiates throughout the separated region from that point. This flow structure at the lower Reynolds numbers produces a less complex primary separation line geometry bordering the attached flow zone. Shock interference patterns near the wing tip are also shown in these figures. The general heating levels on the wing upper surface decrease at lower Reynolds numbers as illustrated by a comparison of figures 9(g), 10(f), and 11(f). Locally higher heating caused by shock interference effects can also be seen in the phase change contours on the forward portion of the wing in figures 10(f) and 11(f).

Heat Transfer and Oil Flow Data at 30° Angle of Attack

Bottom View.- Figure 12 contains heating and oil flow data for $\alpha = 30^\circ$ and $Re_\infty = 2.0 \times 10^6$. Figure 12(a) shows a slightly oblique view of windward surface phase change contours. The corresponding oil flow patterns are in figure 12(b). A comparison of the fuselage phase change

levels with increasing angle of attack on the windward centerline. A symmetrical pair of low heating zones just inboard of the wing root occupy approximately the same location as similar features observed at $\alpha = 20^\circ$. However, the low heating zones at $\alpha = 30^\circ$ are not as extensive as at the lower angle of attack.

Streaks are visible on the wings in both the oil flow photograph and the phase change diagram. The vortex impingement along the wing root and streamwise flow ahead of the mid-span expansion line, as well as leading edge effects, are primarily responsible for high heating on the wing. The bow-shock/wing-shock intersection which precipitates the surface flow expansion at downstream locations moves inboard rather rapidly as it approaches the wing's trailing edge. The change in surface flow directions across the expansion line is quite noticeable, and the flow is turned more sharply outboard than at lower angles of attack. The area of lowest heating on the wing is found near the trailing edge where outboard flow from the expansion line converges with inboard flow from the wing tip vortex impingement. As at $\alpha = 20^\circ$, there is no sign of embedded vortices generated by bow shock related leading-edge effects. This phenomenon is apparently damped out rather quickly with increasing angle of attack. Embedded vortices originating at the wing-body junction are only faintly visible in the oil flow. Also note that the wing leading edge stagnation line can be detected just aft of the geometric leading edge.

Oil flow patterns for $Re_\infty = 1.0 \times 10^6$ and $Re_\infty = 0.5 \times 10^6$ at $\alpha = 30^\circ$ are presented in figures 13 and 14, respectively. No embedded vortices are detected in either of the two sets of wing windward surface interference patterns in figures 13(a) and 14(a). Also, as noted before, the wing-tip impingement appears to become weaker at lower Reynolds numbers. The windward flow patterns are otherwise similar at all three free-stream conditions.

Side View.- The side view oil flow patterns at $Re_\infty = 2.0 \times 10^6$ are shown in figure 12(c). Compared with lower angles of attack, the differences observed in these side view patterns include an increase in the angle described by the forward portion of the impingement line wing to 30° and a change in flow patterns affecting the vertical tail. Each increase in angle of attack has resulted in a corresponding increase of the impingement line angle on the model's side such that the forward section of the impingement pattern is parallel to free-stream flow. Phase change measurements in figure 12(d) again show that peak heating on the side fuselage impingement line occurs downstream of its origin. In this case, $h/h_0 > 0.0197$ which continues a trend of decreasing side fuselage peak impingement heating with increasing angle of attack. A larger volume of separated flow above the wing is indicated by the sizable region on the side fuselage just over the wing where there is no movement of the oil in figure 12(c). Flow in the lower half of the side impingement pattern cannot reach the wing at these locations because of surface flow which initially moves forward and then lifts off of the wing, thus forcing the side impingement flow to turn in an axial and finally upward direction. Details of the wing surface flow patterns will be discussed below.

There was very little movement of oil on the vertical tail, but the available patterns suggest a considerable influence of base flow. Figure 12(c) shows a relatively clear indication of a stream of flow originating on the tail's trailing edge near the upper aft corner. A small portion of this stream travels upward and enters the model's wake by lifting off of the tail's upper edge. The remainder of the base flow stream moves forward onto the vertical tail and meets an axial flow component. Both flows then turn downward and leave the tail's surface along its trailing and lower edges. Phase change results in figure 12(d) indicate that the vertical tail in general experiences relatively low heating rates.

Figures 13(b) and 14(b) show the side view oil flow patterns at $Re_{\infty} = 1.0^6 \times 10^6$ and 0.5×10^6 , respectively. There is very little upper fuselage oil movement aft of the canopy for either case. Except for minor differences in patterns on the vertical tail, surface flow directions at all three test Reynolds numbers are essentially the same.

Top View.- An oblique view of the leeward surface phase change contours at $\alpha = 30^\circ$ for $Re_{\infty} = 2.0 \times 10^6$ are shown in figure 12(e). Figure 12(e) contains an overall top view of oil flow patterns and figure 12(g) is a closeup of surface flow in the nose and canopy region. High heating rates on the canopy are a result of flow impingement from the leeward meridian nose vortex. Values of h/h_0 on the canopy's forward face exceed 0.0146. No further melting occurred on the upper fuselage corresponding to the large low-shear area where there was no oil movement. Note the unsymmetrical surface patterns to either side of the superstructure on the upper fuselage in figure 12(g).

Top fuselage surface flow patterns at the two lower Reynolds numbers for $\alpha = 30^\circ$ are shown in figures 13(c) and 14(c). The leeward meridian vortex impingement begins close to the nose at all free-stream conditions. A comparison with figure 12(f) shows that the vortex interaction with the superstructure and canopy produces Reynolds number dependent flow asymmetries both aft of the canopy and on the flat upper fuselage surface.

Surface flow patterns on the wing at $Re_{\infty} = 2.0 \times 10^6$ for $\alpha = 30^\circ$ are shown in figure 12(h). The separated region has expanded forward and covers a larger area than at lower angles of attack. There is no indication of any influence from the bow-shock/wing-shock interaction on the attached flow near the wing's leading edge. Two distinct impingement patterns dominate the separated flow region. An impingement can be seen near the wing's trailing edge and close to the fuselage. Some of the flow from this feature goes directly to the trailing edge, but the majority of it travels slightly outboard and then forward where the patterns finally curve abruptly to meet the separation line bordering the attached flow zone. A part of the flow from this inboard wing impingement is forced up the side of the fuselage and causes the upward curvature of flow associated with the side fuselage impingement discussed earlier and shown in figure 12(c). The streamwise and outboard flow on the wing's upper surface

resulting from the side fuselage impingement is restricted to extreme forward locations in the separated region due to the reversed flow from the inboard wing impingement. The second impingement pattern in the separated region occupies a line parallel to the trailing edge at outboard locations. Flow immediately aft of the impingement line travels directly to the trailing edge while flow ahead of the impingement location sweeps forward in curving patterns. An irregular line of flow separation is formed between flows from the two impingement patterns at approximately 30 percent of the wing's span. Phase change contours in figure 12(e) reveal only general heating trends on the wing. High heating rates occur on the wing's leading and trailing edges with lower heating deeper within the separated region.

Separated flow patterns on the wing at $Re_{\infty} = 1.0 \times 10^6$ in figure 13(d) are nearly the same as for $Re_{\infty} = 2.0 \times 10^6$. Surface flow directions at $Re_{\infty} = 0.5 \times 10^6$ in figure 14(d) indicate a circulation pattern at approximately the 30-percent span position which is similar to the wing leeside separated flow characteristics observed at $\alpha = 20^\circ$ and $Re_{\infty} = 2.0 \times 10^6$. The area of the wing influenced by separated flow becomes smaller as Reynolds number decreases.

Heat Transfer and Oil Flow Data at 35° Angle of Attack

Bottom View.- Test results at $\alpha = 35^\circ$ and $Re_{\infty} = 2.0 \times 10^6$ are shown in figure 15. Heating along the windward centerline in figure 15(a) decreases with increasing axial length, except for a small increase near the body flap's trailing edge. This is the result of increased windward surface heating at 35° incidence elevating the temperature of the thin body flap material causing premature phase change melting. Phase change contours on the wings resemble those at $\alpha = 30^\circ$, but overall heating levels are higher. The expansion line on the wing shown by oil flow in figure 15(b) continues to slant farther inboard with increasing angle of attack. The wing tip vortex impingement, formed by the transmitted leading edge bow-shock/wing-shock interaction effects at lower angles of attack, does not seem to be present at $\alpha = 35^\circ$. Increasing angle of attack produces a greater overall outboard flow component at large spanwise distances on the wing. This results in a more nearly uniform flow field with diminished local pressure gradients which eventually eliminate the conditions necessary to form a vortex. However, surface flow near the wing tip is traveling in a more streamwise direction than flow which passes through the bow-shock/wing-shock expansion line. The low heating zones at large spanwise distances on the wings in figure 15(a) are centered on the region where these flows merge. The wing's leading edge stagnation line is moving farther aft on the windward surface with increasing angle of attack.

Figures 16 and 17 contain heat transfer and oil flow data for $\alpha = 35^\circ$ and $Re_{\infty} = 1.0 \times 10^6$ and 0.5×10^6 , respectively. Windward surface oil flow patterns in figures 16(a) and 17(a) are nearly identical to those at $Re_{\infty} = 2.0 \times 10^6$. The corresponding phase change heating contours are

given figures 16(b) and 17(b). Bottom centerline heating continues to decrease down the entire length of the model for $Re_{\infty} = 1.0 \times 10^6$. Unsymmetrical heating on the wings is believed to be due to an uneven coating of the phase change paint. A small rise in heating rate occurs along the body flap's trailing edge in figure 17(b) at $Re_{\infty} = 0.5 \times 10^6$, like that for $Re_{\infty} = 2.0 \times 10^6$. The irregular appearance of elevated trailing edge heating as a function of Reynolds number is further evidence that this is probably a conduction effect on the thin body flap. A comparison of figures 15(a), 16(b), and 17(b) shows that the transmitted effects of the wing-shock formation continue to produce significant heating near the wing at high angles of attack whereas the wing-shock/bow-shock interaction has ceased to be an important factor in windward surface heating.

Side View.- Side view oil flow patterns on the aft portion of the model are shown in figure 15(c) for $Re_{\infty} = 2.0 \times 10^6$. The inclination of the initial segment of the side fuselage impingement line is 35° with respect to the model's axis. This is in rough agreement with the corresponding phase change contours in figure 15(d), and it continues the relationship observed at other test conditions showing that the impingement line inclination is equal to the model's angle of attack. There are other features on the side fuselage contained in these figures that are common to the test cases discussed earlier. A shock wave that is generated at the wing-body junction can be traced in the oil flow on the model's side. Surface flow on the vertical tail in figure 15(c) is similar to that for $\alpha = 30^\circ$. The aft upper corner of the vertical tail experiences upward and reversed flow. At lower locations, flow turns forward and then quickly downward. There are only faintly visible indications of oil movement over the remainder of the tail. Perhaps the curvature over the aft segment of the separation line on the side fuselage is related to the general downward flow dominating the vertical tail. Also, peak heating on the side fuselage impingement line still occurs considerably downstream of the wing-body junction. However, peak side fuselage impingement heating of $h/h_0 > 0.0255$ is greater than at $\alpha = 30^\circ$, thus reversing the downward trend in side fuselage heating with increasing angle of attack that was established for test conditions at lower incidence. This may represent a change in the character of the flow affecting the side fuselage impingement.

Side-view phase change heating contours for $Re_{\infty} = 1.0 \times 10^6$ and 0.5×10^6 at $\alpha = 35^\circ$ in figures 16(c) and 17(c) respectively, display most of the characteristics attributed to the high Reynolds number test. Impingement heating above the wing is one of the primary points of interest. Comparing data from these figures with that in figure 15(d) shows decreasing heating rates on the side fuselage impingement line as Reynolds number becomes smaller, as was the case at $\alpha = 20^\circ$. Surface flow patterns on the vertical tail in figures 16(d) and 17(d) change with Reynolds number. An area of generally reversed flow is located along the tail's trailing edge at $Re_{\infty} = 1.0 \times 10^6$. Oil movement ahead of this region is indistinct, but it should be in a downward and streamwise direction in order to turn reversed flow both downward and upward on the respective lower and upper portions of the tail. An entirely different vertical flow pattern exists at $Re_{\infty} = 0.5 \times 10^6$. Flow on the lower

portion of the tail moves downward while the remainder of the surface directions are toward the trailing edge. These patterns seem to radiate from the forward area of the vertical tail as if caused by flow impingement.

Top View.- The phase change data in figure 15(e) show more extensive heating on the superstructure for $\alpha = 35^\circ$ than for other moderate-to-high angle-of-attack test conditions at $Re_\infty = 2.0 \times 10^6$. This seems to correspond to a greater movement of oil on the leeward surface as illustrated in figures 15(f) and 15(g). Surface flow ahead of the vertical tail in figure 15(g) is located within the area of enhanced heat transfer measured close to the rear of the model.

The wing's trailing edge in figure 15(g) contains three stagnation points along a continuous impingement line. The most prominent impingement is located at approximately the 40-percent span position. Flow immediately aft of the impingement leaves the wing over the trailing edge. Ahead of the impingement point, flow radiates forward spreading over nearly all of the separated region. The presence of this type of flow has a large effect on the location and shape of the primary separation line aft of the wing's leading edge. The location of the outboard trailing edge stagnation point is not as well defined. However, at approximately the mid-span location, the inboard component of its flow can be seen opposing the outboard movement of flow from the 40-percent span stagnation point. Similarly, the outboard direction of flow from the innermost stagnation point, which is located close to the fuselage, is countered by inboard surface directions from the central impingement at about 25 percent of the wing's span.

Test results for the lower Reynolds numbers at $\alpha = 35^\circ$ are presented in figures 16 and 17. Figure 16(e) and $Re_\infty = 1.0 \times 10^6$ shows heating on the canopy's forward face that is lower than for $Re_\infty = 2.0 \times 10^6$. Upper fuselage heating at $Re_\infty = 0.5 \times 10^6$ proved to be less than $h/h_0 = 0.0119$ at all locations as shown in figure 17(e). Similar surface flow patterns were found in the nose and canopy region at all of the free-stream test conditions. This can be seen by comparing figures 15(f), 16(f), and 17(f). Oil flow patterns in the wing separated region at the lower Reynolds numbers in figures 16(g) and 17(g) are controlled by three trailing-edge impingements as was the case at $Re_\infty = 2.0 \times 10^6$. The inboard impingement dominates a larger portion of the separated flow as Reynolds number decreases. There is a corresponding decrease in the effect of the mid-span impingement. Also, a considerably larger area of leading edge attached flow is produced at low Reynolds numbers.

Heat Transfer and Oil Data at 40° Angle of Attack

Bottom View.- Figure 18 contains heating and oil flow data for $\alpha = 40^\circ$ and $Re_\infty = 2.0 \times 10^6$. No phase change measurements are available for the windward surface at any of the test conditions for $\alpha = 40^\circ$. Oil flow patterns on the bottom surface for $Re_\infty = 2.0 \times 10^6$ are shown in figure 18(a) although these patterns are not as clear as those for lower angles of

attack. The expansion line resulting from the three-dimensional interaction of the bow shock and wing shock can be clearly seen slanting inward on the right wing's lower surface. The angle of the shock interaction with respect to the model's axis is much greater than at low angles of attack where it was first noted. Also, flow near the wing tips travels more nearly outboard than at lower incidence. Once again, there is no visible influence of interference effects transmitted downstream from the bow-shock/wing-shock intersection on the wing windward surface at this high angle of attack.

Figures 19 and 20 show oil flow at $Re_{\infty} = 1.0 \times 10^6$ and 0.5×10^6 , respectively. The same oil flow patterns were observed on the windward surface in figures 19(a) and 20(a) as at $Re_{\infty} = 2.0 \times 10^6$. The wing leading edge stagnation line can be seen to have moved farther aft of the geometric leading edge with an increase in angle of attack for the three test cases represented by figures 18(a), 19(a), and 20(a).

Side View.- The inclination angle for the initial segment of the side fuselage impingement line at $Re_{\infty} = 2.0 \times 10^6$ in figure 18(b) is 40° , as expected from the series of measurements made for lower angles of attack. Figure 18(c) shows that values of h/h_0 in the side fuselage impingement region exceed 0.0299, which is greater than at $\alpha = 35^\circ$. The separation line on the side fuselage trails steeply downward at the rear of the model, even more so than at $\alpha = 35^\circ$. This is presumably due to a greater influence of flow from the model's base and separated regions, although there was little movement of oil on the vertical tail and upper fuselage that would allow an interpretation of the specific flow interactions that might be responsible.

Side view surface patterns at $Re_{\infty} = 1.0 \times 10^6$ and 0.5×10^6 are shown in figures 19(b) and 20(b), respectively. No phase change data are available for these tests. There are vague indications of flow traveling in different directions on the vertical tail in the two photographs. Also, the aft end of the flow separation line is located higher on the side fuselage at lower Reynolds numbers. This may be an indication of more complex structures in the leeside and base flow fields at higher Reynolds numbers.

Top View.- Figure 18(d) shows surface directions for $Re_{\infty} = 2.0 \times 10^6$ which affirm the general lack of oil movement on the CCV's upper fuselage at high angles of attack. Extensive regions of leeside flow reversal in asymmetrical patterns, like those in the closeup photograph in figure 18(e), have also been shown to be a characteristic of this configuration. Flow reversal occurs farther forward on the left side of the model than on the right at $\alpha = 40^\circ$, and it results in flow separation where vortex flow from the nose region is encountered. No phase change data were obtained on the leeward surfaces for any Reynolds number at $\alpha = 40^\circ$.

Leeside oil flows for the two lower Reynolds numbers are given in figures 19(c) and 20(c). Asymmetrical top fuselage patterns near the forward end of the superstructure for $Re_{\infty} = 1.0 \times 10^6$ are similar to those for $Re_{\infty} = 2.0 \times 10^6$ in figure 18(d). Low shear at $Re_{\infty} = 0.5 \times 10^6$ prevented detection of upper fuselage surface patterns at this angle of attack. A comparison of figure 18(d) with figure 20(c) shows that the width of the nose vortex impingement pattern becomes smaller with decreasing Reynolds number.

Surface flow directions on the wing leeside at $\alpha = 40^\circ$ and $Re_{\infty} = 2.0 \times 10^6$ are shown in figure 18(f). The separated region now covers most of the wing's upper surface with attached flow occupying a narrow strip along the leading edge. There is once again a line of flow impingement parallel to the wing's trailing edge, this time with two stagnation points. One of the stagnation points is close to the fuselage, and the other is near the 40-percent span station. The combined flows from these impingements travel directly forward at inboard locations until reaching the separation line near the leading edge. The impingement flow curves more in an outboard direction at large spanwise locations on the wing. Outboard and streamwise flow from the side fuselage impingement is relegated to the extreme forward corner of the wing's separated region. Traces of flow reattachment can be seen near the aft end of the top fuselage. This may be related to the large downward shift of the side fuselage separation line shown in figure 18(b).

Figures 19(d) and 20(d) contain the wing flow patterns for $Re_{\infty} = 1.0 \times 10^6$ and 0.5×10^6 , respectively. The separated flow surface directions are similar to those at $Re_{\infty} = 2.0 \times 10^6$. However, there is only one stagnation point on the trailing edge impingement line for $Re_{\infty} = 0.5 \times 10^6$. As noted before, the area of attached flow near the wing leading edge becomes larger at low Reynolds numbers. The flow impingement pattern on the aft end of the upper fuselage in figure 20(d) for $Re_{\infty} = 0.5 \times 10^6$ is much different than at higher Reynolds numbers.

CONCLUDING REMARKS

The thermal environment of a proposed single-stage-to-orbit control-configured vehicle has been assessed for simulated entry conditions at Mach 10. The tests were conducted at angles of attack from 0° to 40° and at Reynolds numbers of 2.0×10^6 , 1.0×10^6 , and 0.5×10^6 . Heat-transfer data were obtained using the phase change paint technique. These data were supplemented by oil flow patterns which allowed a correlation between flow-field structures and heating contours observed on the model. The wing lower surface at low-to-moderate angles of attack is the only region of this configuration where additional thermal protection may be required as a result of embedded vorticity generated by shock interactions.

There are two complex sets of interference patterns on the wing windward surface. One set of patterns originates near the wing-body junction in response to formation of the wing-shock. The other interference pattern is the result of the bow-shock/wing-shock intersection farther outboard. Severe heating associated with these interference effects appeared as streaks in the phase change paint tests. Oil flow revealed the presence of embedded vorticity as well as large-scale flow impingement in each of the affected areas. The number of streaks observed in phase change paint associated with embedded vorticity seems to be a maximum at approximately 10° to 20° angle of attack. Peak heating in the streaks corresponds to $h/h_0 \approx 0.17$ near forward locations on the wing with 40 percent decrease in heating over the entire length of these features. The streaks diminish in number and in resultant heating with increasing incidence until becoming completely damped out near $\alpha = 30^\circ$. Higher Reynolds numbers created more pronounced embedded vorticity patterns in both phase change paint and oil flows.

The most significant localized heating occurring on the CCV's side fuselage was caused by vortex impingement above the wing. Peak heating on the impingement line is located far downstream of the wing-body junction where the vortex forms. This is believed to be caused by a variation in the axial distribution of local flow properties along the impingement line in response to spanwise changes in local properties along the wing's leading edge where the impinging flow originates. This is similar to the relationship that has been established between the Space Shuttle Orbiter strake leading edge properties and side fuselage impingement heating distributions. The CCV side fuselage impingement heating increased with higher values of Reynolds number. Side fuselage impingement heating decreased with increasing angle of attack for $\alpha \leq 30^\circ$, and it increased for $\alpha > 30^\circ$. This reversal in trend may represent a change in the nature of the flow affecting the configuration's side fuselage.

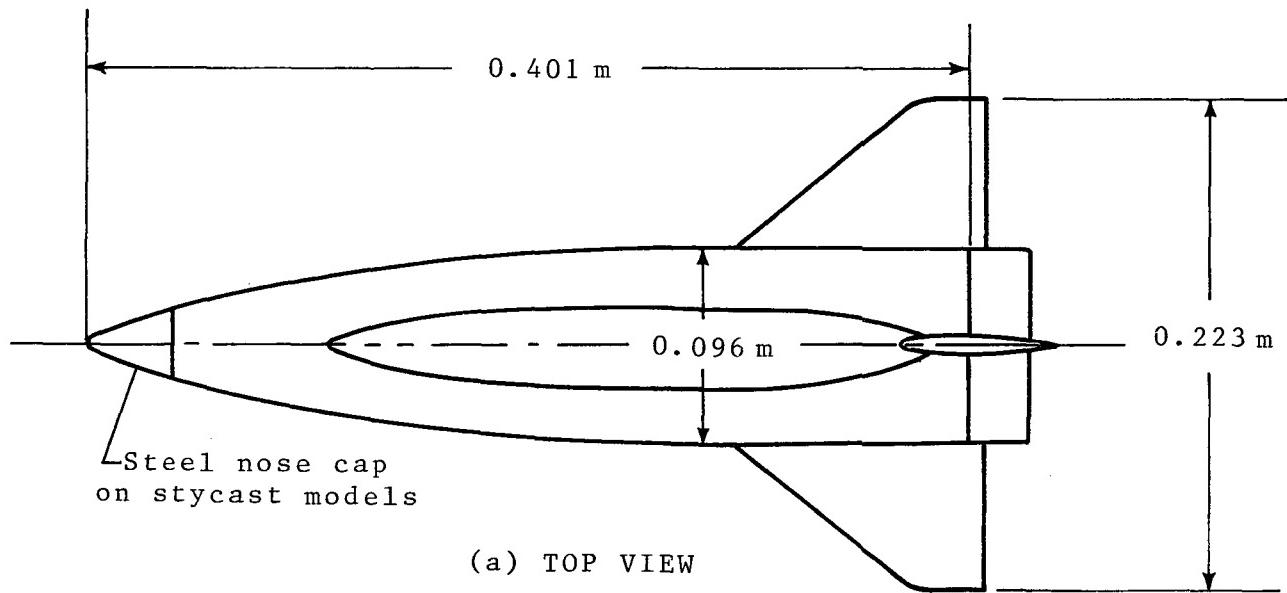
The CCV's leeward fuselage generally experienced a wake-type flow and low heating beginning at an angle of attack of less than 10° perhaps as a result of the model's relatively wide cross-sectional geometry. Exceptions to this were the vicinity of the canopy where flow impingement occurred and also isolated strips of vortex impingement trailing downstream from the forward end of the CCV's superstructure at low angle of attack.

REFERENCES

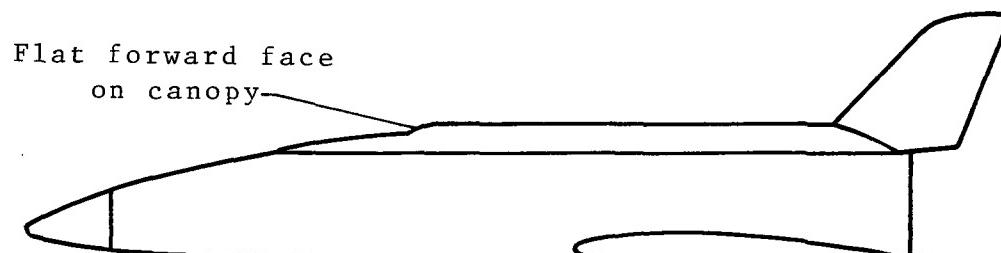
1. Freeman, D. C. and Powell, R. W.: "Impact of Far-Aft Center of Gravity for a Single Stage to Orbit Vehicle." Journal of Spacecraft and Rockets, Vol. 17, No. 4, July-August 1980.
2. Schaefer, William T., Jr: "Characteristics of Major Active Wind Tunnels at the Langley Research Center." NASA TM X-1130, 1965.
3. Dunavant, James C. and Stone, Howard W.: "Effect of Roughness on Heat Transfer to Hemisphere Cylinders at Mach 10.4 and 11.4." NASA TN D-3871, 1967.
4. Jones, Robert A. and Hunt, James L.: "Use of Temperature-Sensitive Coatings for Obtaining Quantitative Aerodynamic Heat-Transfer Data." AIAA Journal, Vol. 2, No. 7, July 1964, pp. 1354-1356.
5. Hunt, James L., Pitts, Joan I., and Richie, Christine B.: "Application of Phase-Change Technique to Thin Sections with Heating on Both Surfaces." NASA TN D-7193, August 1973.
6. Chen, P. S. and Jones, D. J.: "Three-dimensional Laminar Boundary-Layer Separation on a Flat Plate Due to Flow Confrontation with a Half Cone at Incidence." National Research Council of Canada, Aeronautical Report LR-485, June 1967.
7. Edney, Barry: "Anomalous Heat Transfer and Pressure Distributions on Blunt Bodies at Hypersonic Speeds in the Presence of an Impinging Shock." FFA Report 115, Aeronautical Research Institute of Sweden, 1968.
8. Bertin, John J., Williams, Frank E., and Baker, Robert C.: "Aerothermodynamic Measurements for Space Shuttle Configurations in Hypersonic Wind Tunnels." NASA TM X-2507, pp. 470-501, February 1972.
9. Seegmiller, H. Lee: "Shock Interference Heating and Density Ratio Effects; Part I-Flow Field Visualization, Thermocouple Measurements and Analysis." NASA TM X-2272, pp. 185-215, April 1971.
10. McDevitt, John B and Mellenthin, Jack A.: "Upwash Patterns on Ablating and Nonablating Cones at Hypersonic Speeds." NASA TN D-5346, July 1969.
11. Seegmiller, H. Lee: "Surface-Flow Visualization Investigation of a High Cross Range Shuttle Configuration at a Mach Number of 7.4 and Several Reynolds Numbers." NASA TM X-62036, June 1970.

REFERENCE (CON'T)

12. Marvin, J. G., Lockman, W. K., Mateer, G. G., Seegmiller H. Lee, Pappas C. C., DeRose C., and Kaatari G. E.: "Flow Fields and Aerodynamic Heating of Space Shuttle Orbiters." NASA TM X-2272, pp. 21-73, April 1971.
13. Morkovin, Mark V.: "Observations on Streamwise Vortices in Laminar and Turbulent Boundary Layers." NASA CR-159061, April 1979.
14. Black L. H. and Cuffel, R. F.: "Changes in Heat Transfer from Turbulent Boundary Layers Interacting with Shock Waves and Expansion Waves." AIAA Journal, Vol. 8, No. 10, pp. 1871-1873, October 1970.
15. Keyes, J. Wayne and Hains, Frank D.: "Analytical and Experimental Studies of Shock Interference Heating in Hypersonic Flows." NASA TN D-7139, May 1973.
16. Poll, D. I. A.: "Some Aspects of the Flow Near A Swept Attachment Line with Particular Reference to Boundary Layer Transition." Cranfield College of Aeronautics, C of A Report 7805, August 1978.
17. Helms, Vernon T. III: "Leeward Centerline and Side Fuselage Entry Heating Predictions for the Space Shuttle Orbiter." NASA CP-2283, pp. 913-947, March 1983.
18. Maskell, E. C.: "Flow Separation in Three-Dimensions." RAE Aeronautical Report 2565, November 1955.
19. Hunt, James L. and Creel, Theodore R. Jr.: "Shock Interferences Heating and Density Ratio Effects; Part II-Hypersonic Density Ratio Effects." NASA TM X-2272, pp. 217-243, April 1971.

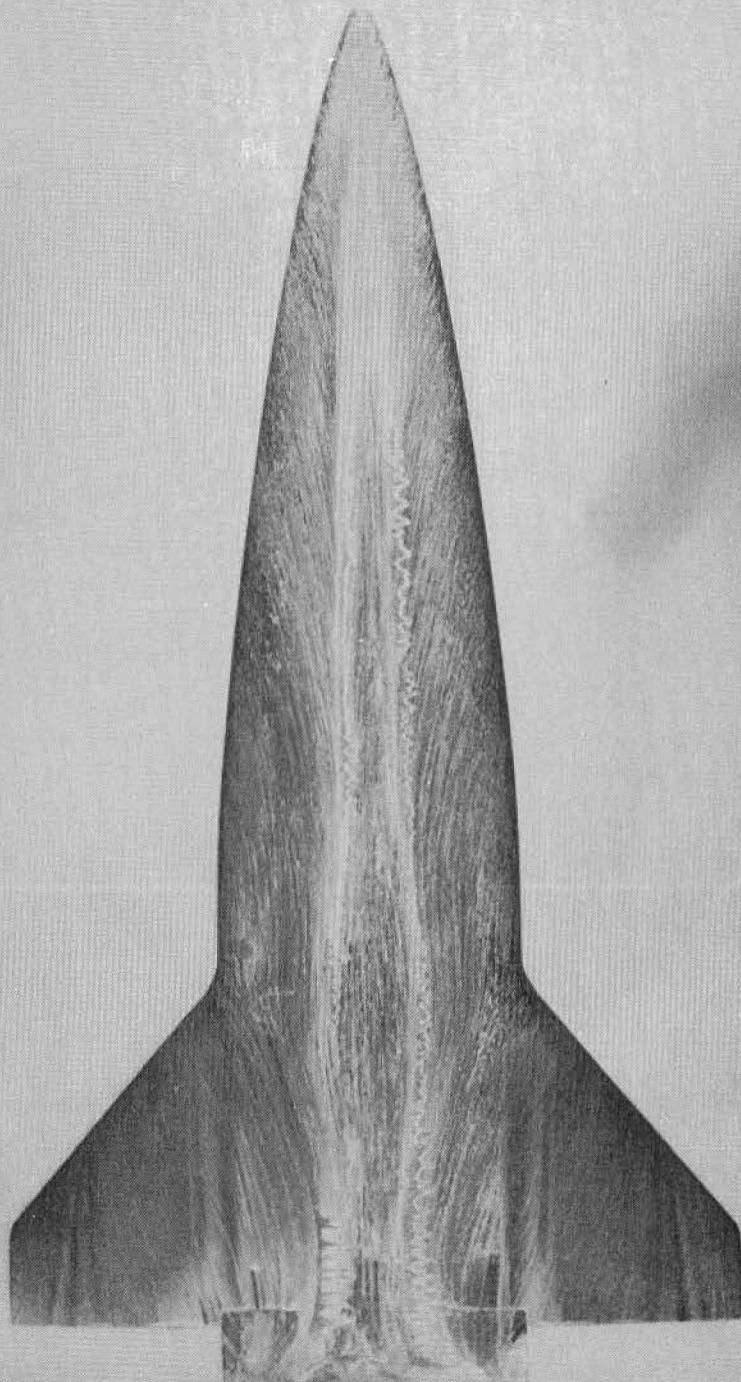


(a) TOP VIEW



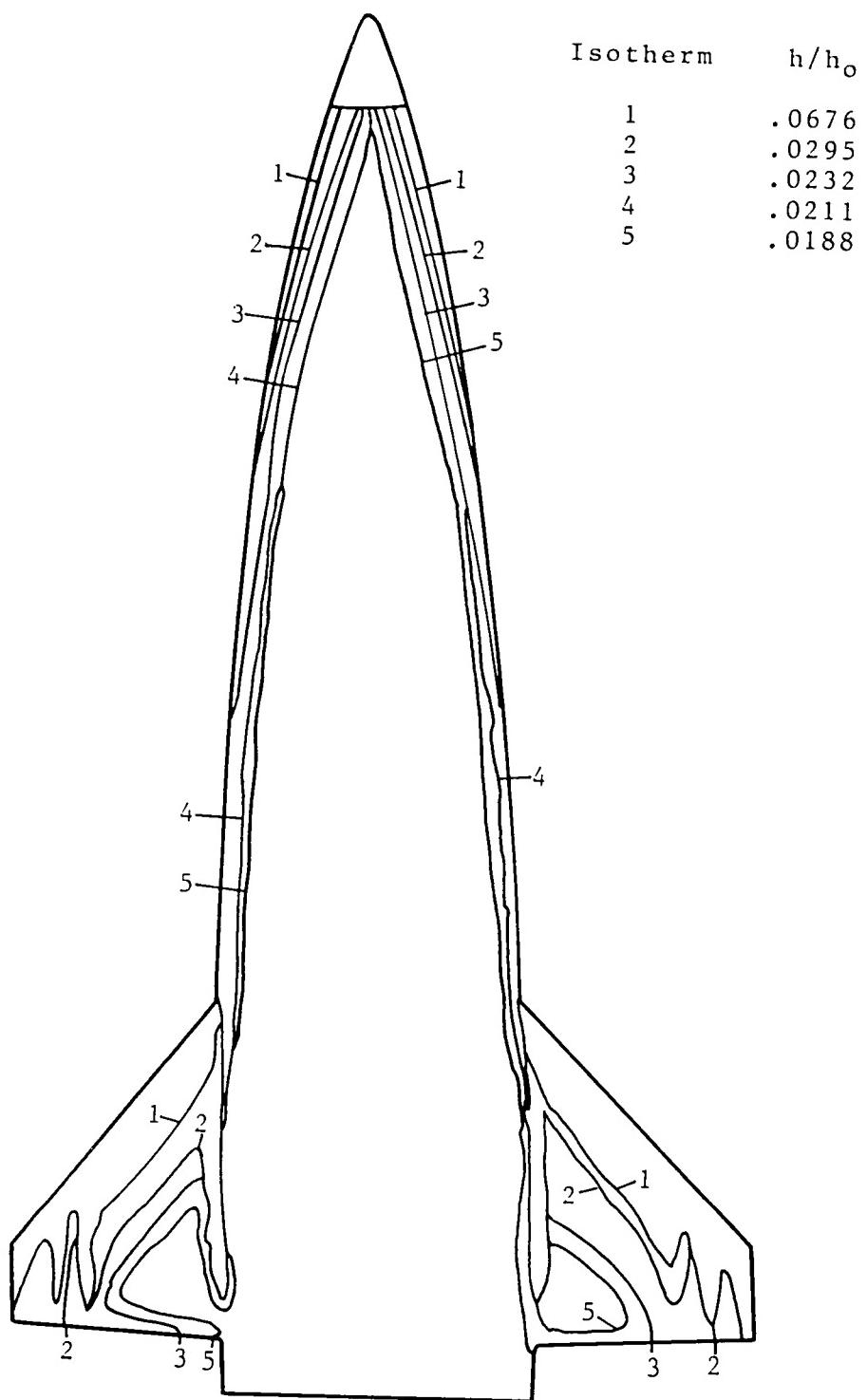
(b) SIDE VIEW

Figure 1.- Diagram showing CCV geometry.



(a) Oil flow - bottom view.

Figure 2.- Heat transfer data and oil flow patterns at $\alpha = 0^\circ$ and $Re_\infty = 2.0 \times 10^6$.

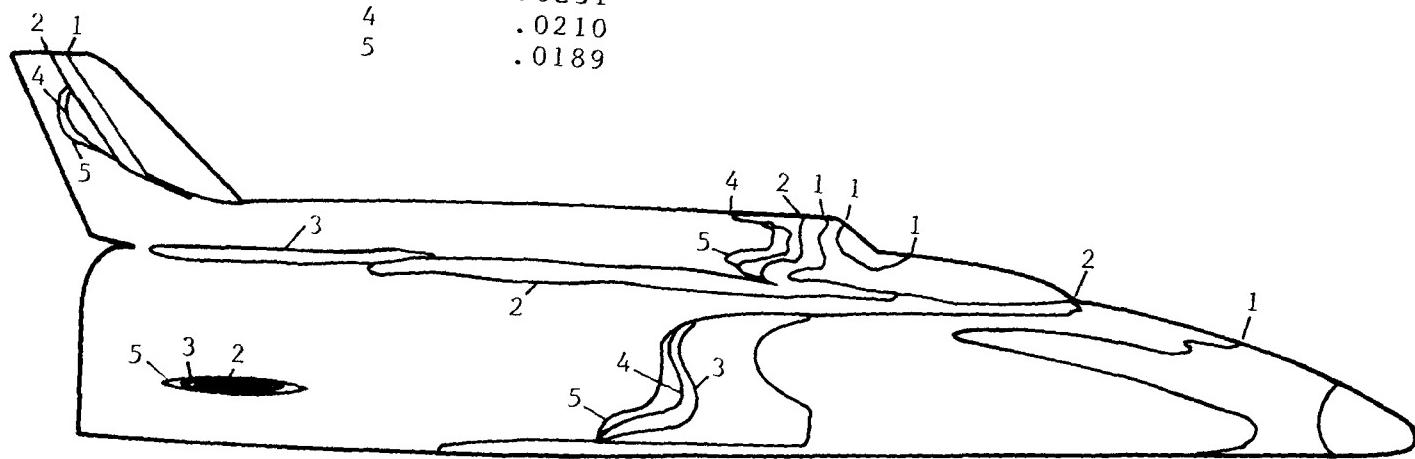


(b) Heating contours - bottom view.
Figure 2.- Continued.

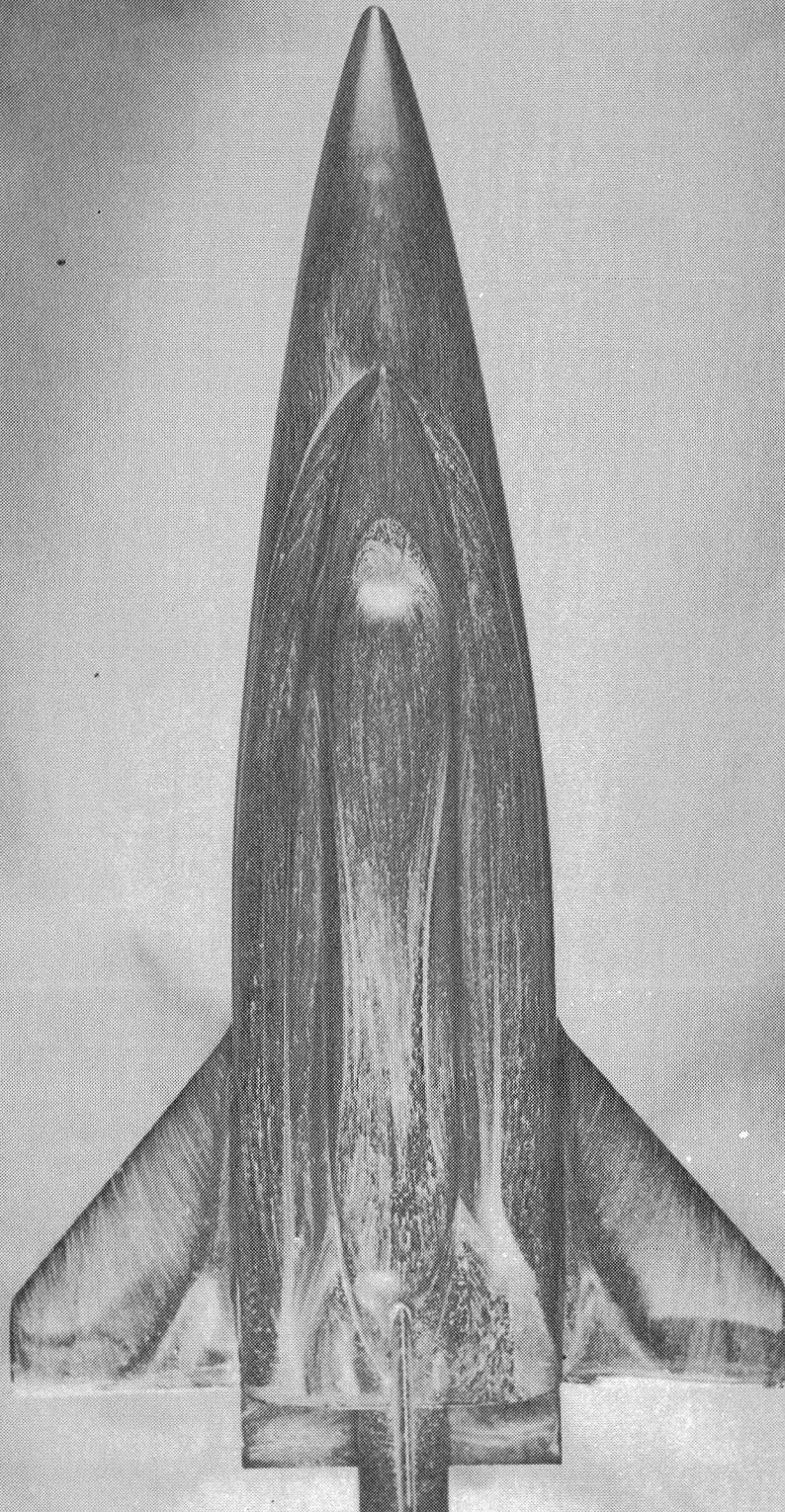


(c) Oil flow - side View.
Figure 2.- Continued.

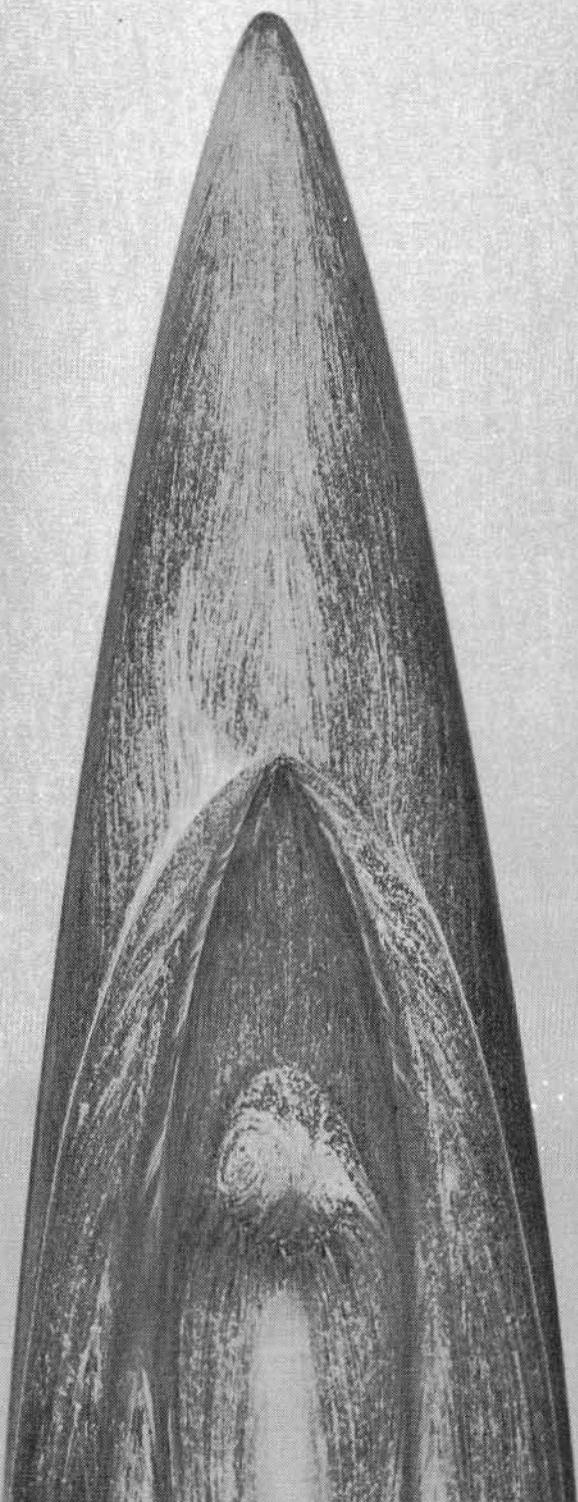
Isotherm	h/h_o
1	.0448
2	.0320
3	.0231
4	.0210
5	.0189



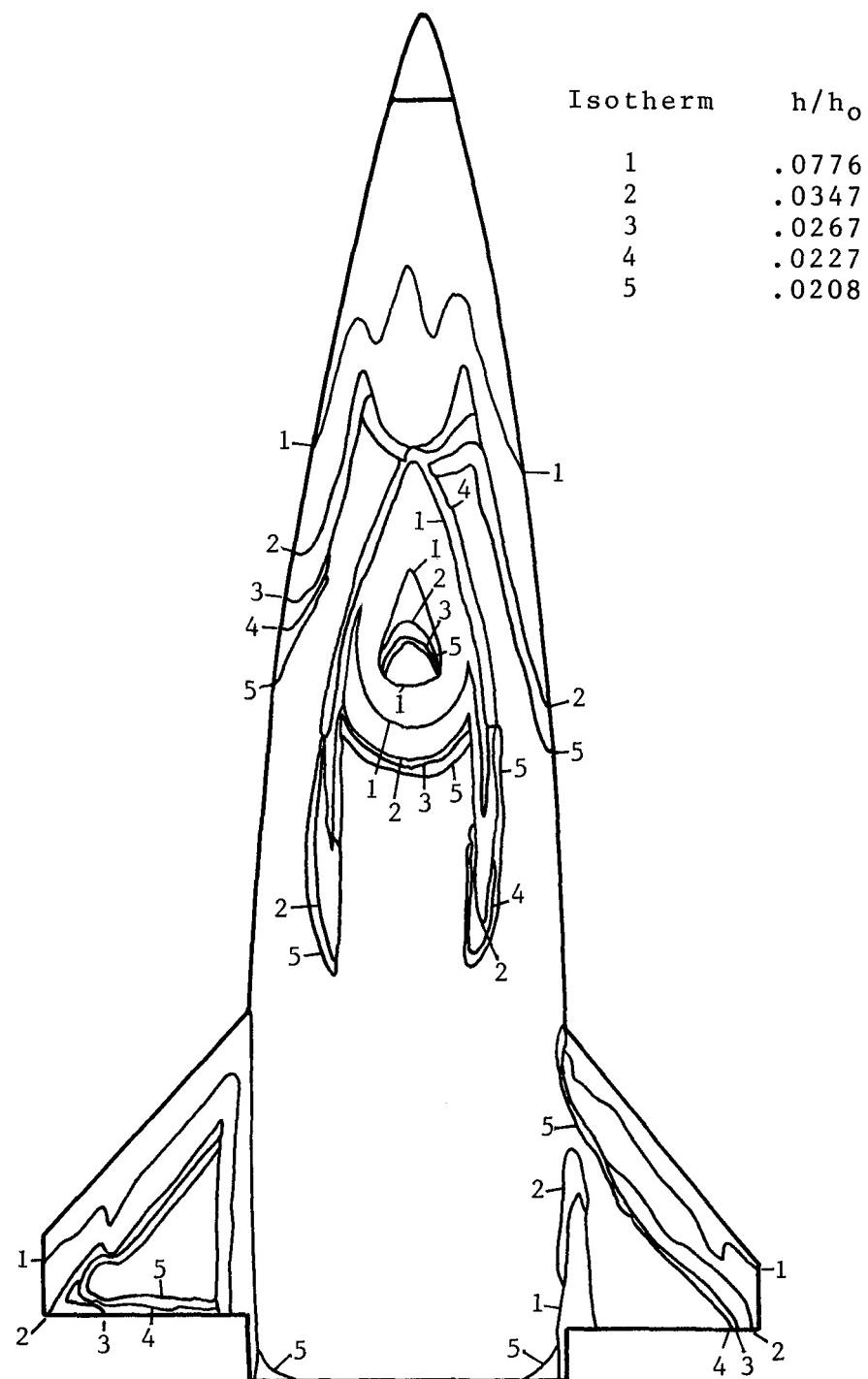
(d) Heating contours - side view.
Figure 2.- Continued.



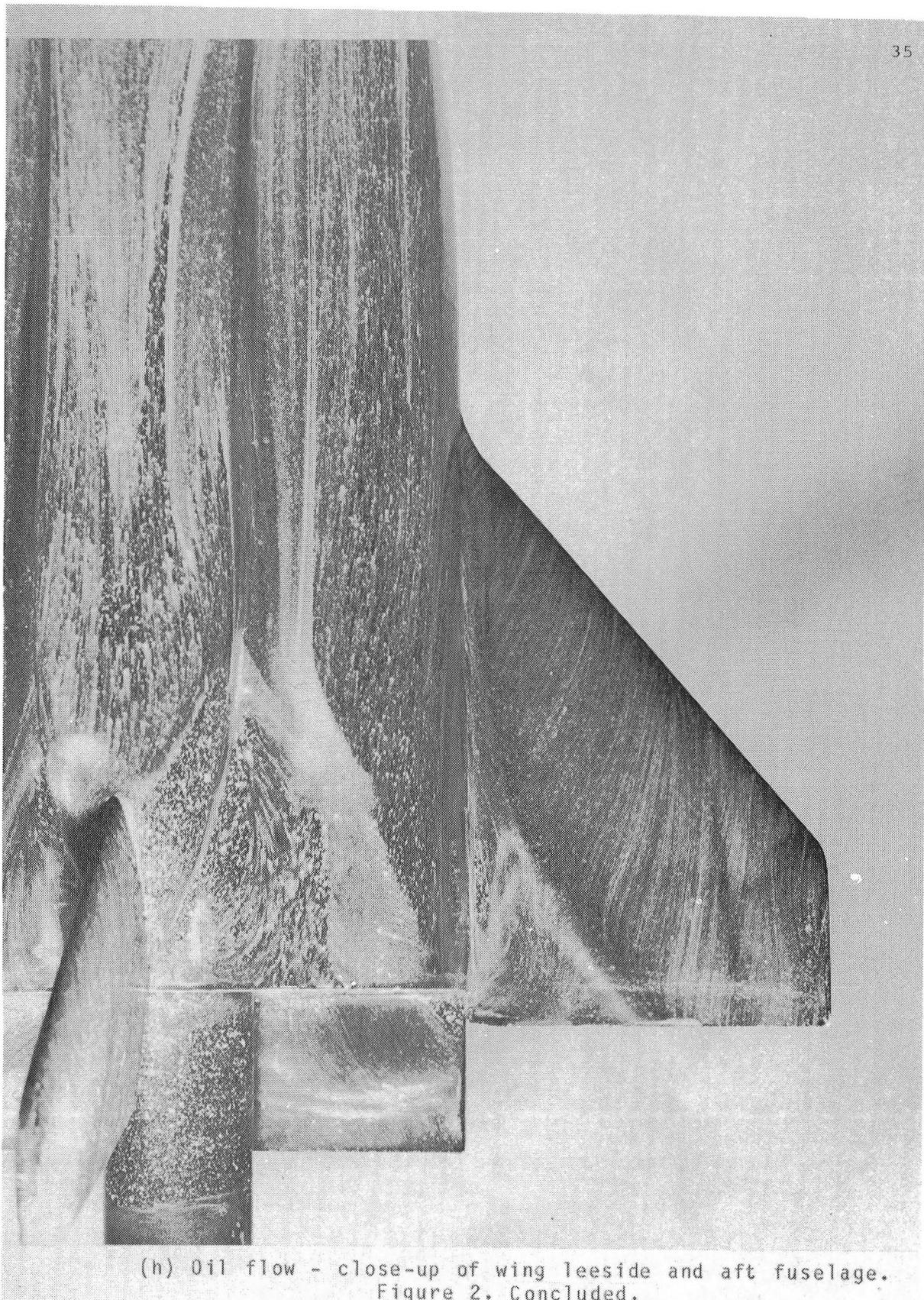
(e) Oil flow - top view.
Figure 2. Continued.



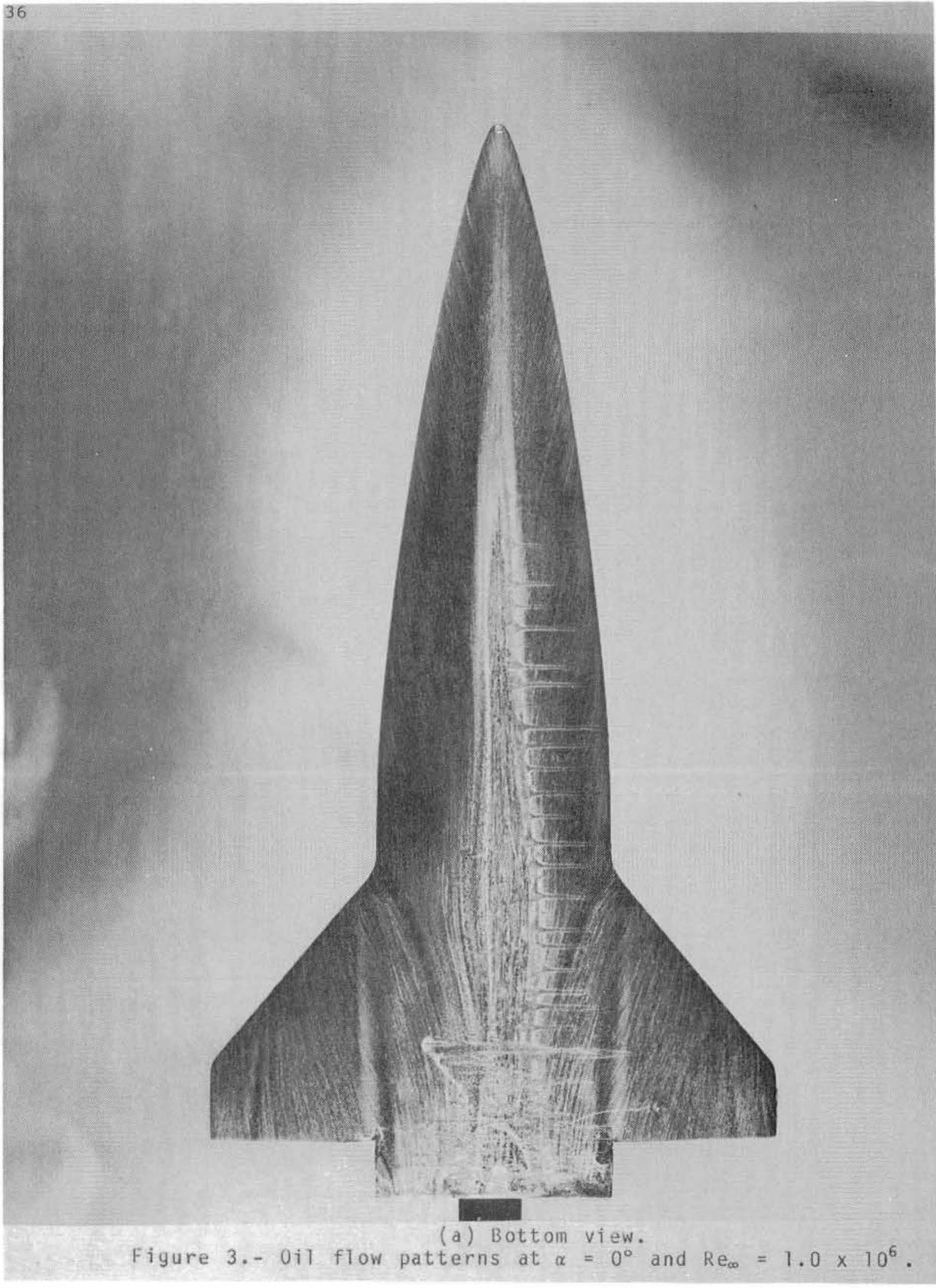
(f) Oil flow - closeup of canopy.
Figure 2.- Continued.

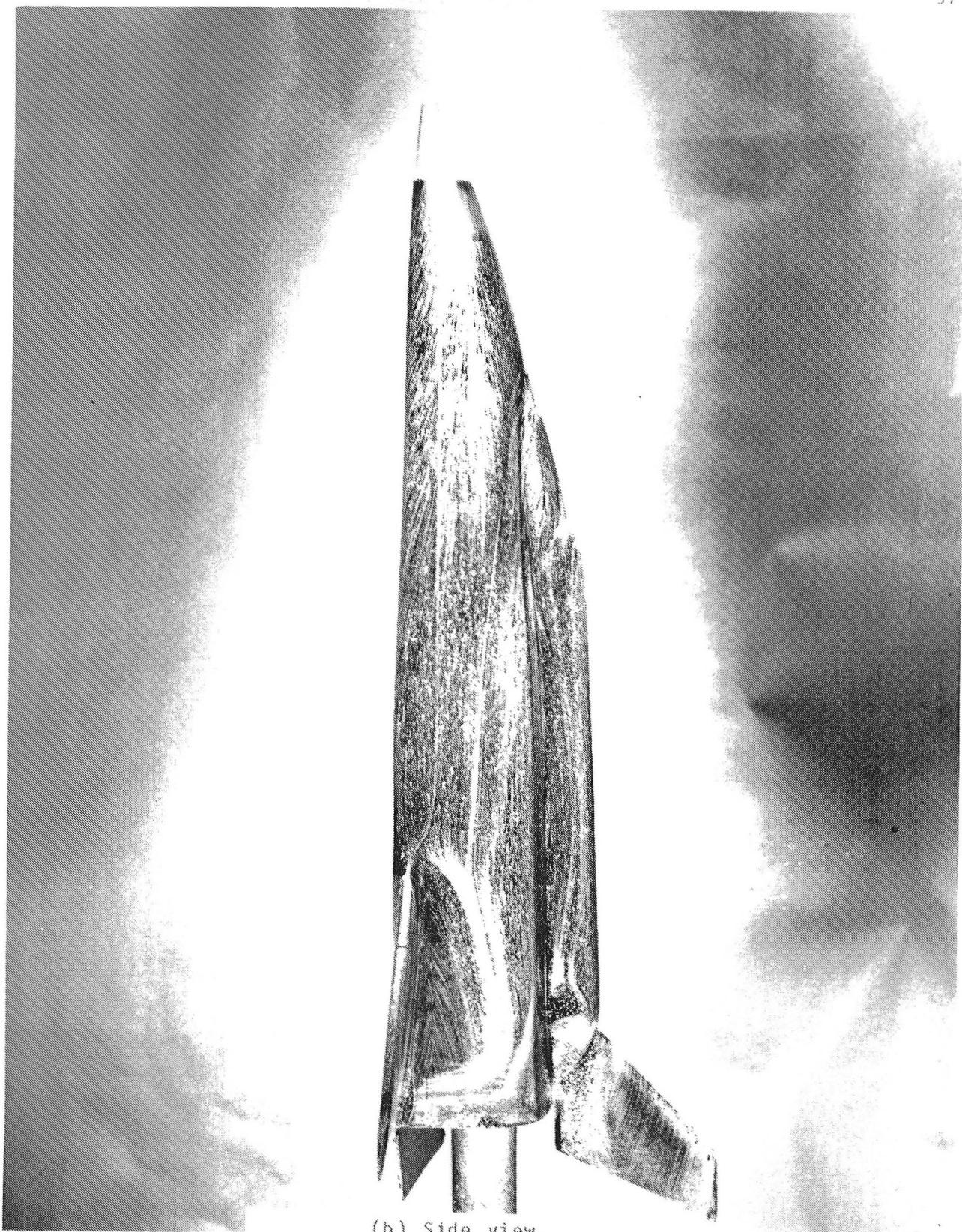


(g) Heating contours - top view.
Figure 2.- Continued.

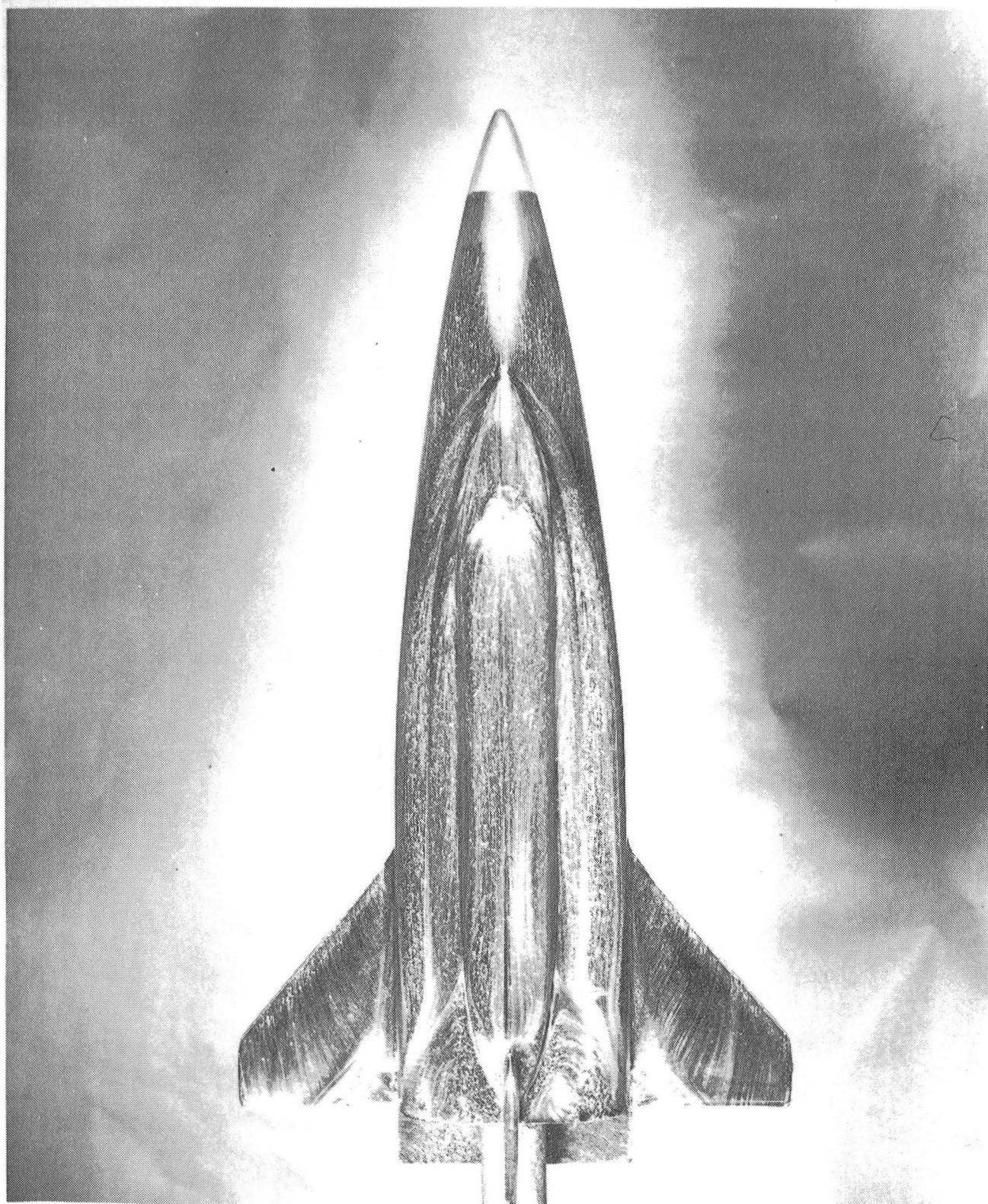


(h) Oil flow - close-up of wing leeside and aft fuselage.
Figure 2. Concluded.

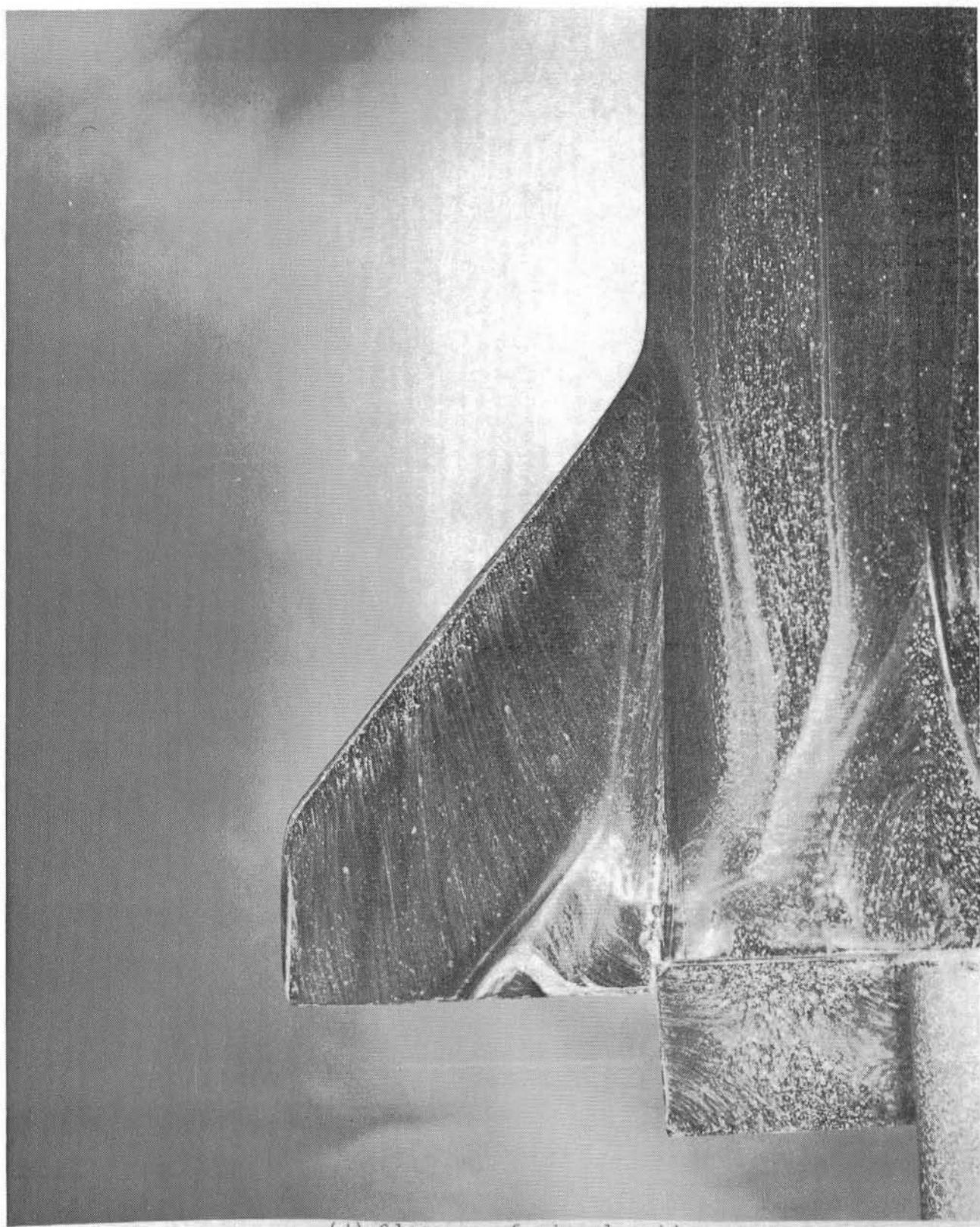




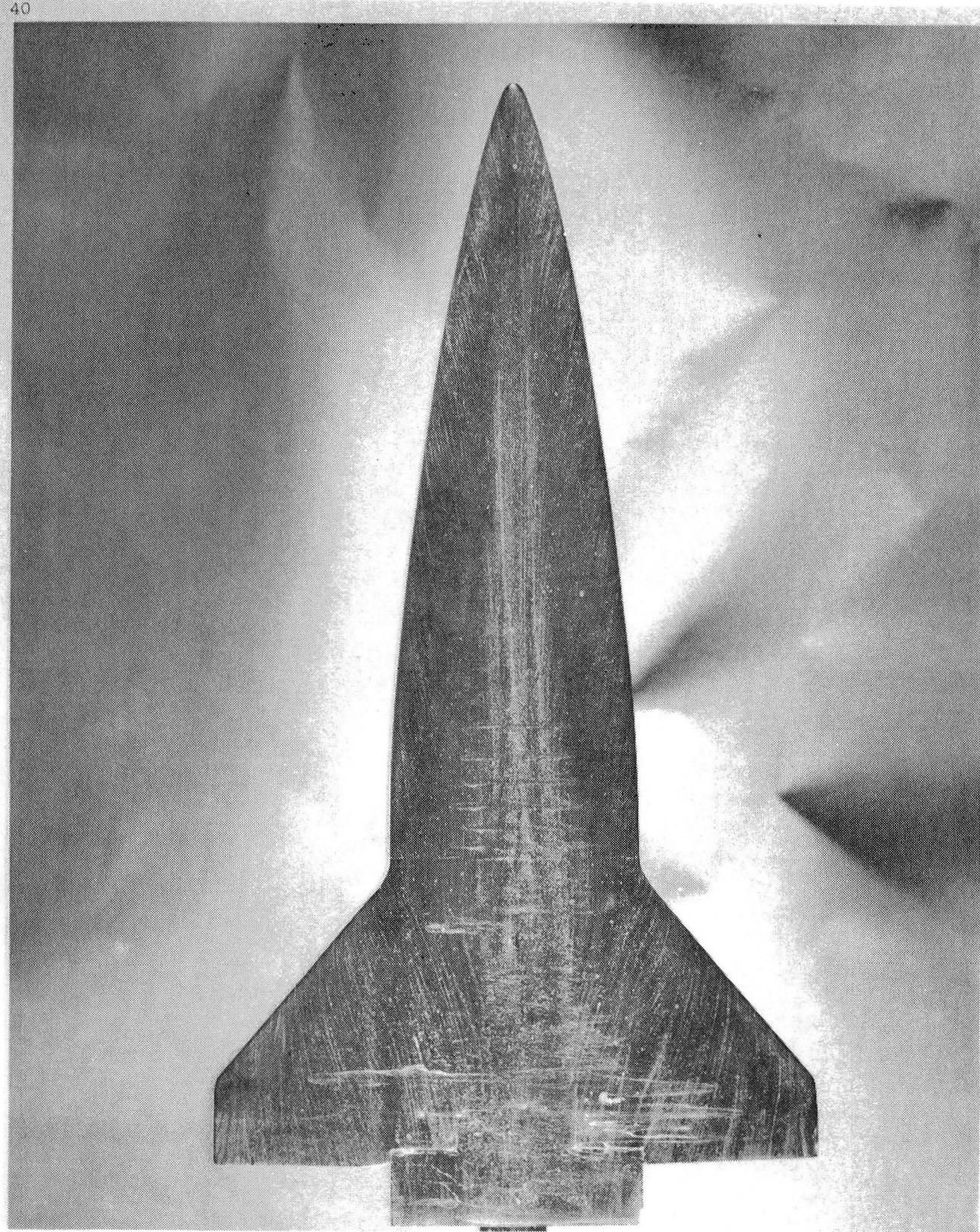
(b) Side view.
Figure 3.- Continued.



(c) Top view.
Figure 3.- Continued.

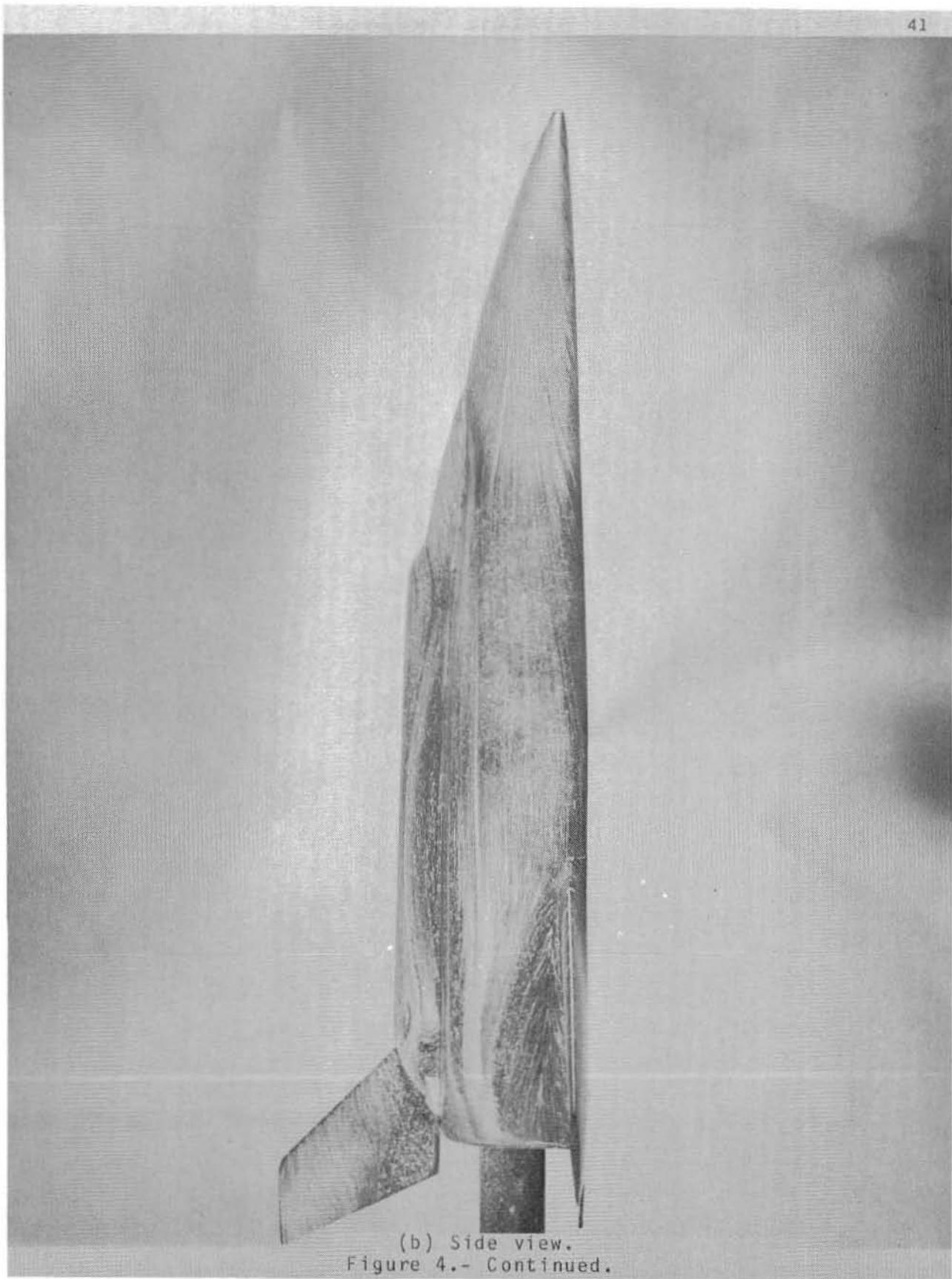


(d) Close-up of wing leeside.
Figure 3.- Concluded.

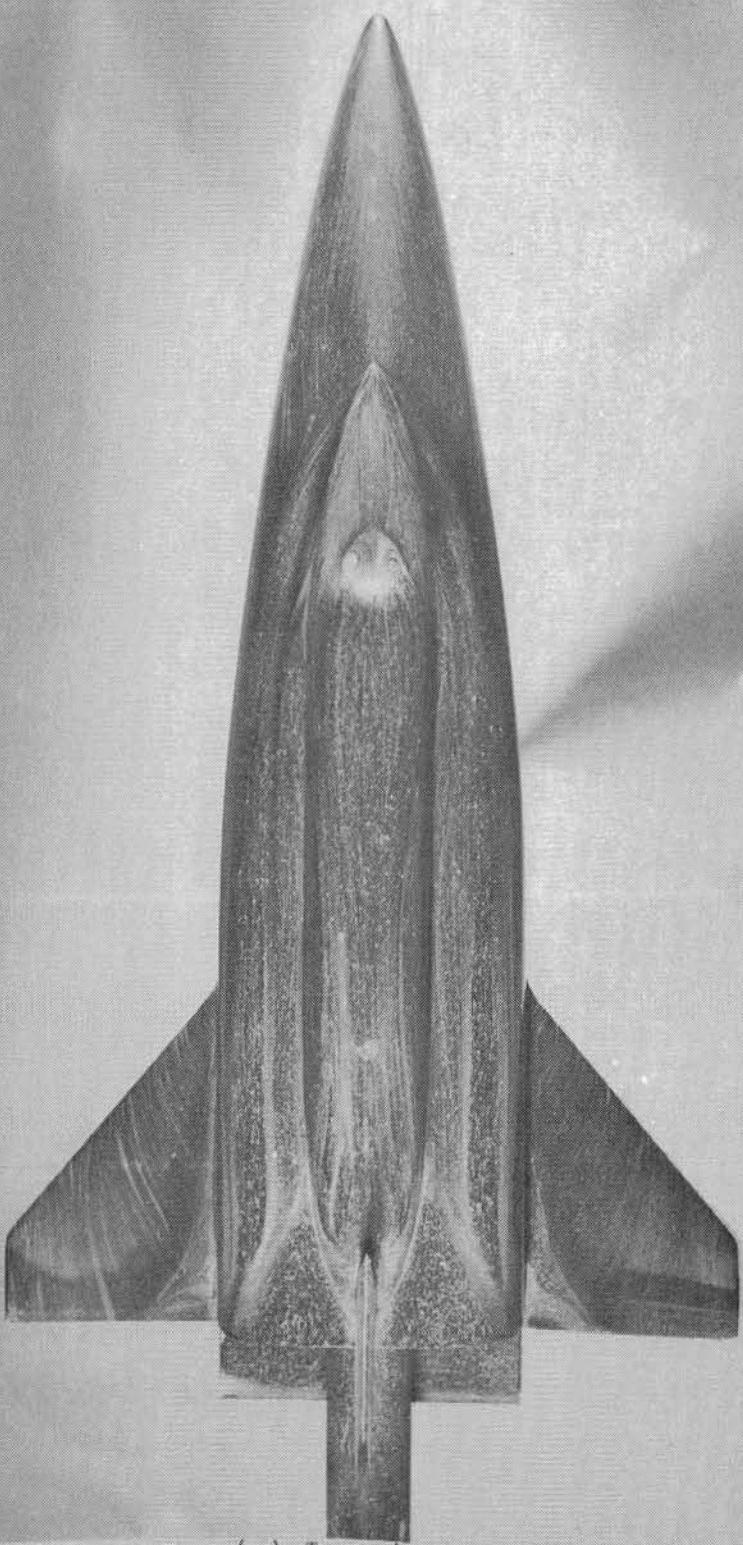


(a) Bottom view.

Figure 4.- Oil flow patterns at $\alpha = 0^\circ$ and $Re_\infty = 0.5 \times 10^6$.



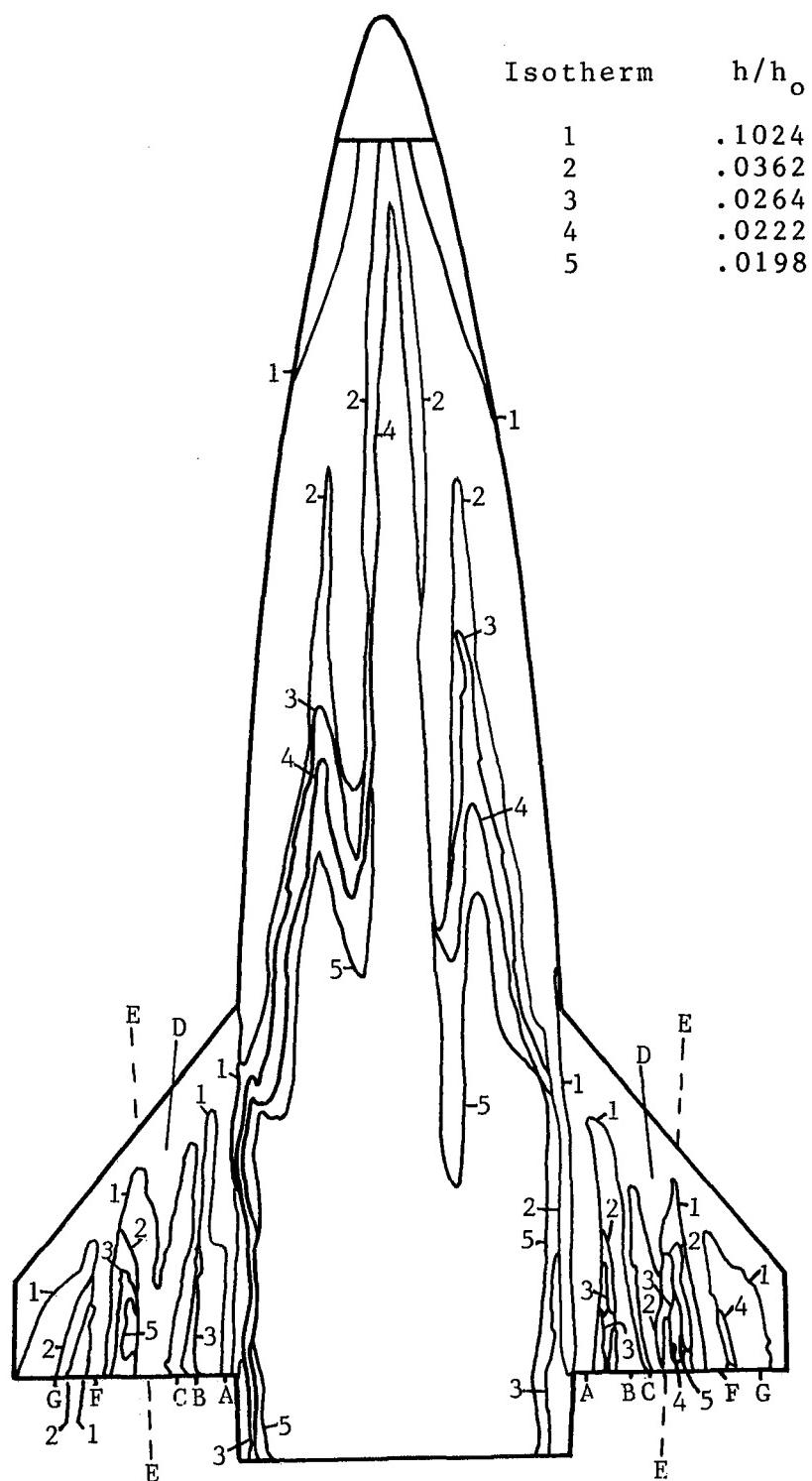
(b) Side view.
Figure 4.- Continued.



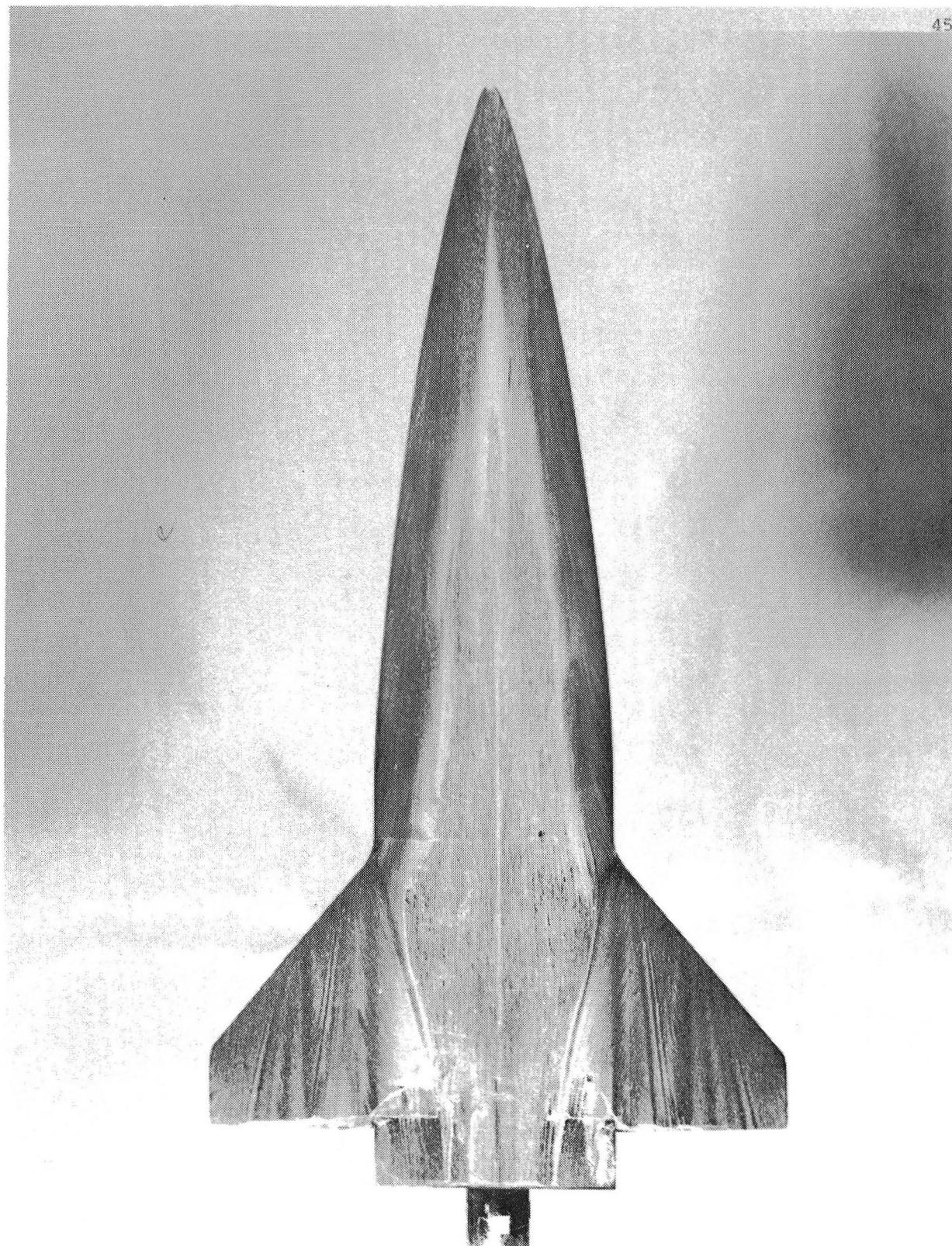
(c) Top view.
Figure 4.- Continued.



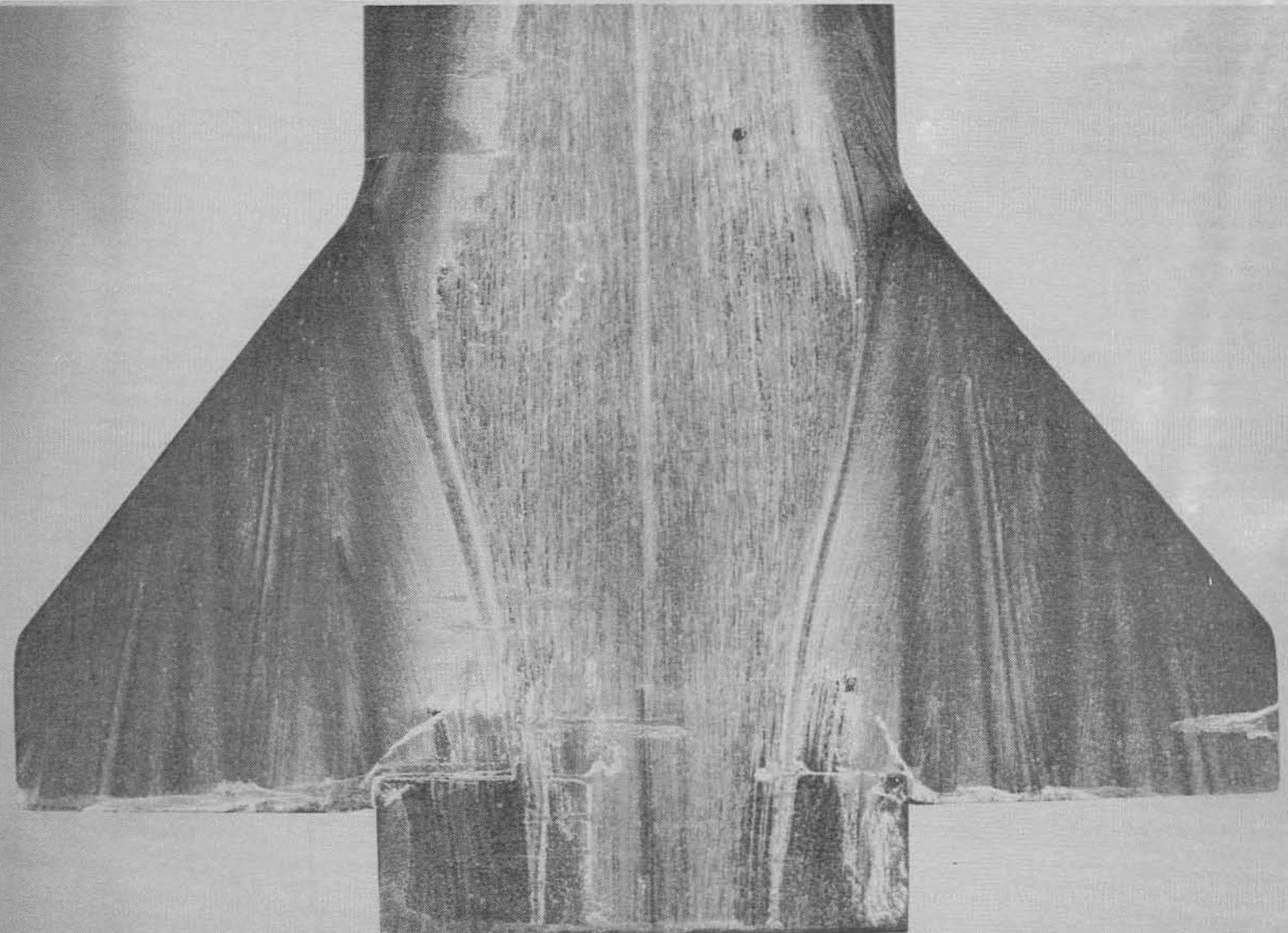
(d) Close-up of wing leeside.
Figure 4.- Concluded.



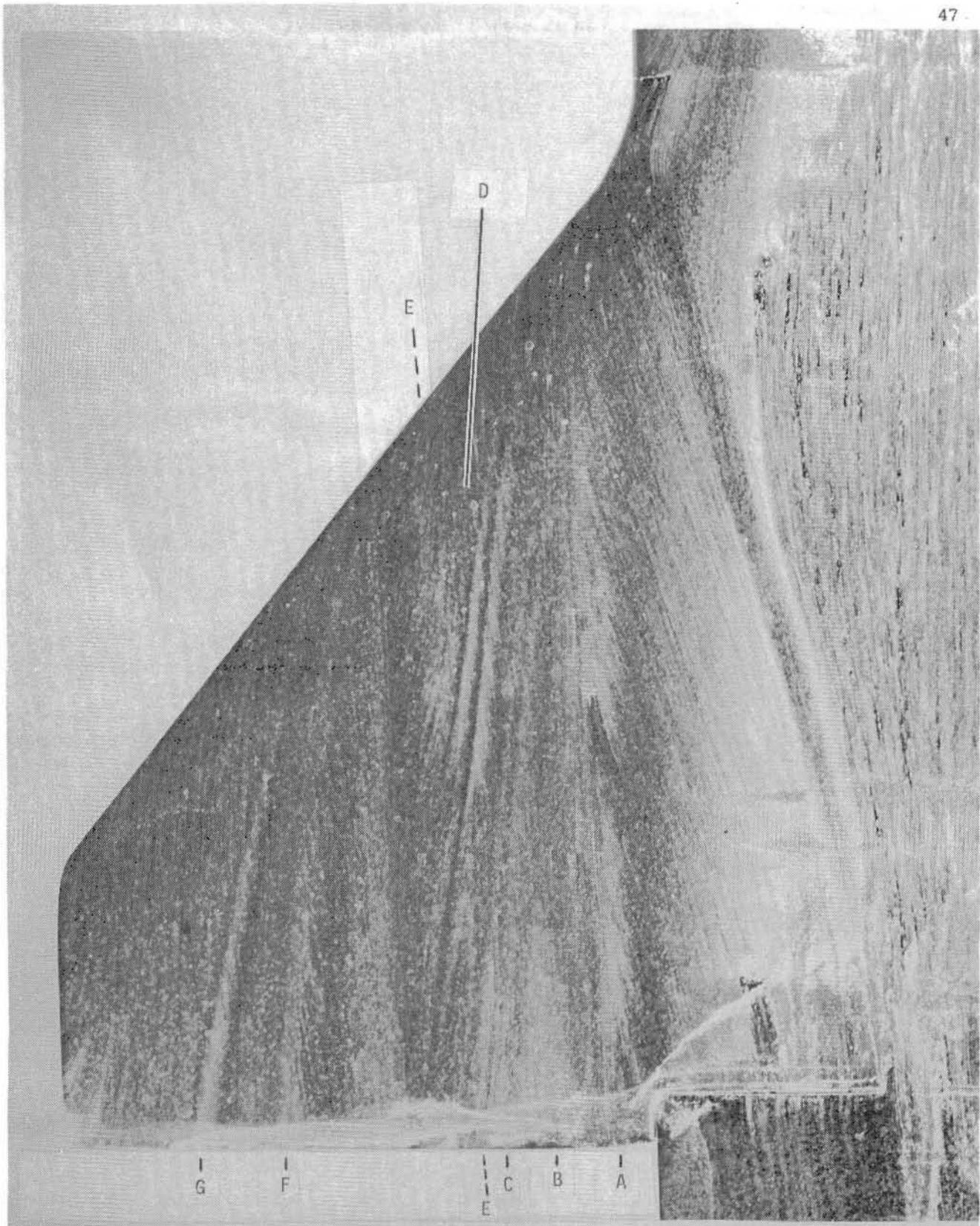
(a) Heating contours - bottom view.
 Figure 5.- Heat transfer data and oil flow patterns at $\alpha = 10^\circ$ and $Re_\infty = 2.0 \times 10^6$.



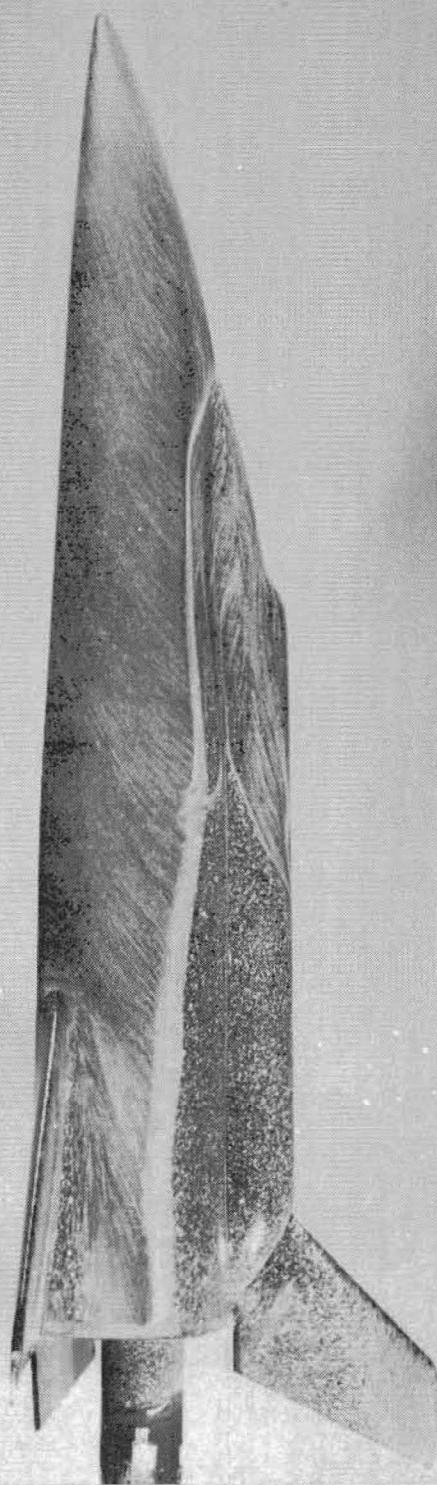
(b) Oil flow -bottom view.
Figure 5.- Continued.



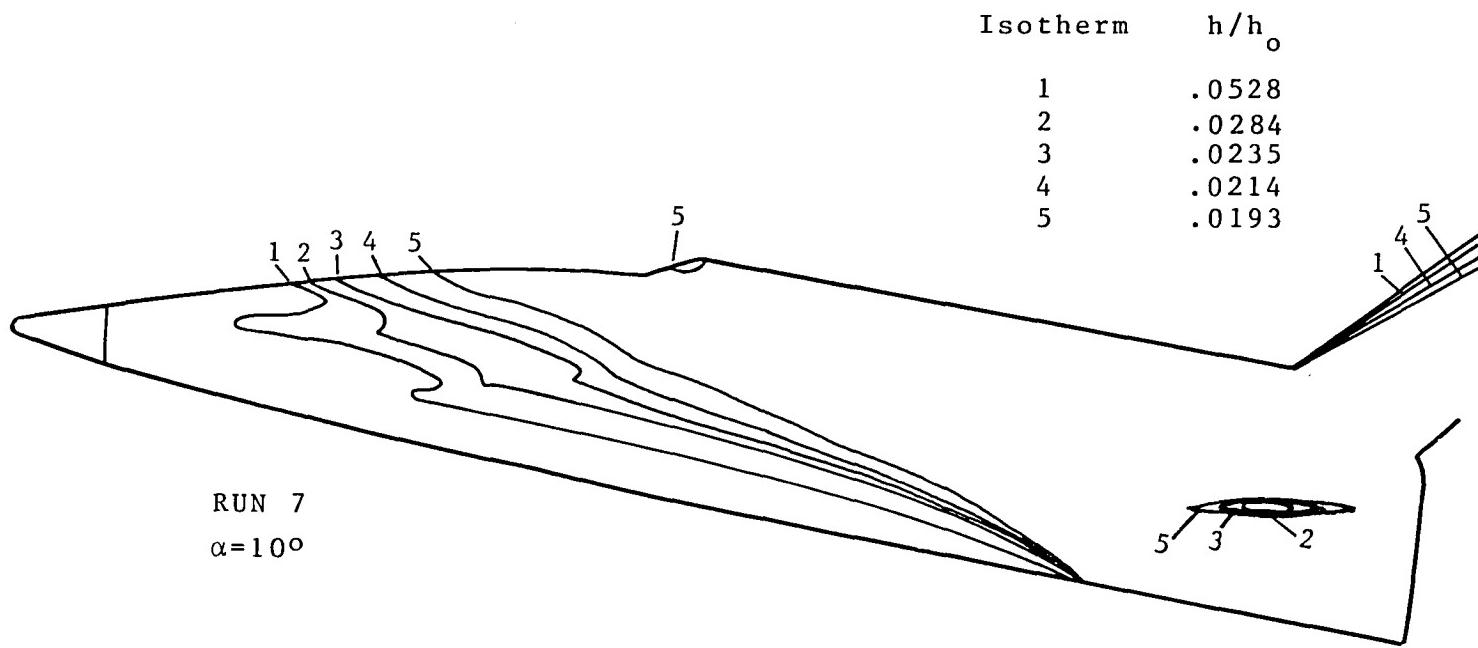
(c) Oil flow-wing interference patterns.
Figure 5.- Continued.



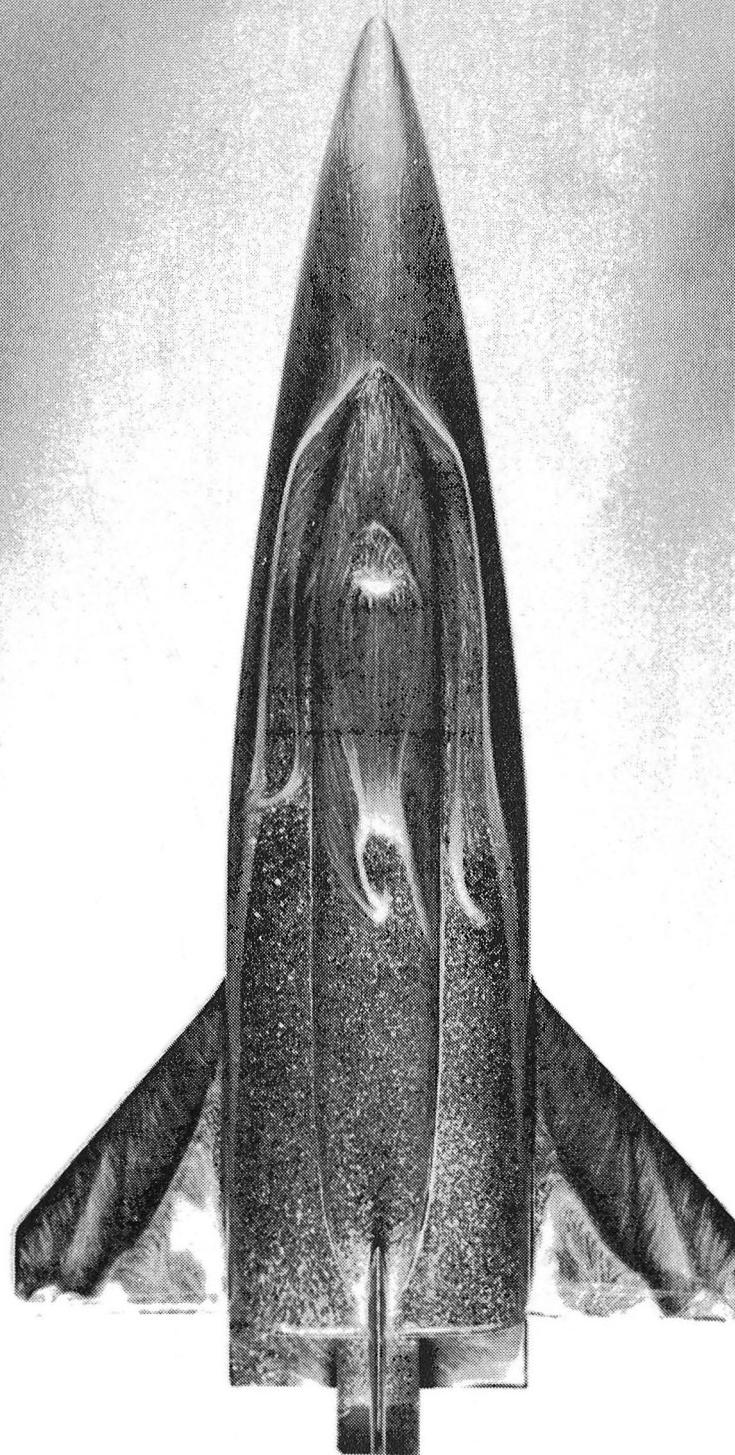
(d) Oil flow-interference patterns on left wing.
Figure 5.- Continued.



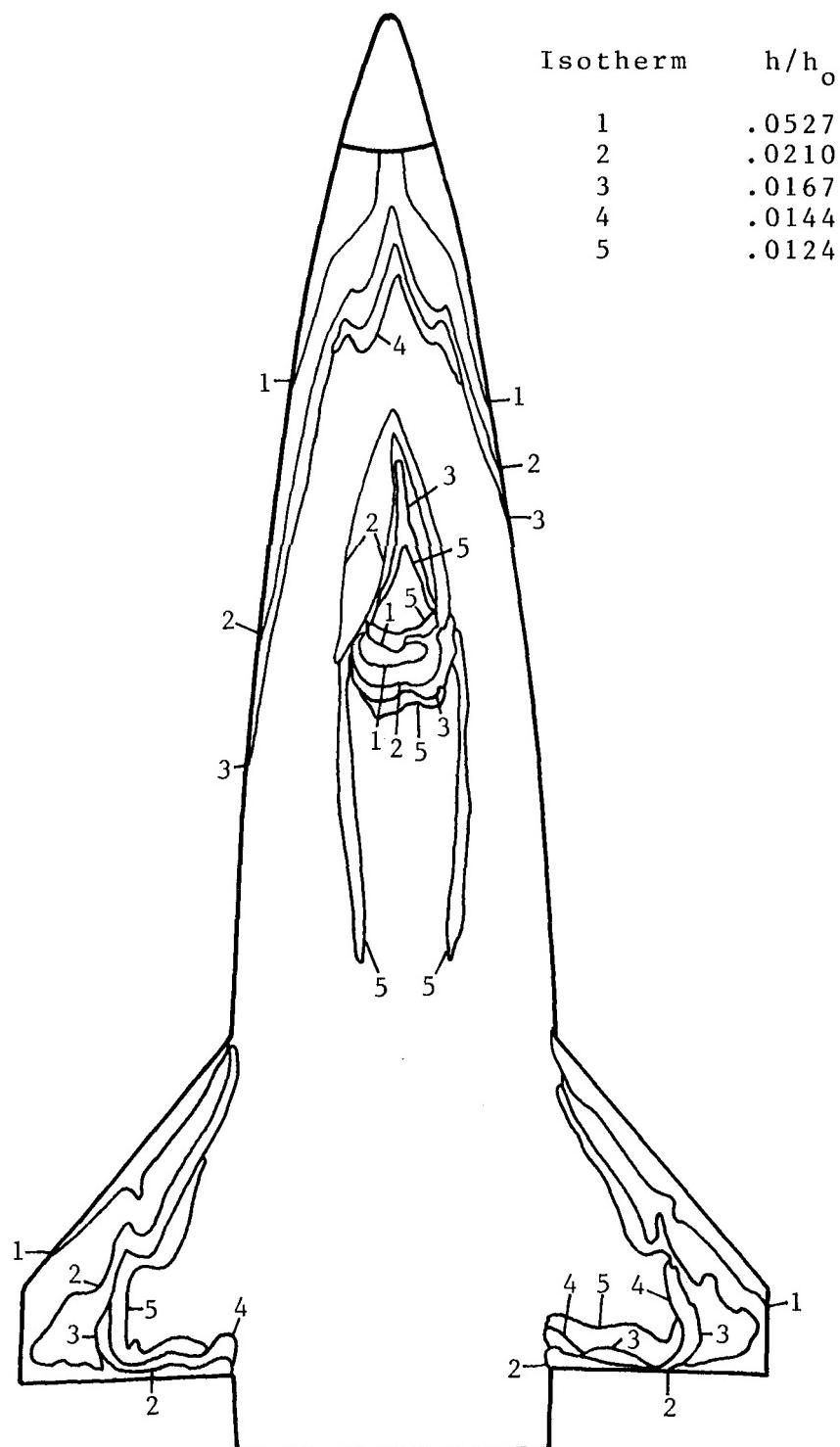
(e) Oil flow - side view.
Figure 5.- Continued.



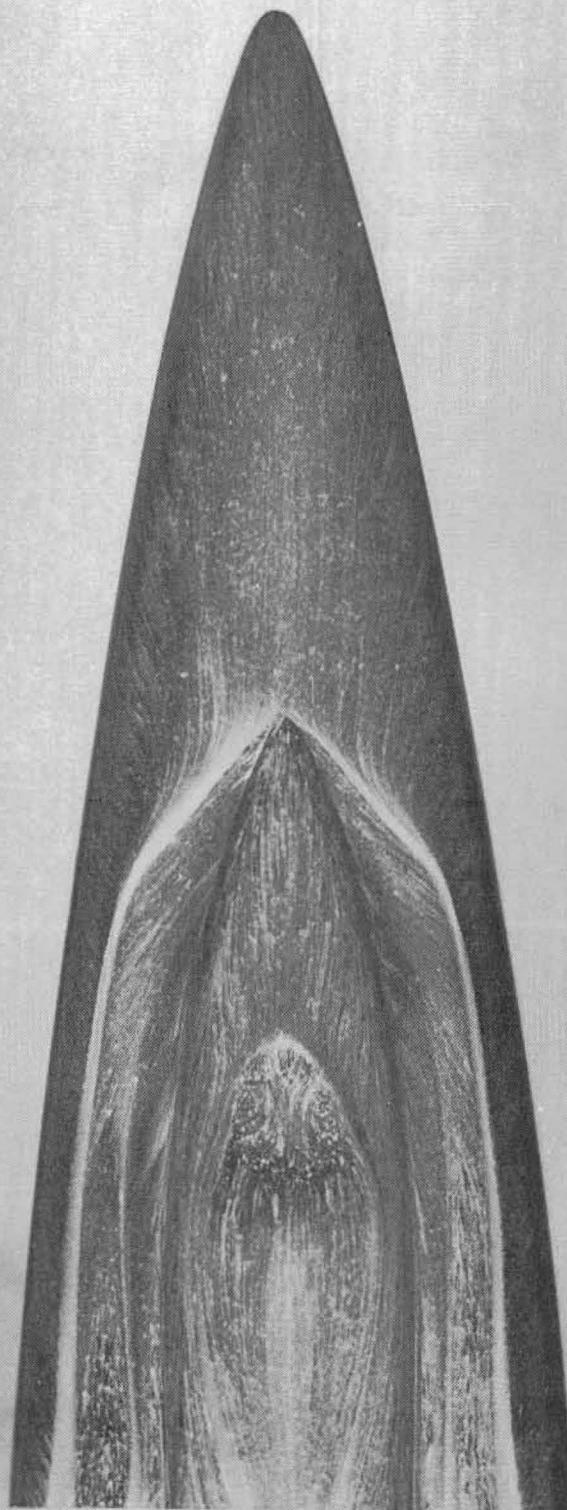
(f) Heating contours - side view.
 Figure 5.- Continued.



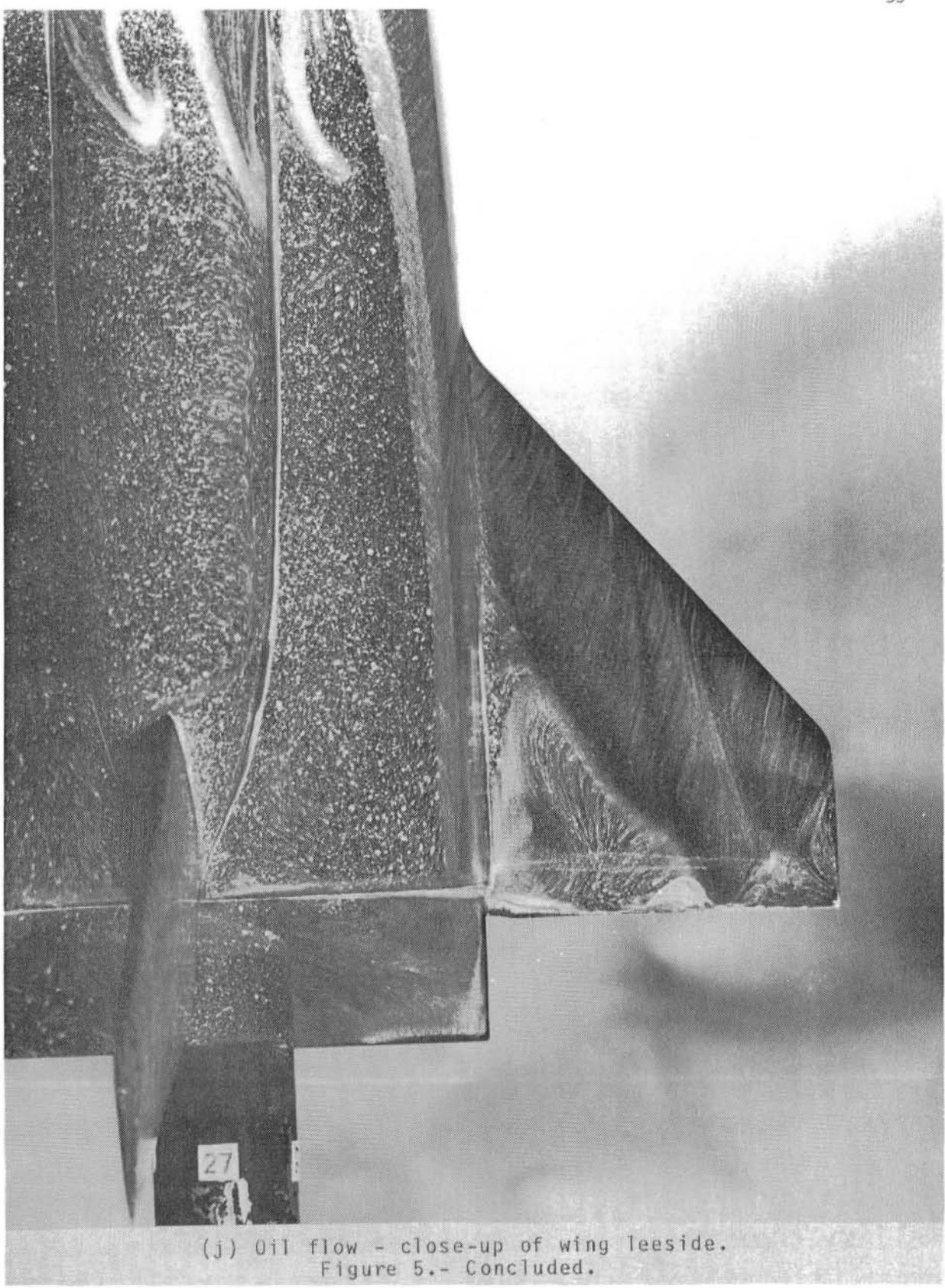
(g) Oil flow - top view.
Figure 5.- Continued.



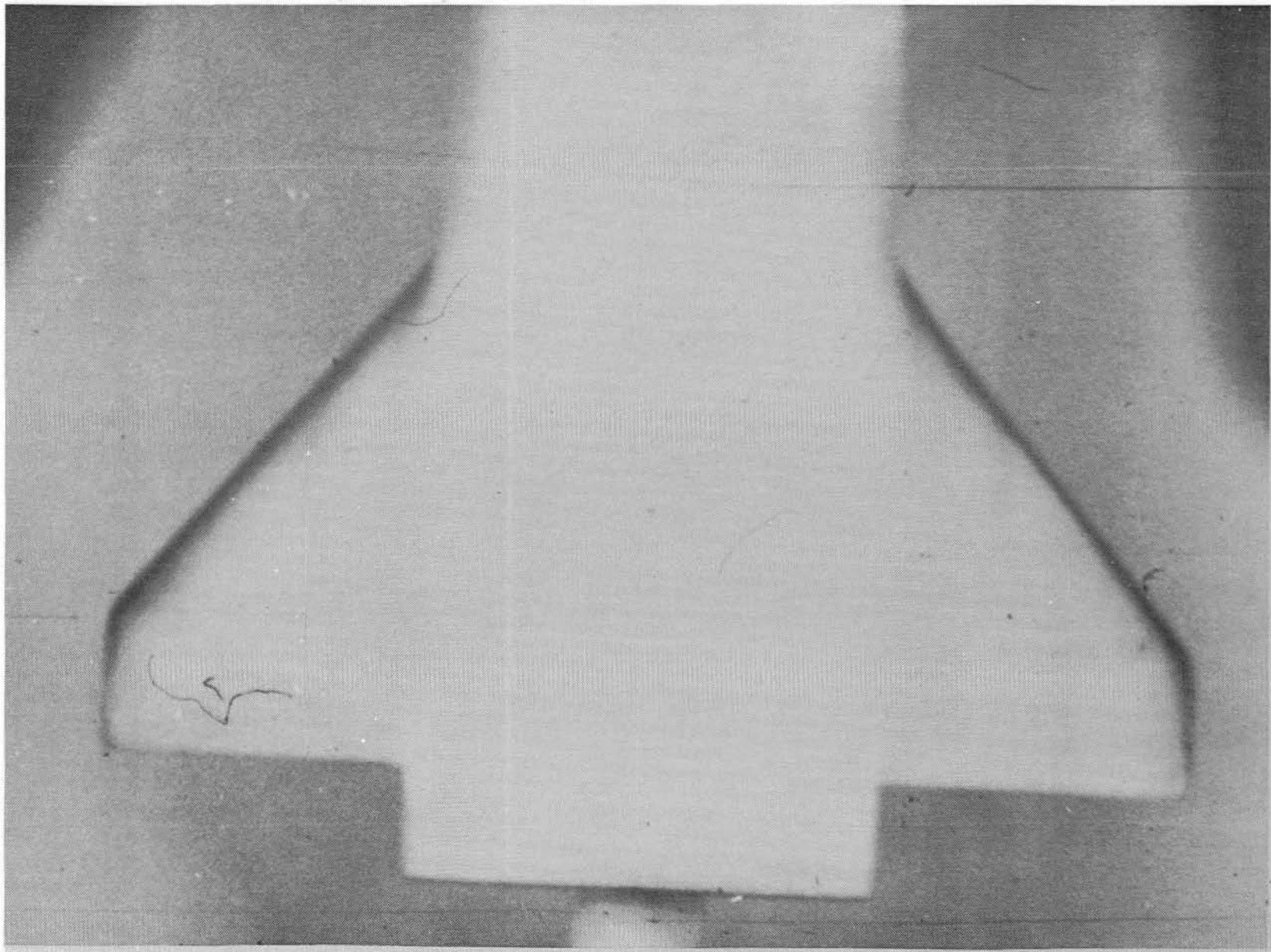
(h) Heating contours - top view.
Figure 5.- Continued.



(i) Oil flow - close-up of canopy.
Figure 5.- Continued.

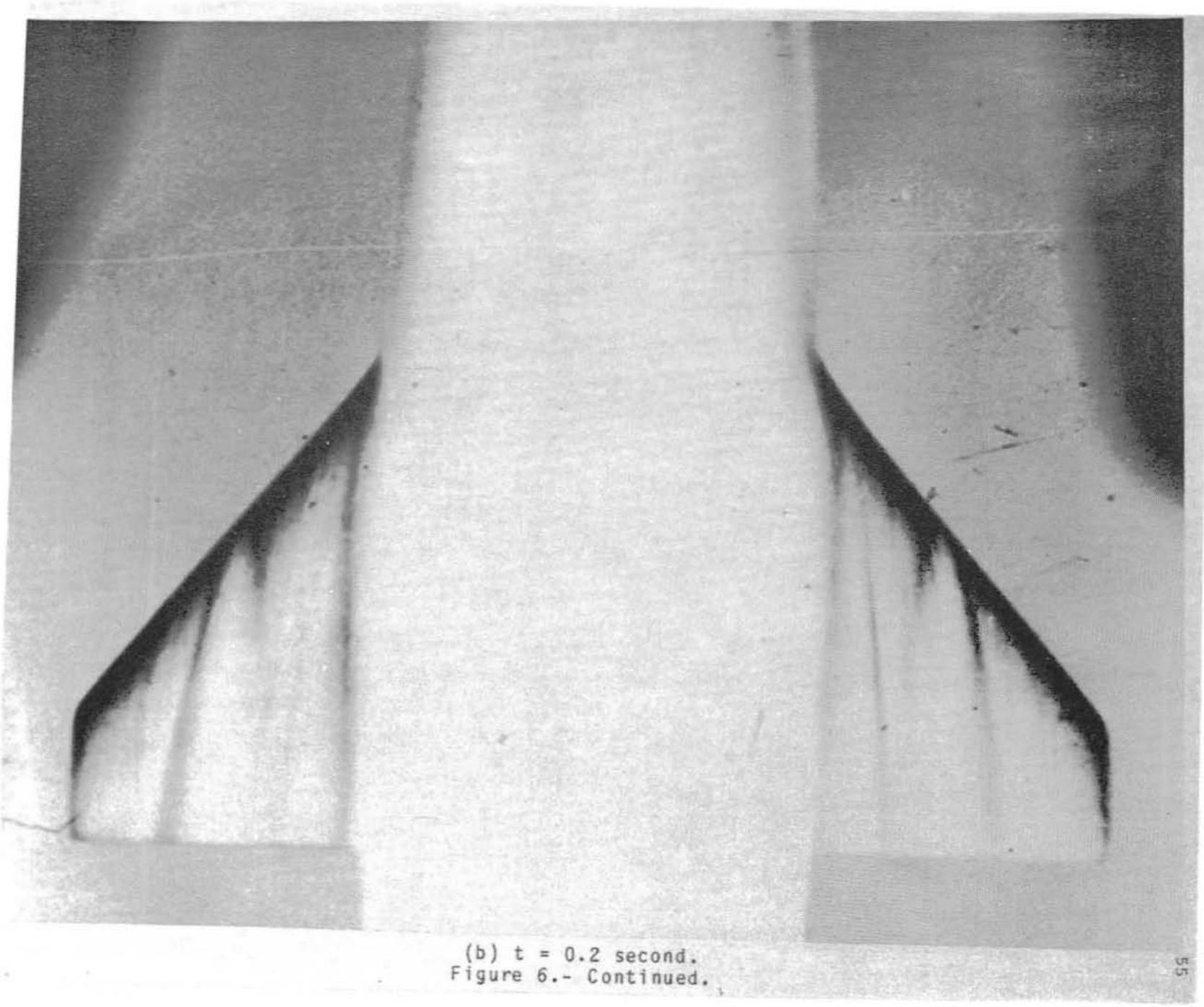


(j) Oil flow - close-up of wing teeside.
Figure 5.- Concluded.

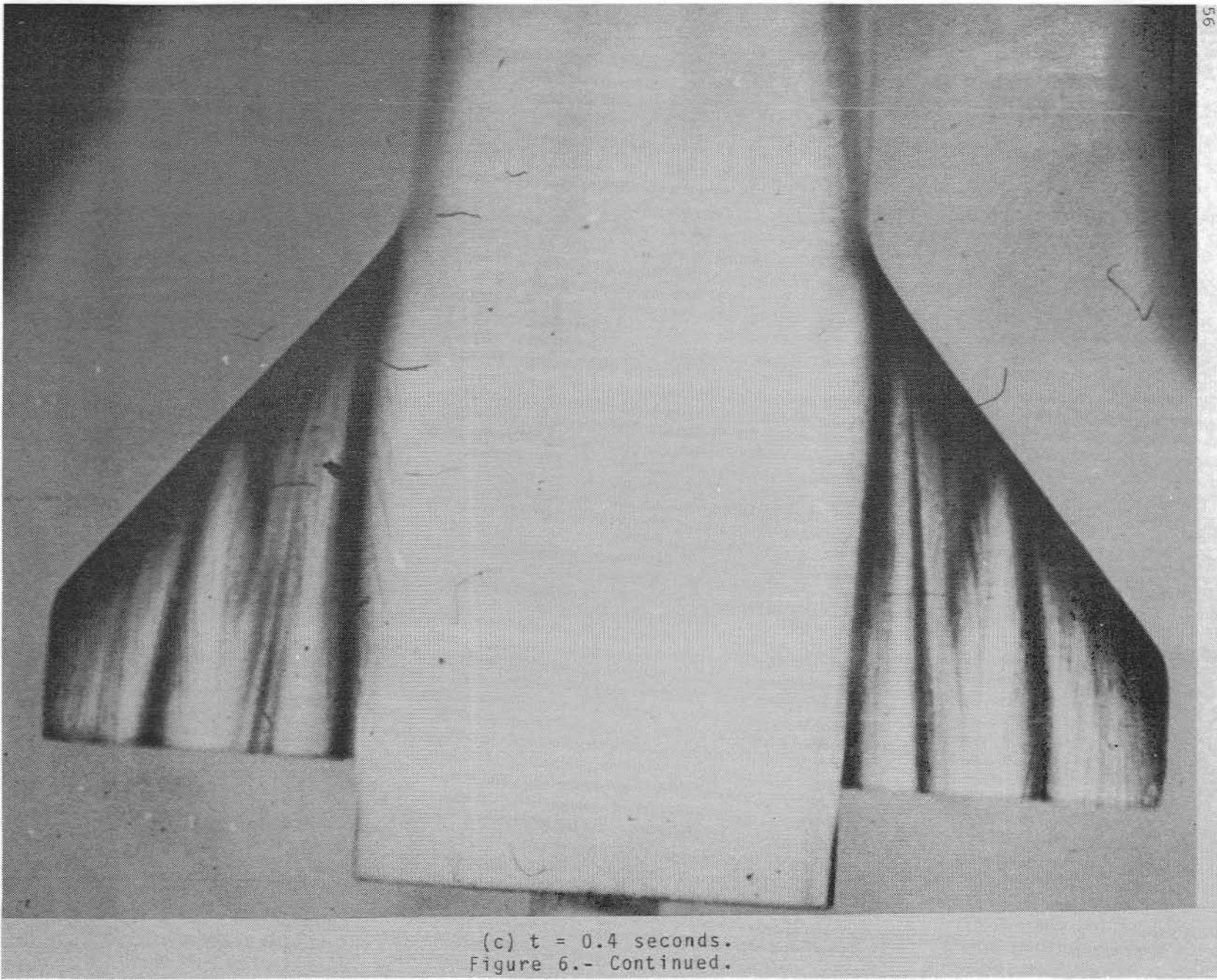


(a) $t = 0.1$ second.

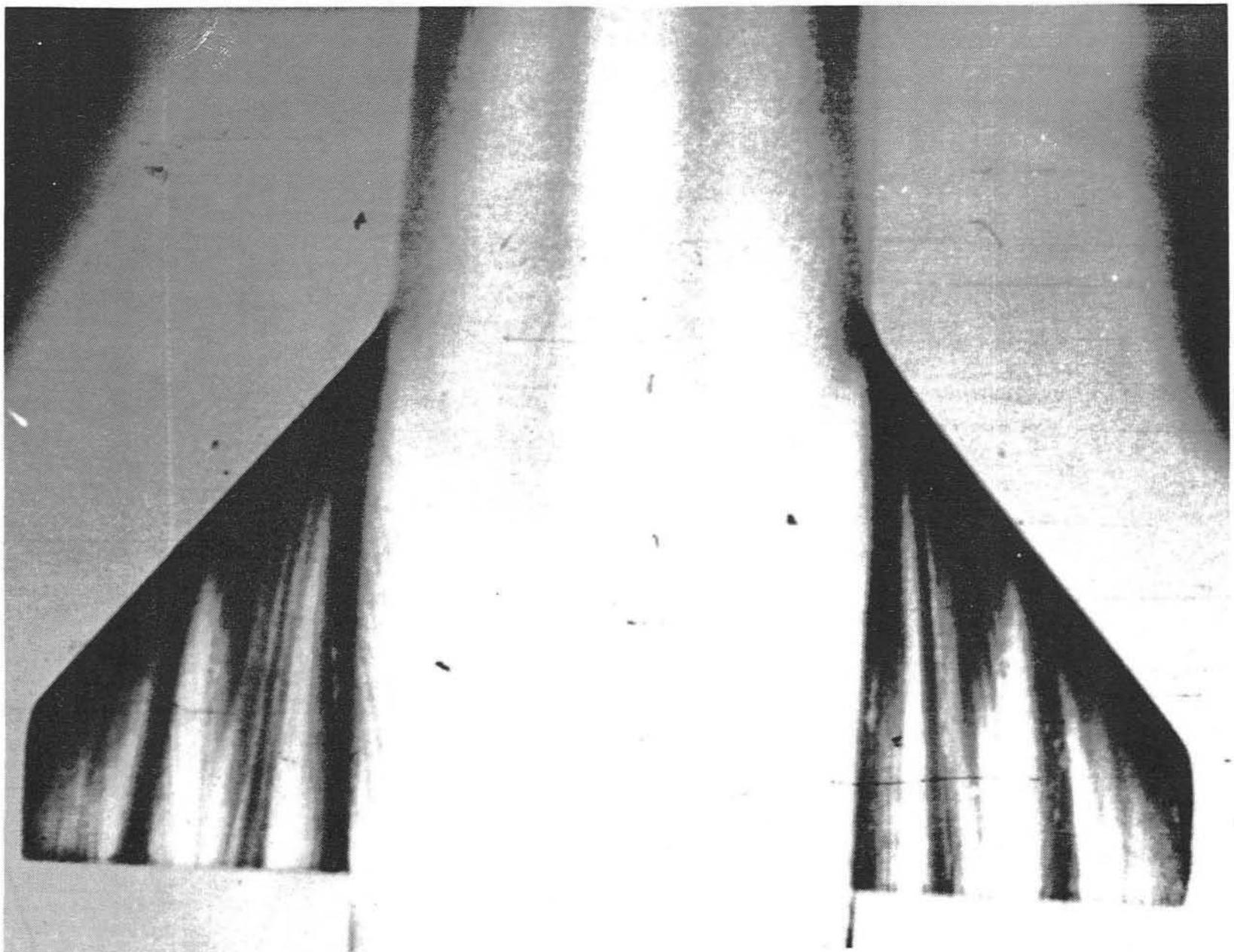
Figure 6.- Development of wingward surface streak heating pattern in phase change paint at $\alpha = 10^\circ$ and $Re_\infty = 2.0 \times 10^6$.



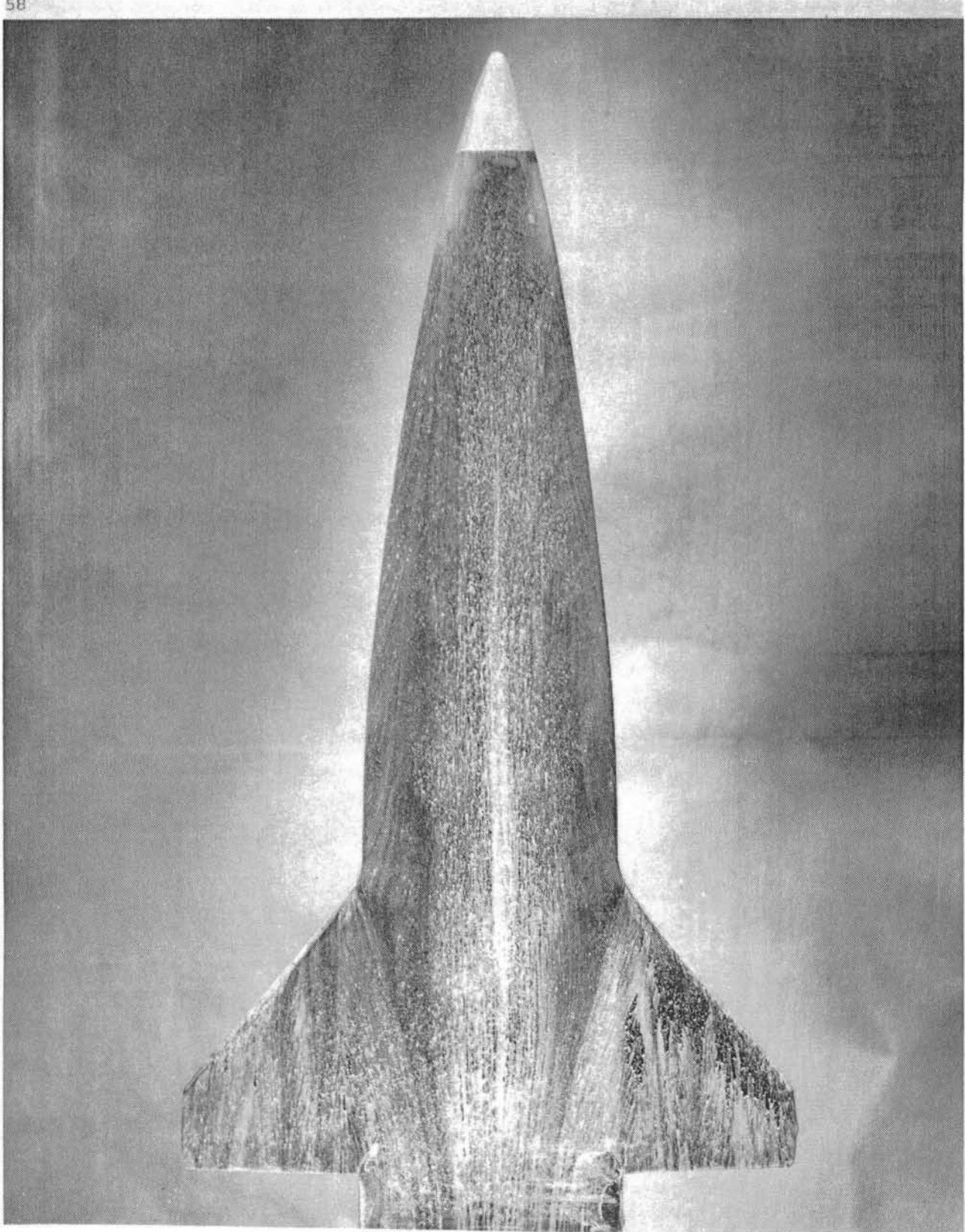
(b) $t = 0.2$ second.
Figure 6.- Continued.



(c) $t = 0.4$ seconds.
Figure 6.- Continued.

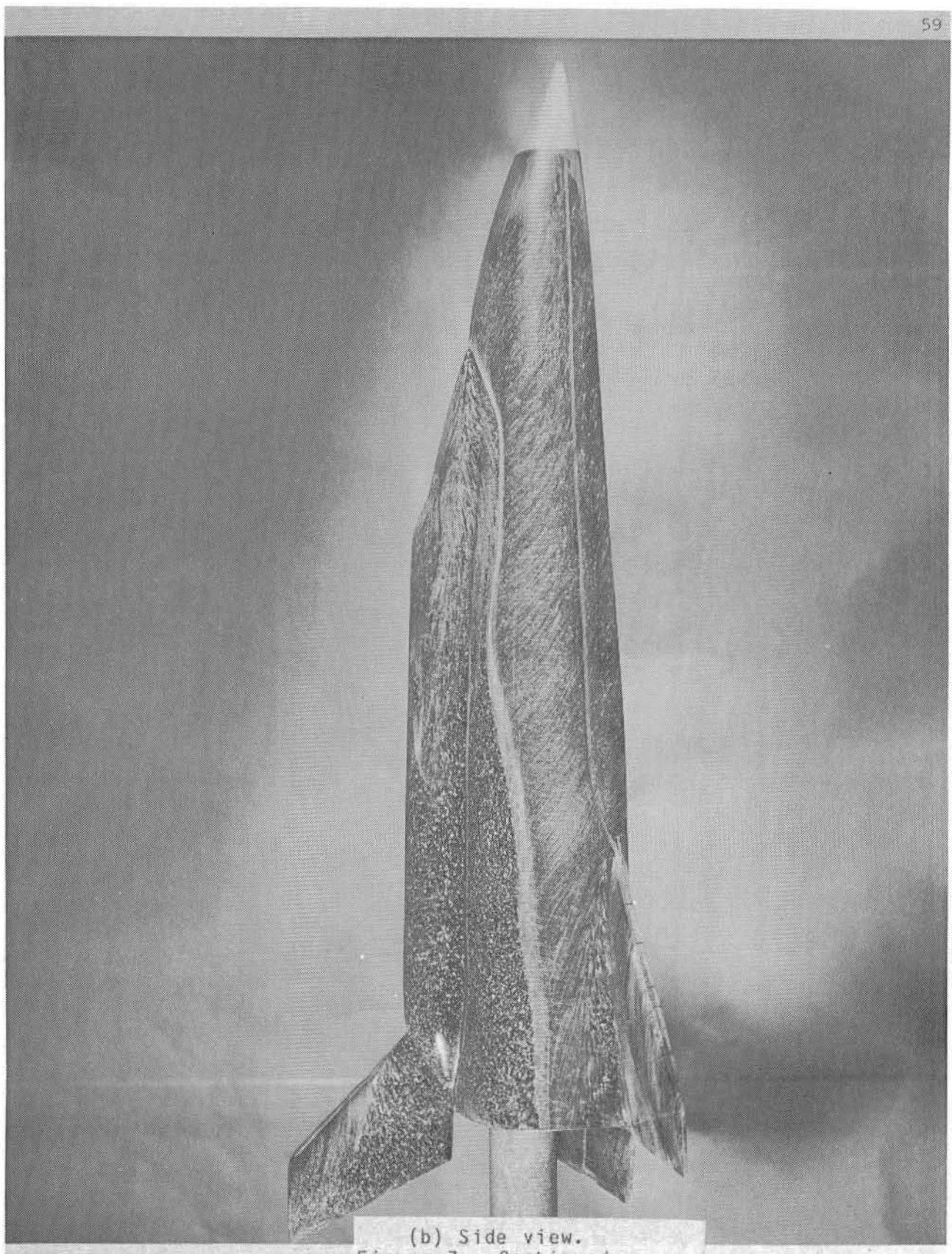


(d) $t = 0.8$ second.
Figure 6.- Concluded

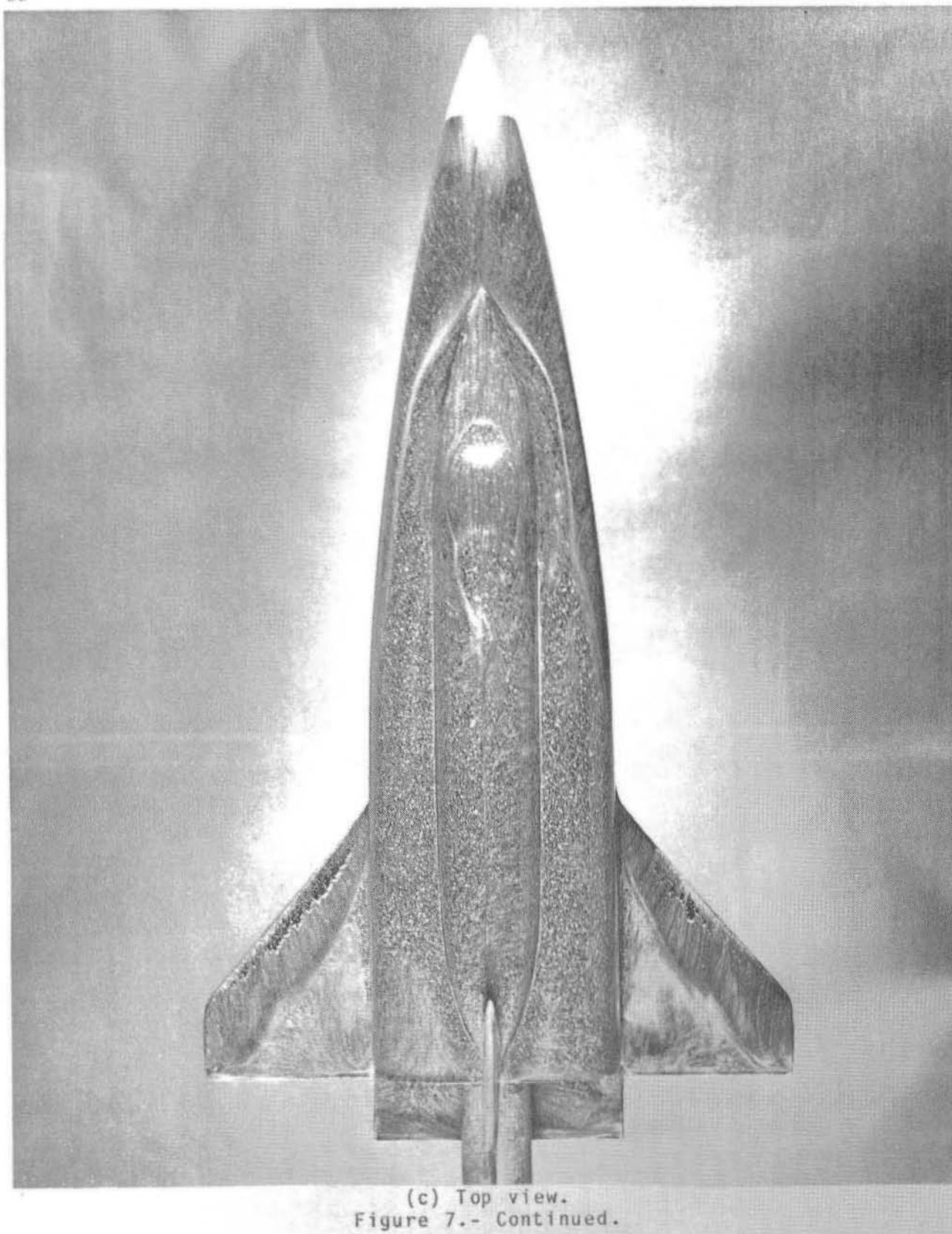


(a) Bottom view.

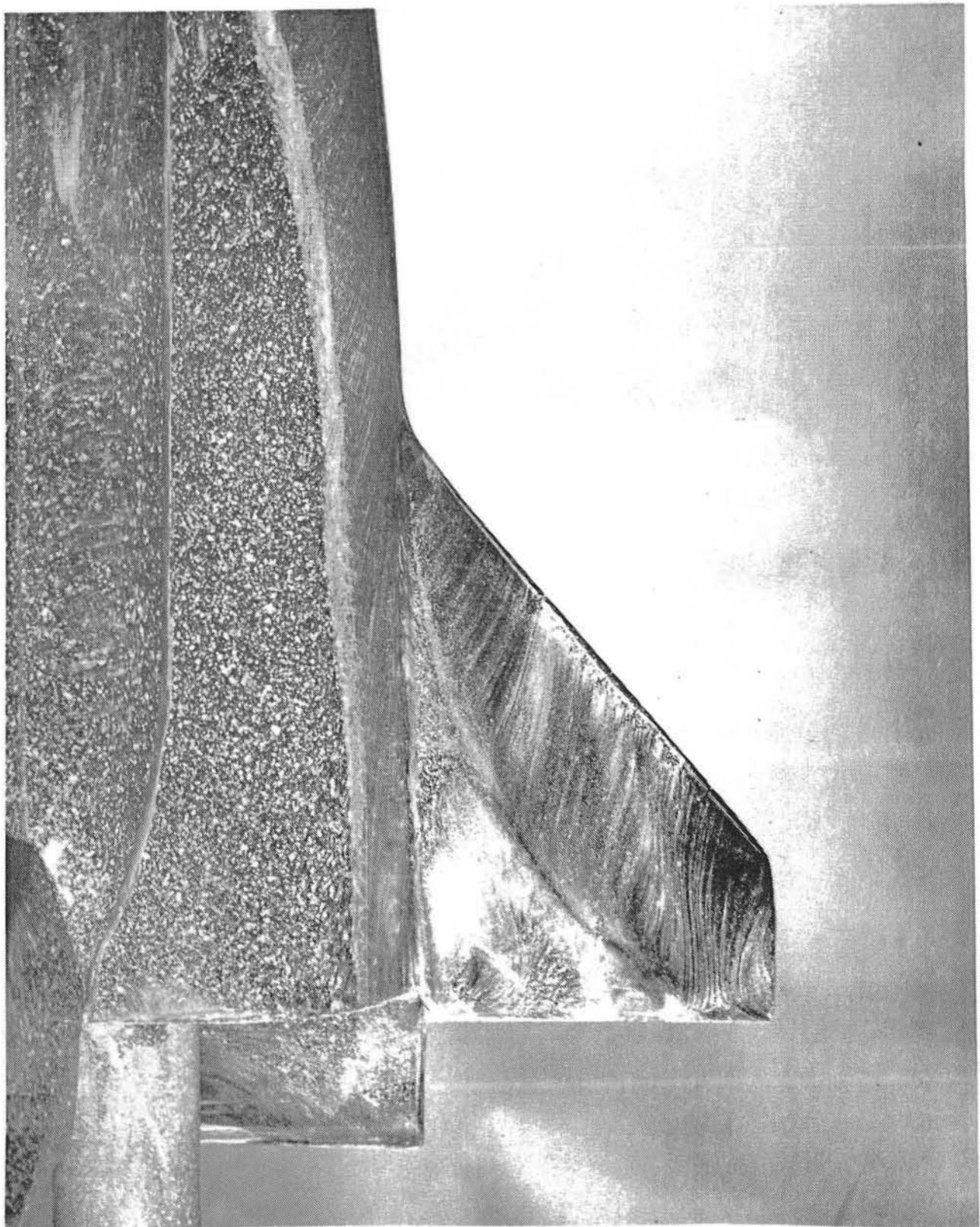
Figure 7.- Oil flow patterns at $\alpha = 10^\circ$ and $Re_\infty = 1.0 \times 10^6$.



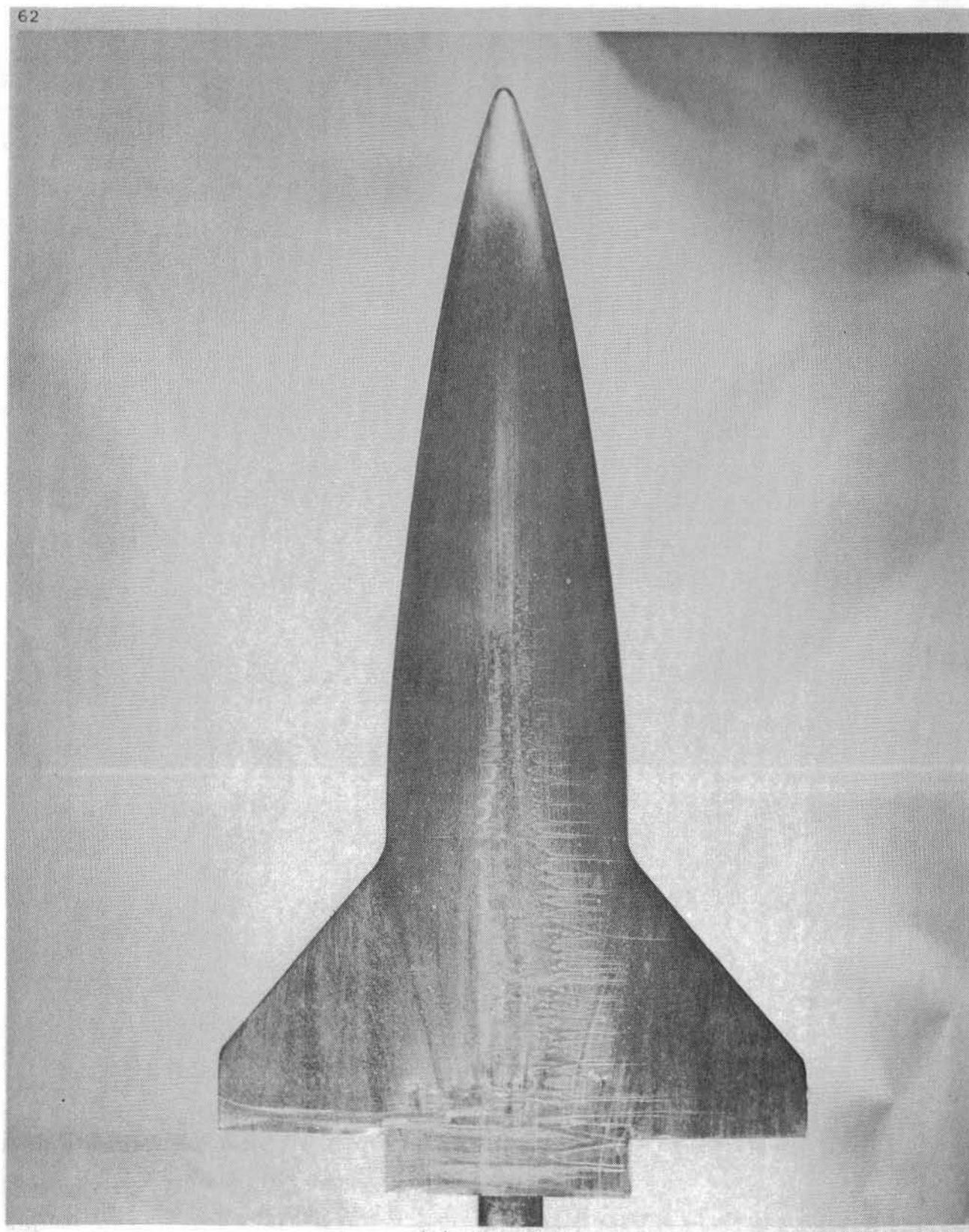
(b) Side view.
Figure 7.- Continued.



(c) Top view.
Figure 7.- Continued.

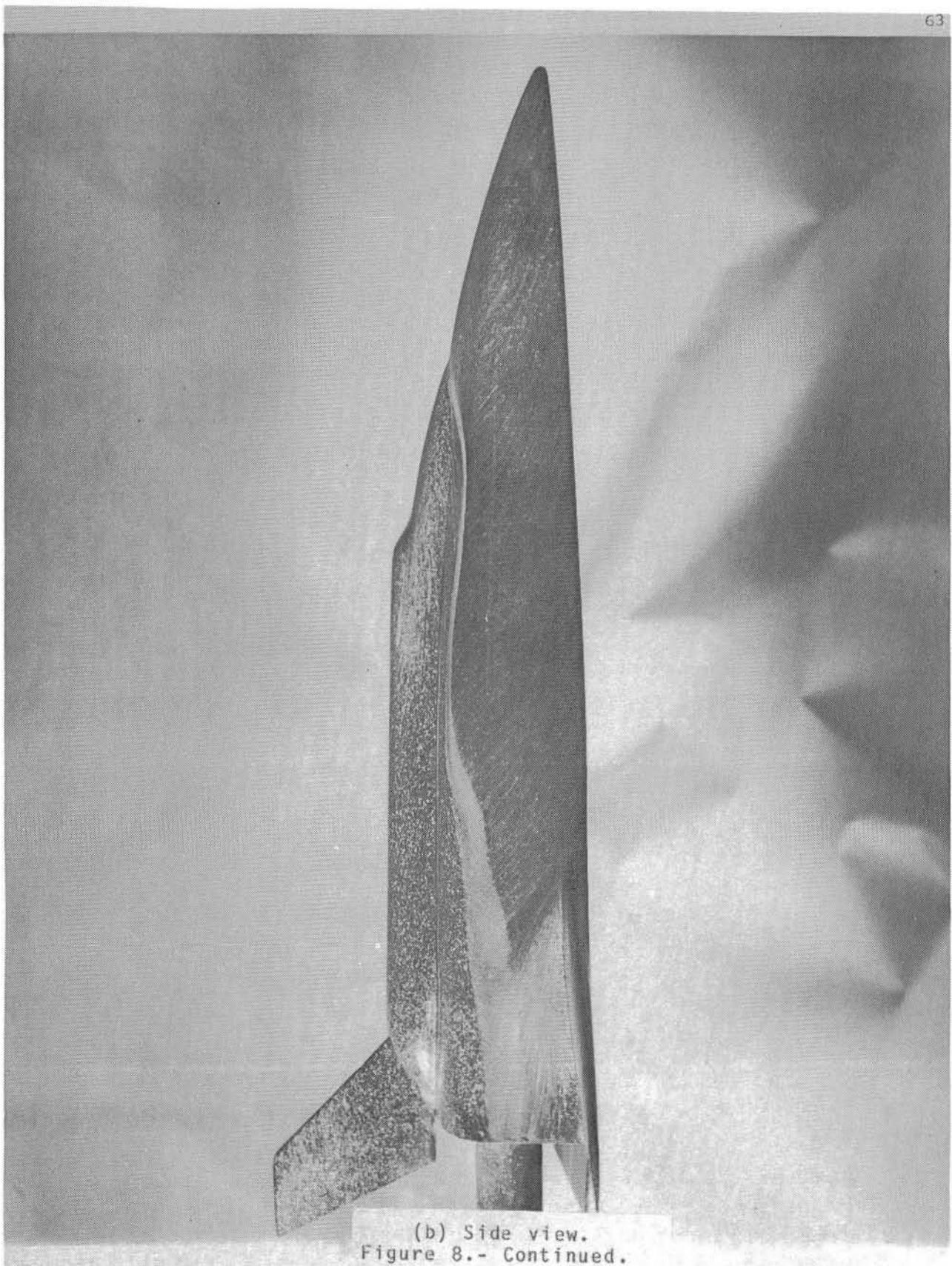


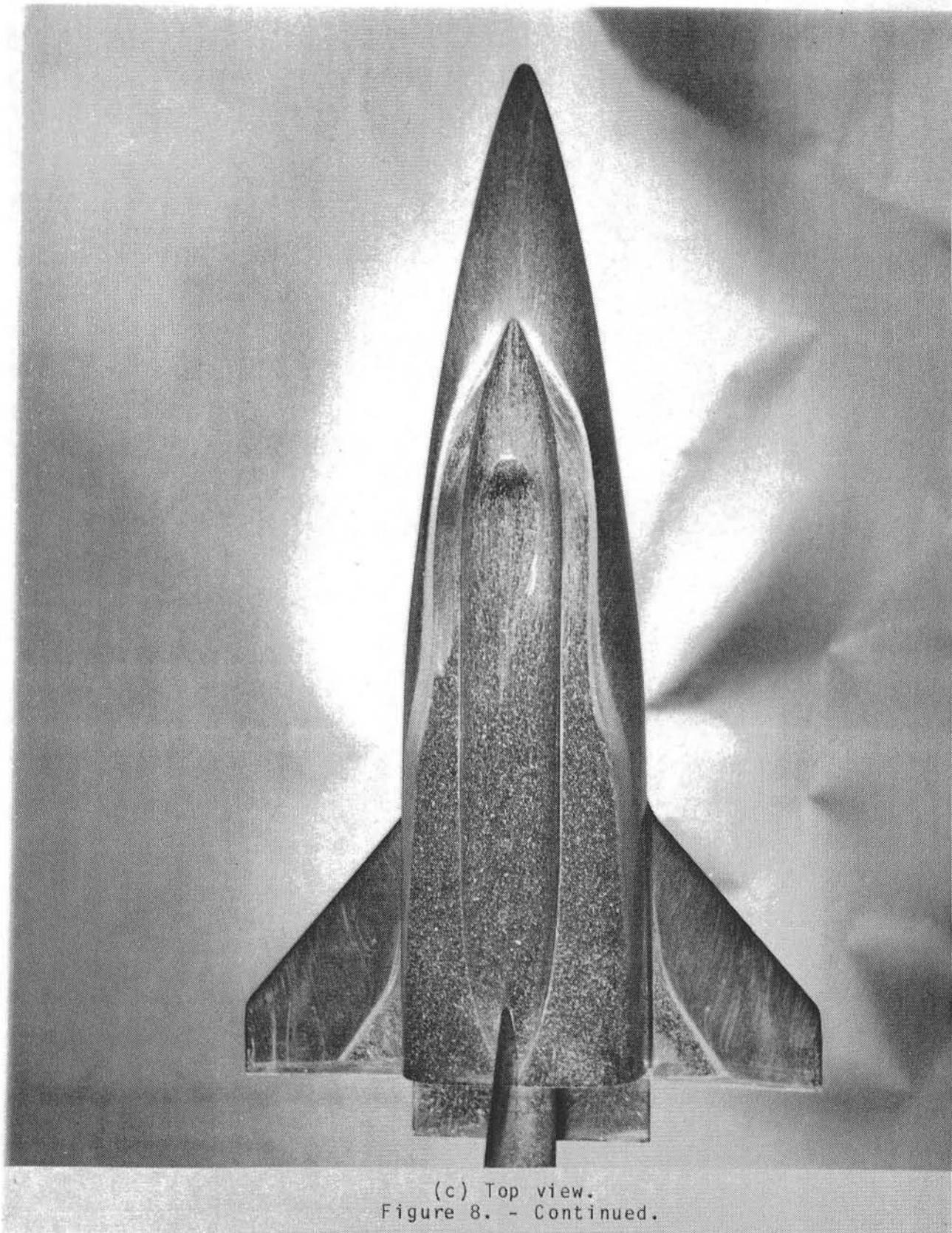
(d) Close-up of wing leeside.
Figure 7.- Concluded



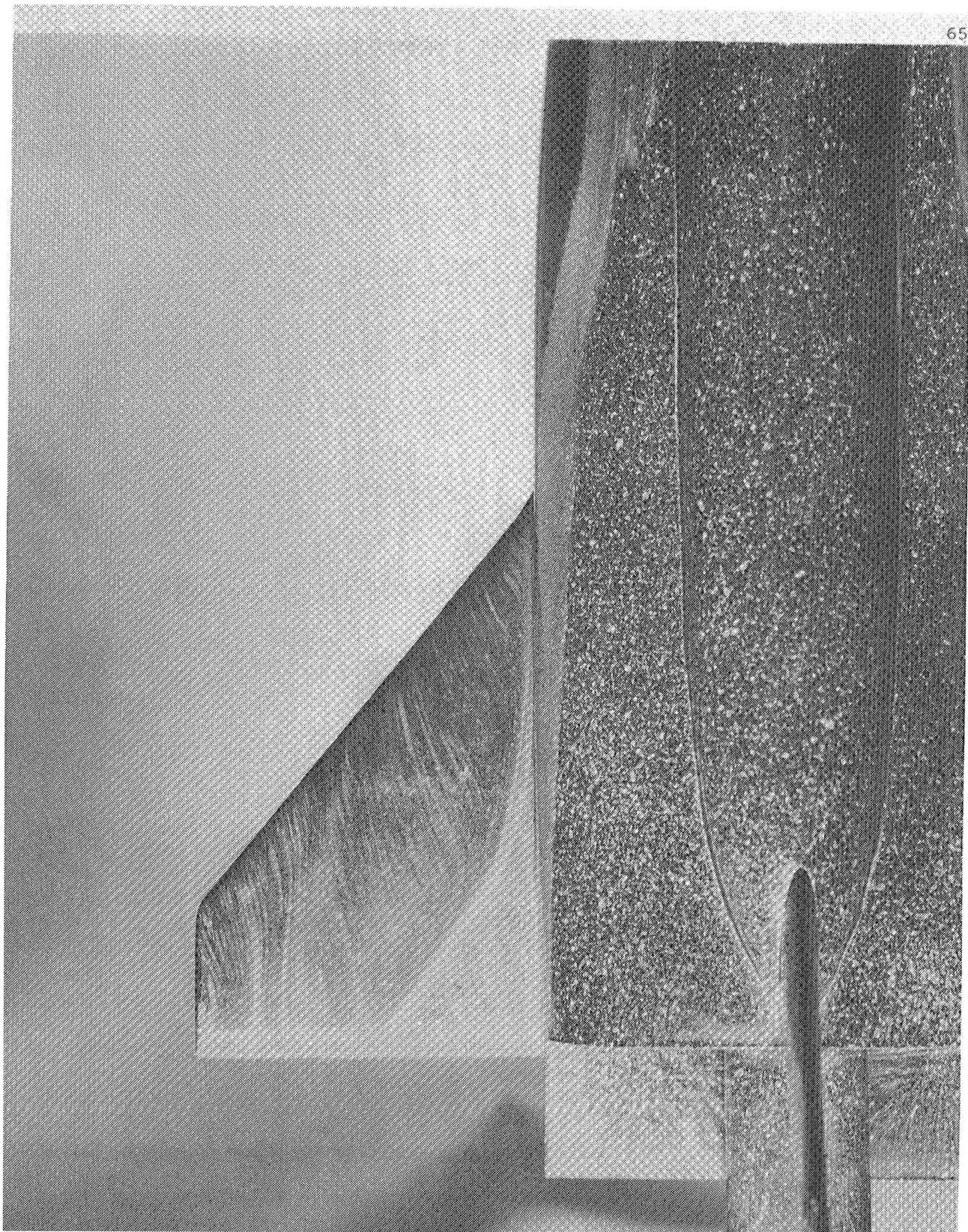
(a) Top view.

Figure 8.- Oil flow patterns at $\alpha = 10^\circ$ and $Re_\infty = 0.5 \times 10^6$.

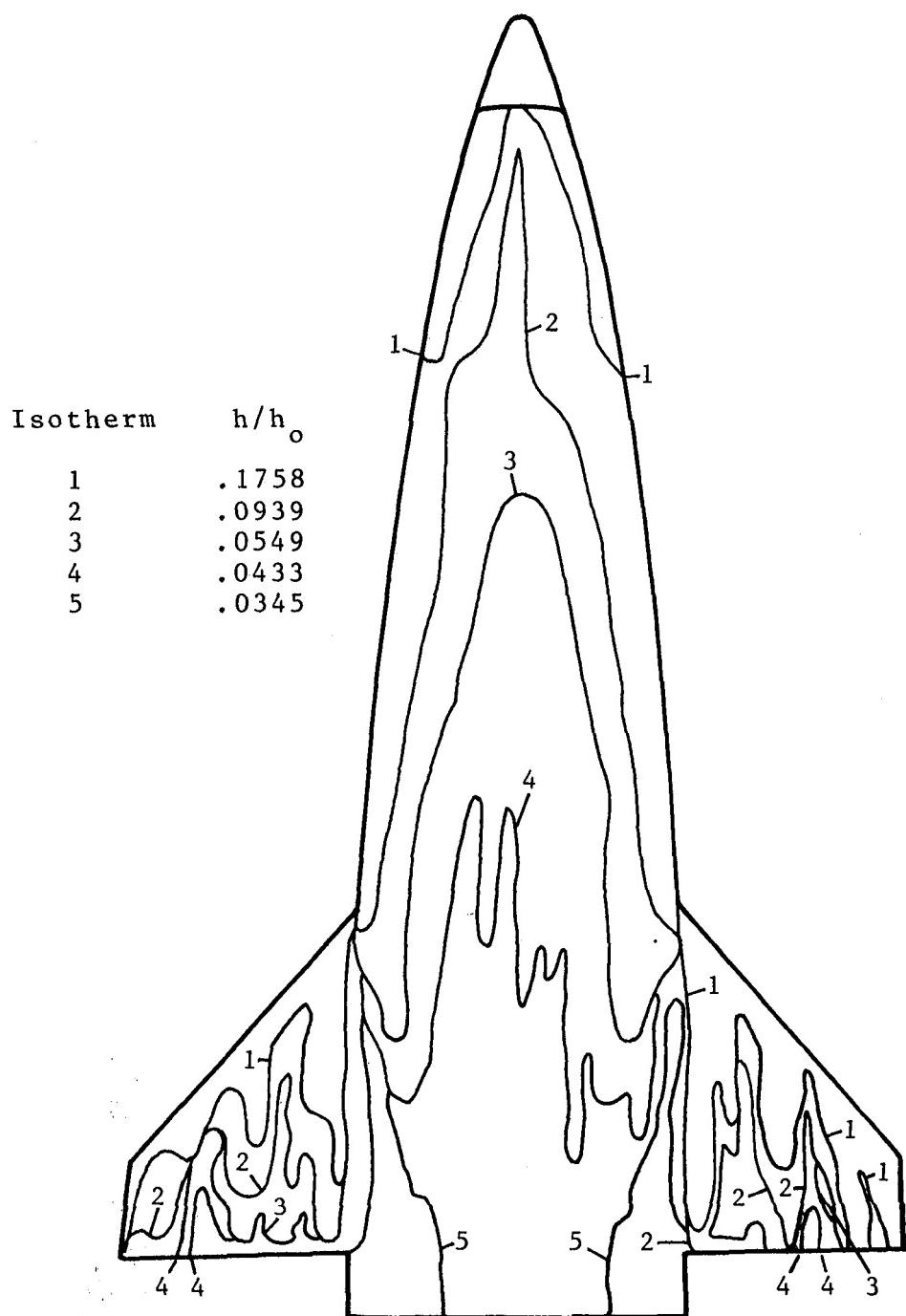




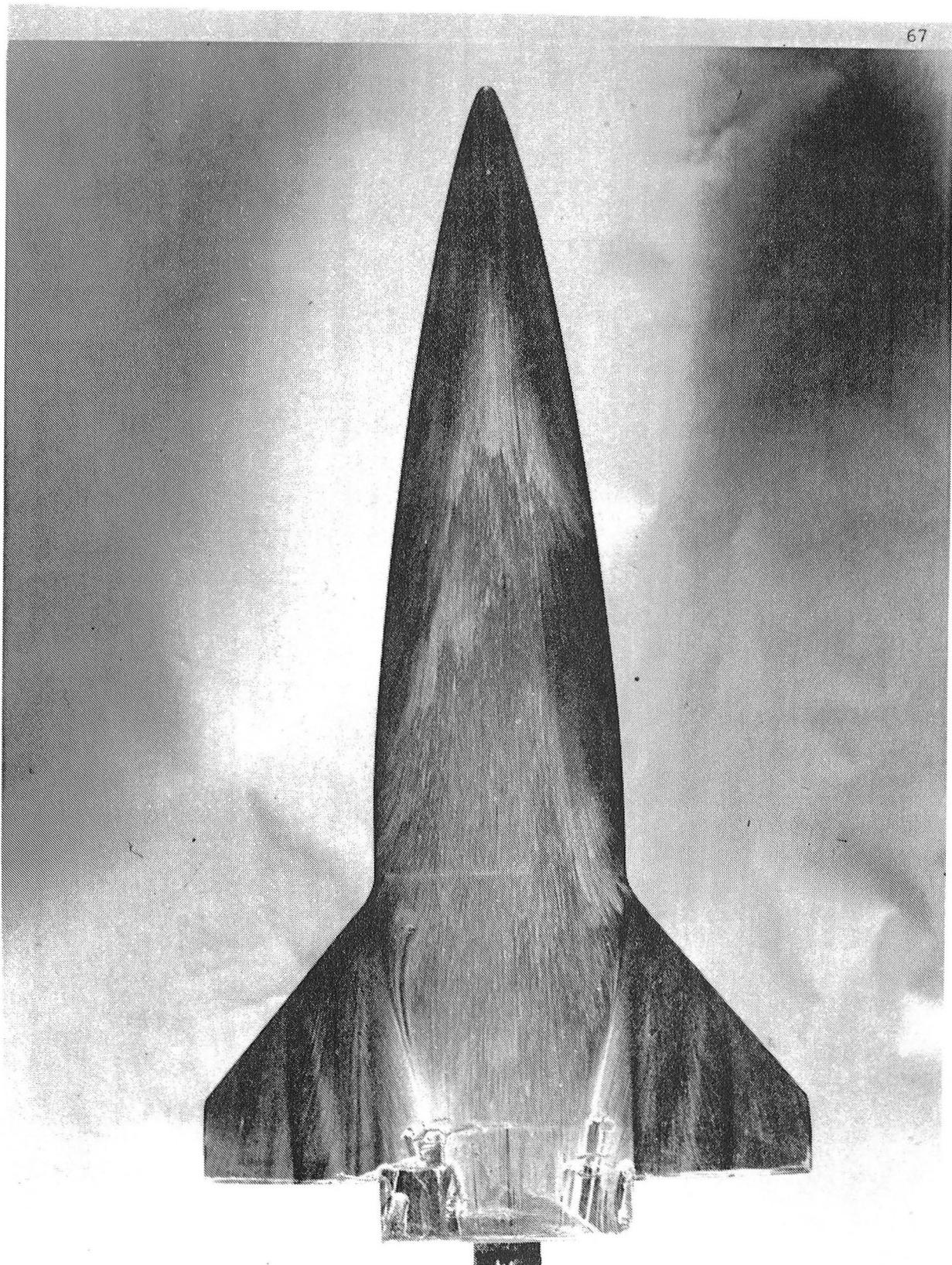
(c) Top view.
Figure 8. - Continued.



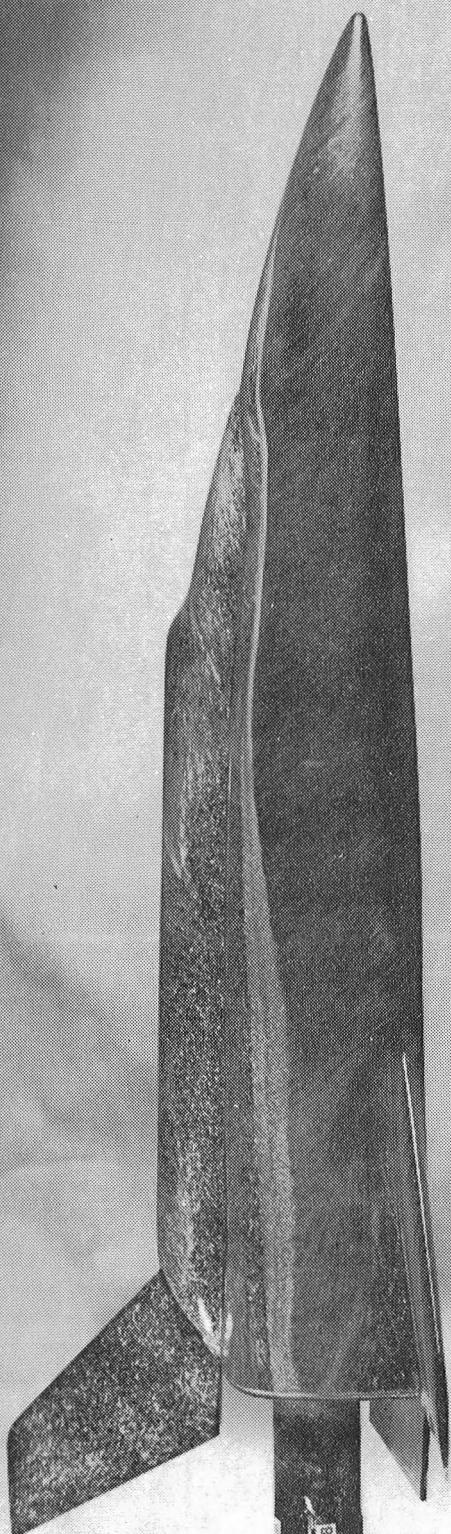
(d) Close-up of wing leeside.
Figure 8.- Concluded.



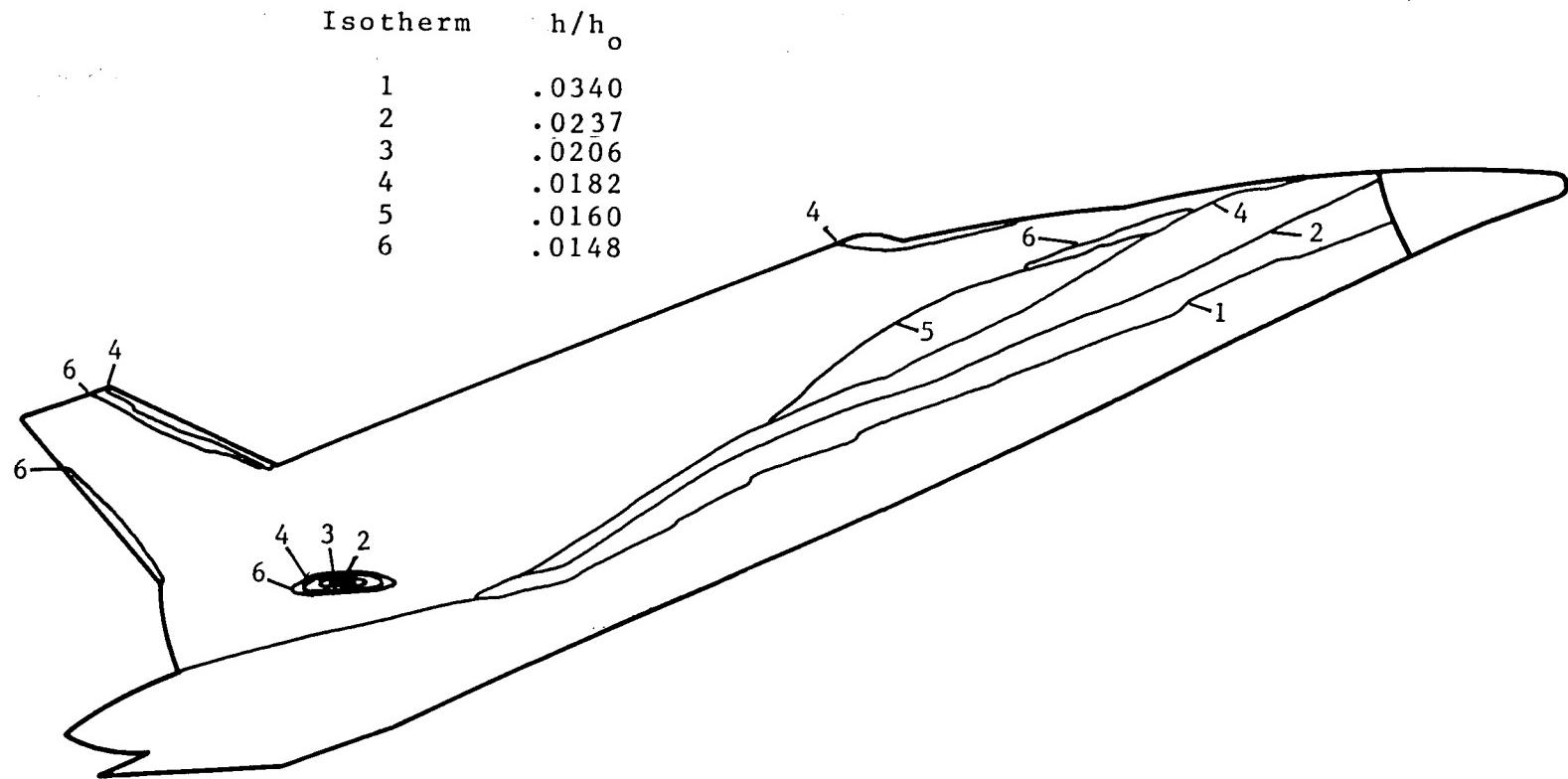
(a) Heating contours - bottom view.
 Figure 9.- Heat transfer and oil flow patterns at $\alpha = 20^\circ$ and $Re_\infty = 2.0 \times 10^6$.



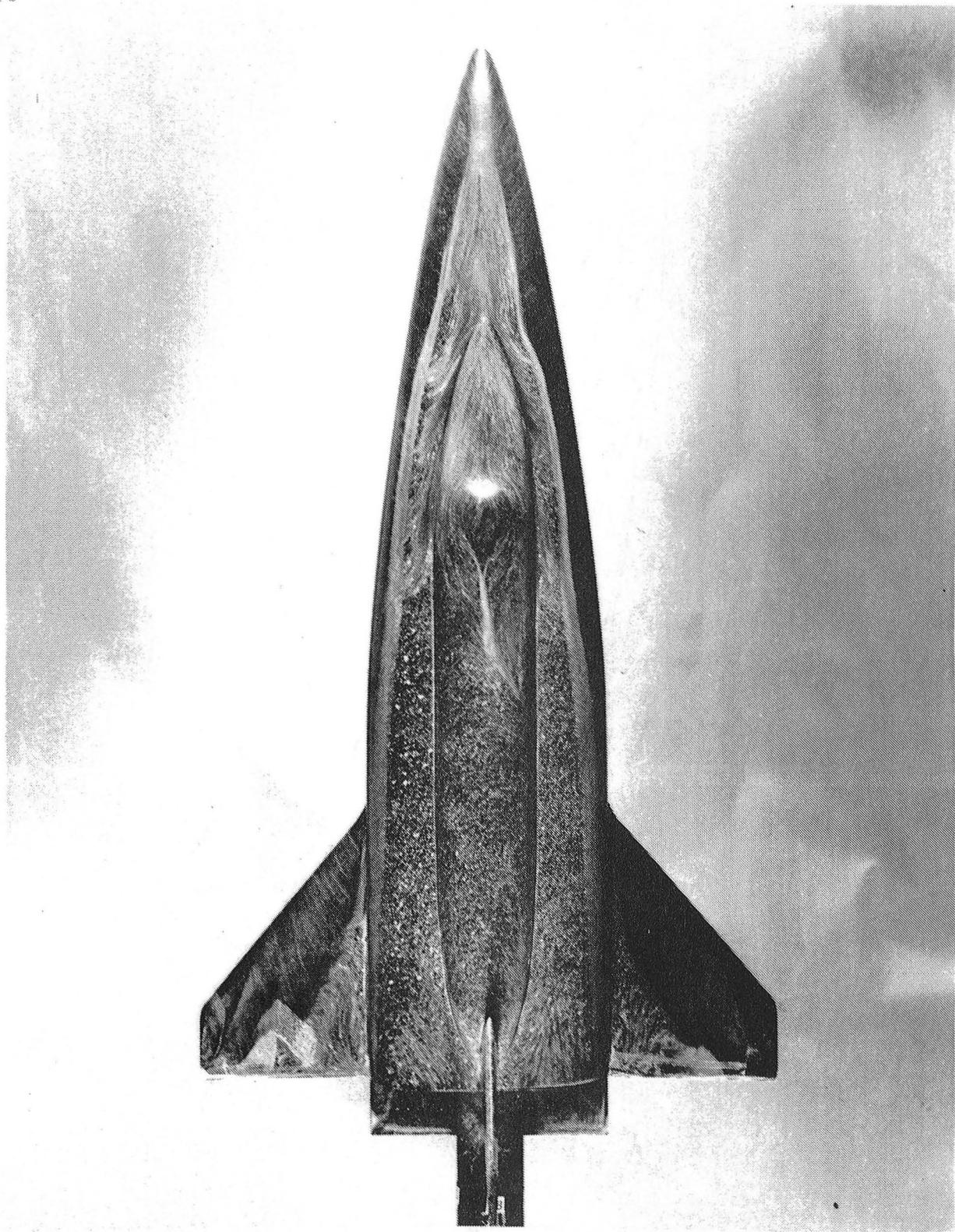
(b) Oil flow - bottom view.
Figure 9.- Continued.



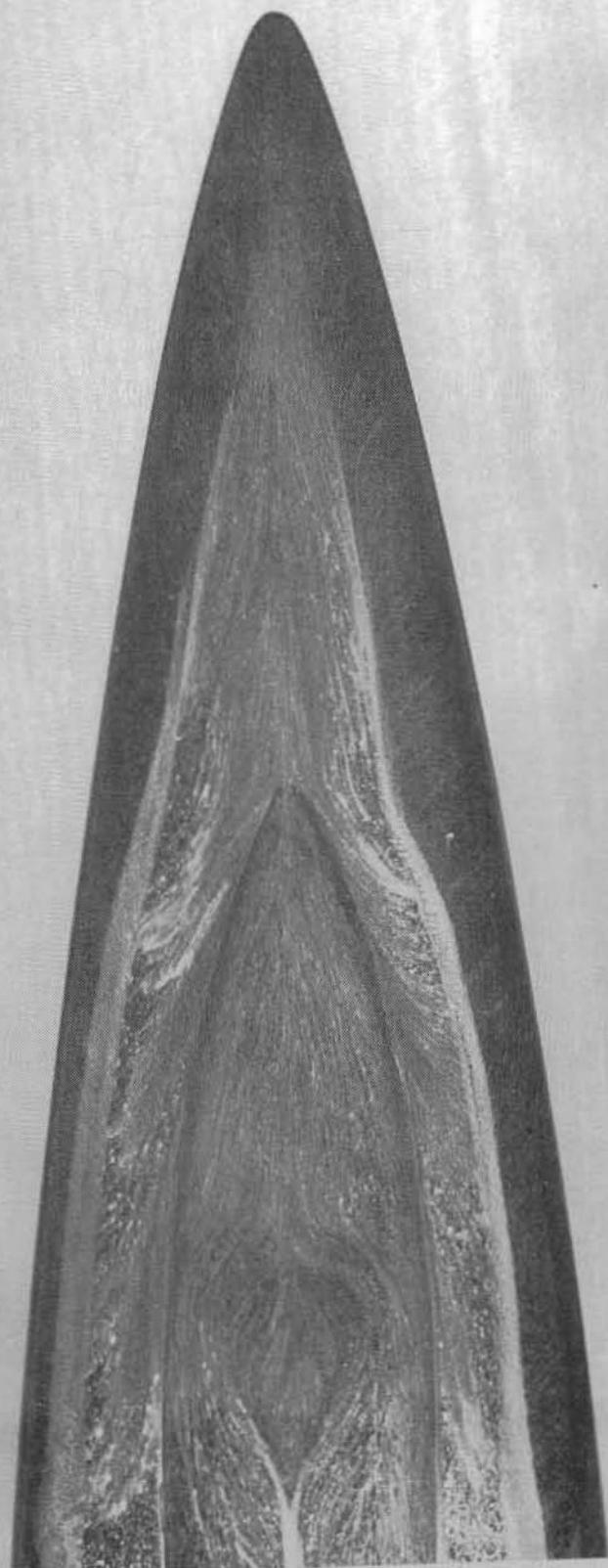
(c) Oil flow - side view.
Figure 9.- Continued.



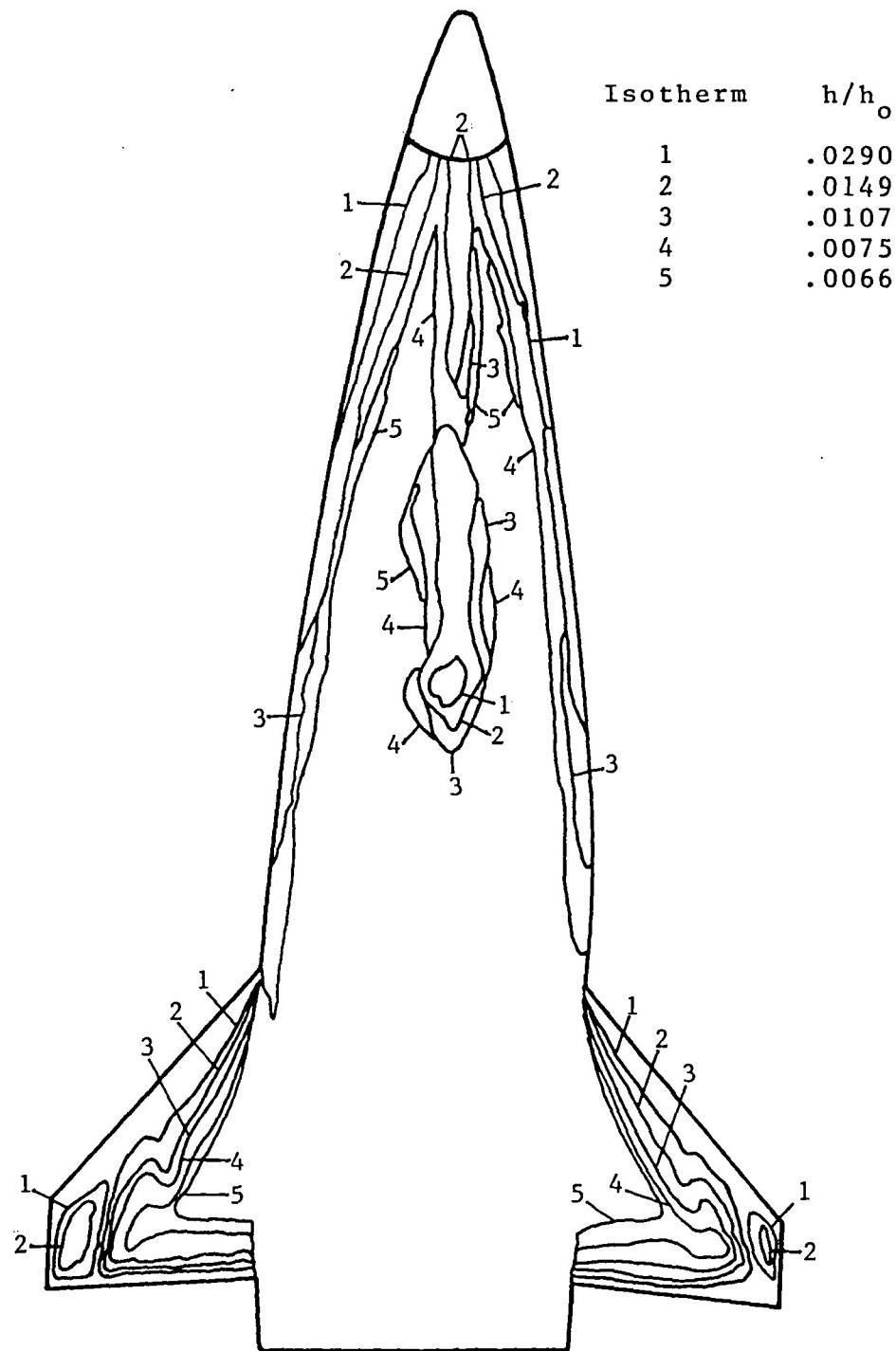
(d) Heating contours - side view.
Figure 9.- Continued.



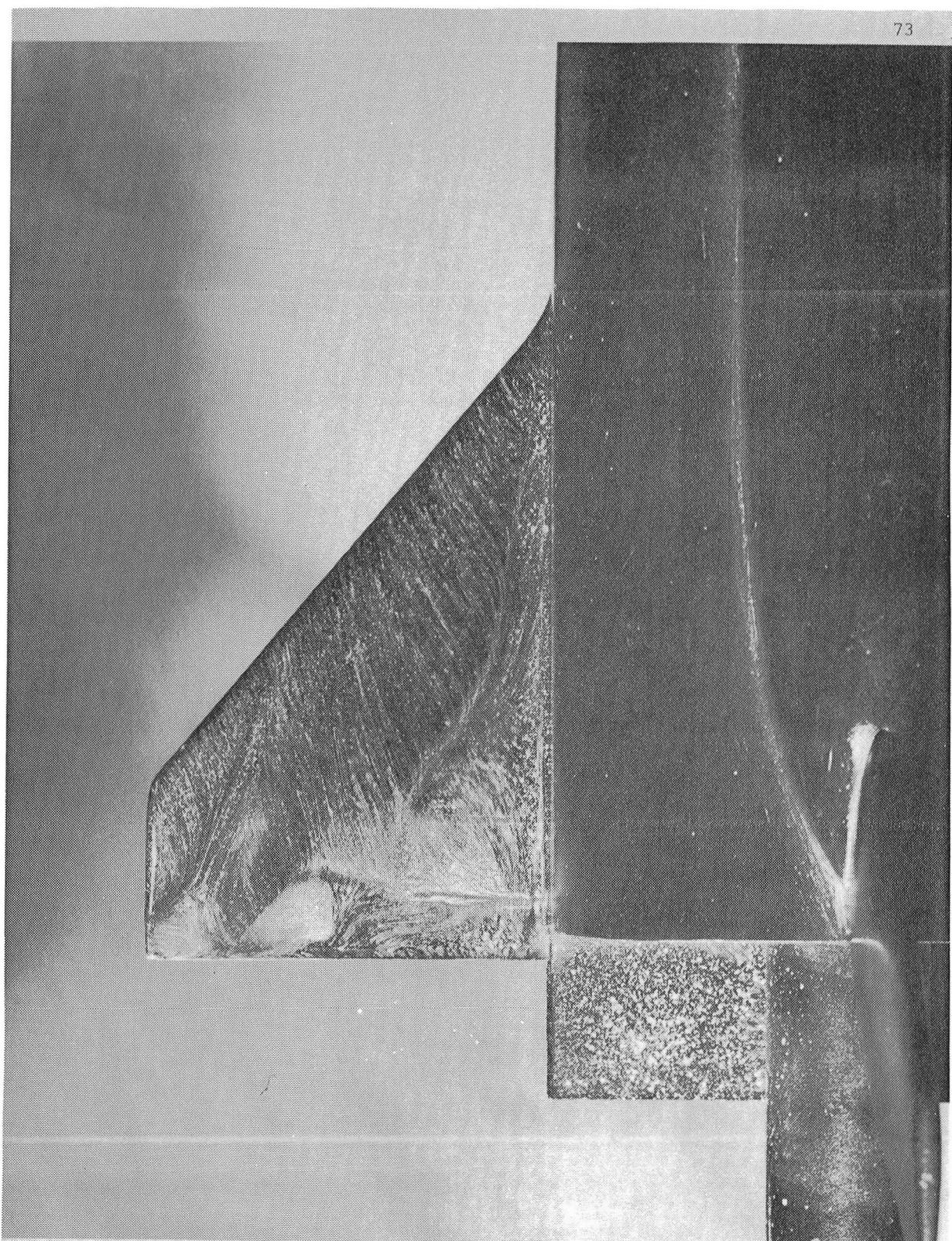
(e) Oil flow - top view.
Figure 9.- Continued.



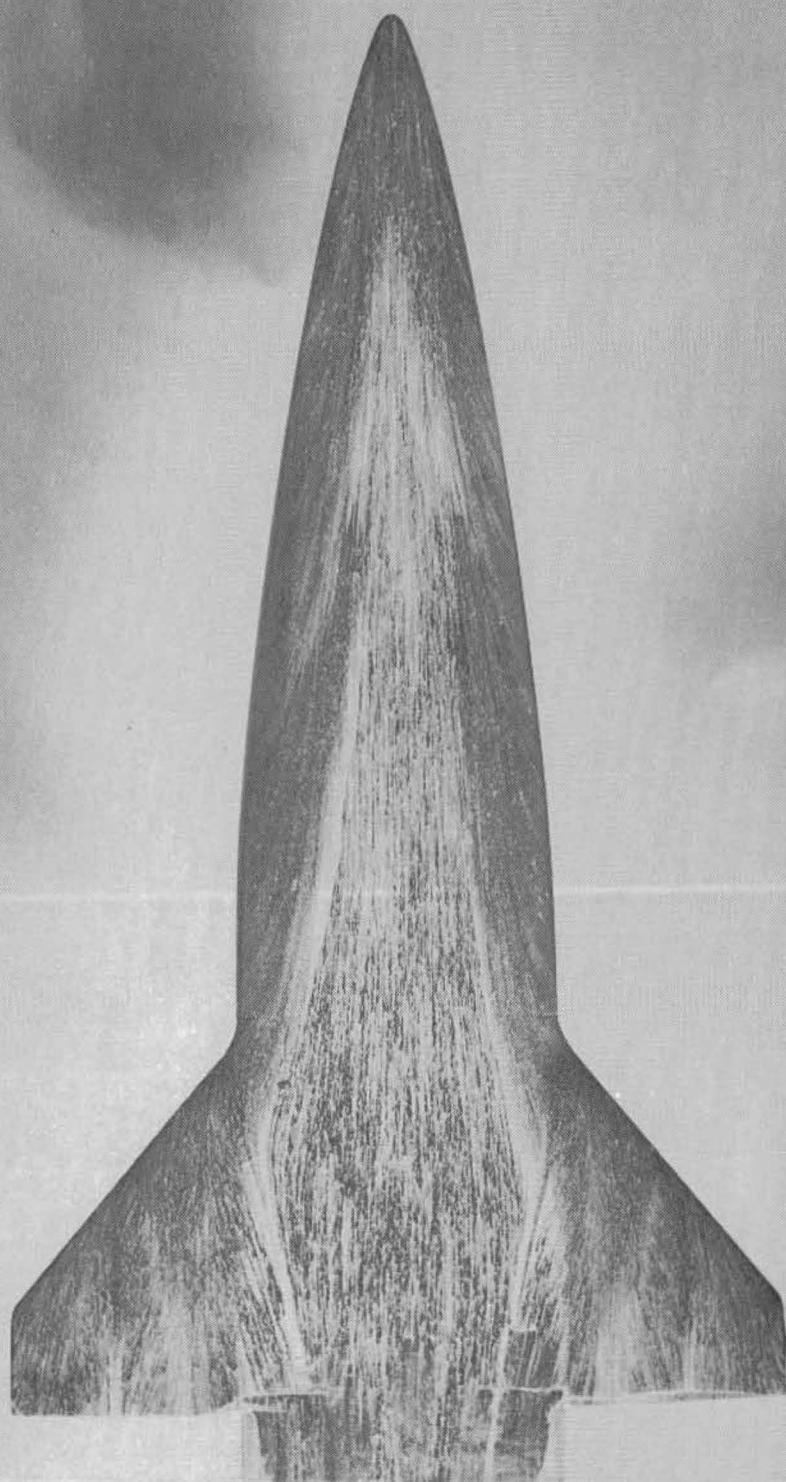
(f) Oil flow - close-up of canopy.
Figure 9.- Continued.



(g) Heating contours - top view.
Figure 9.- Continued.

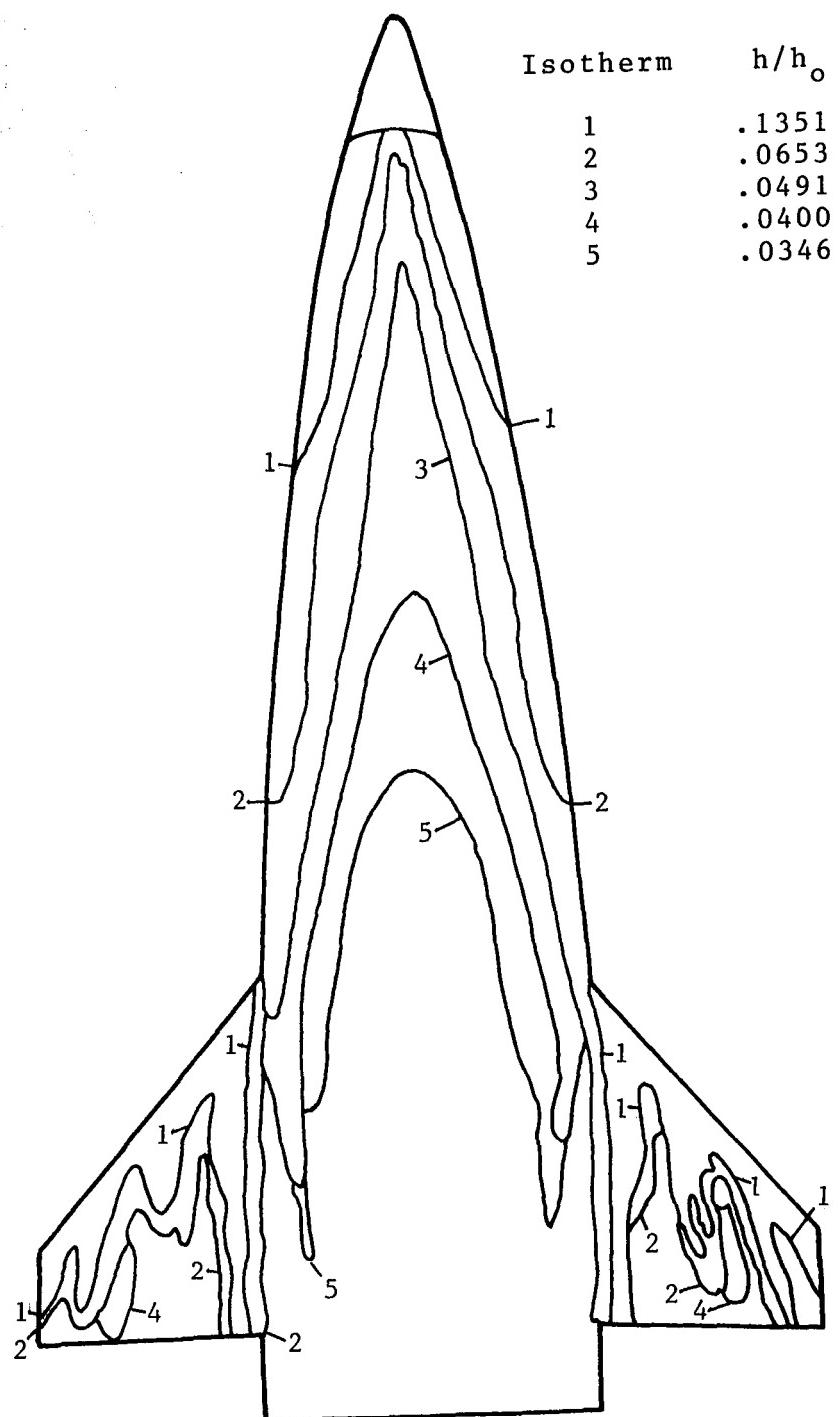


(h) Oil flow - close-up of wing leeside.
Figure 9. Concluded.

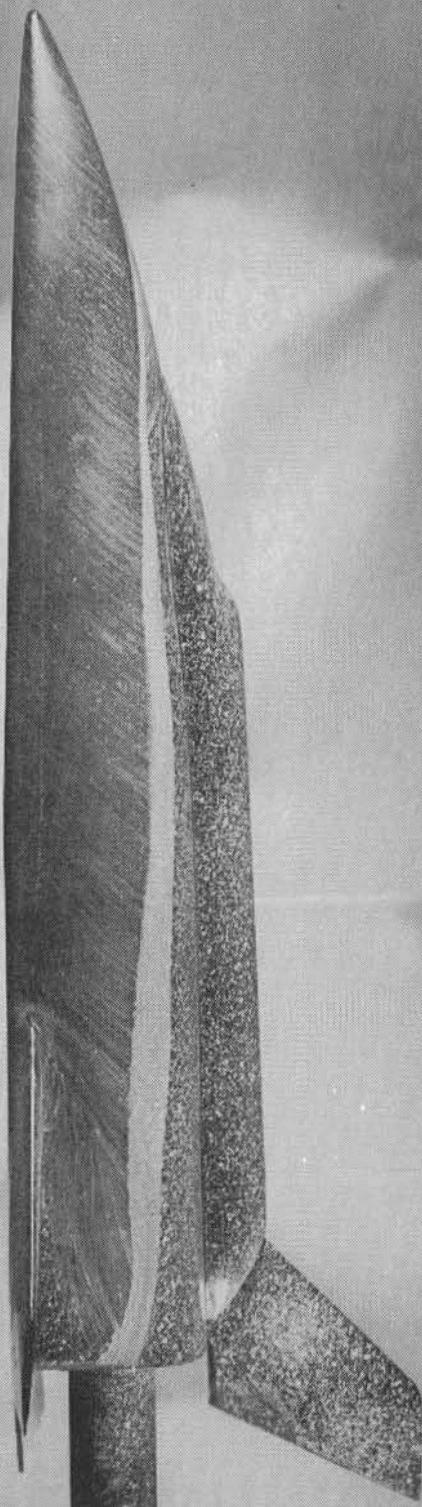


(a) Oil flow - bottom view.

Figure 10.- Heat transfer data and oil flow patterns at $\alpha = 20^\circ$ and $Re_\infty = 1.0 \times 10^6$



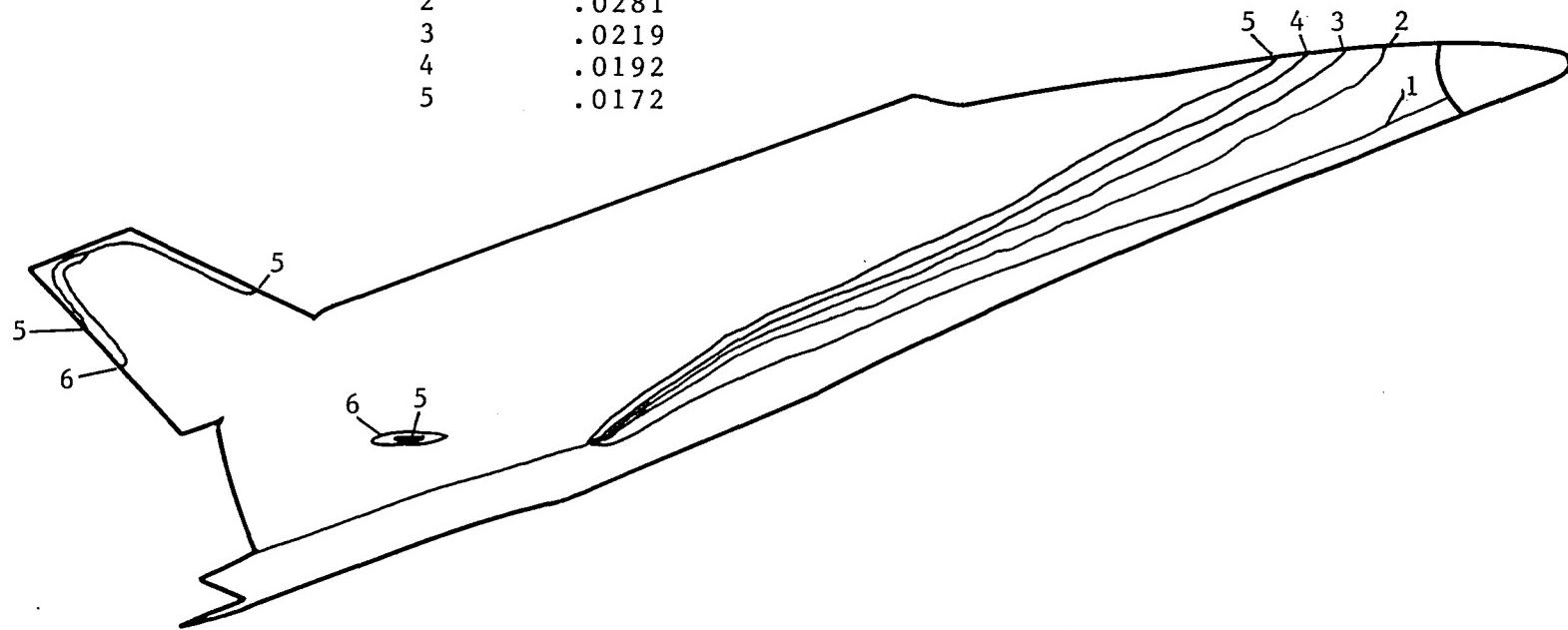
(b) Heating contours - bottom view.
Figure 10.- Continued.



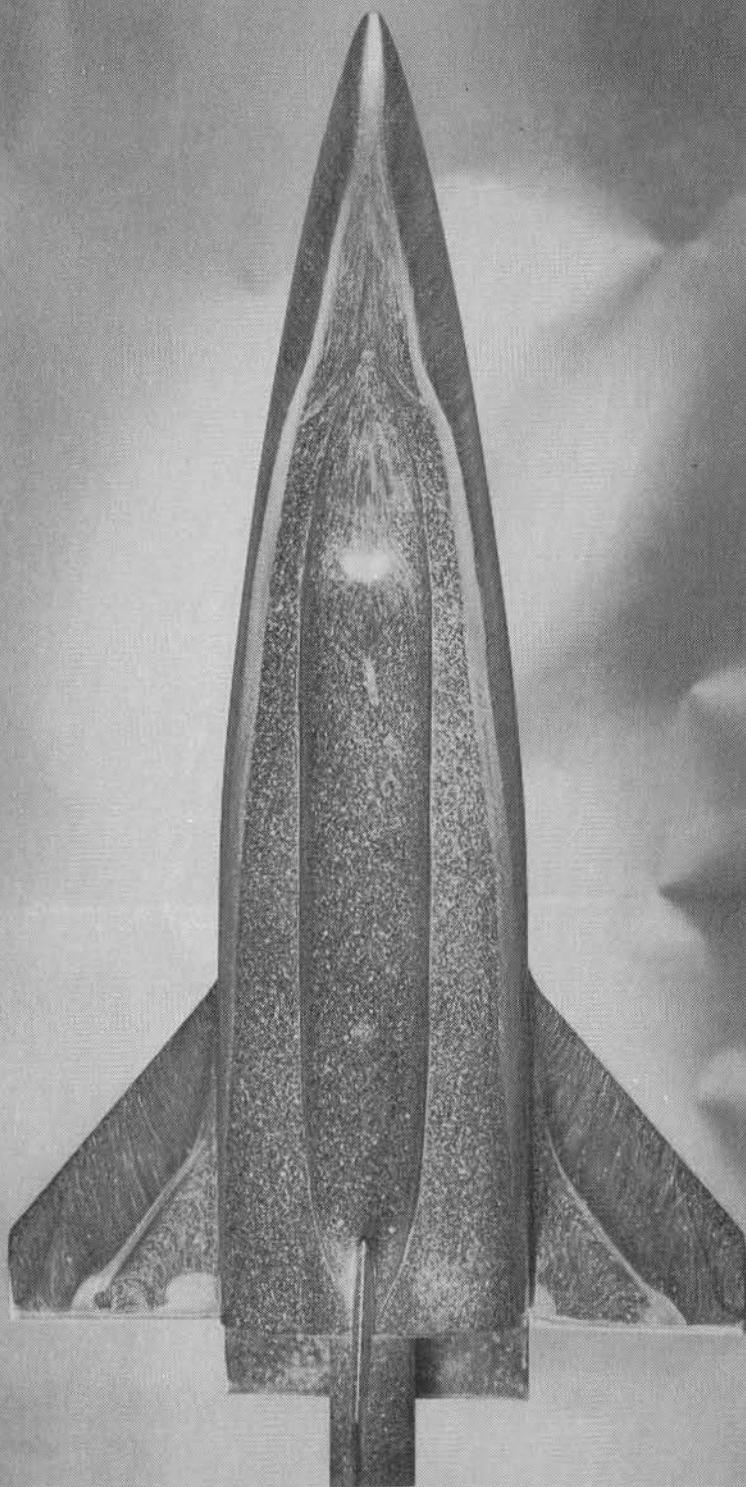
(c) Oil - flow side view.
Figure 10.- Continued.

Isotherm h/h_o

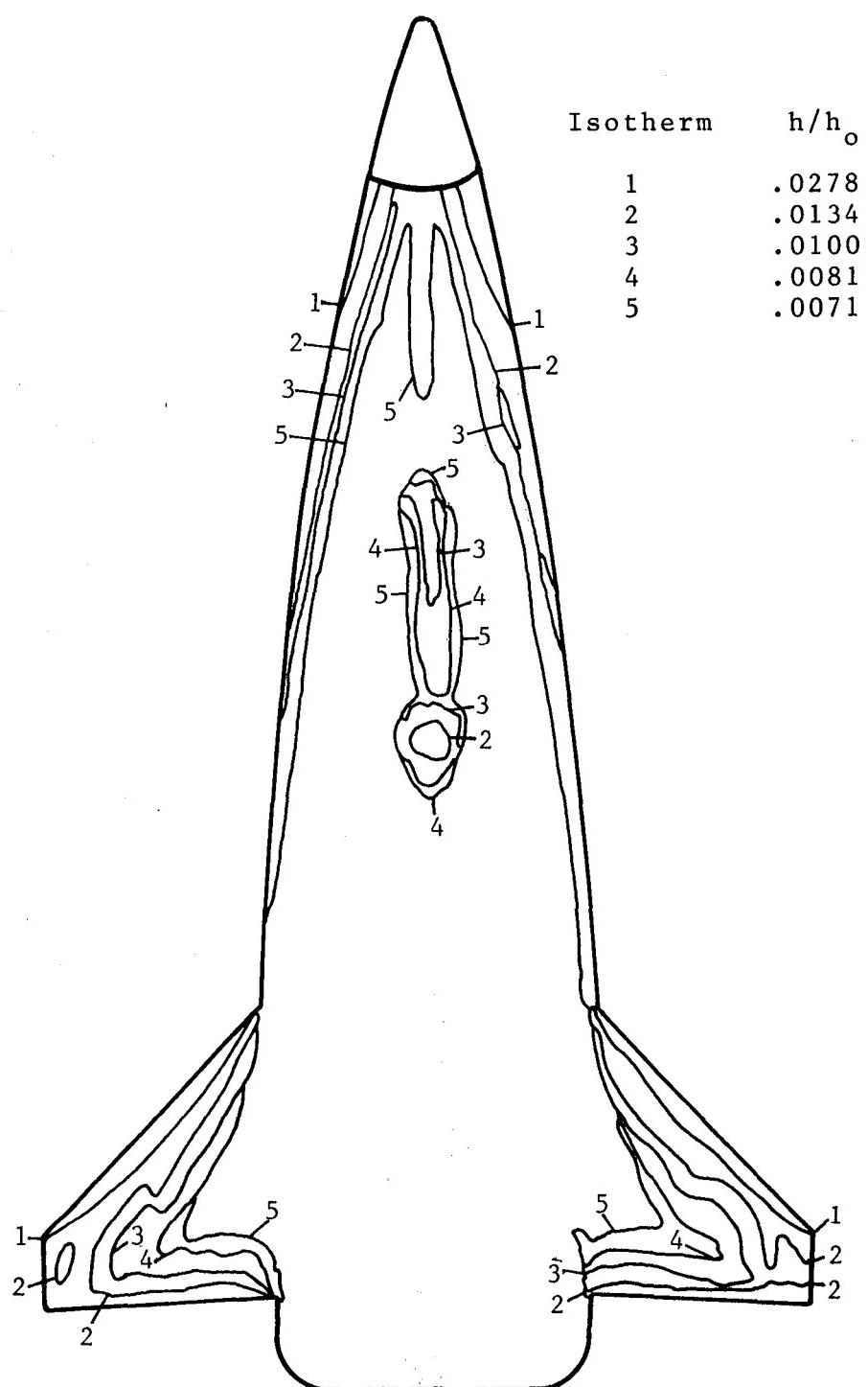
1	.0727
2	.0281
3	.0219
4	.0192
5	.0172



(d) Heating contours - side view.
Figure 10.- Continued.

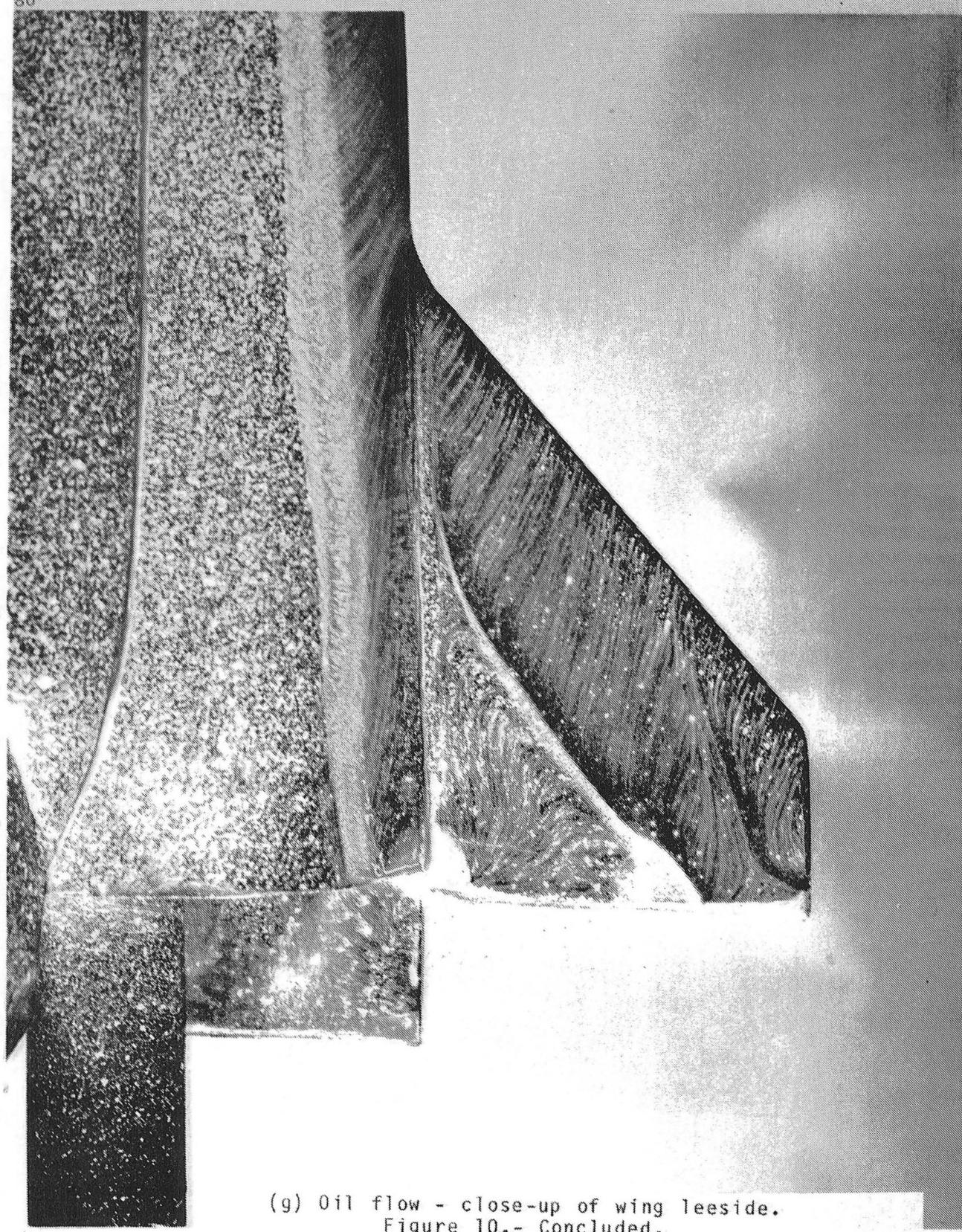


(e) Oil flow - top view.
Figure 10.- Continued.

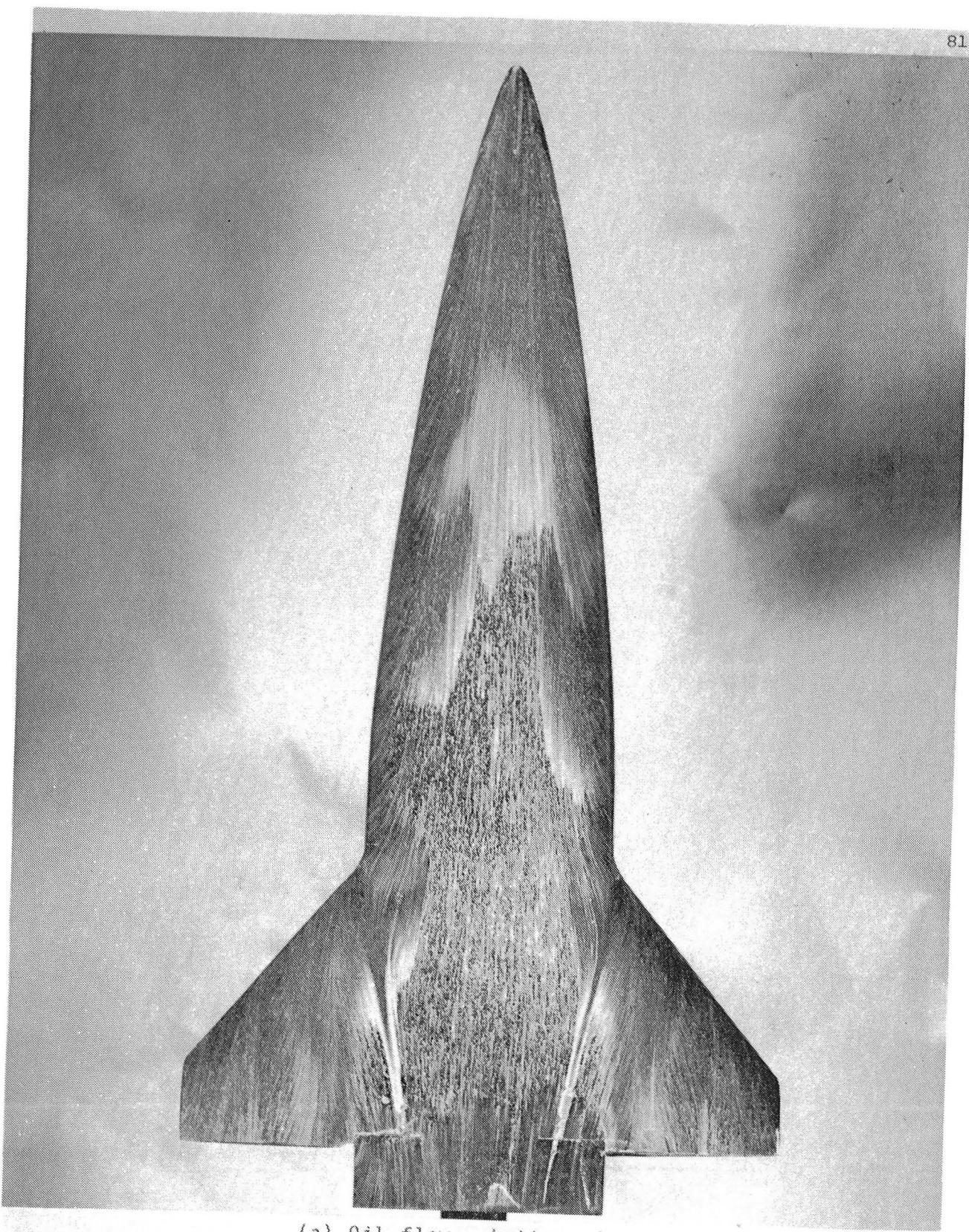


(f) Heating contours - top view.
Figure 10.- Continued.

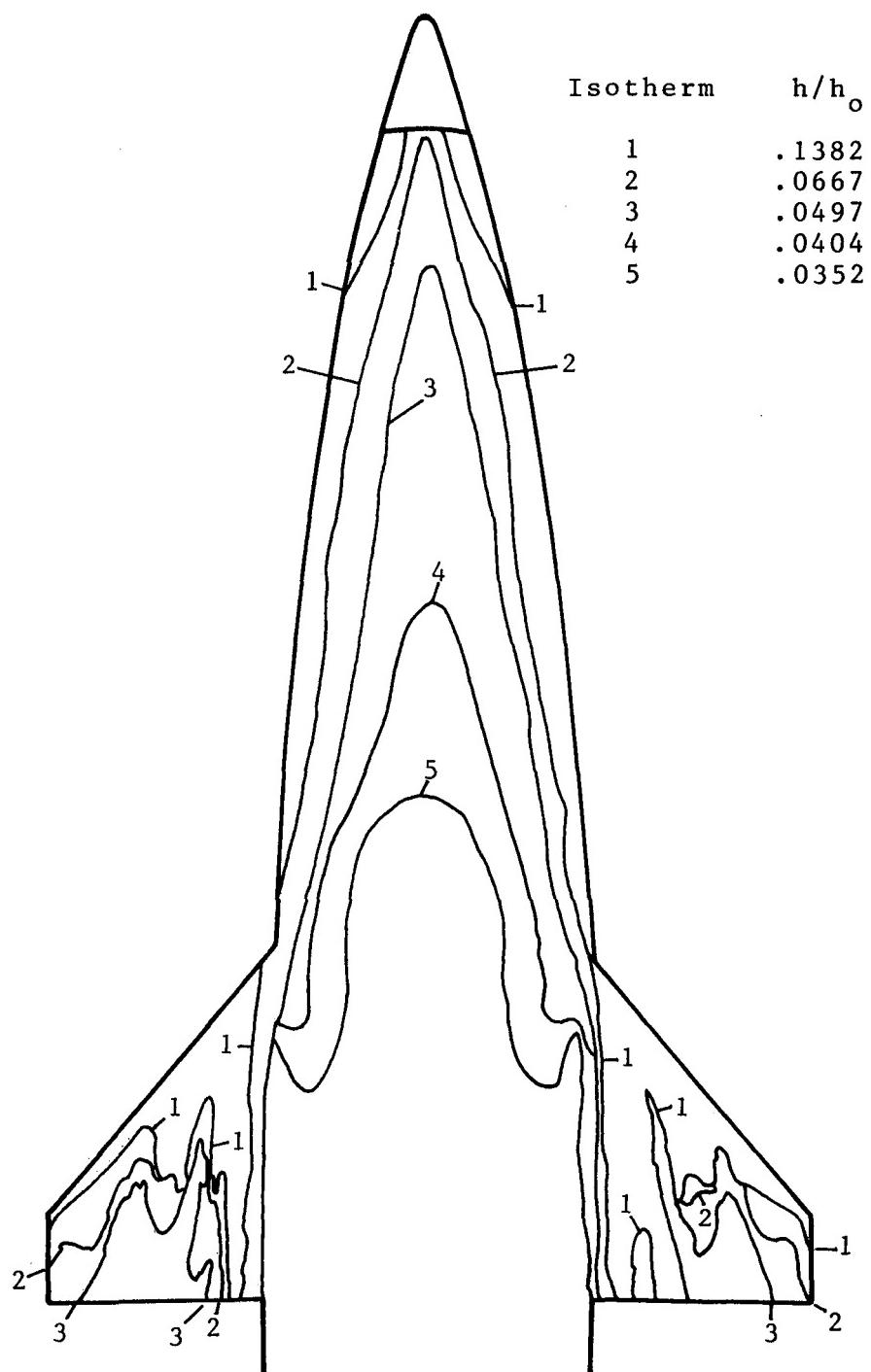
80



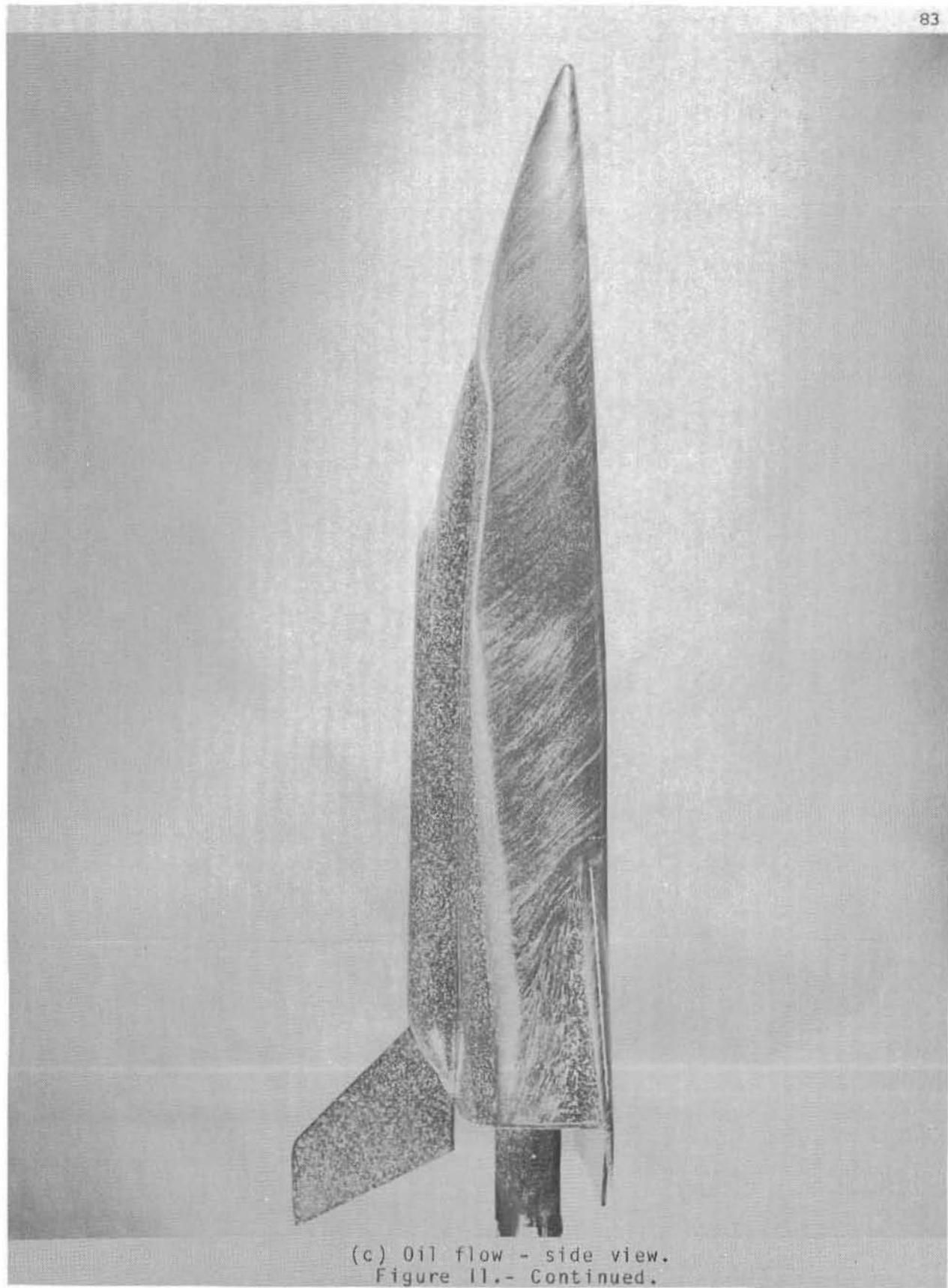
(g) Oil flow - close-up of wing leeside.
Figure 10.- Concluded.



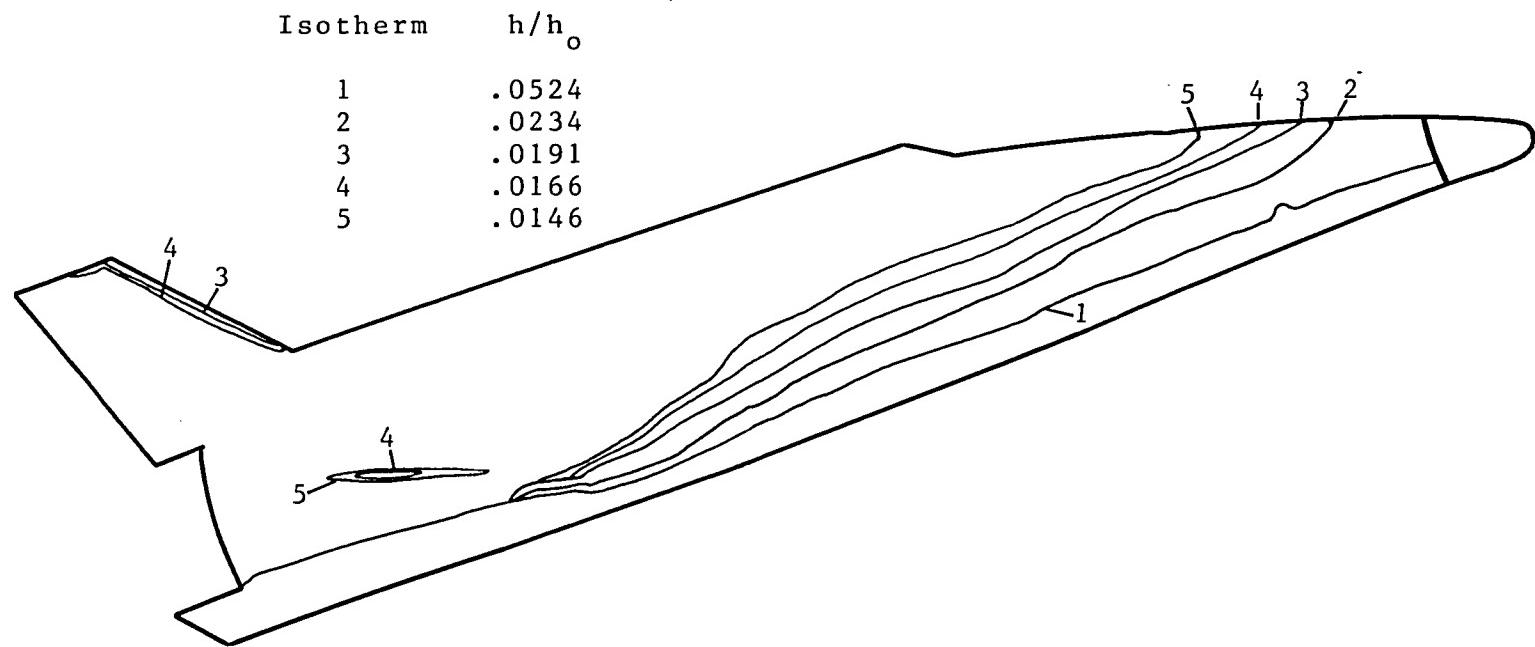
(a) Oil flow - bottom view.
Figure 11.-- Heat transfer data and oil flow patterns at $\alpha = 20^\circ$ and $Re_\infty = 0.5 \times 10^6$.



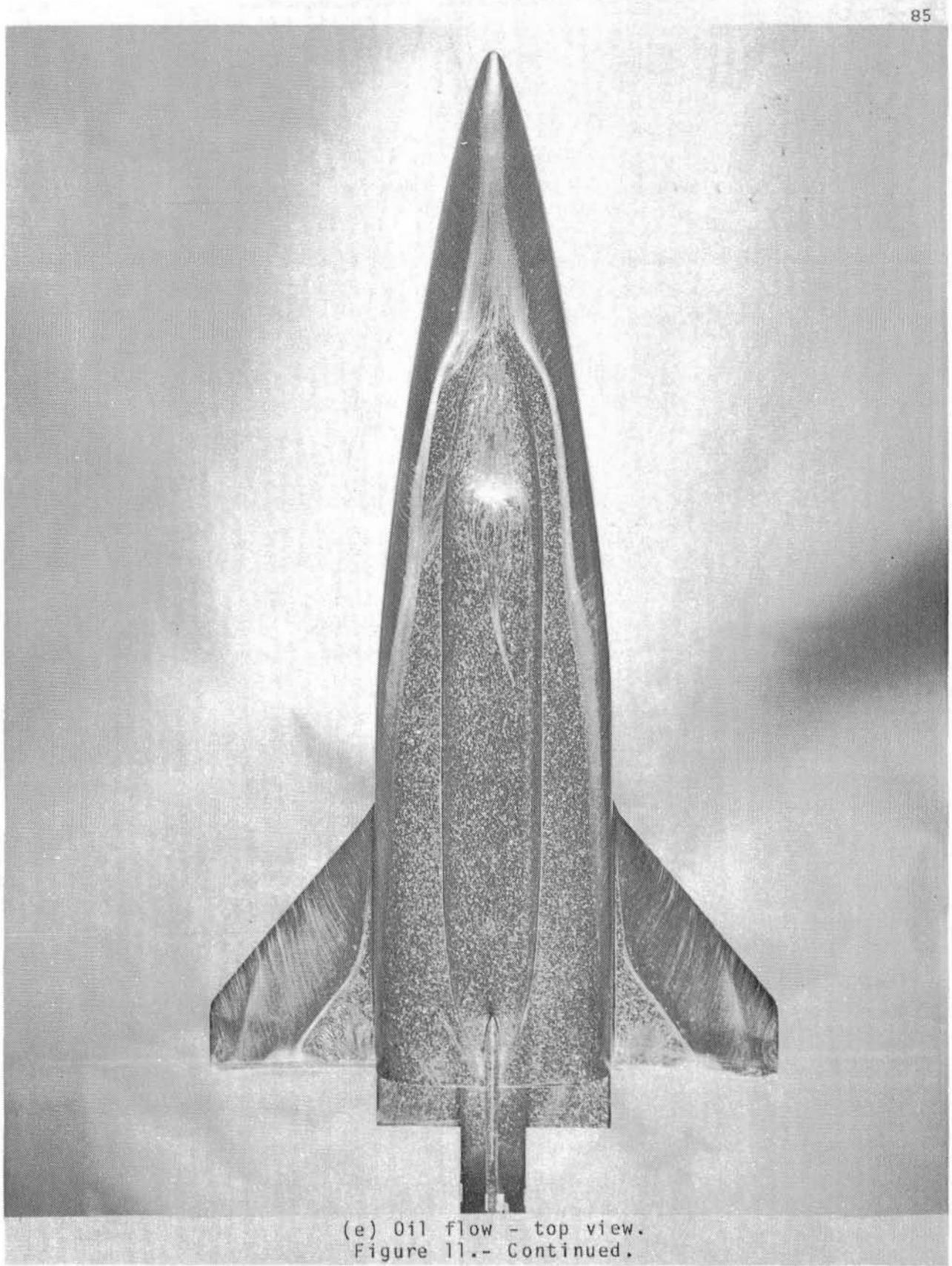
(b) Heating contours - bottom view.
Figure 11.- Continued.



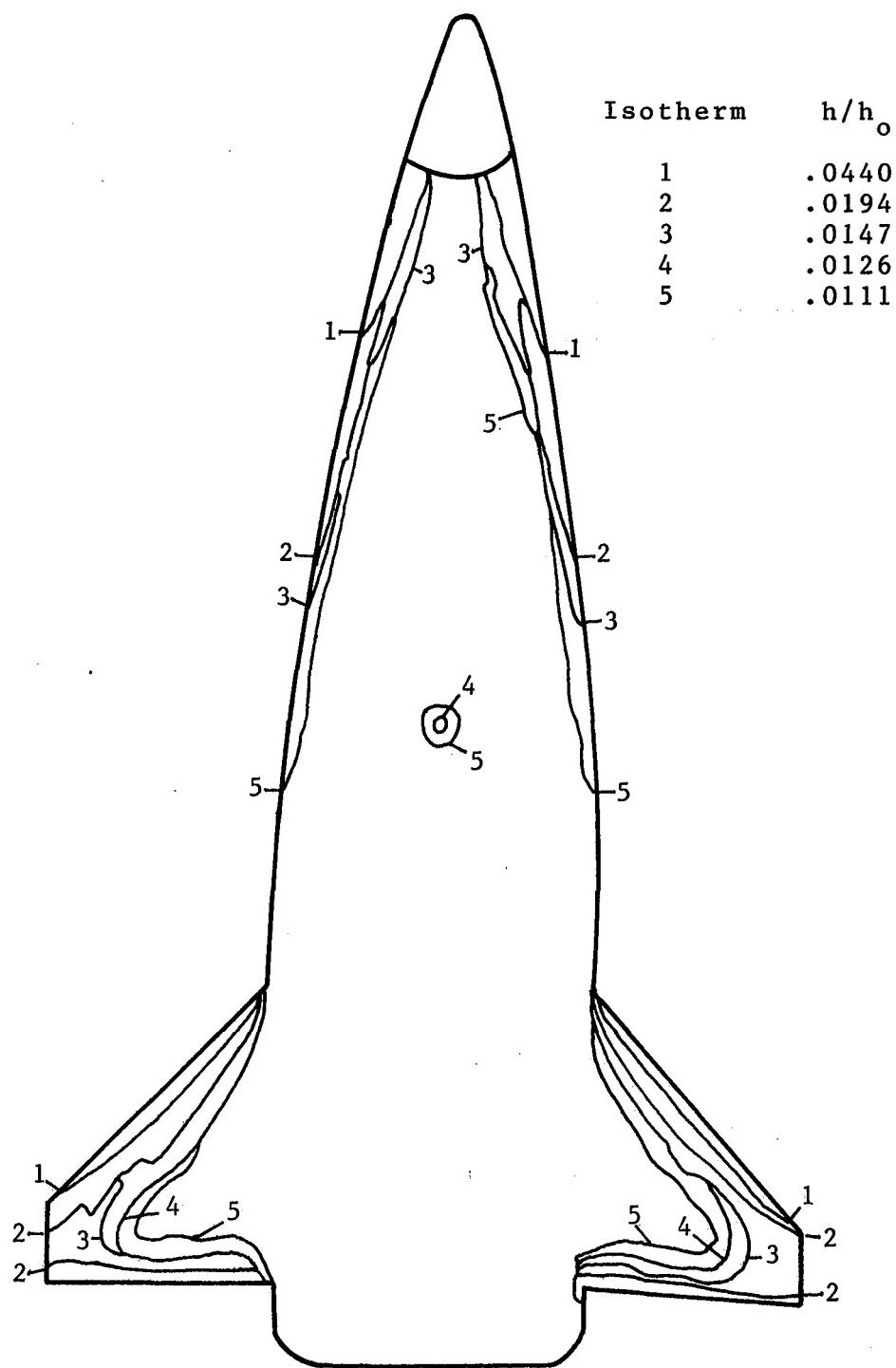
(c) Oil flow - side view.
Figure II.- Continued.



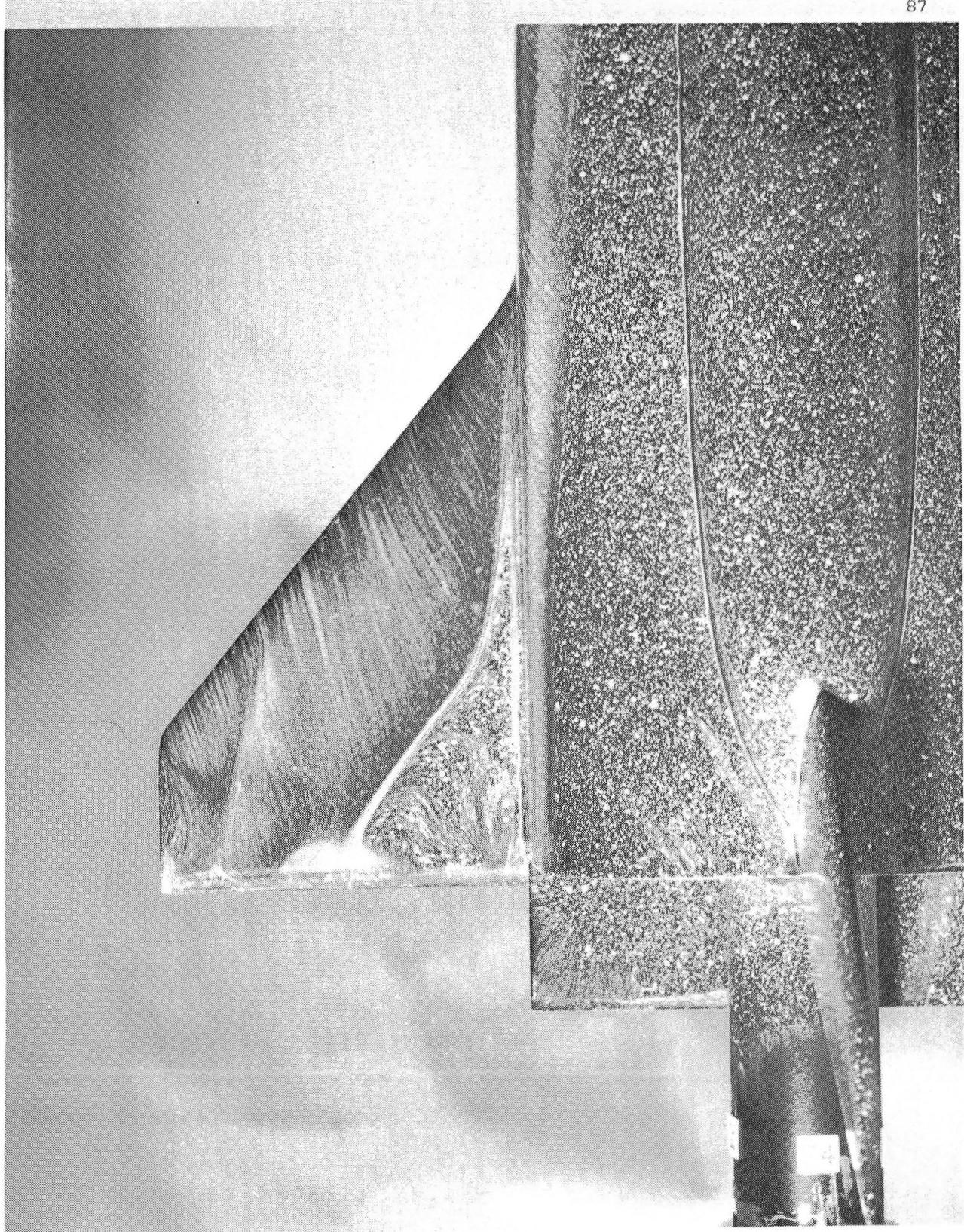
(d) Heating contours - side view.
Figure 11.- Continued.



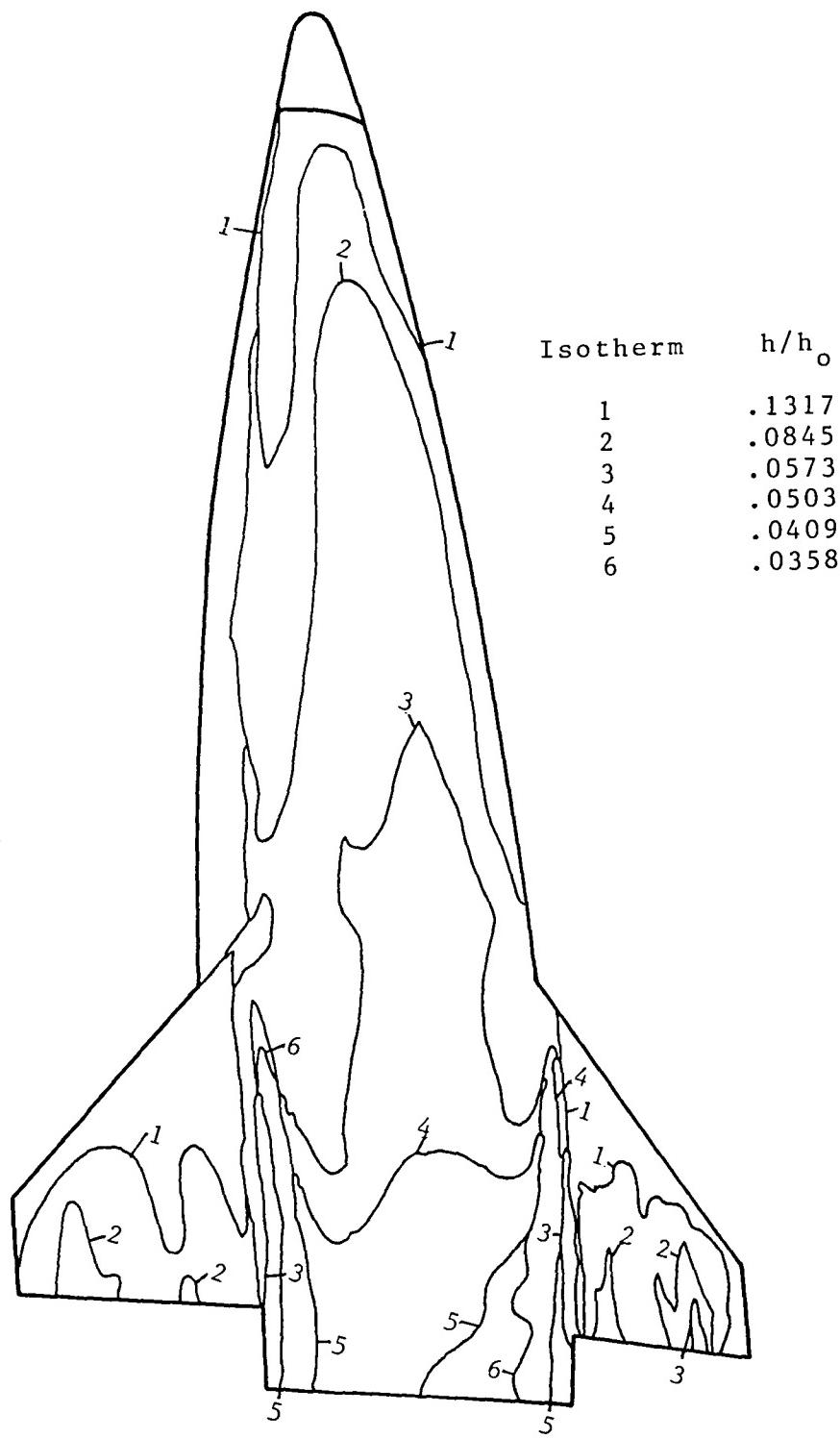
(e) Oil flow - top view.
Figure 11.- Continued.



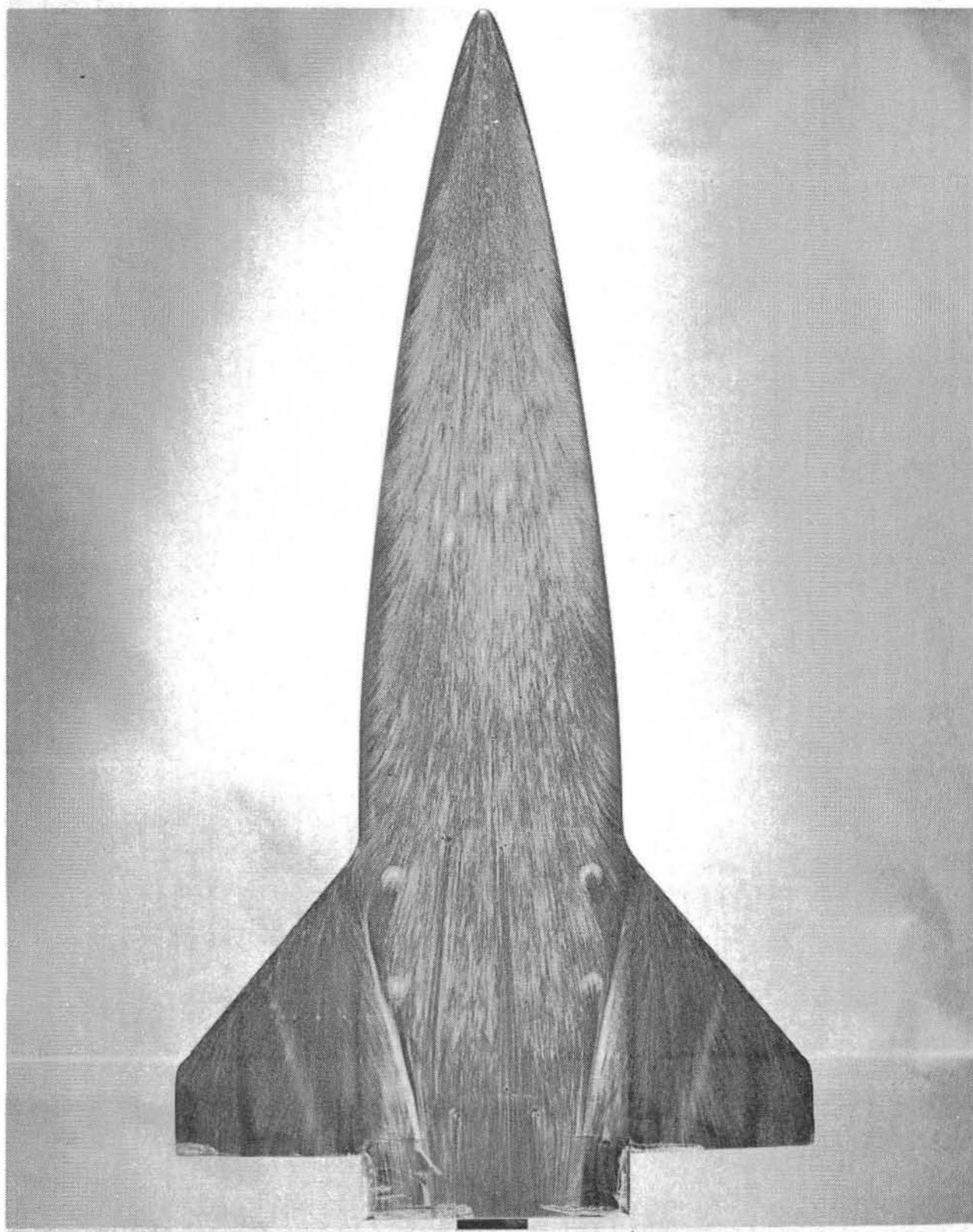
(f) Heating contours - top view.
Figure 11.- Continued.



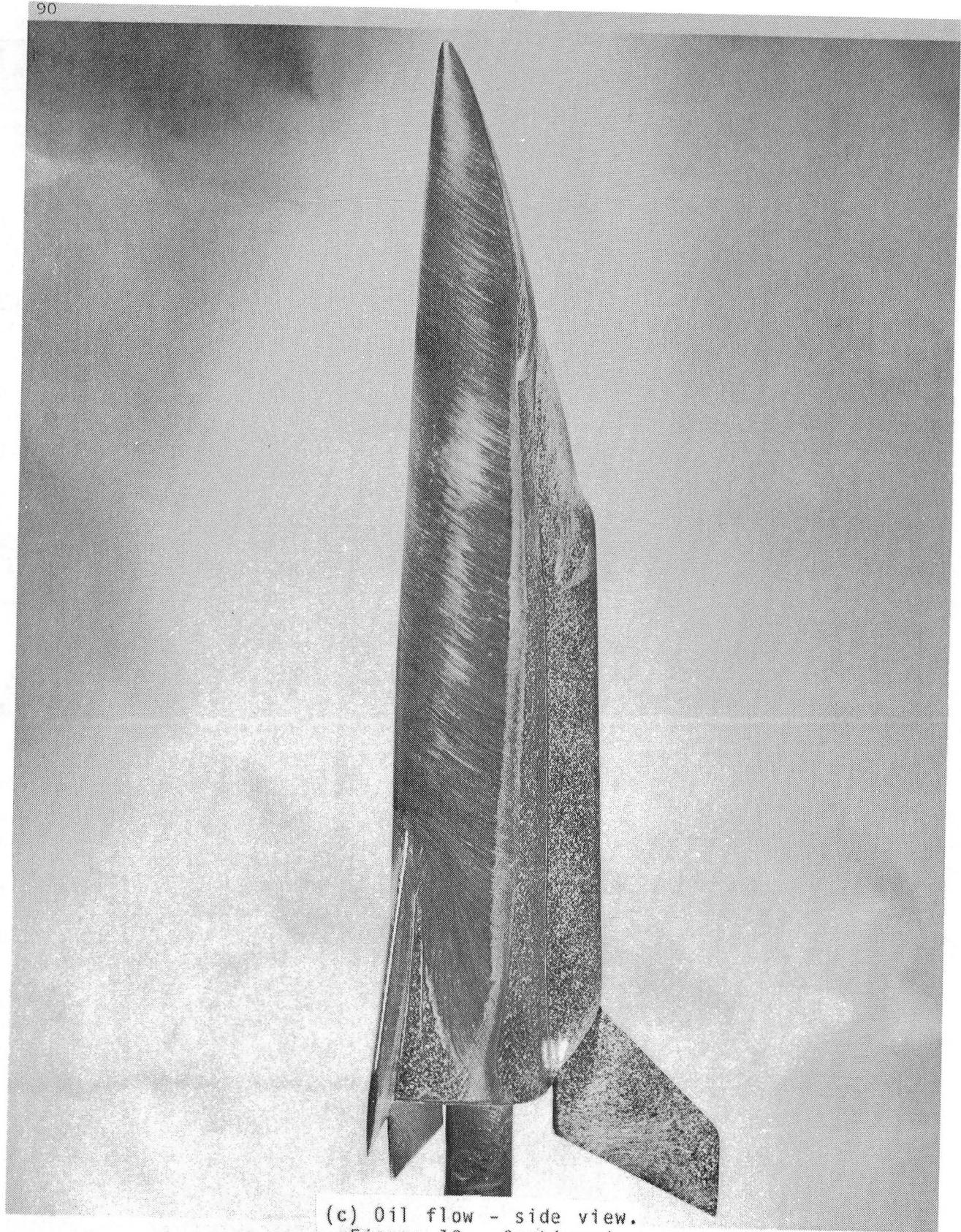
(g) Oil flow - close-up of wing leeside.
Figure II.- Concluded.



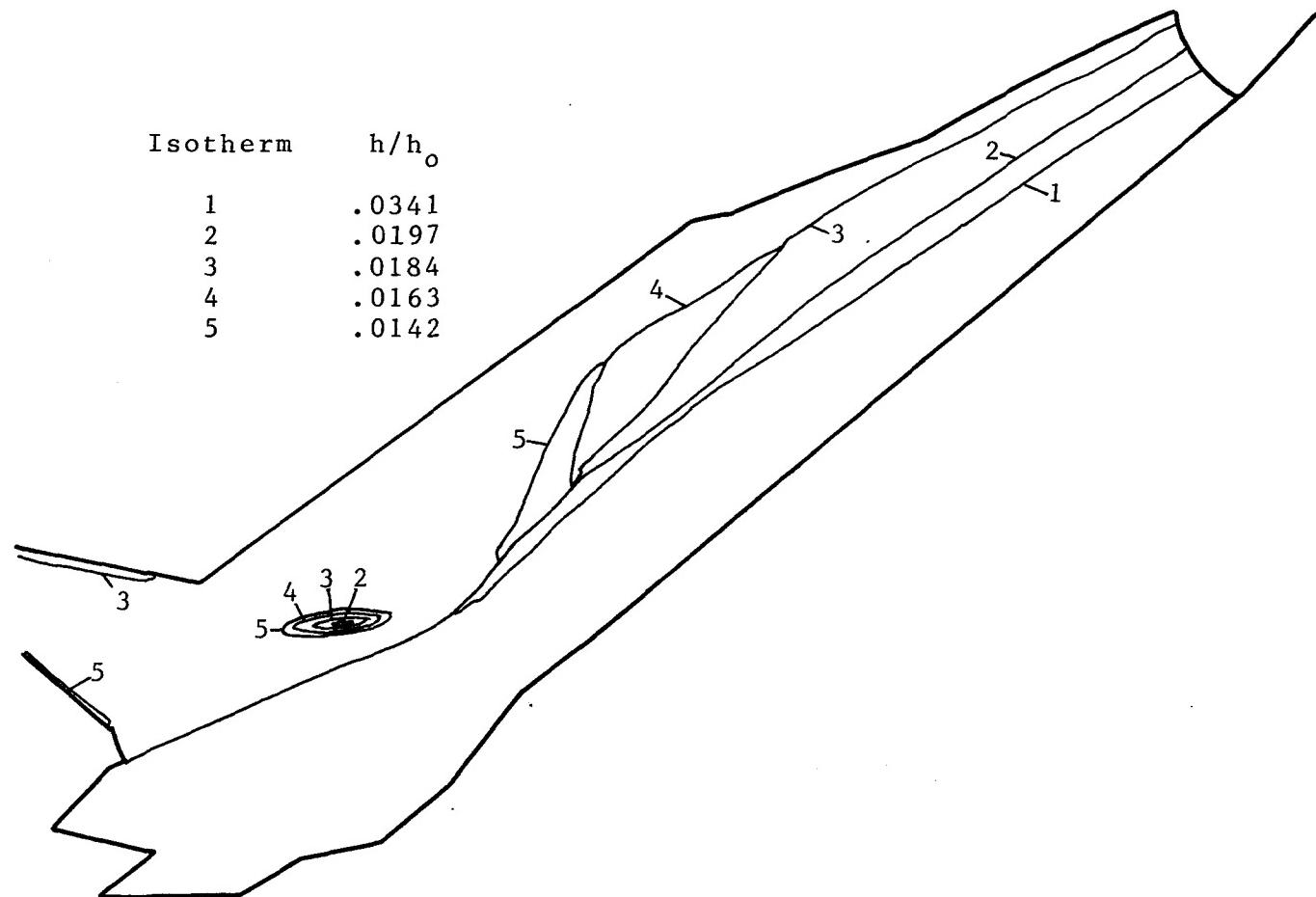
(a) Heating contours - bottom view.
 Figure 12.- Heat transfer data and oil flow patterns at $\alpha = 30^\circ$ and
 $Re_\infty = 2.0 \times 10^6$.



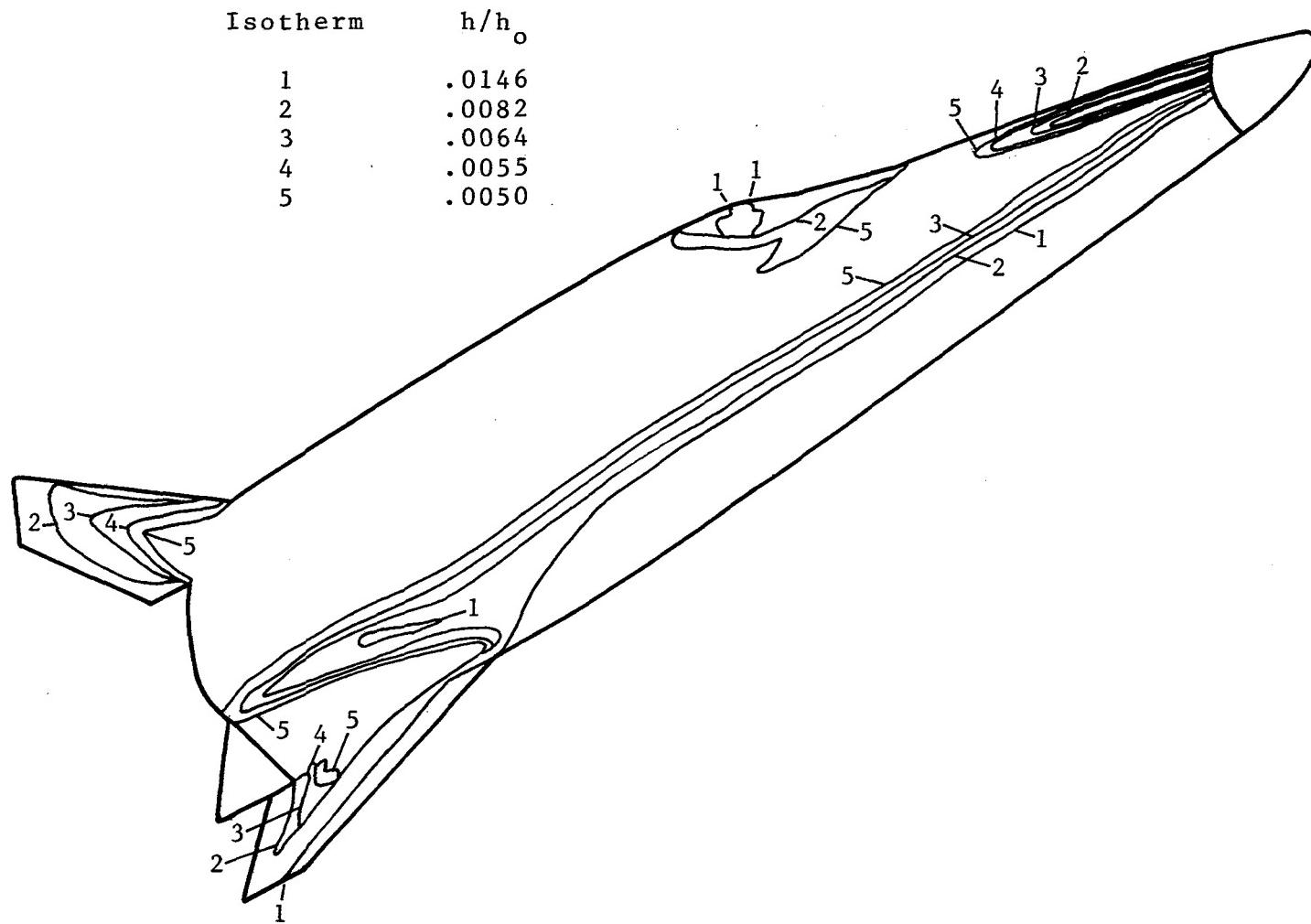
(b) Oil flow - bottom view.
Figure 12.- Continued.



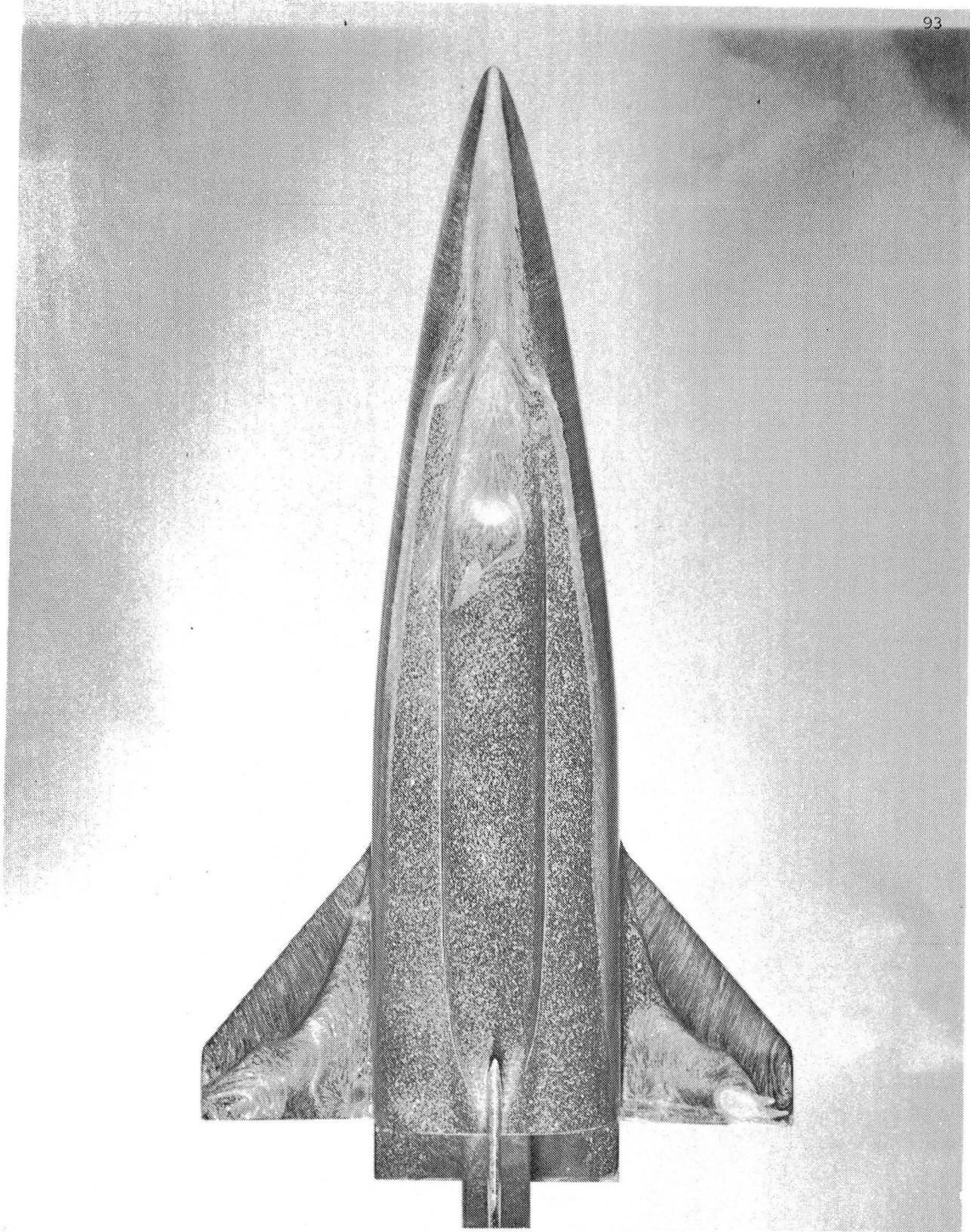
(c) Oil flow - side view.
Figure 12.- Continued.



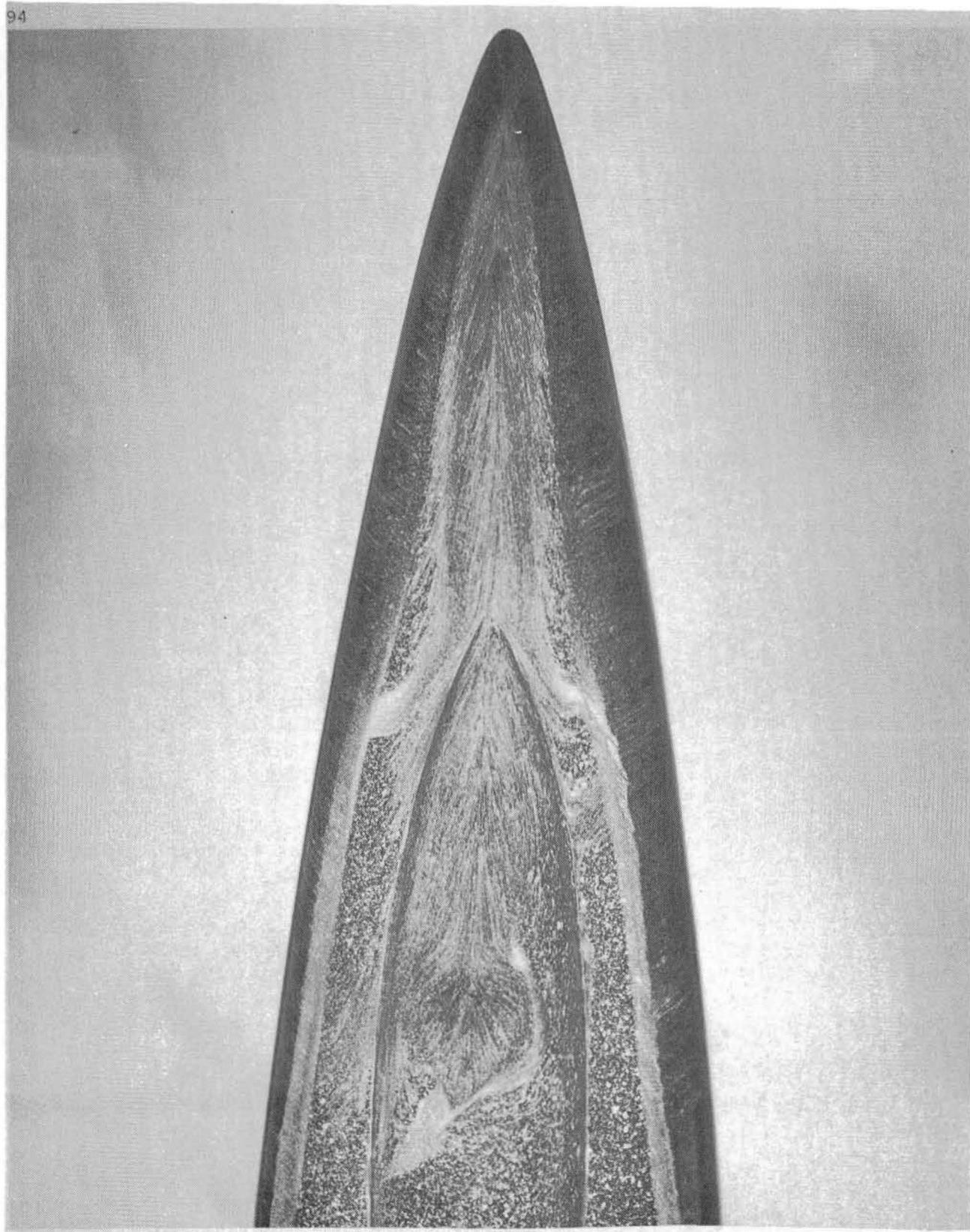
(d) Heating contours - side view.
 Figure 12.- Continued.



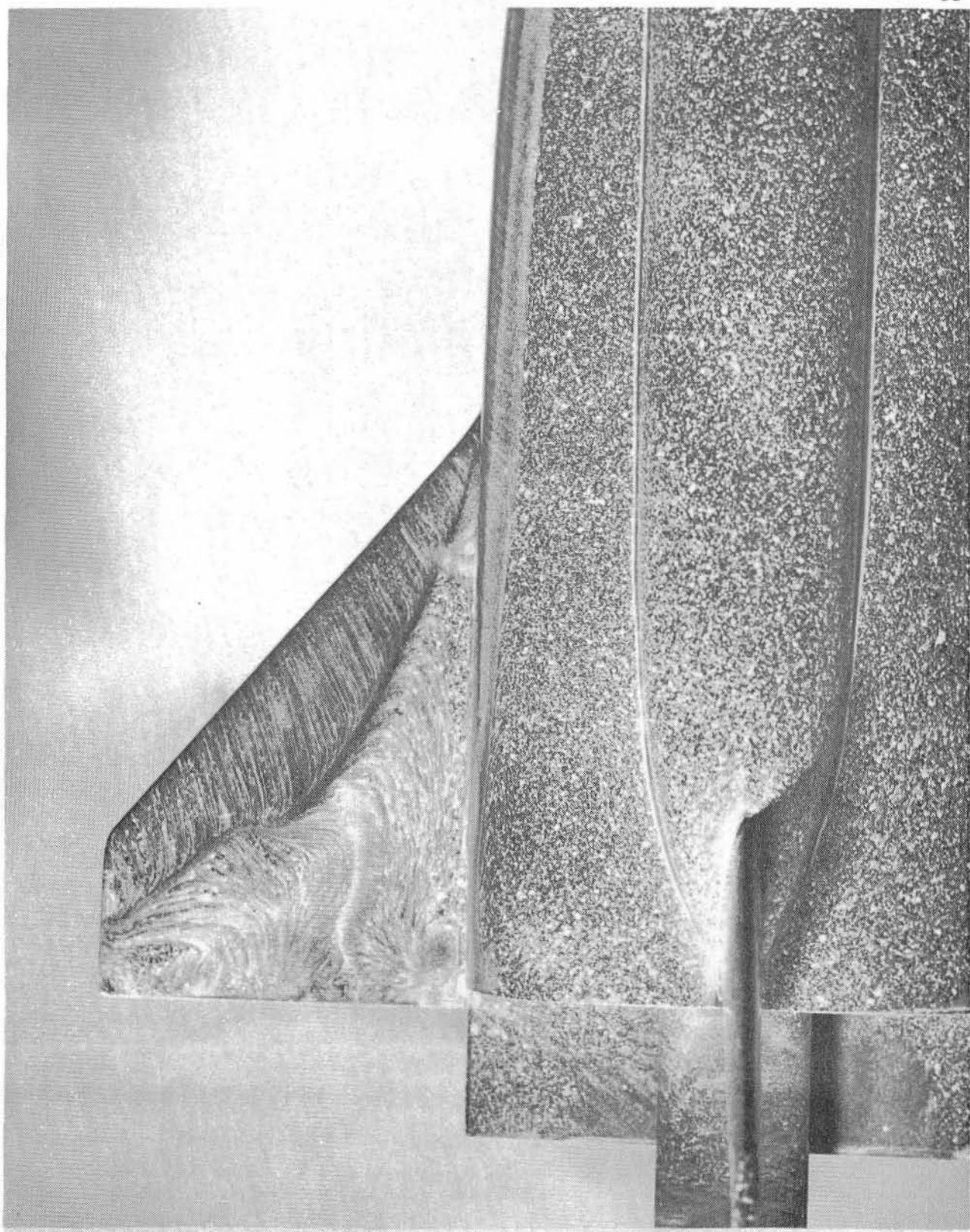
(e) Heating contours - oblique top view.
Figure 12.- Continued.



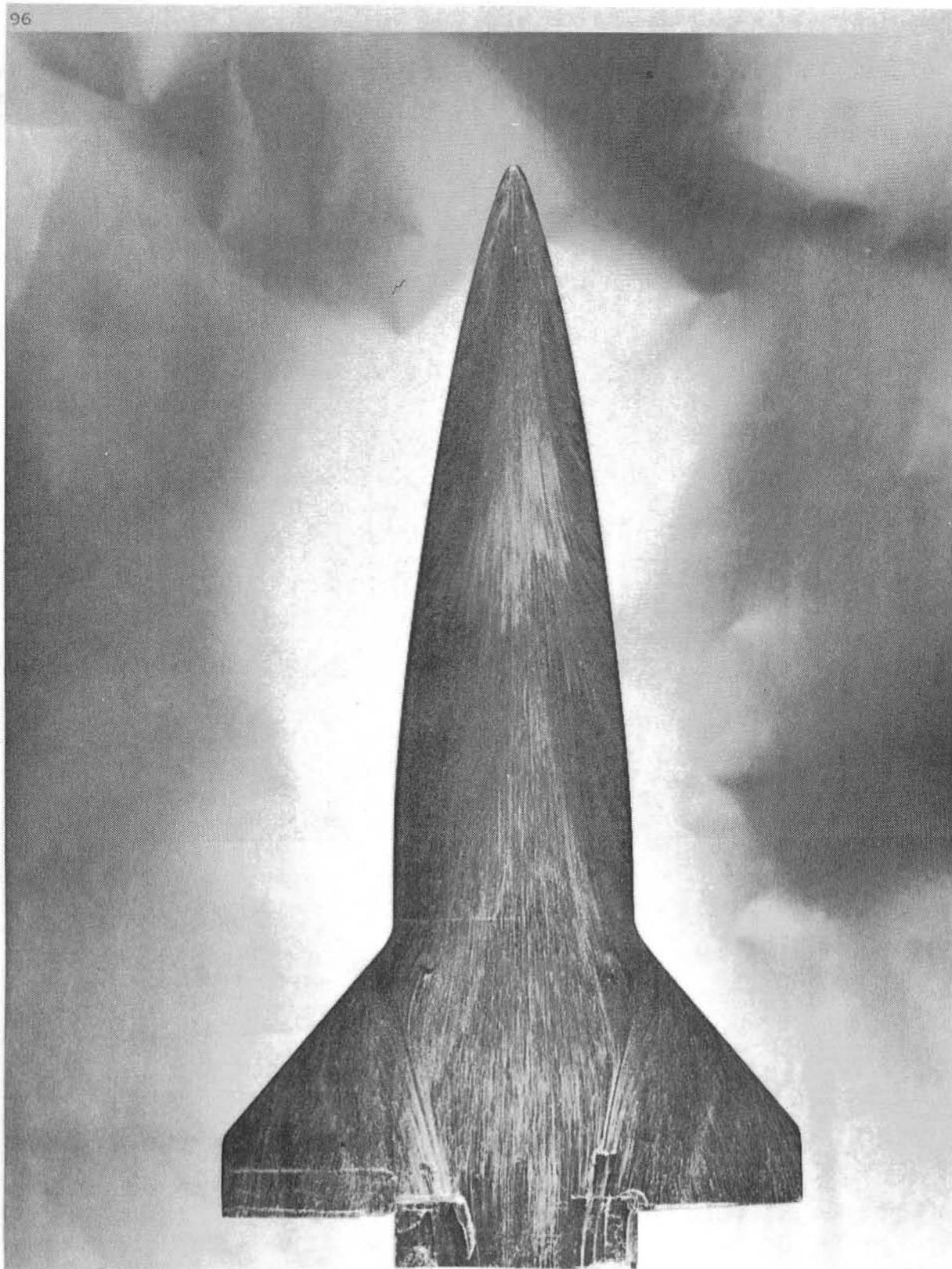
(f) Oil flow - top view.
Figure 12.- Continued.



(g) Oil flow - close-up of canopy.
Figure 12.- Continued.

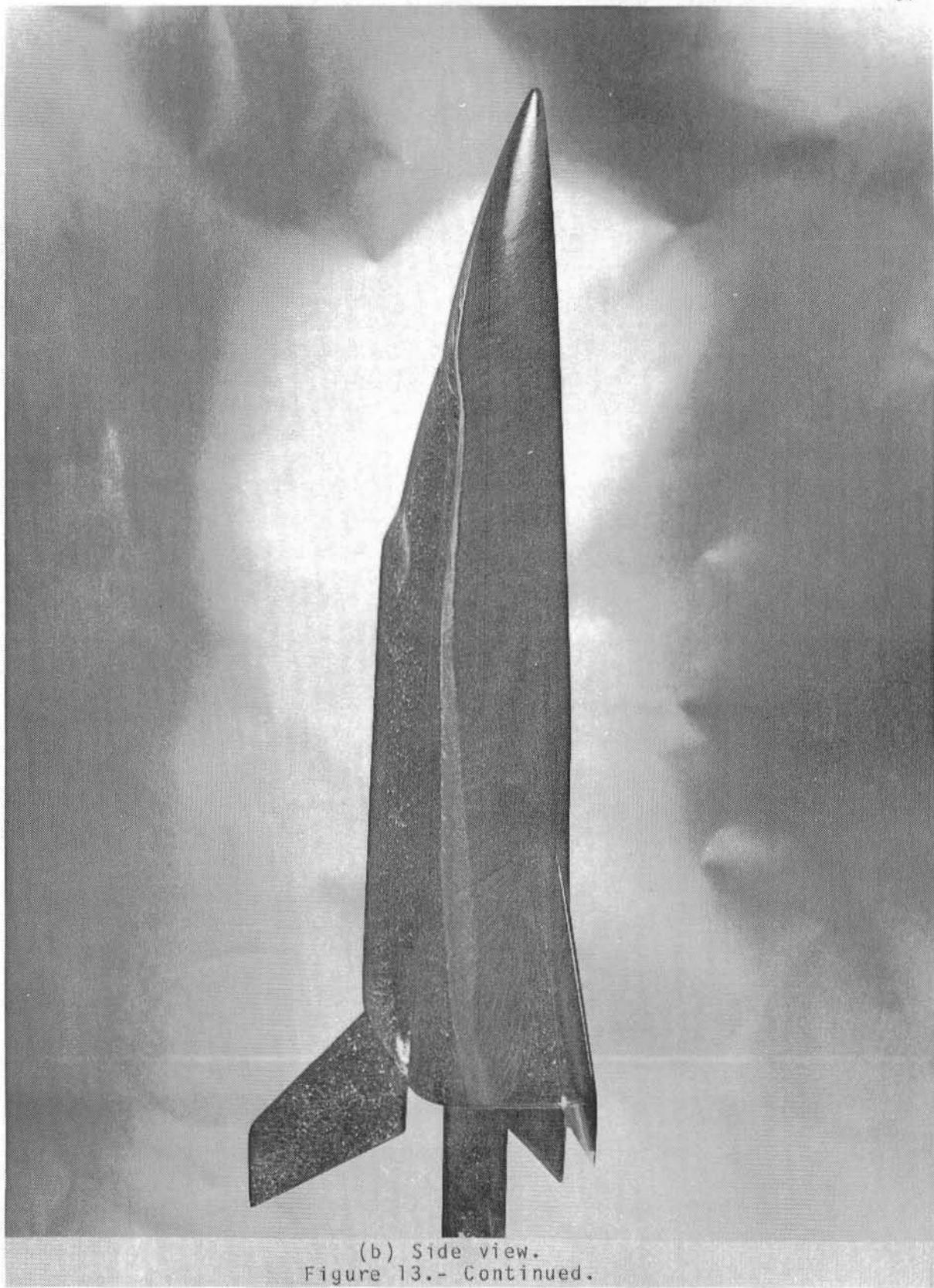


(h) Oil flow - close-up of wing leeside.
Figure 12.- Concluded.

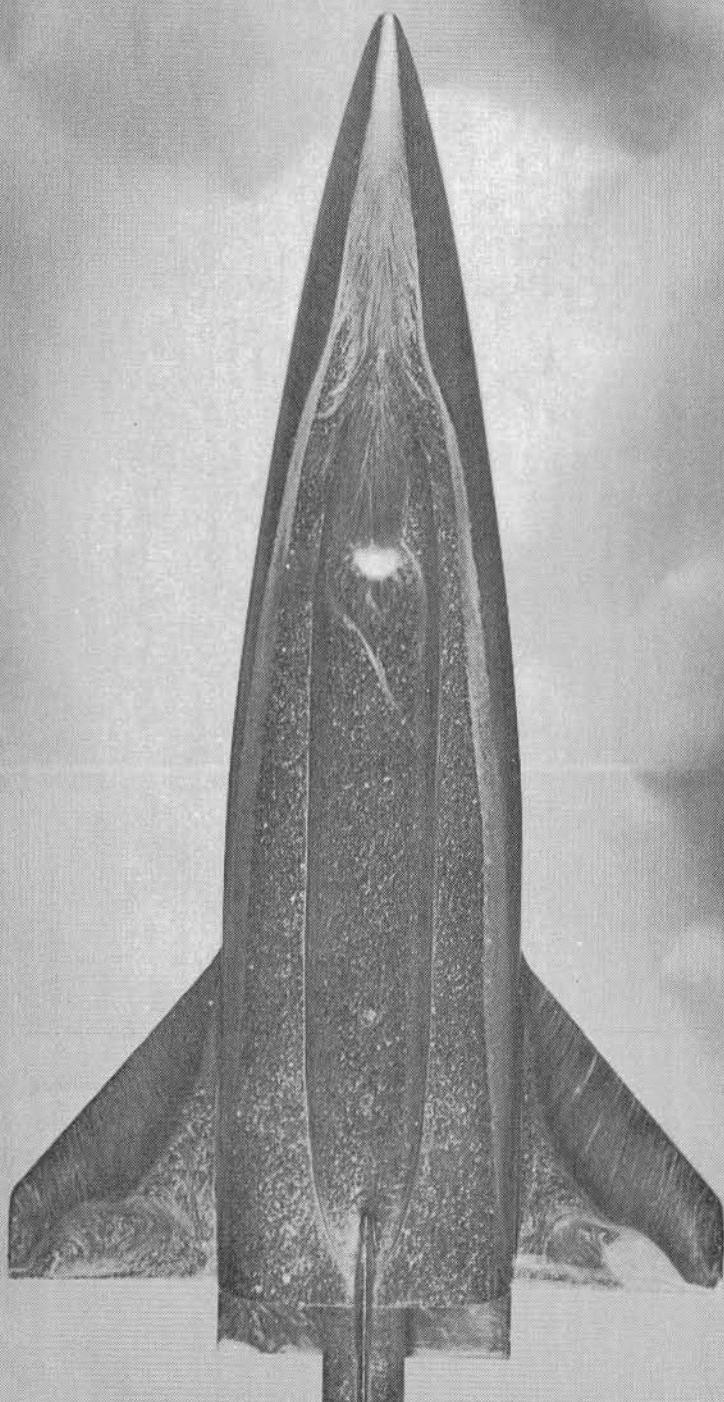


(a) Bottom view.

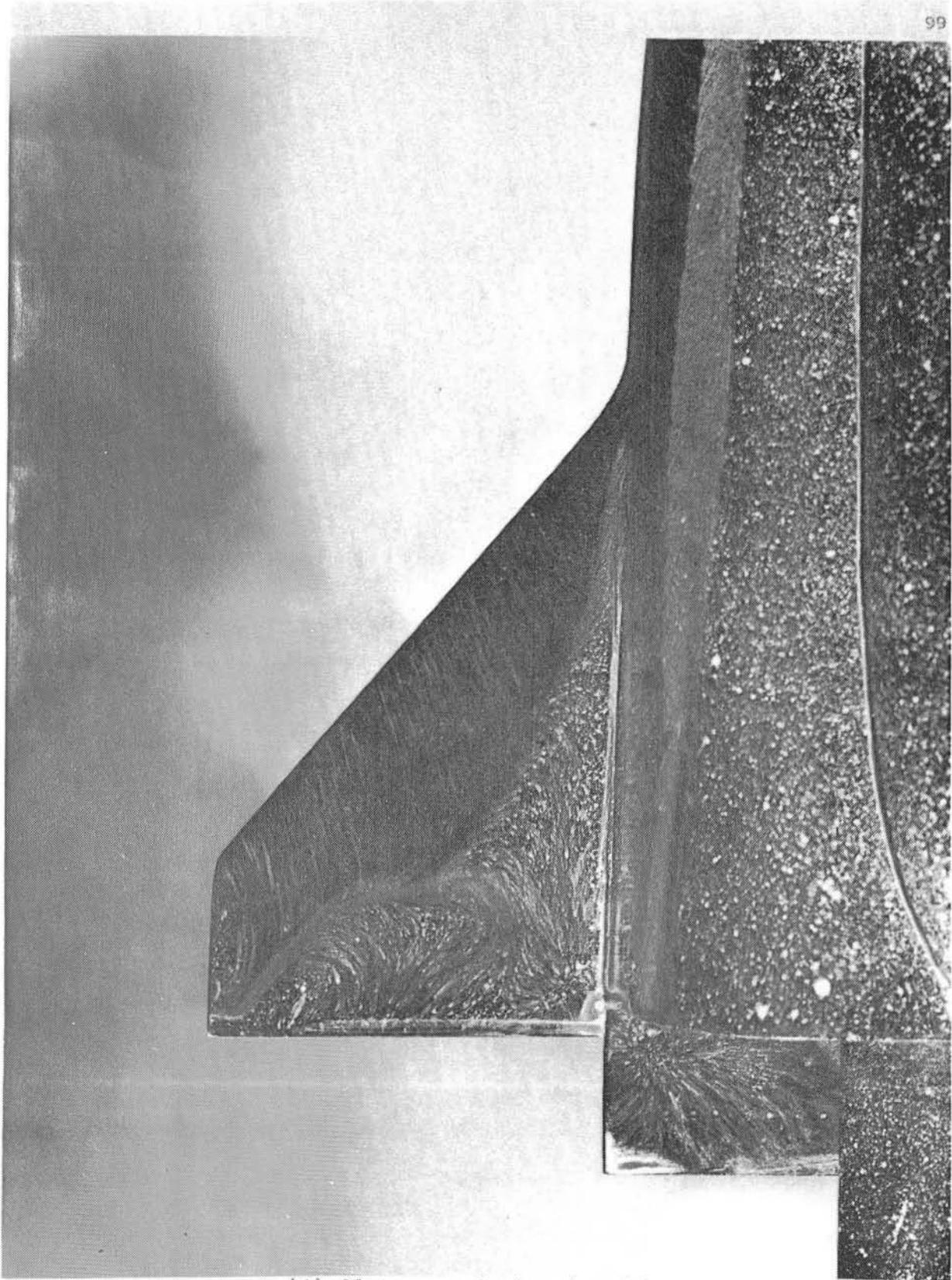
Figure 13. Oil flow patterns at $\alpha = 30^\circ$ and $Re_\infty = 1.0 \times 10^6$.



(b) Side view.
Figure 13.- Continued.

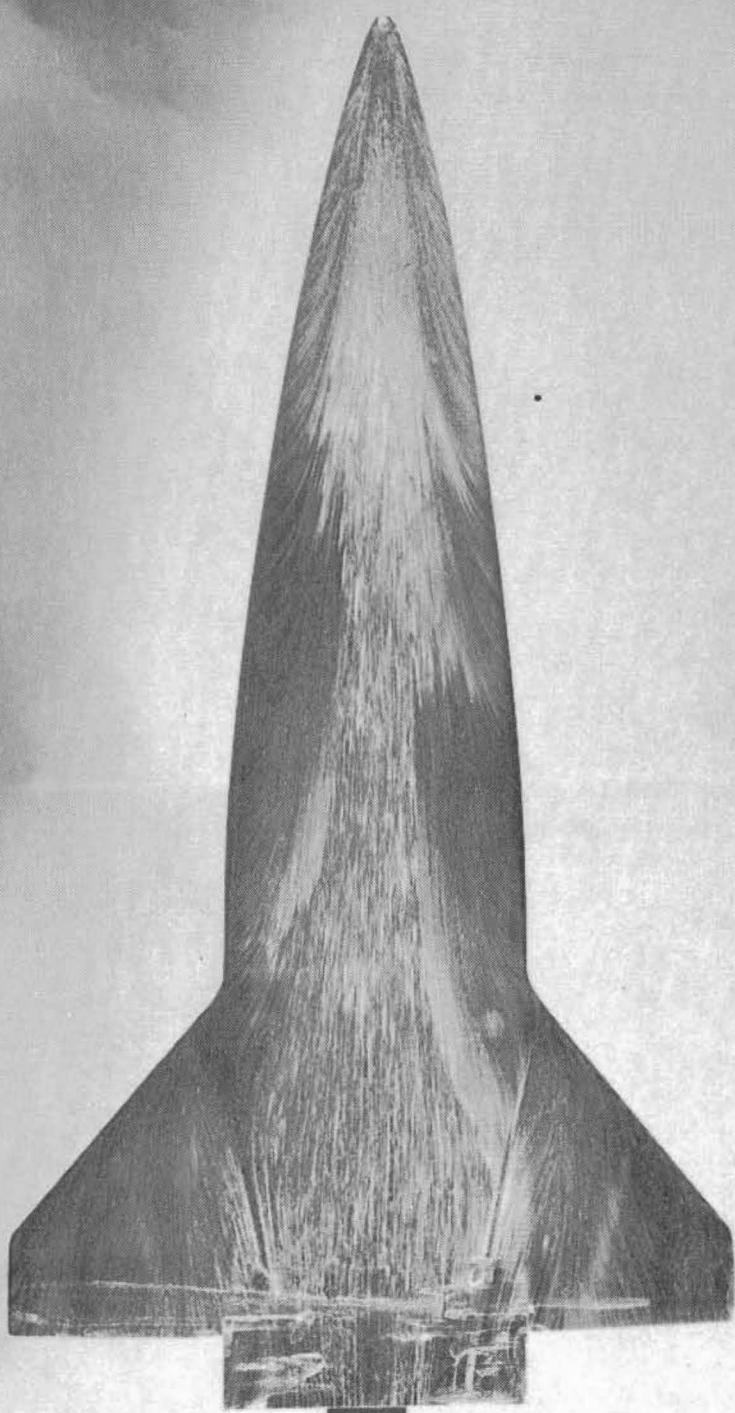


(c) Top view.
Figure 13.- Continued.



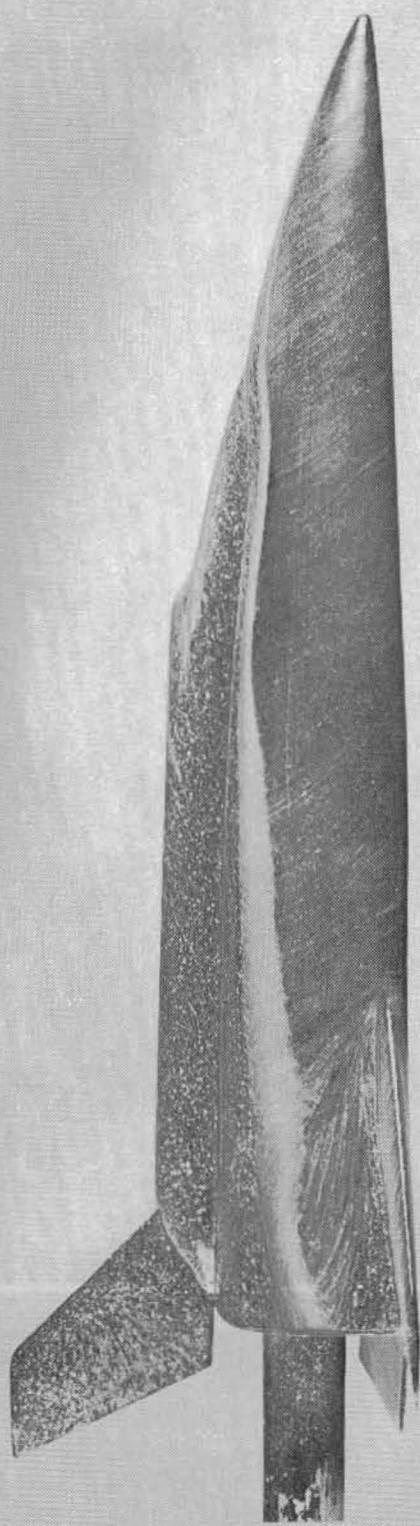
(d) Close-up of wing leeside.
Figure 13.- Concluded.

100

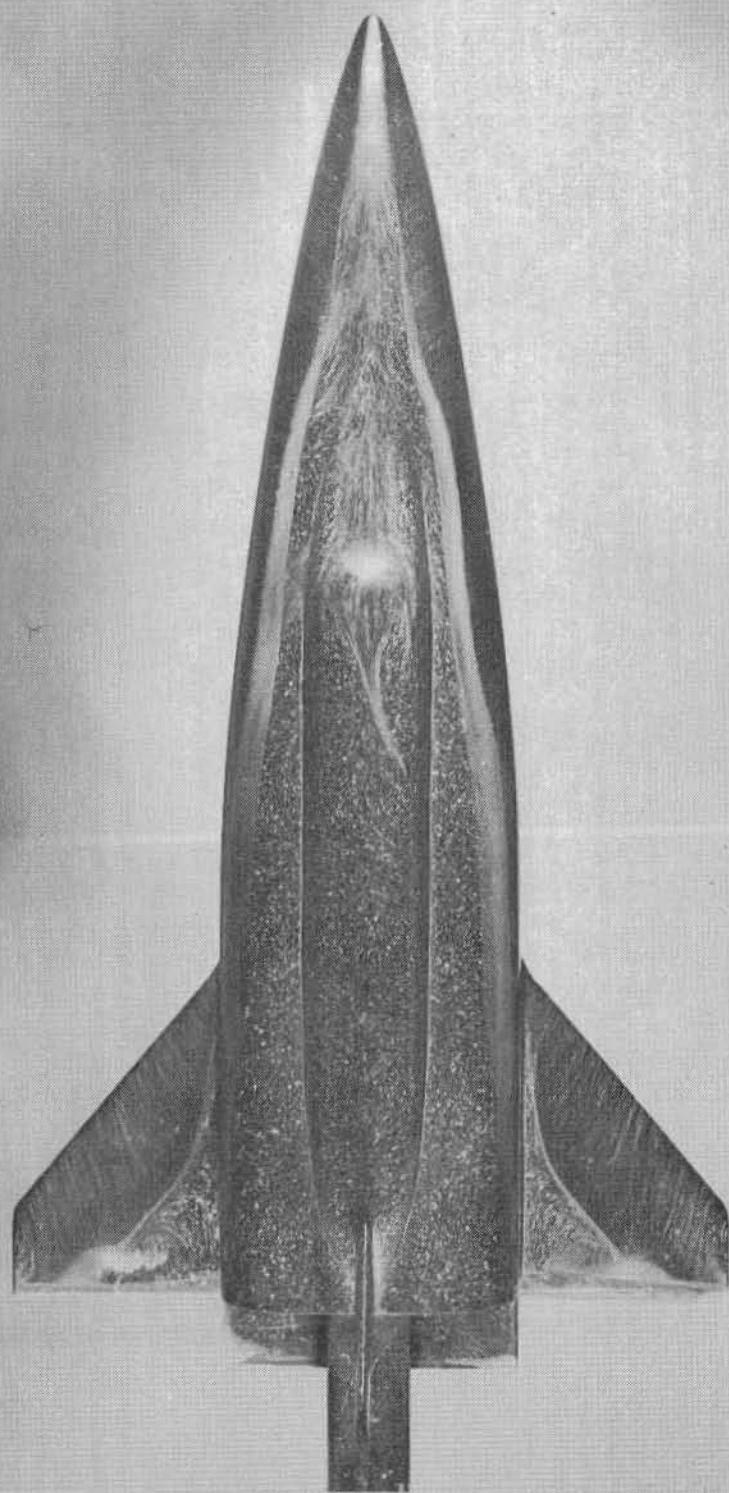


(a) Bottom view.

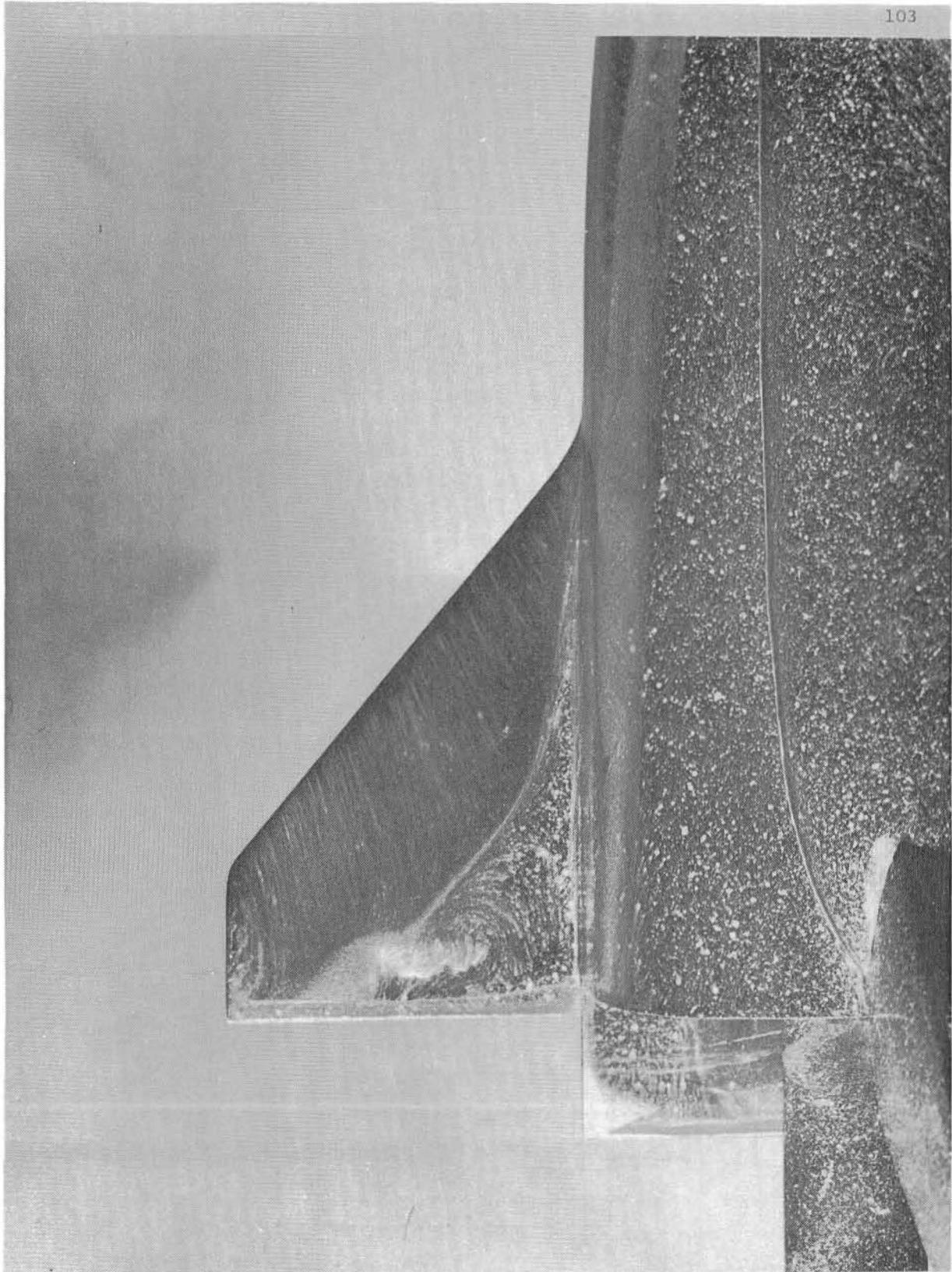
Figure 14.- Oil flow patterns at $\alpha = 30^\circ$ and
 $Re_\infty = 0.5 \times 10^6$.



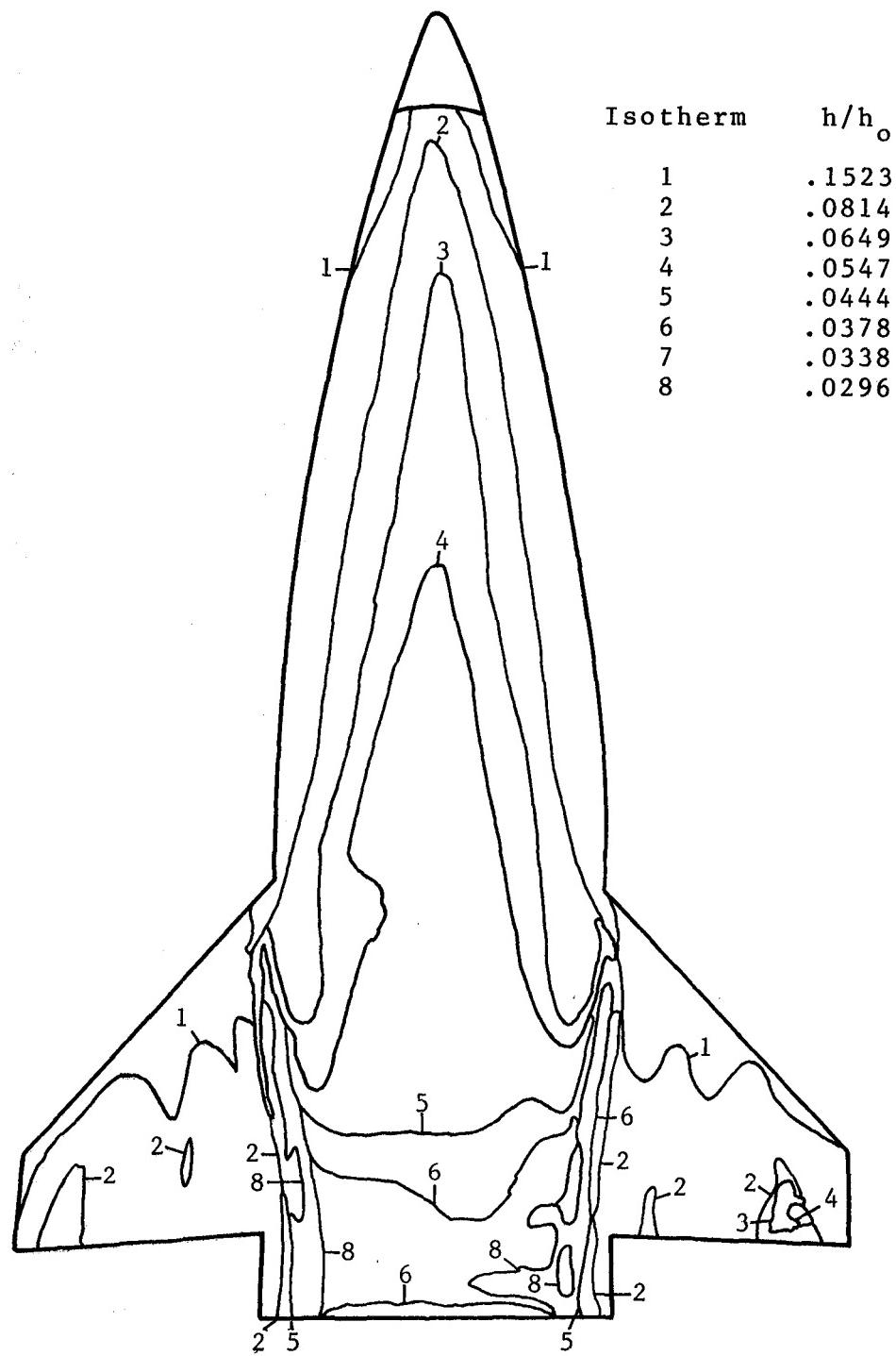
(b) Side view.
Figure 14.- Continued.



(c) Top view.
Figure 14.- Continued.

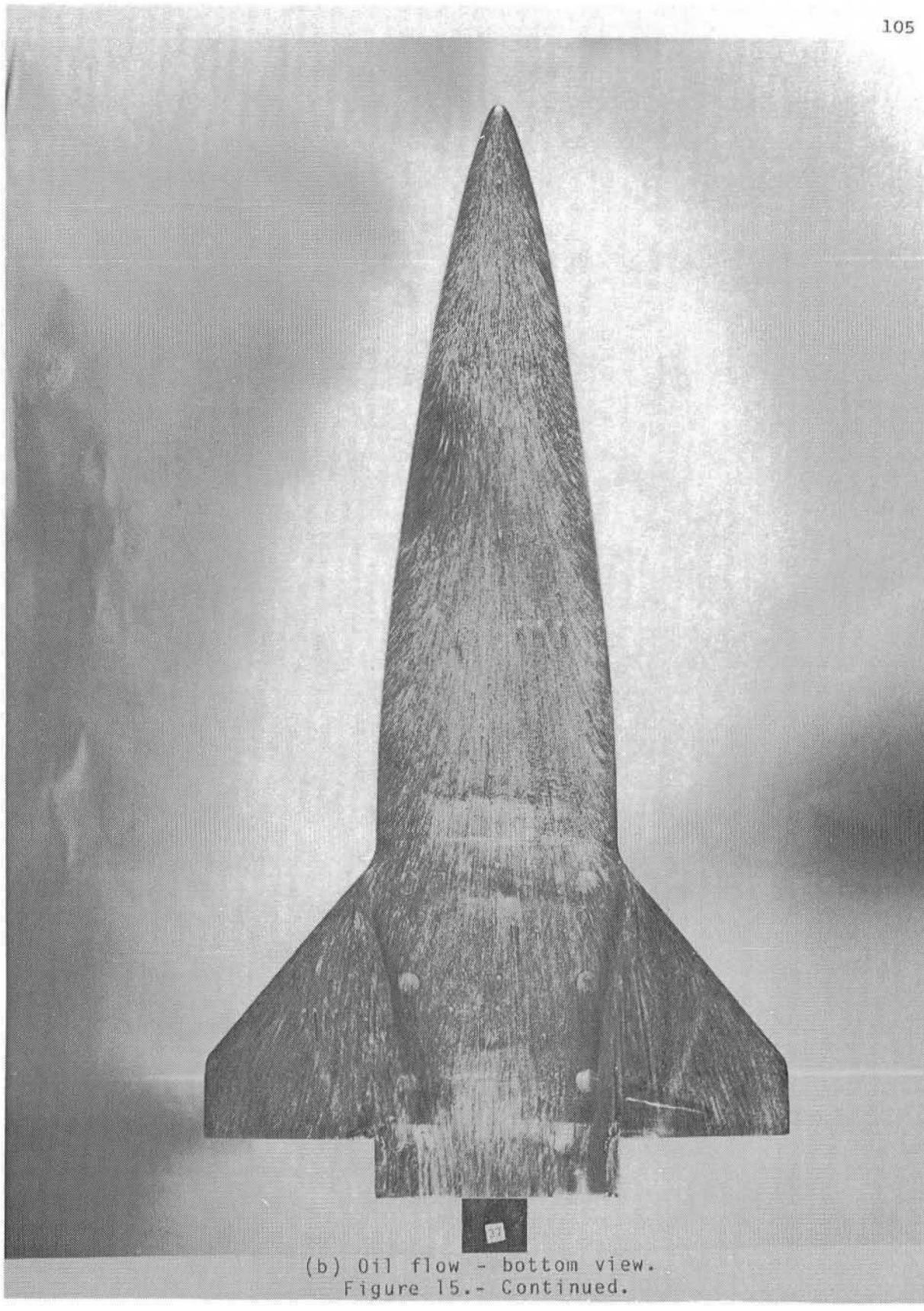


(d) Close-up of wing leeside.
Figure 14.- Concluded.

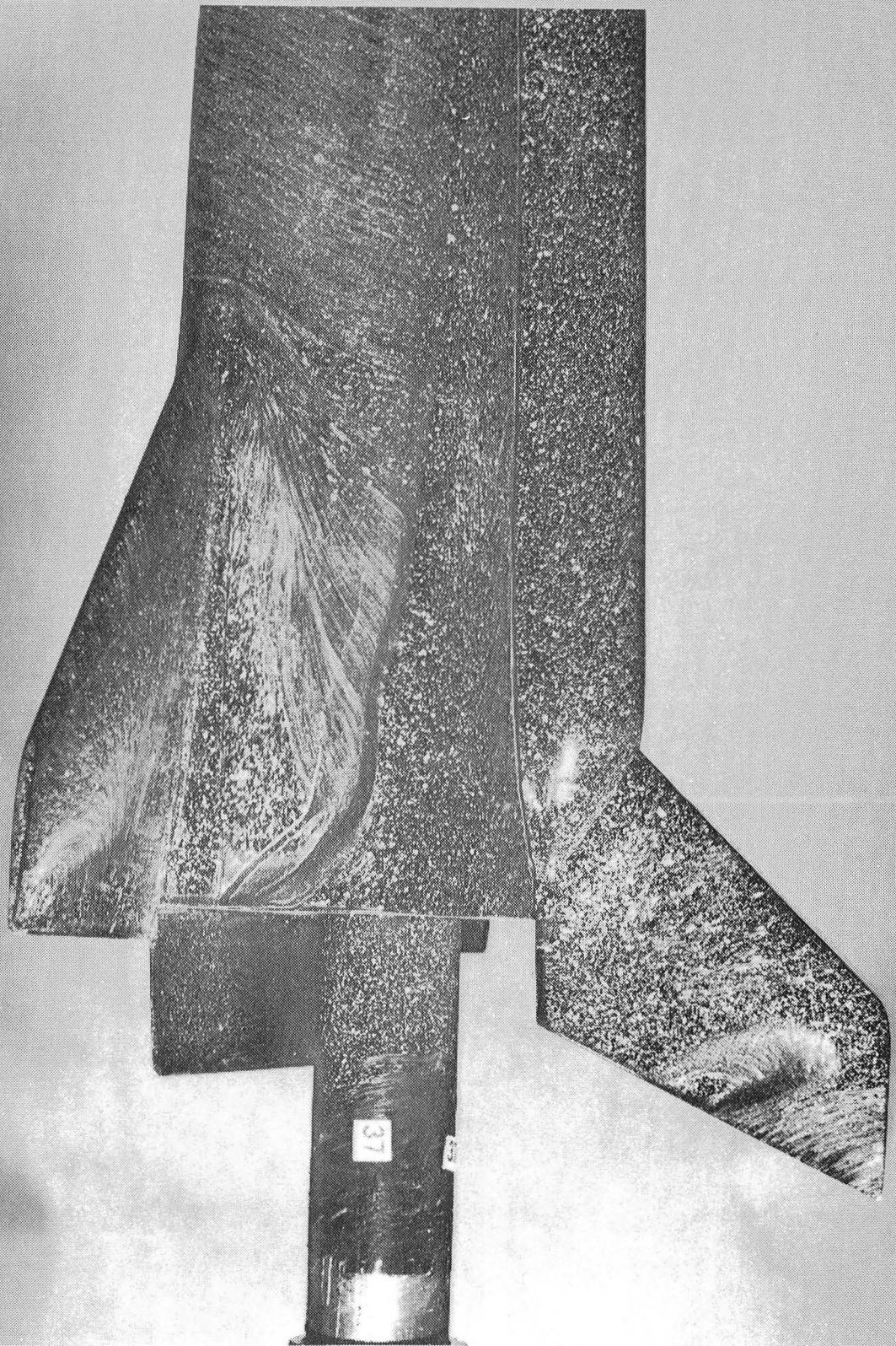


(a) Heating contours - bottom view.

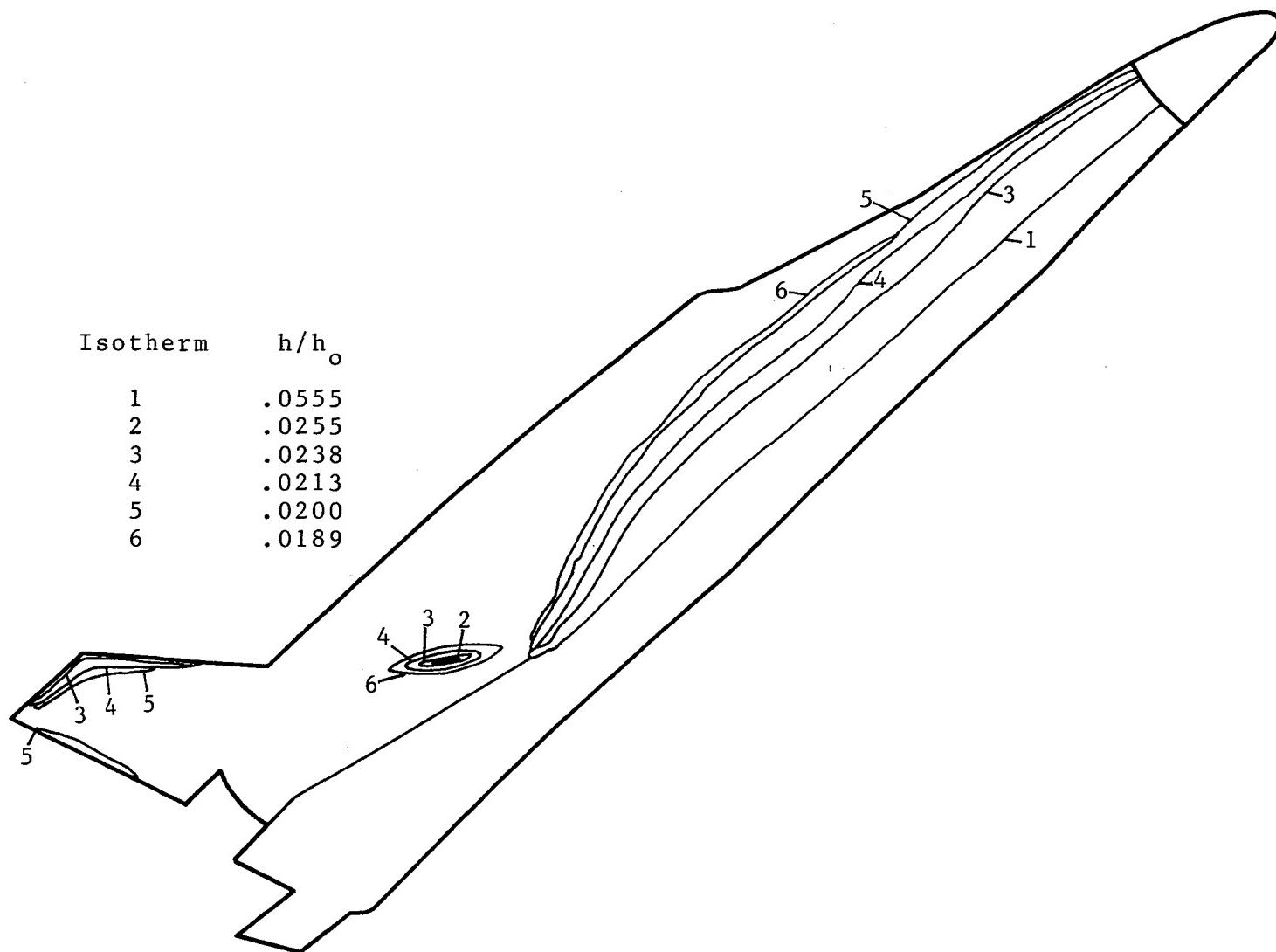
Figure 15.- Heat transfer data and oil flow patterns at $\alpha = 35^\circ$ and $Re_\infty = 2.0 \times 10^6$.



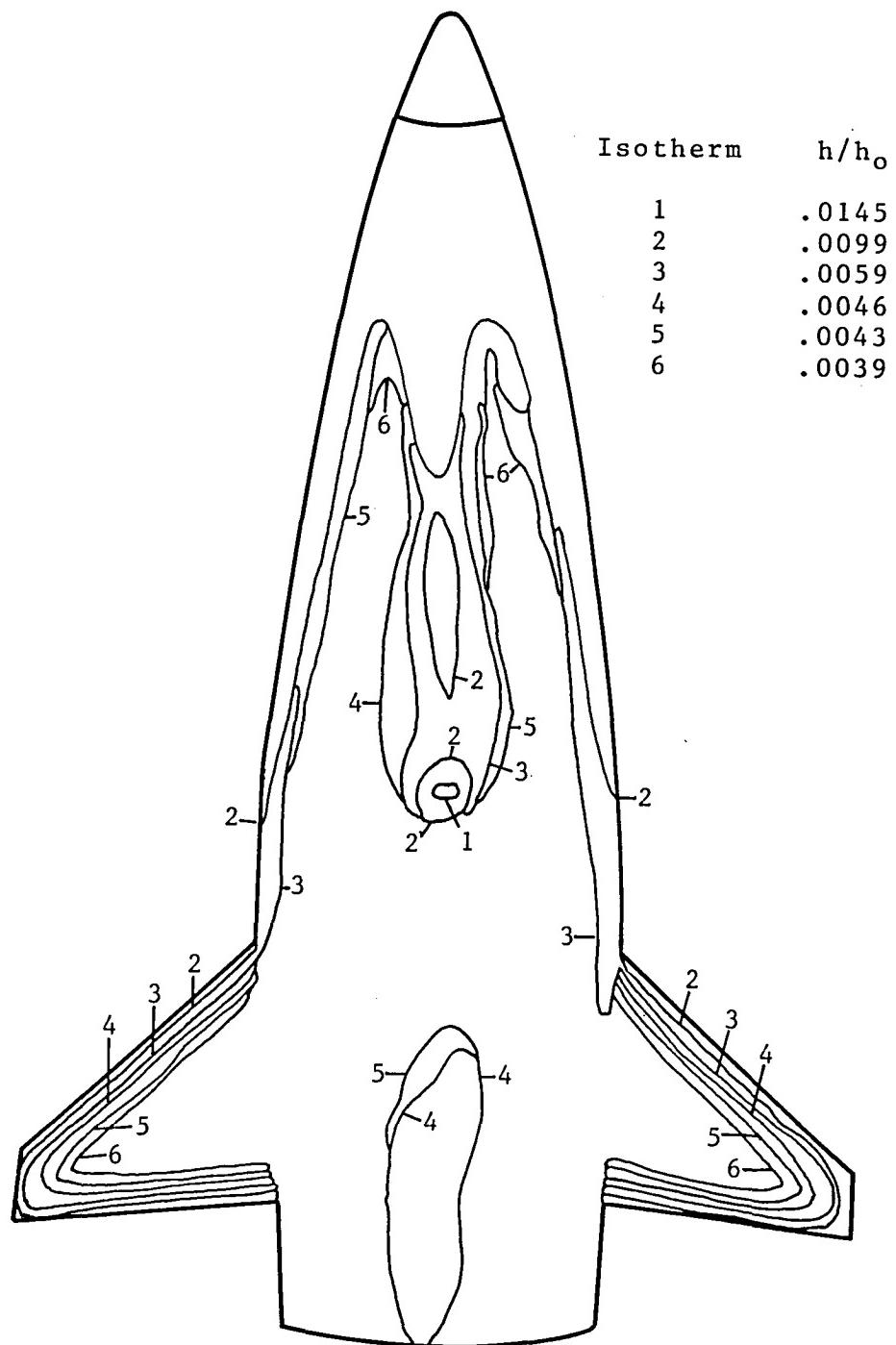
(b) Oil flow - bottom view.
Figure 15.- Continued.



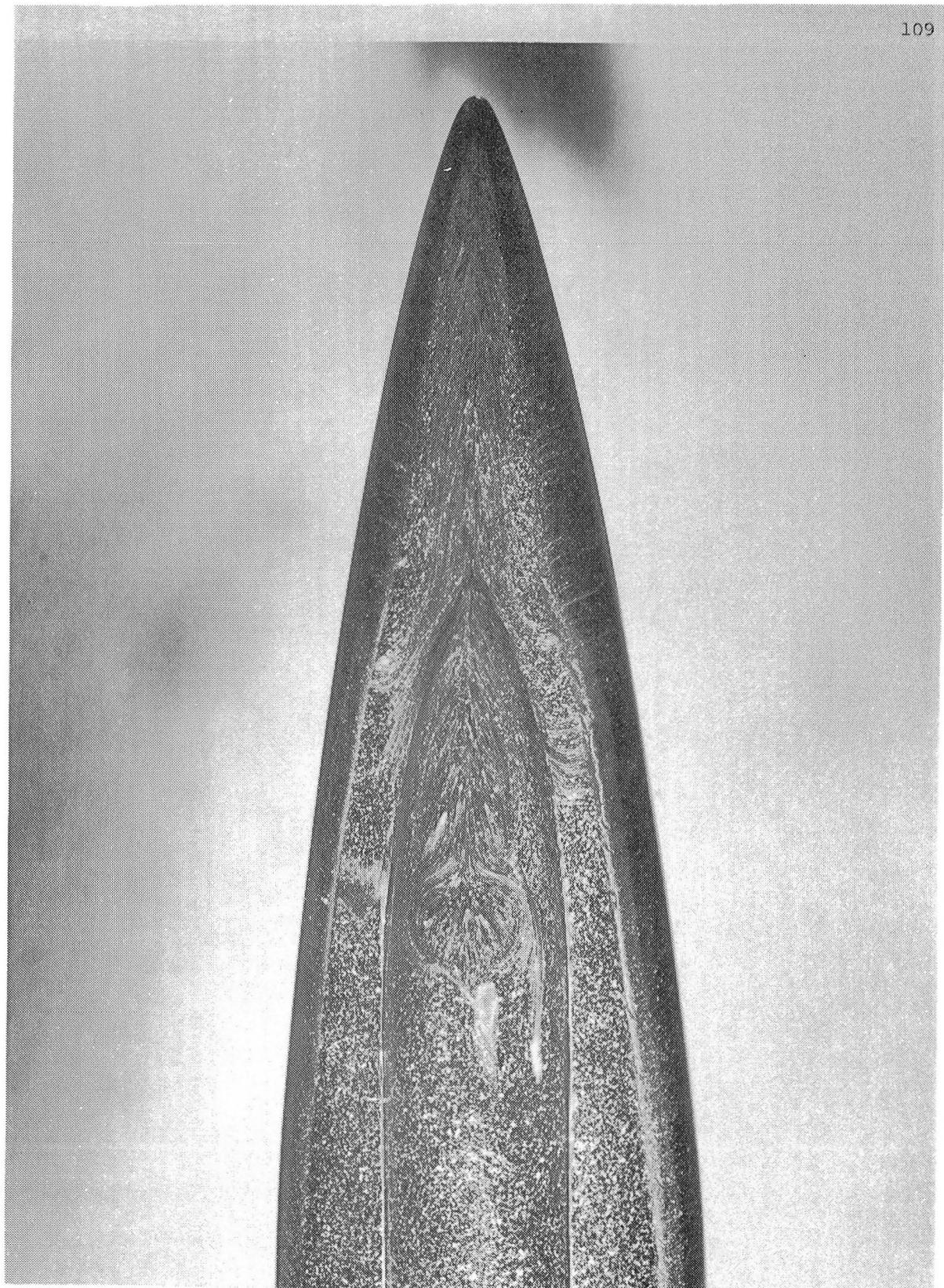
(c) Oil flow - aft side view.
Figure 15.- Continued.



(d) Heat contours - side view.
Figure 15.- Continued.

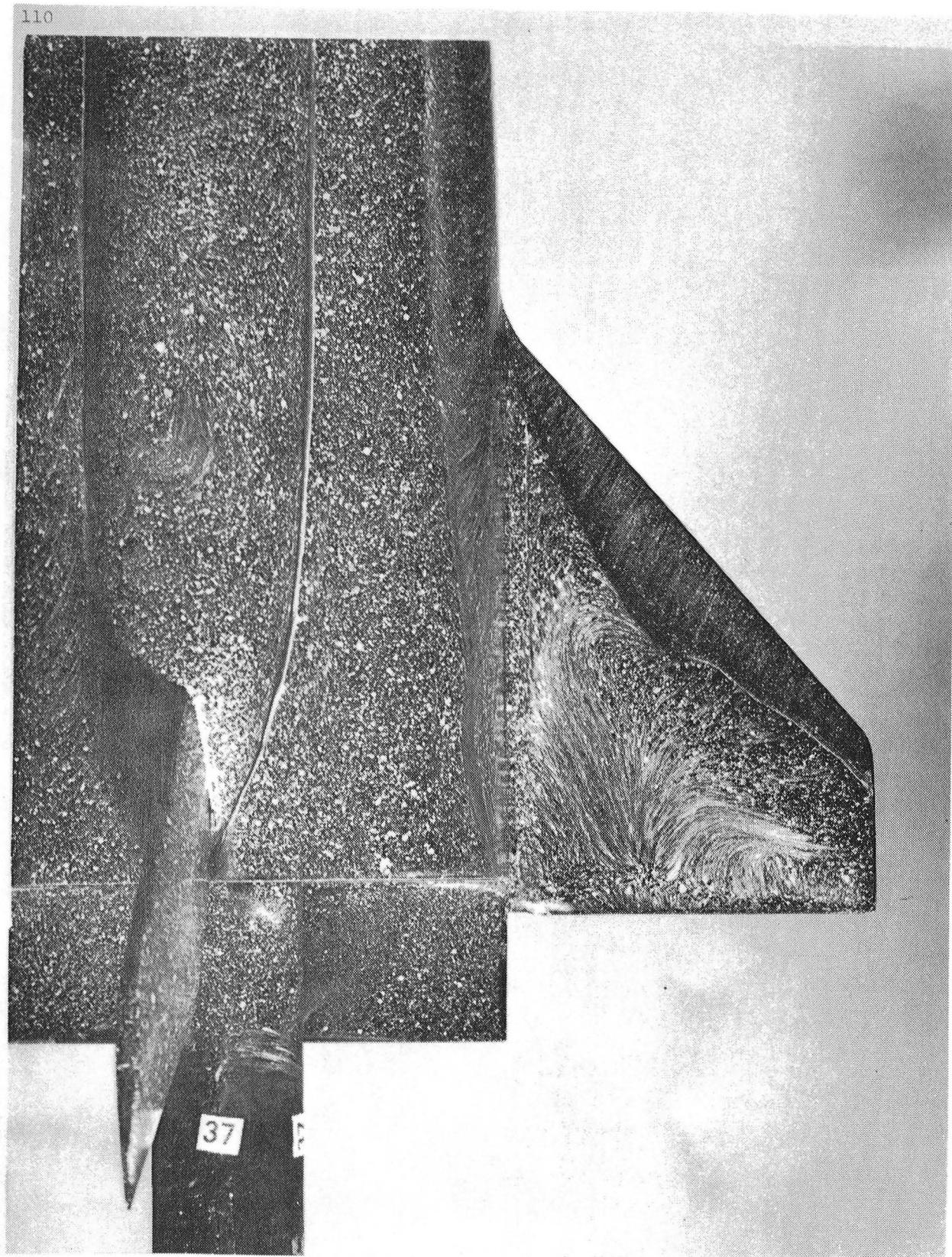


(e) Heating contours - top view.
Figure 15.- Continued.

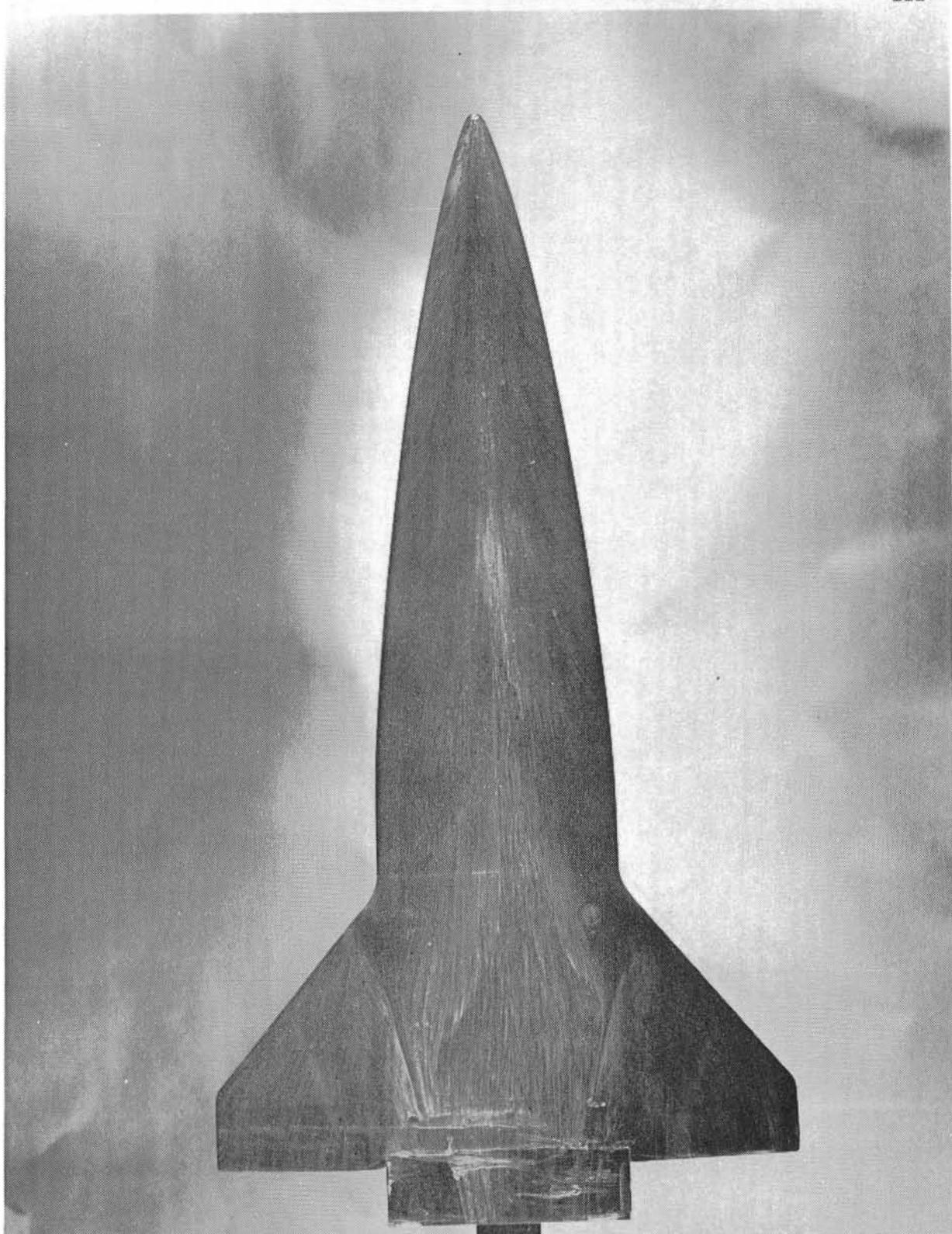


(f) Oil flow - close-up of canopy.
Figure 15.- Continued.

110

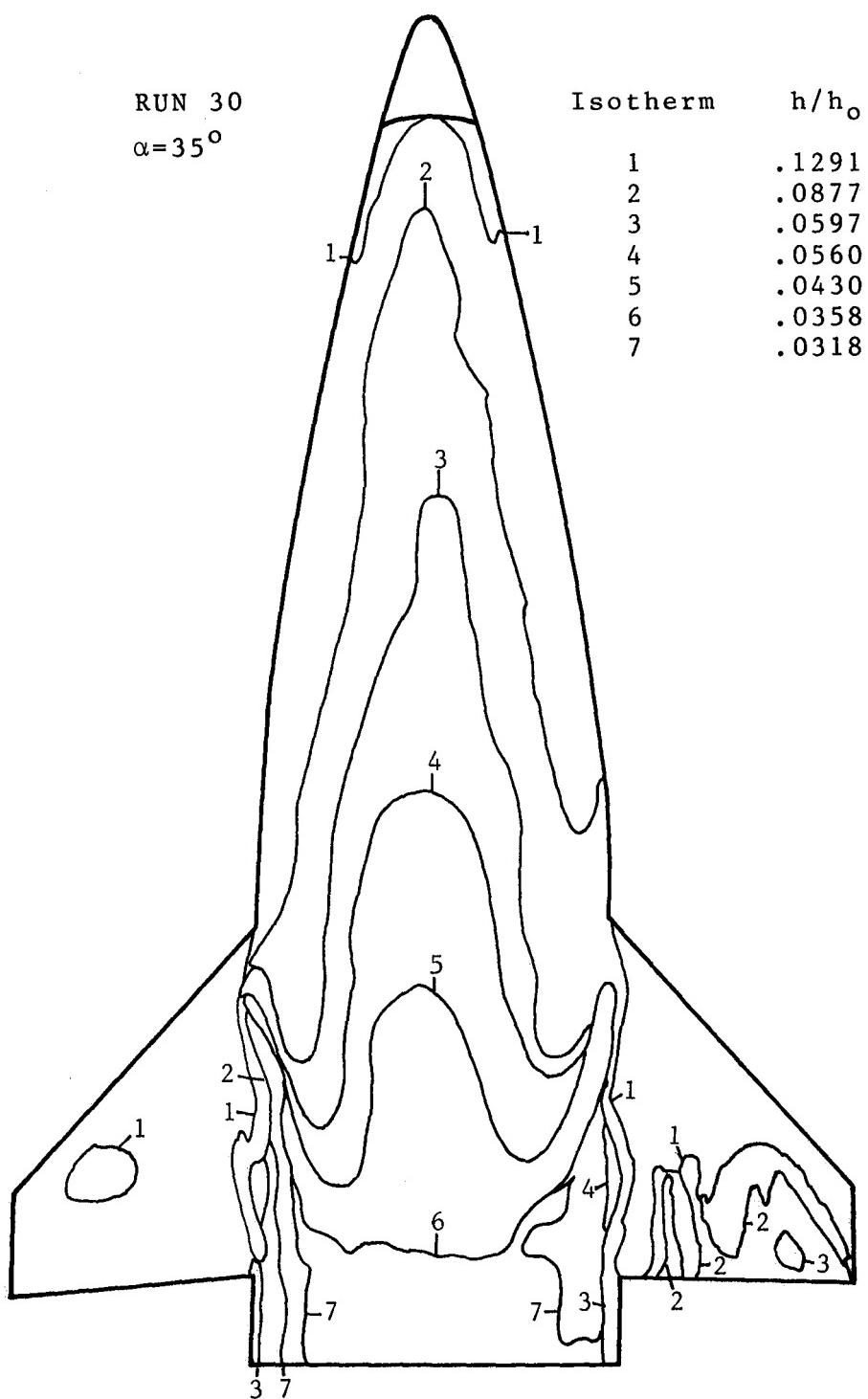


(g) Oil flow - close-up of aft fuselage and wing leeside.
Figure 15.- Concluded.

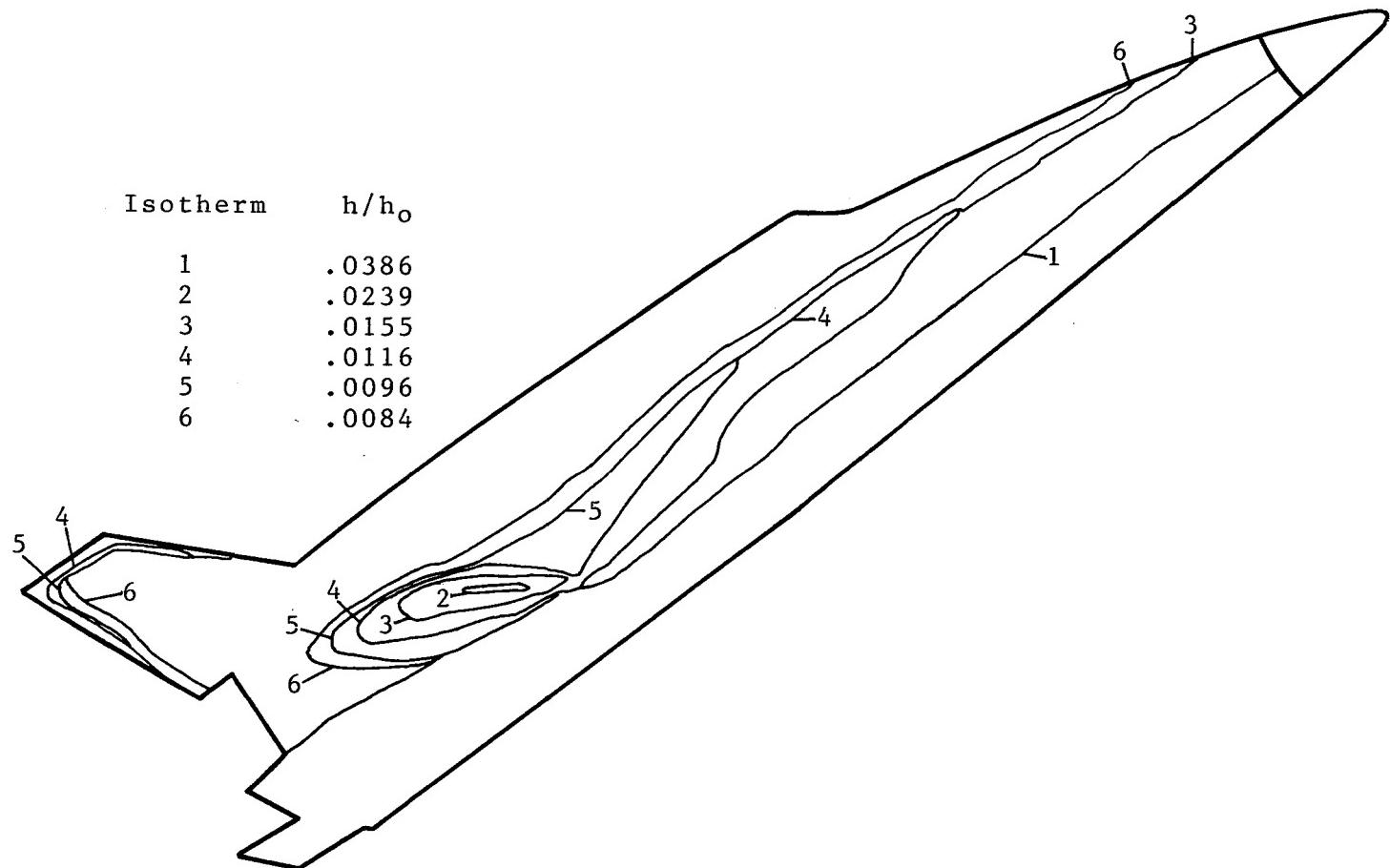


(a) Oil flow - bottom view.

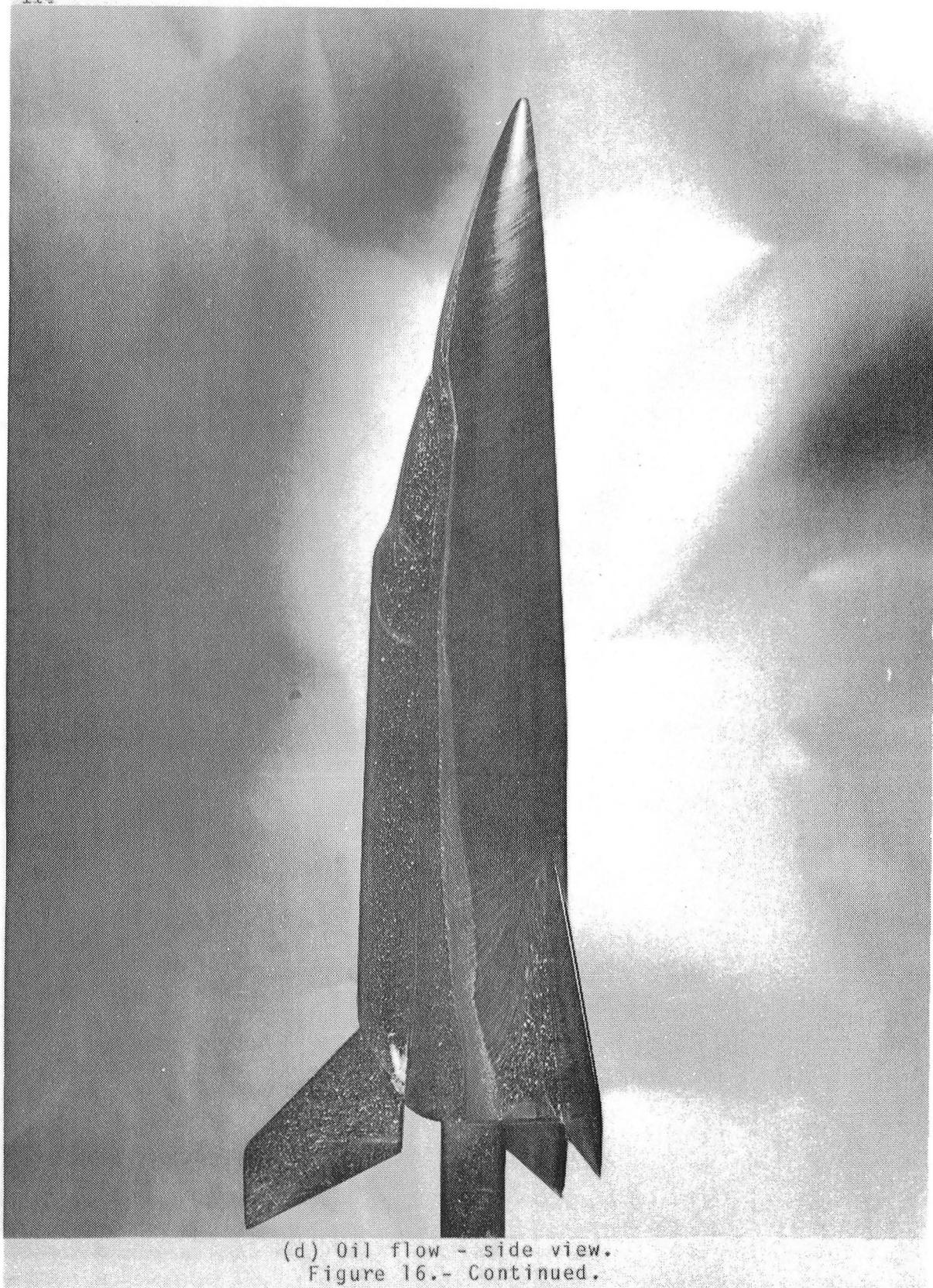
Figure 16.- Heat transfer data and oil flow patterns at $\alpha = 35^\circ$ and $Re_\infty = 1.0 \times 10^6$.



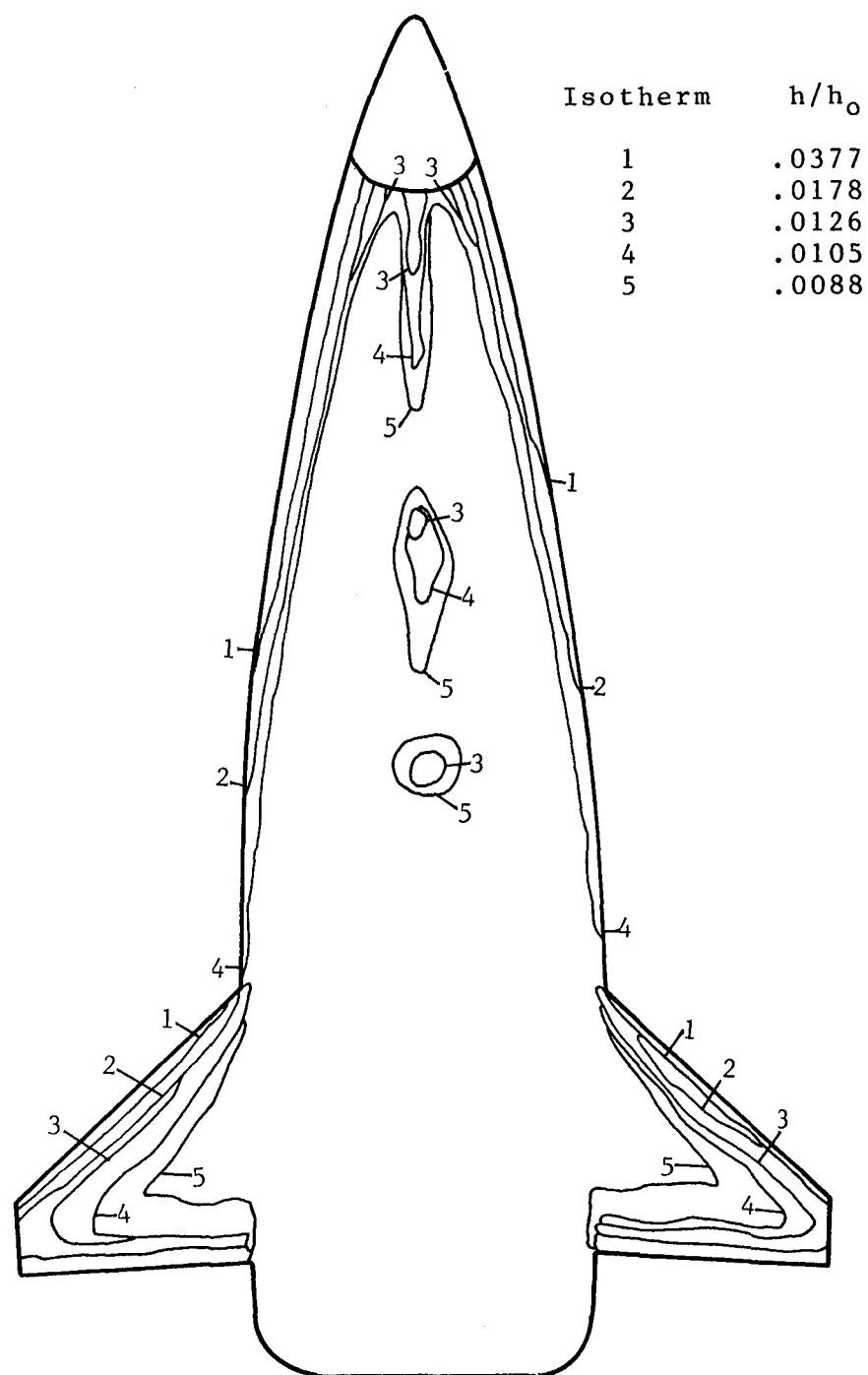
(b) Heating contours - bottom view.
 Figure 16.- Continued.



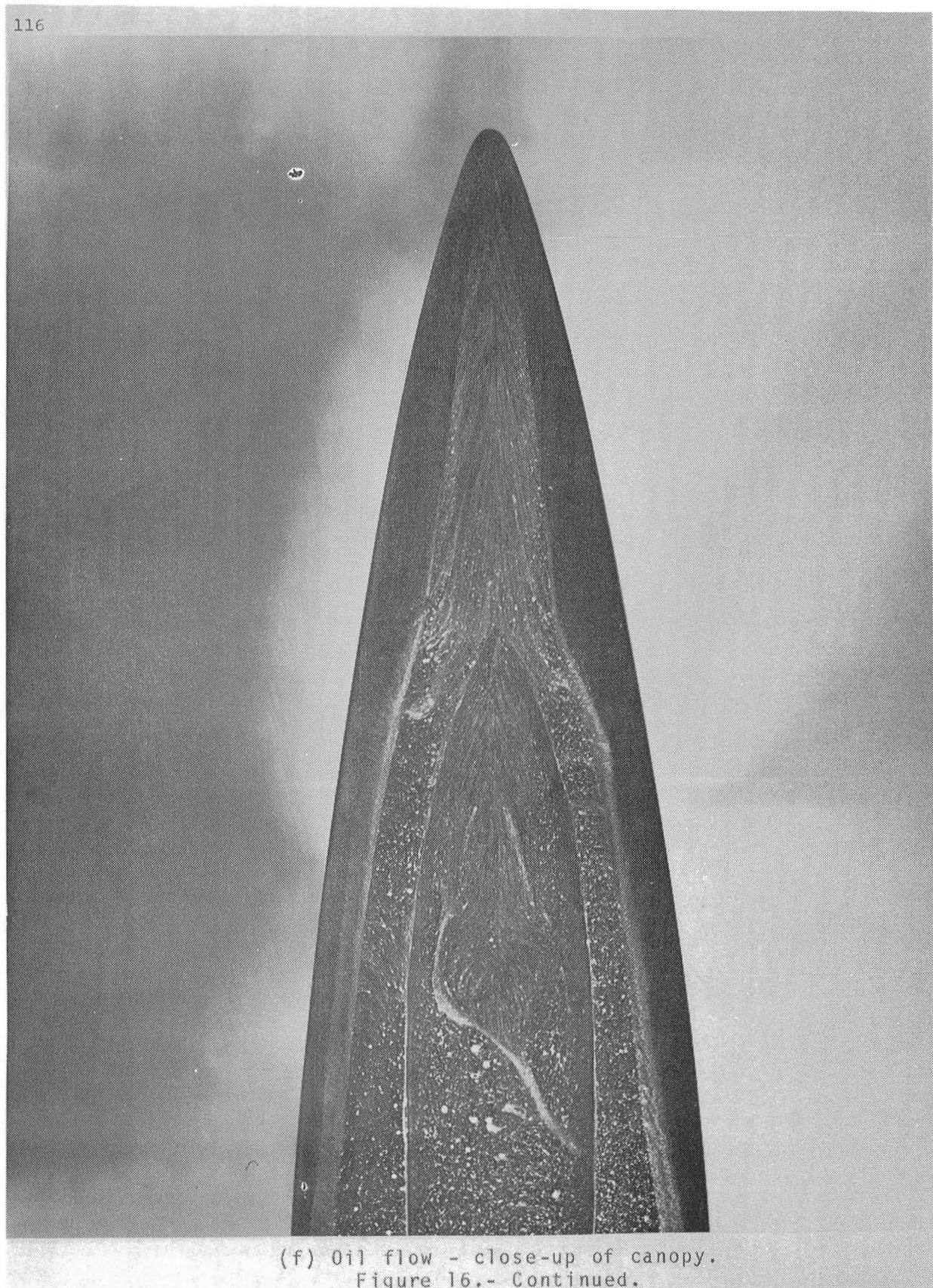
(c) Heating contours - side view.
Figure 16.- Continued.



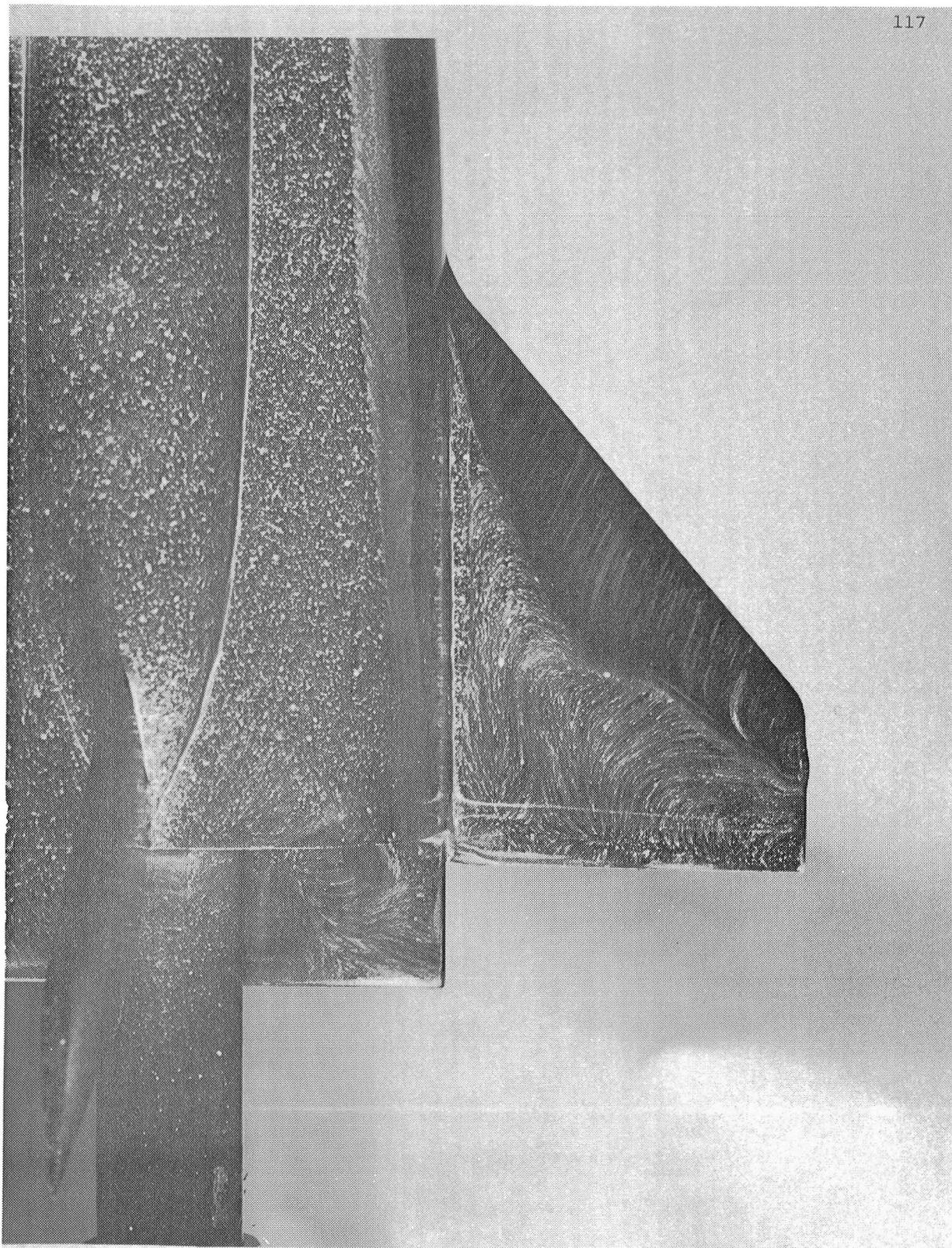
(d) Oil flow - side view.
Figure 16.- Continued.



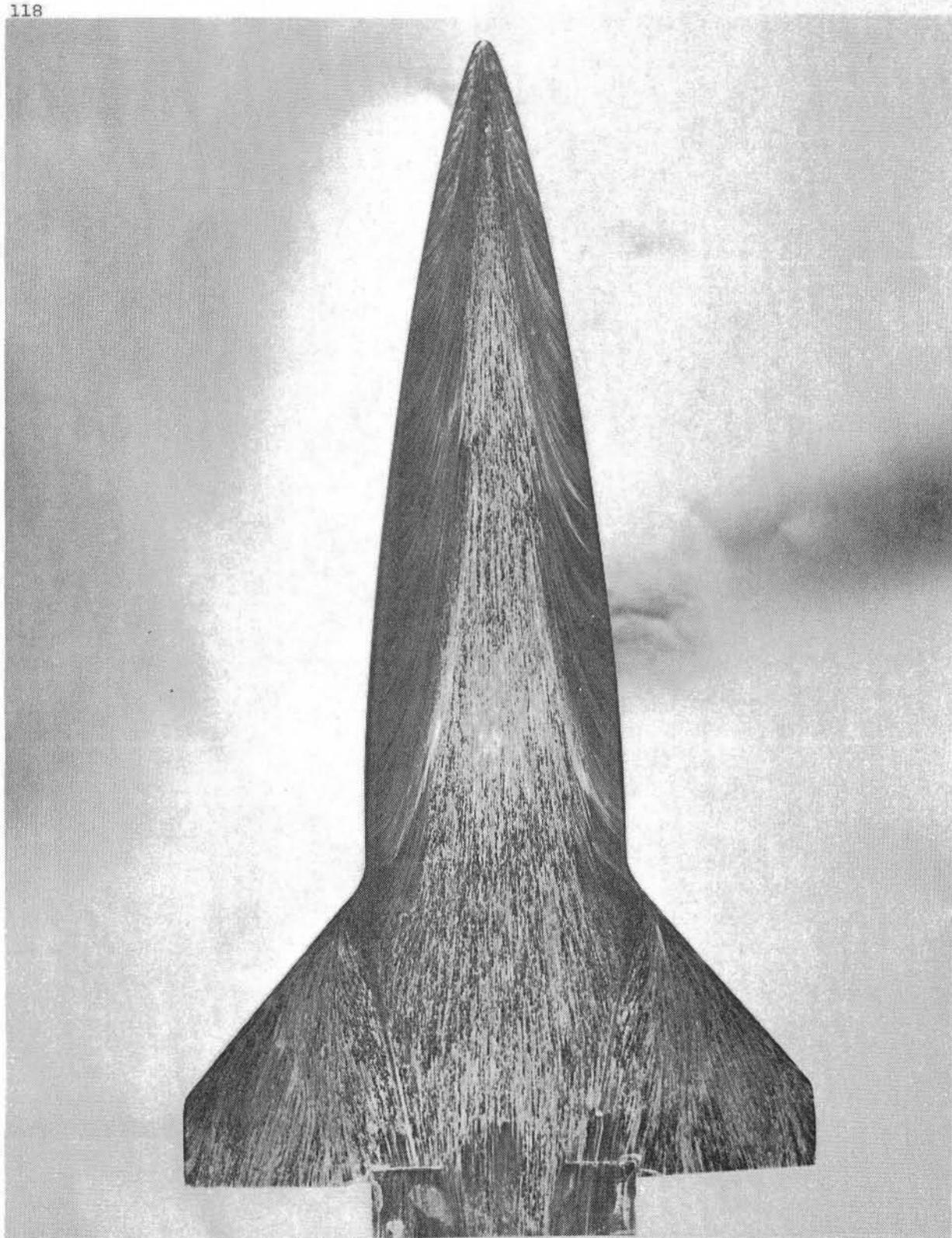
(e) Heating contours - top view.
Figure 16.- Continued.



(f) Oil flow - close-up of canopy.
Figure 16.- Continued.

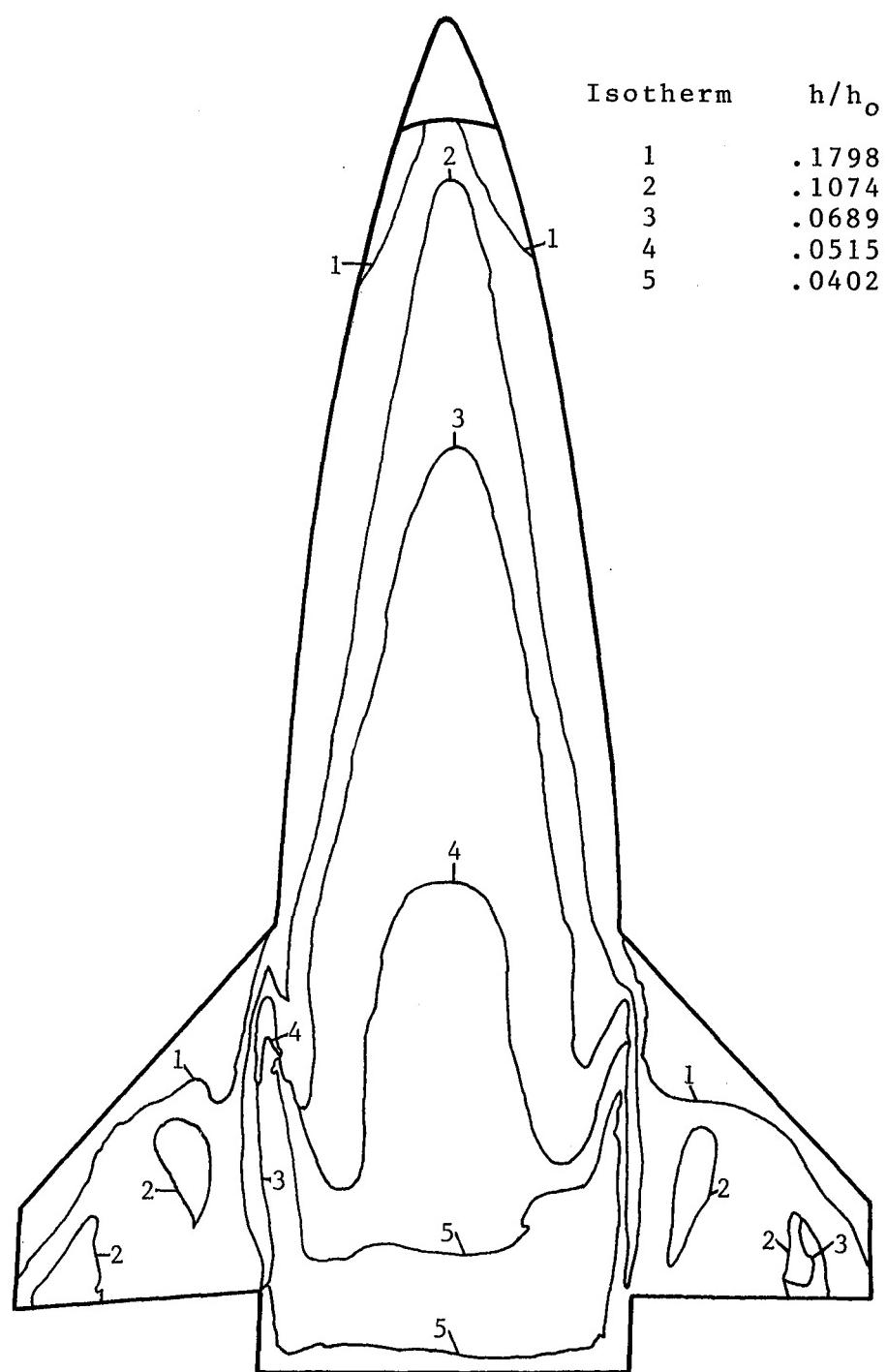


(g) Oil flow - close-up of aft fuselage and wing leeside.
Figure 16. Concluded.

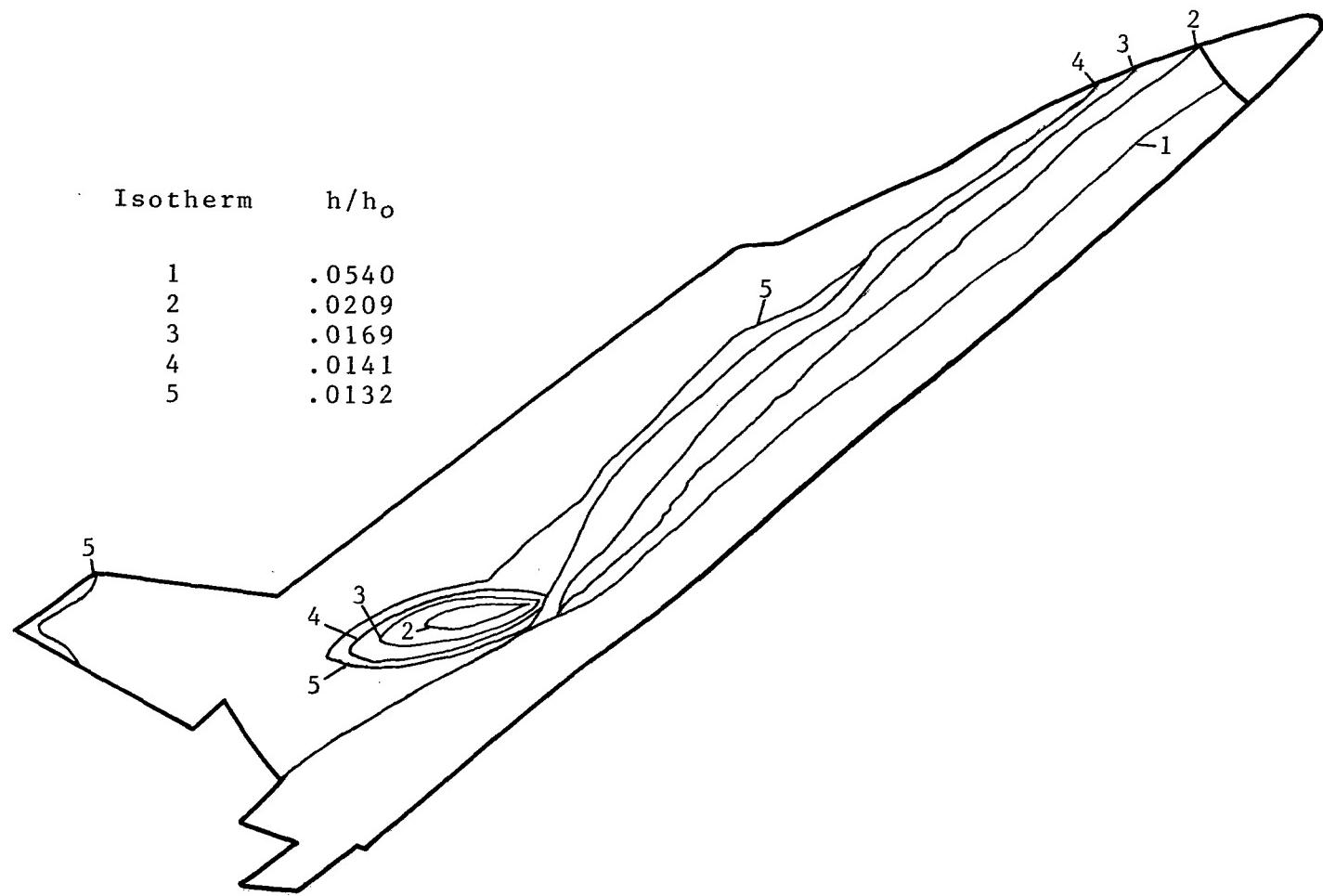


(a) Oil flow - bottom view.

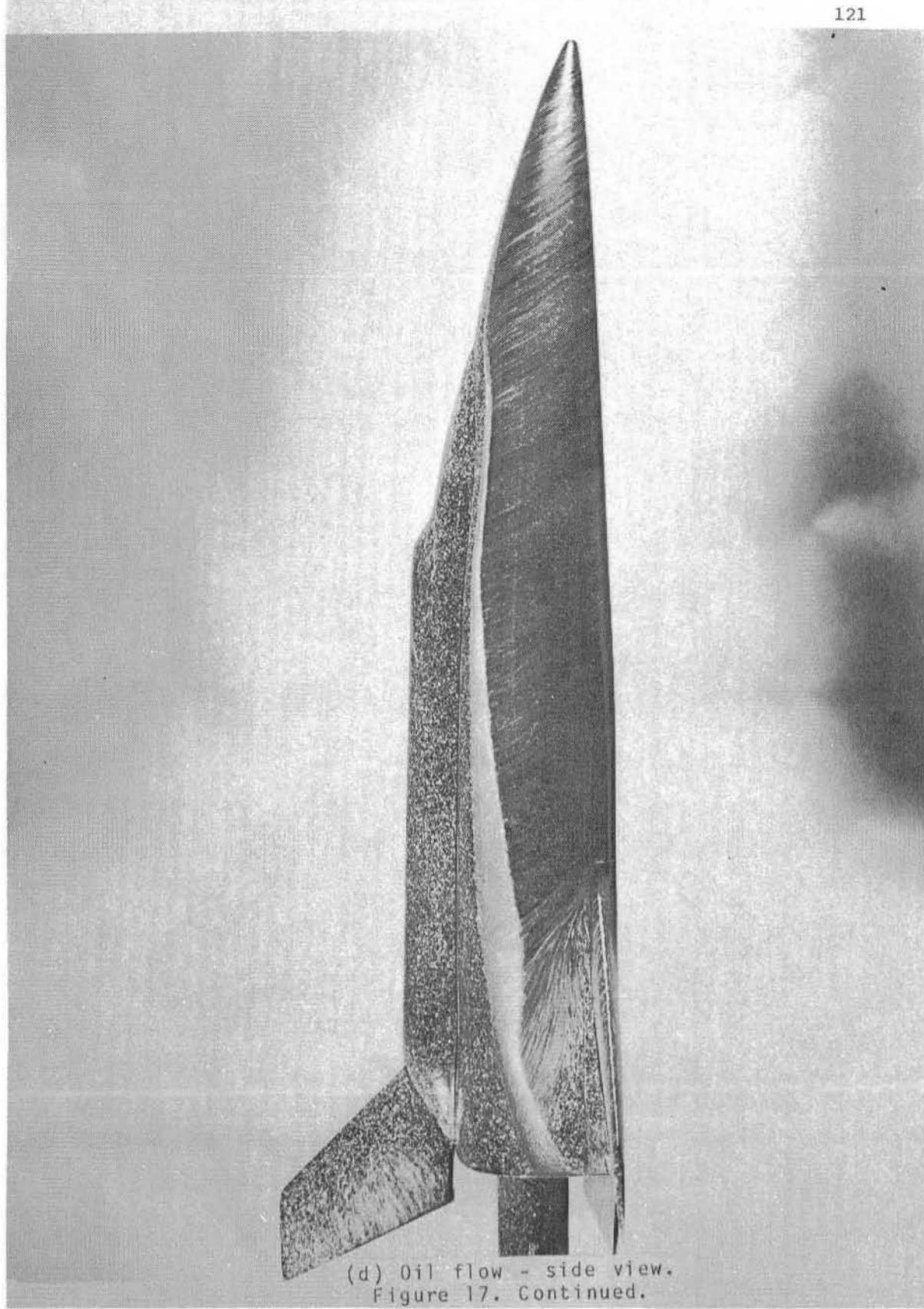
Figure 17.- Heat transfer data and oil flow patterns at $\alpha = 35^\circ$ and $Re_\infty = 0.5 \times 10^6$.



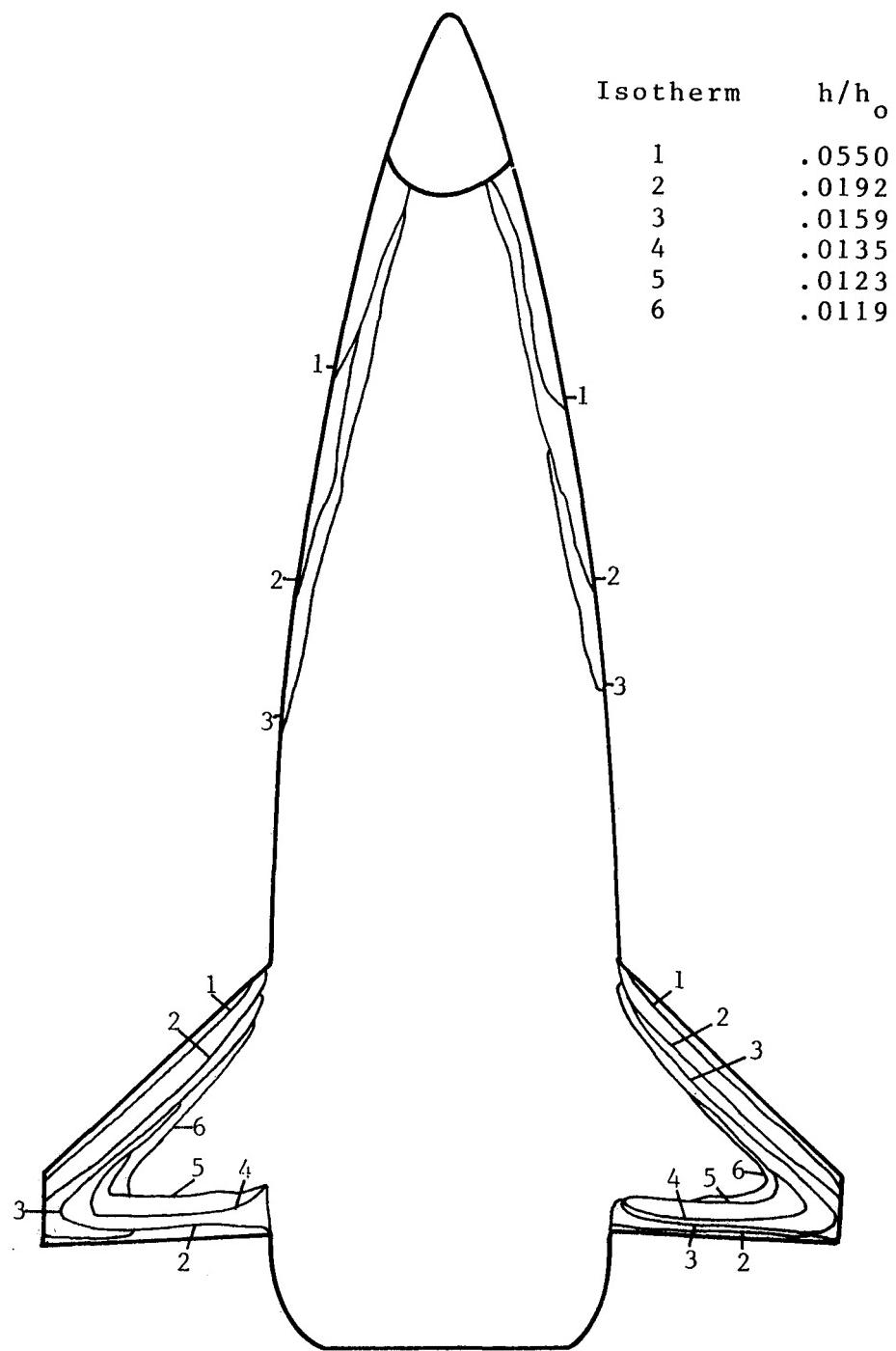
(b) Heating contours - bottom view.
Figure 17.- Continued.



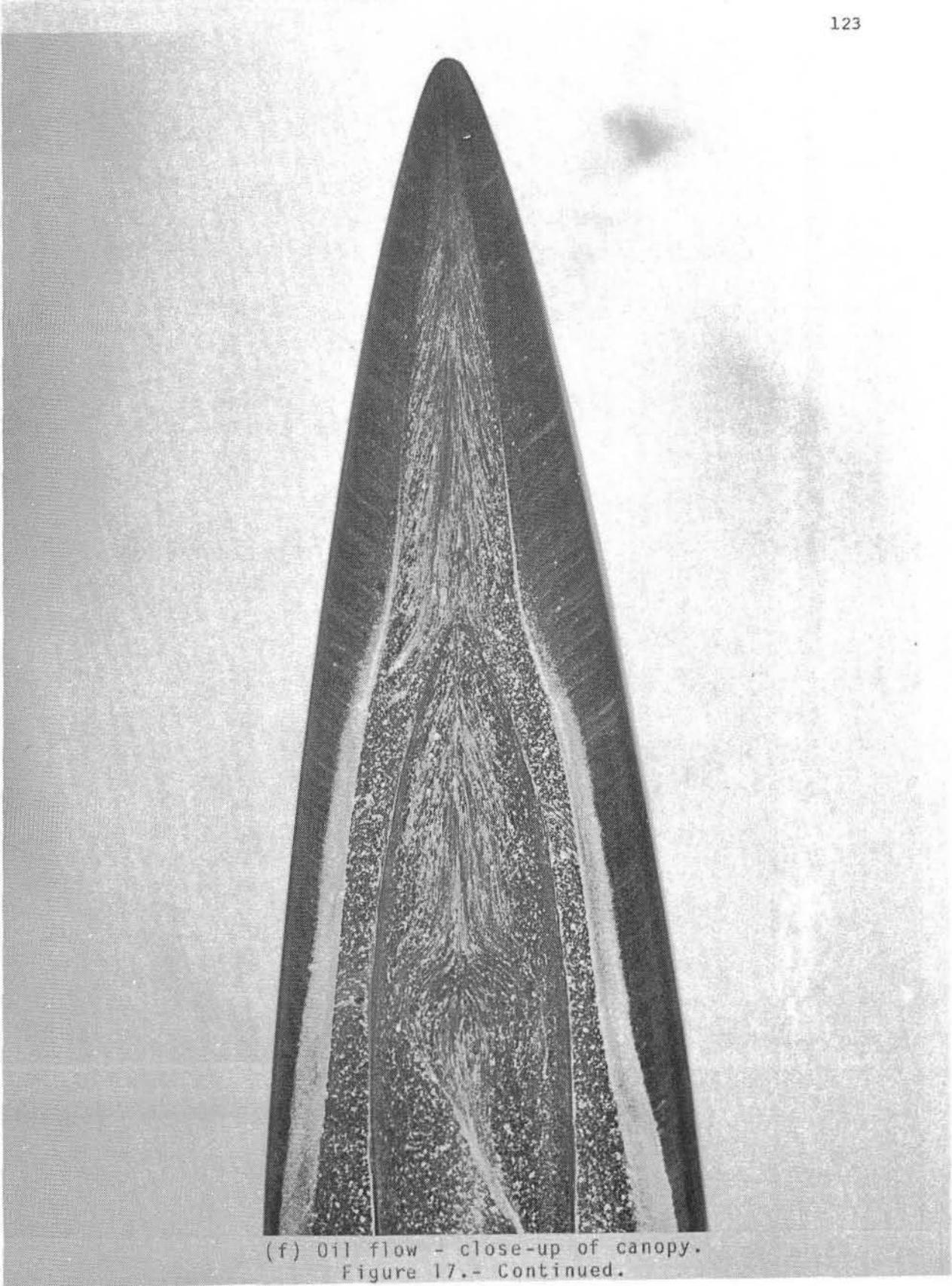
(c) Heating contours - side view.
Figure 17.- Continued.



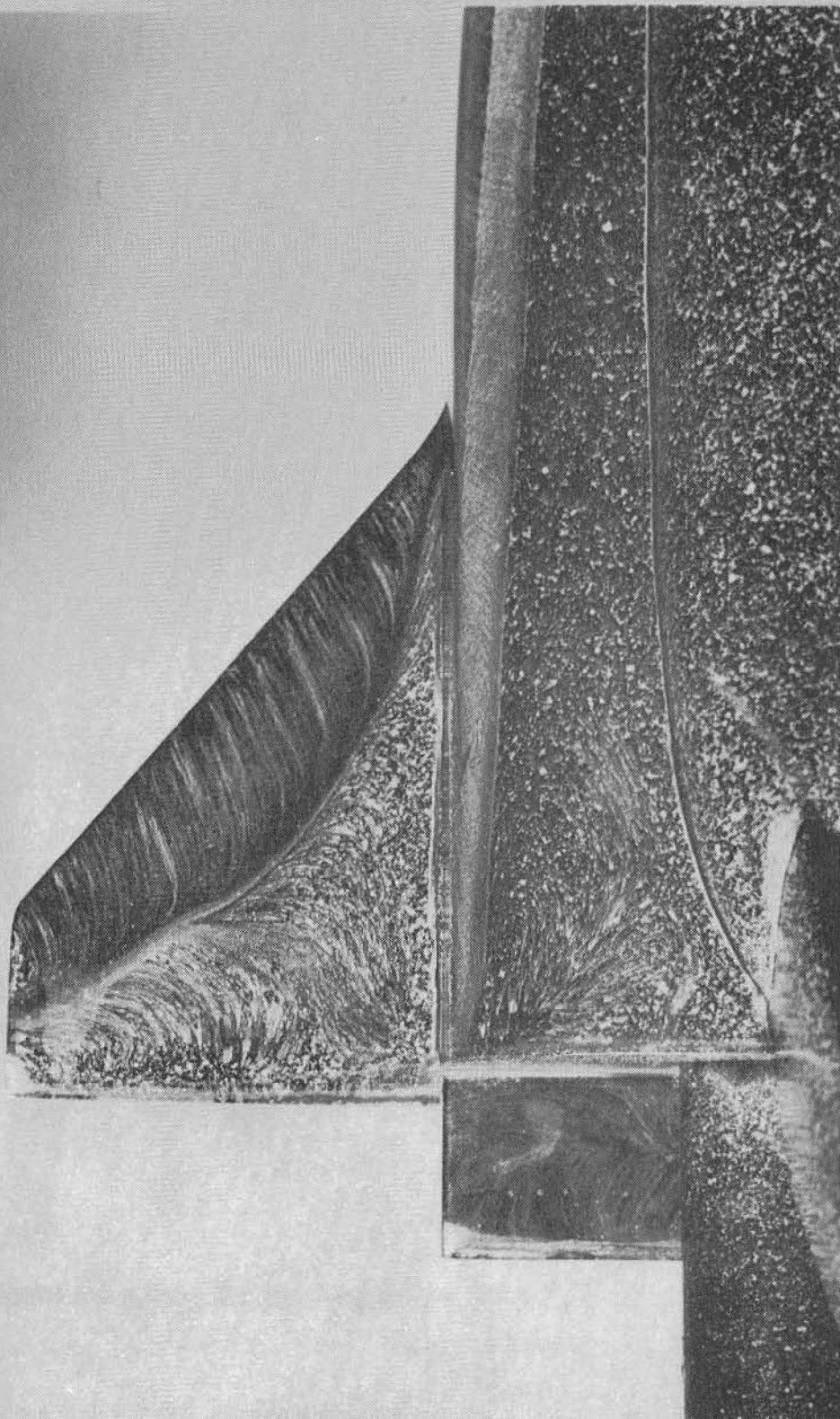
(d) Oil flow - side view.
Figure 17. Continued.



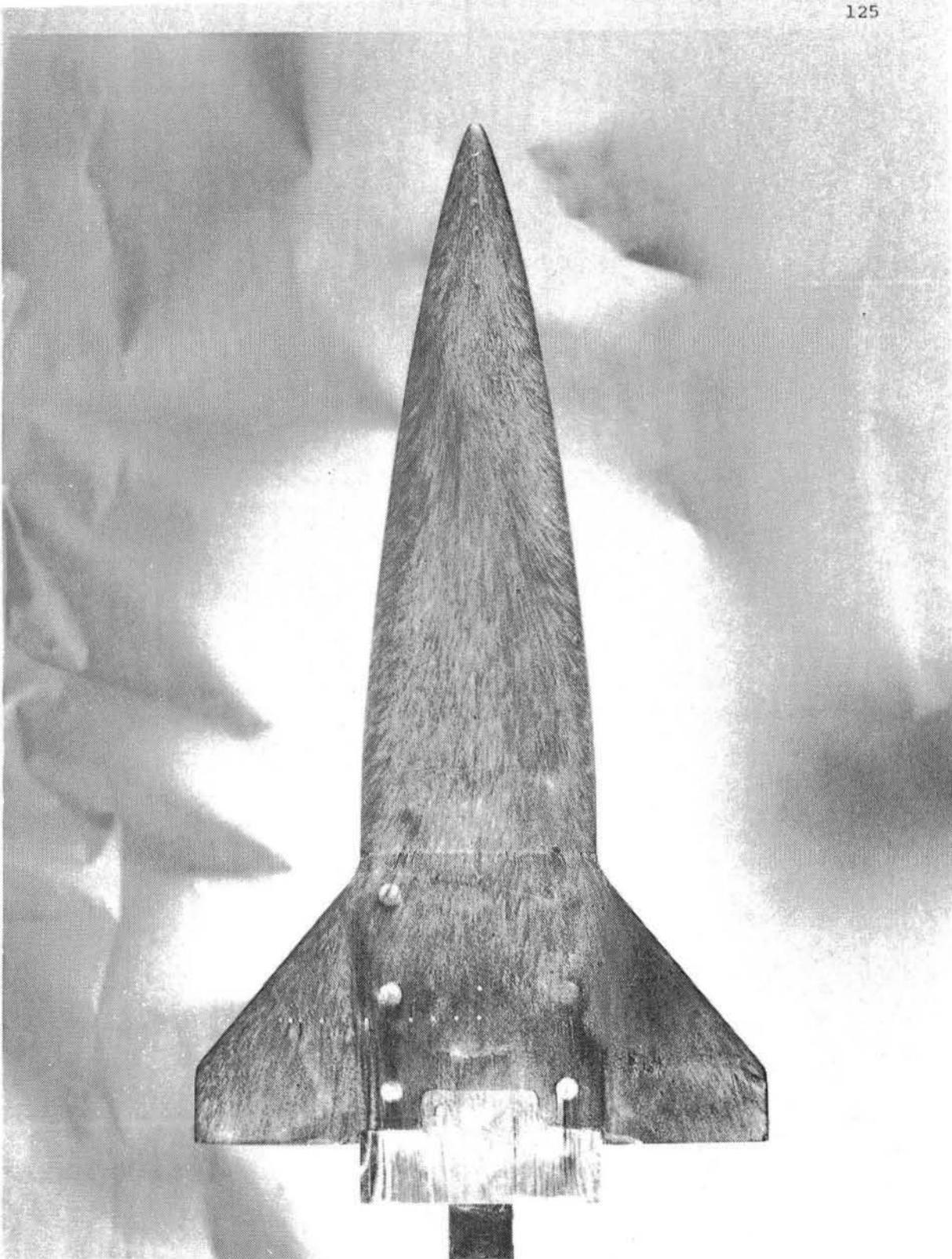
(e) Heating contours - top view.
Figure 17.- Continued.



(f) Oil flow - close-up of canopy.
Figure 17.- Continued.



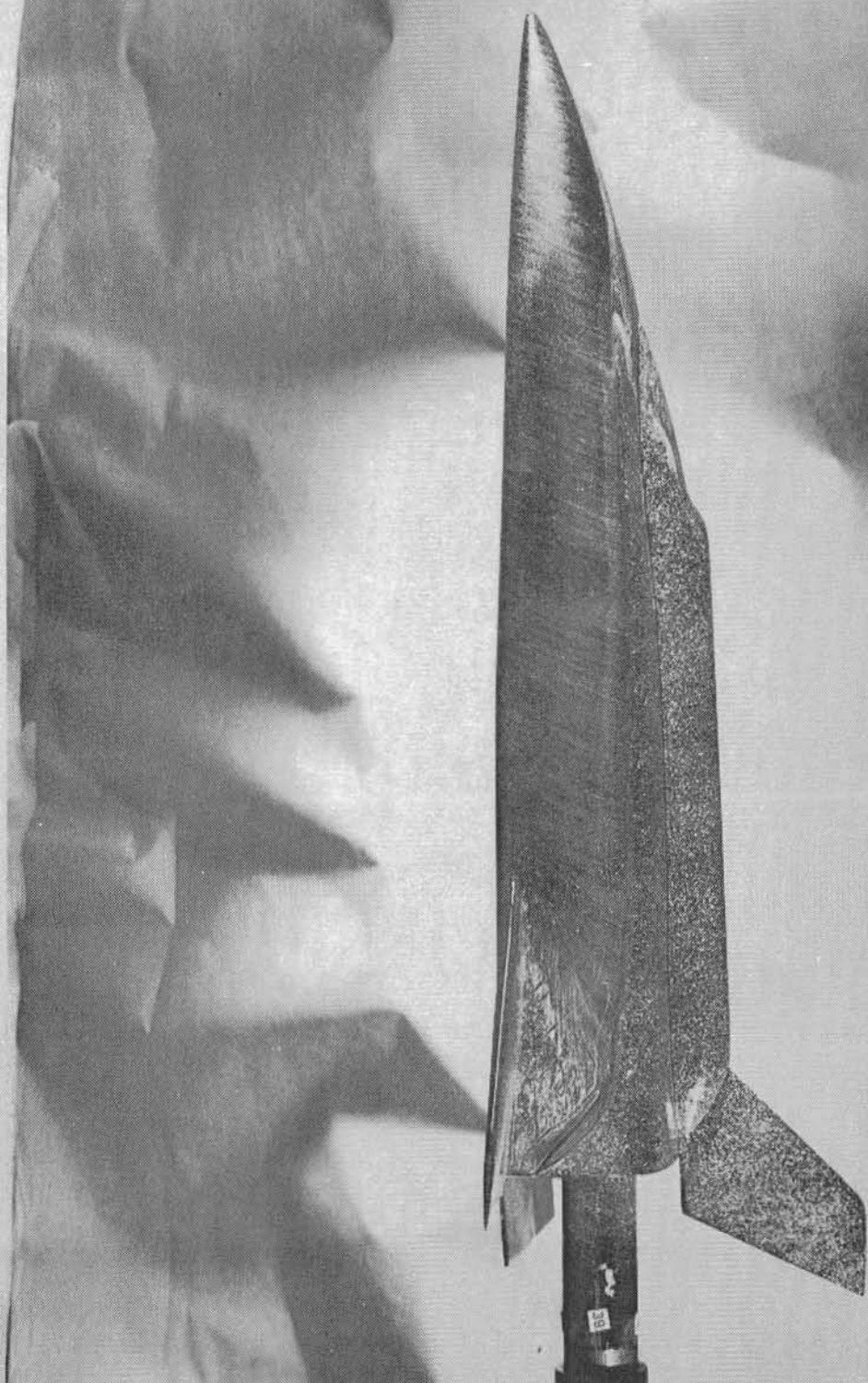
(g) Oil flow - close-up of aft fuselage and wing leeside.
Figure 17.- Concluded.



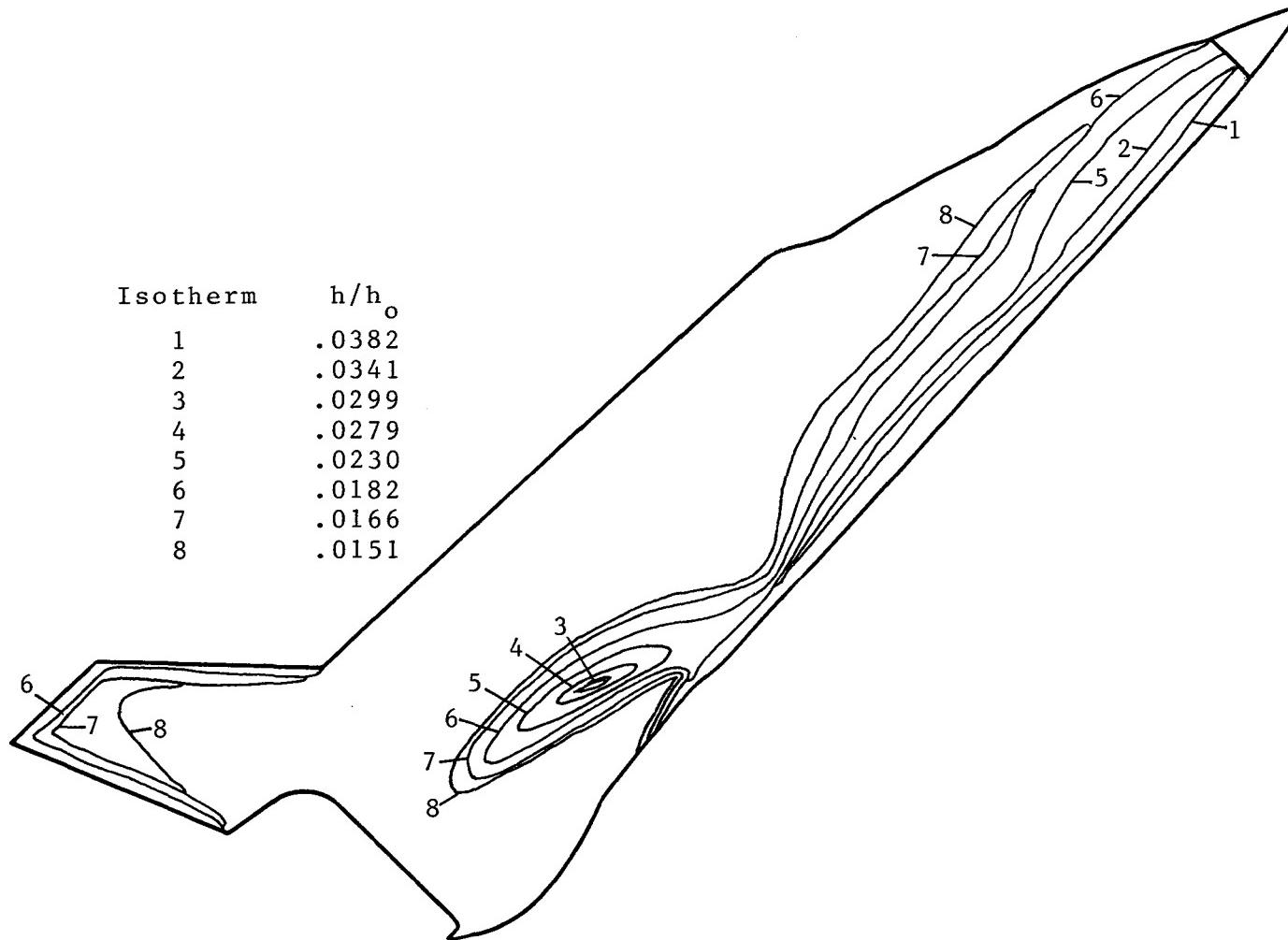
(a) Oil flow - bottom view.

Figure 18.- Heat transfer data and oil flow patterns at $\alpha = 40^\circ$ and
 $Re_\infty = 2.0 \times 10^6$

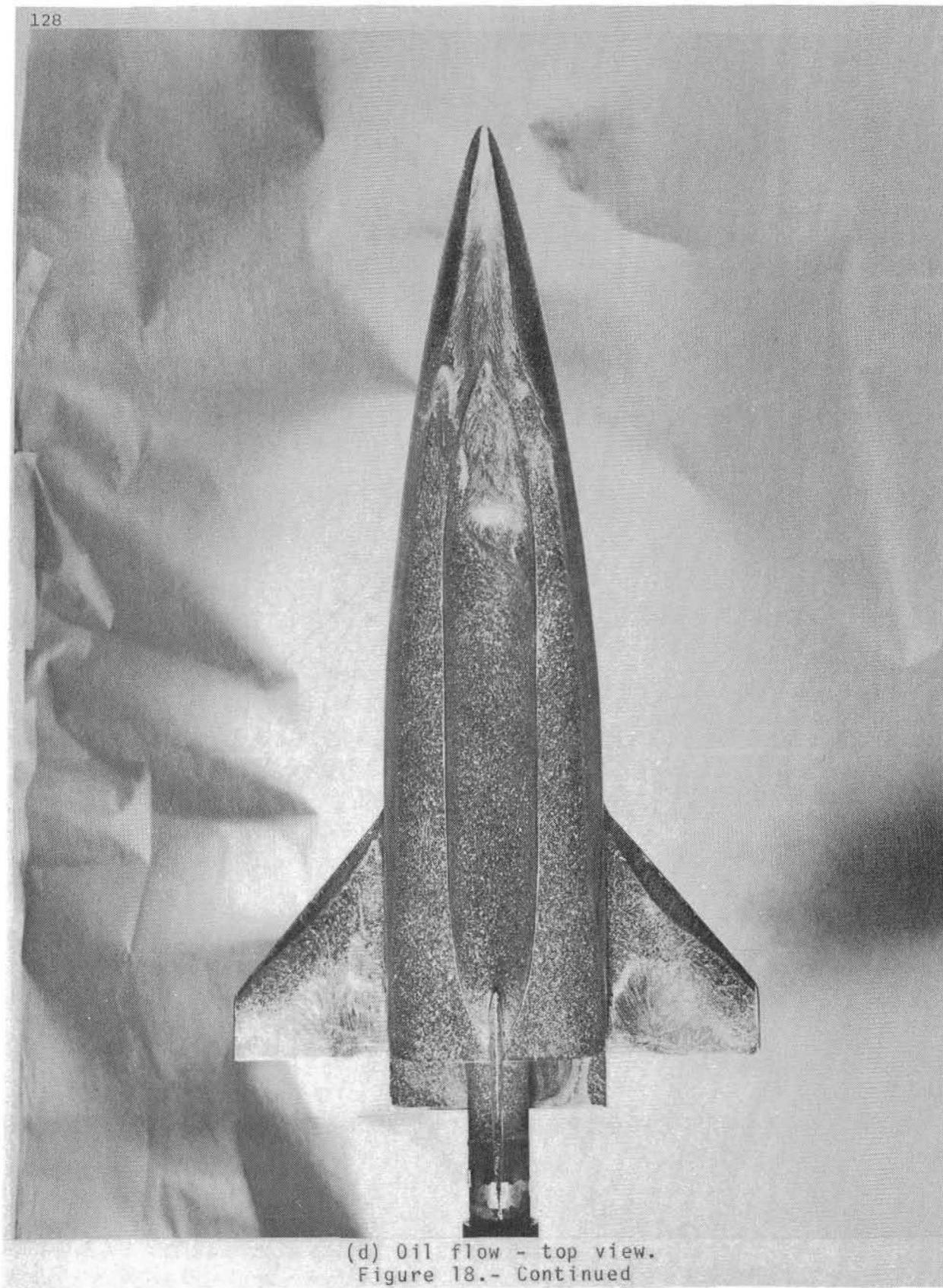
126



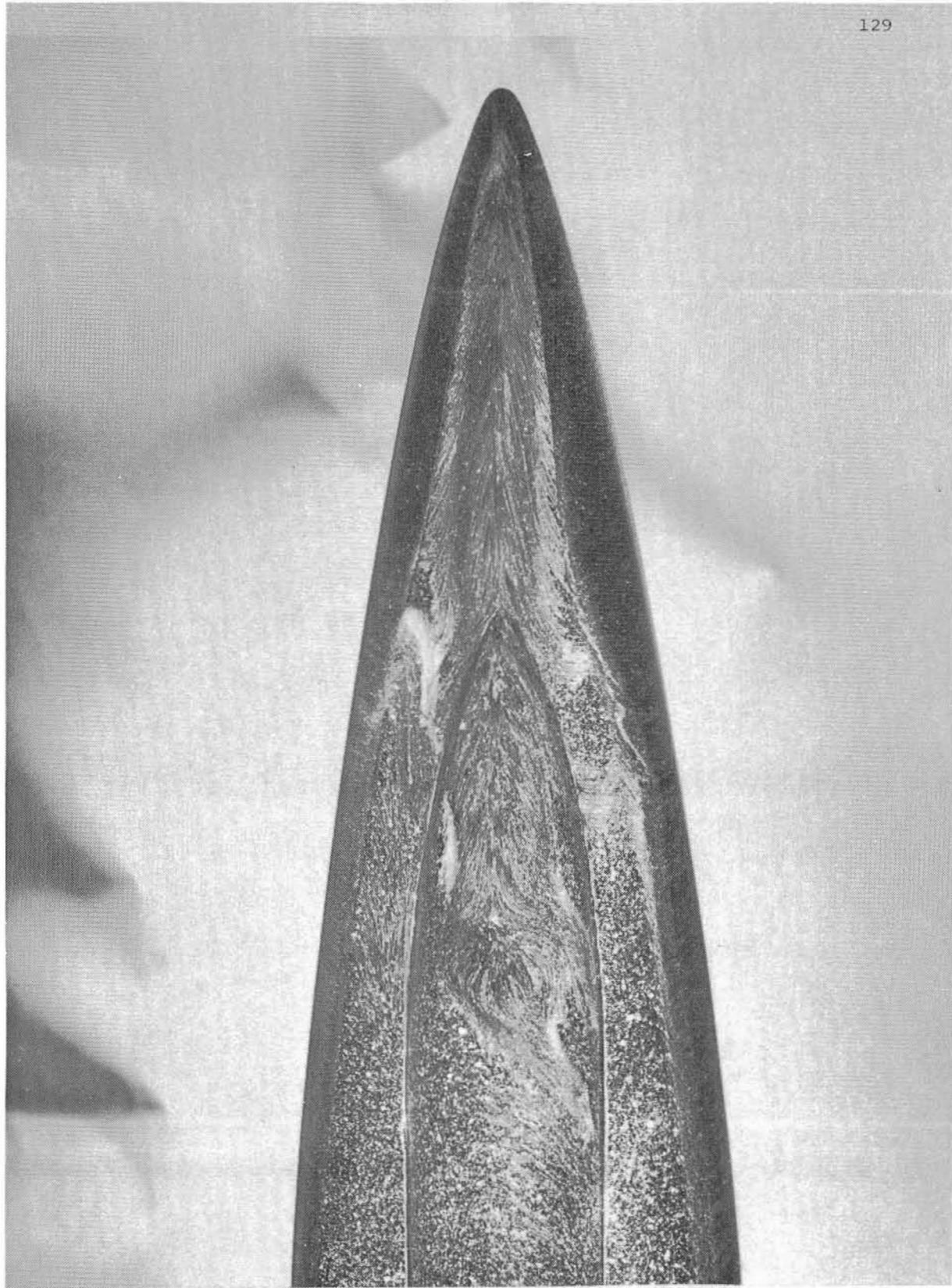
(b) Oil flow - side view.
Figure 18.- Continued.



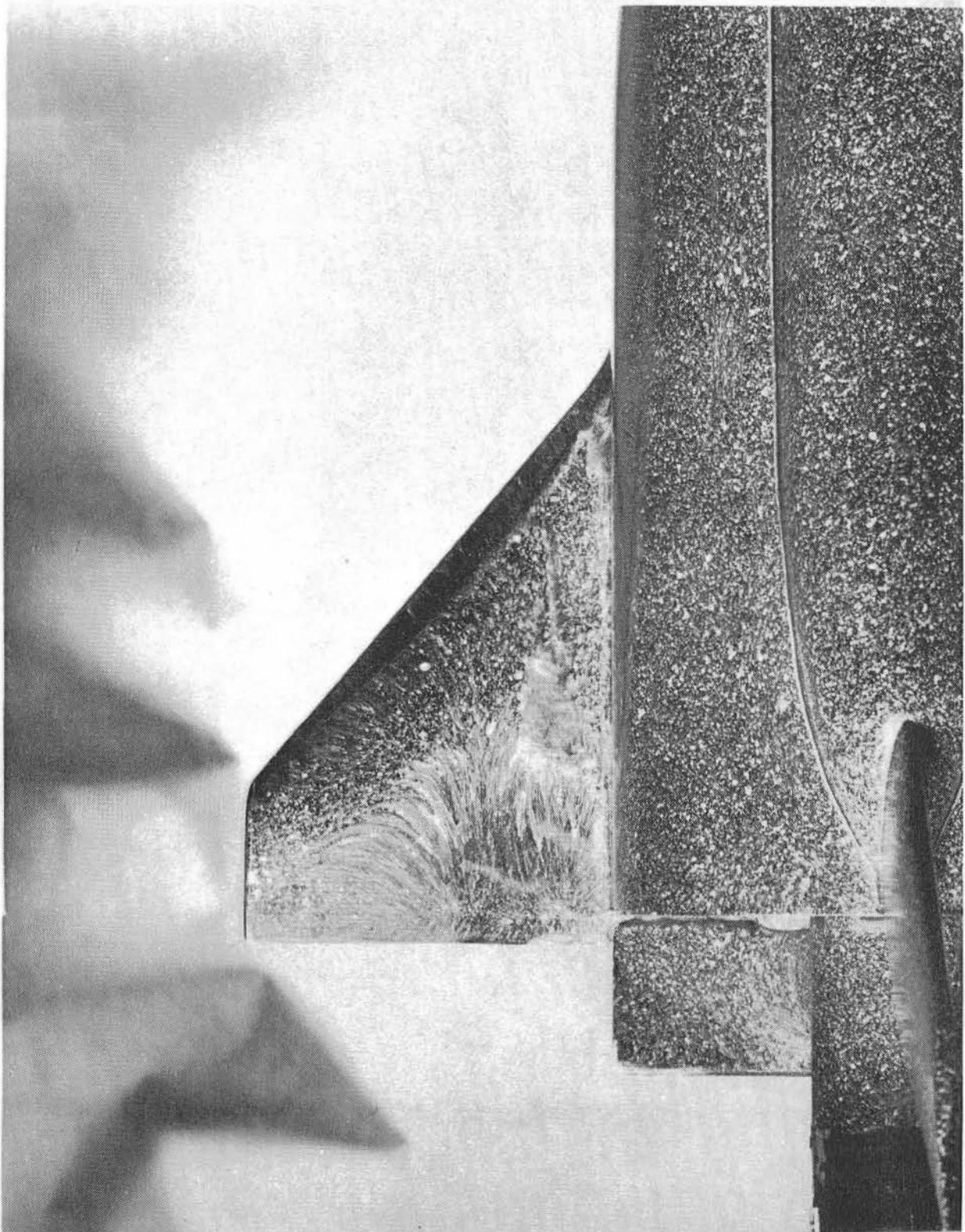
(c) Heating contours - side view.
Figure 18.- Continued.



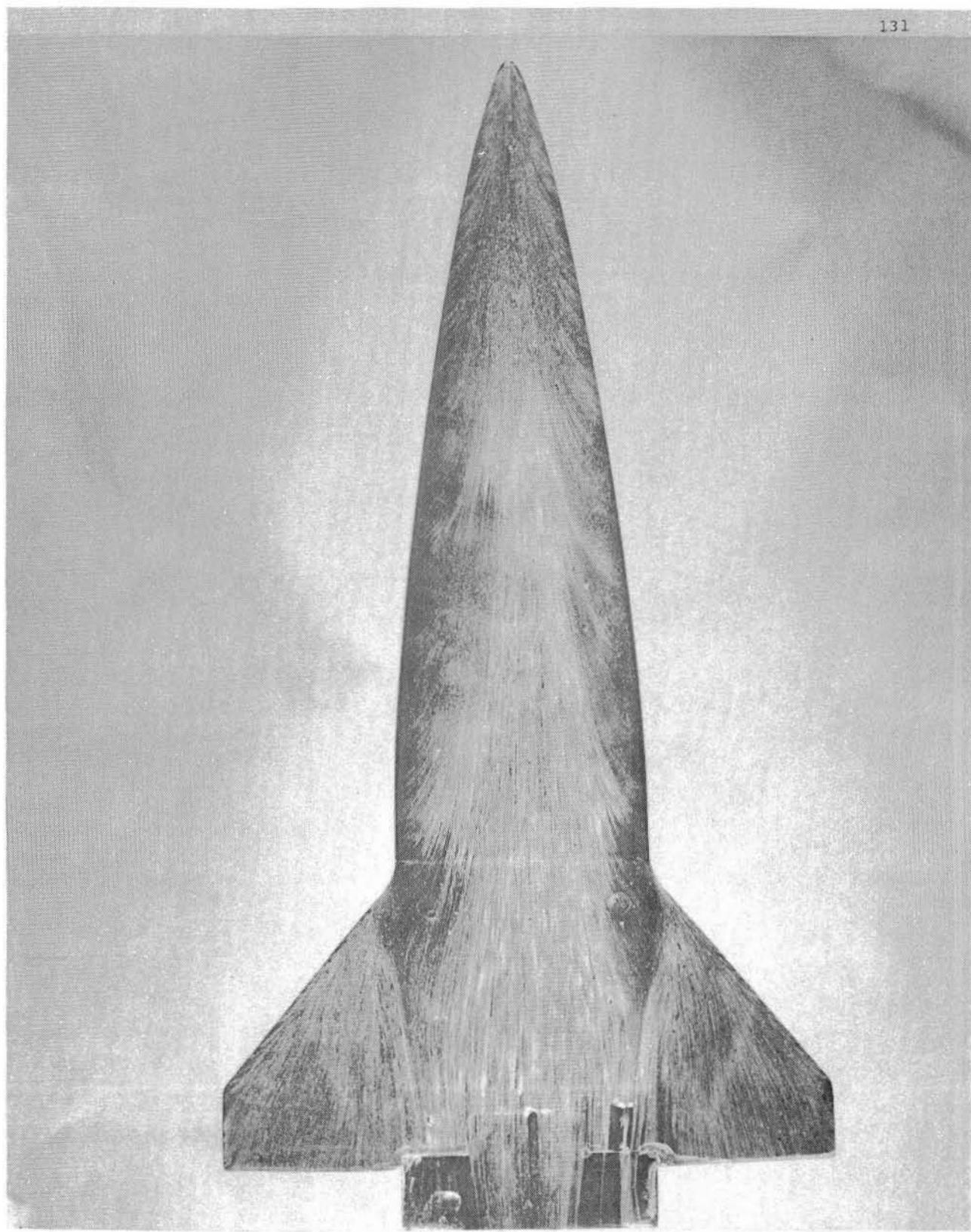
(d) Oil flow - top view.
Figure 18.- Continued



(e) Oil flow - close-up of canopy.
Figure 18.- Continued.

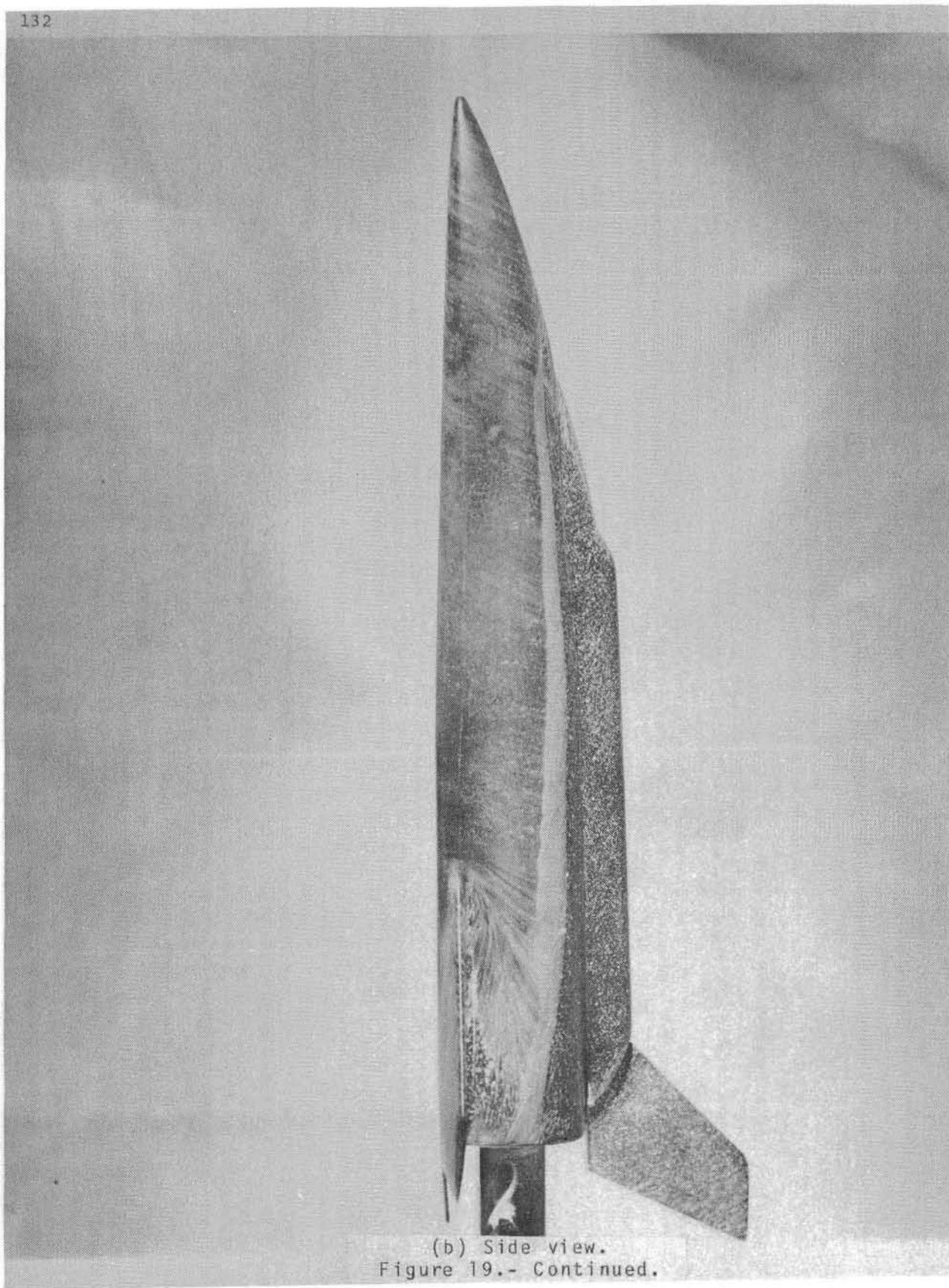


(f) Oil flow - close-up of wing leeside.
Figure 18. Concluded.

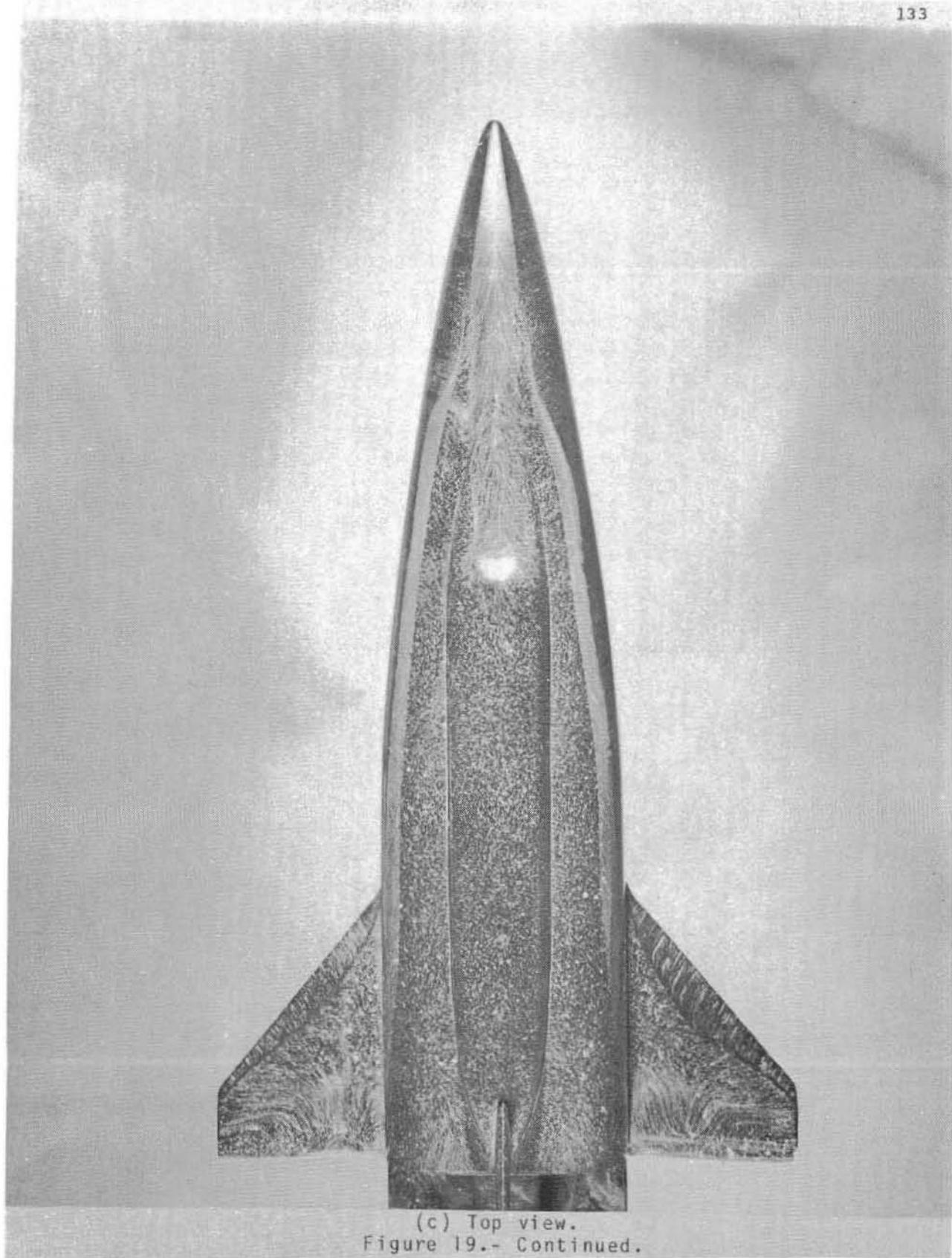


(a) Bottom view.

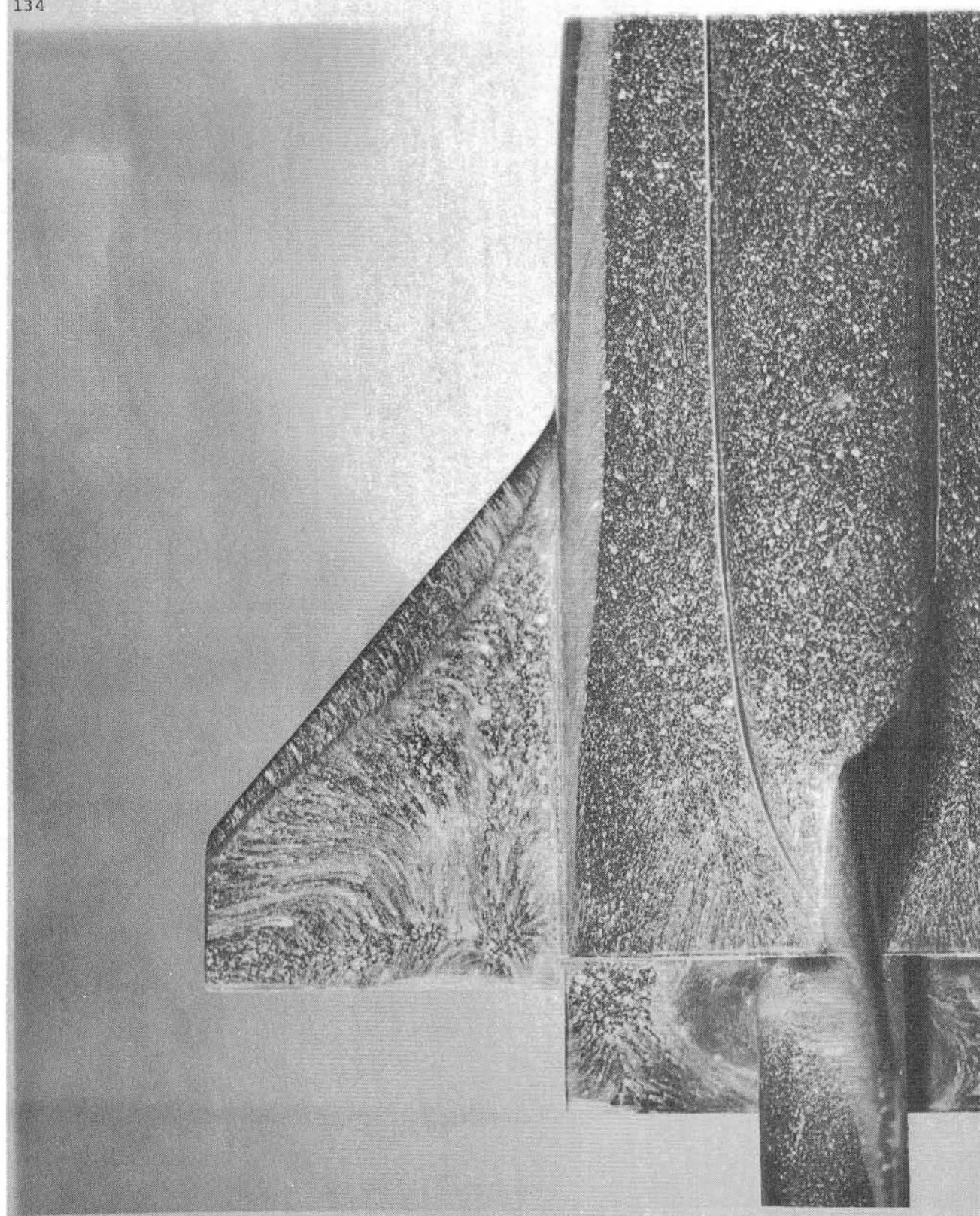
Figure 19.- Oil flow patterns at $\alpha = 40^\circ$ and
 $Re_\infty = 1.0 \times 10^6$.



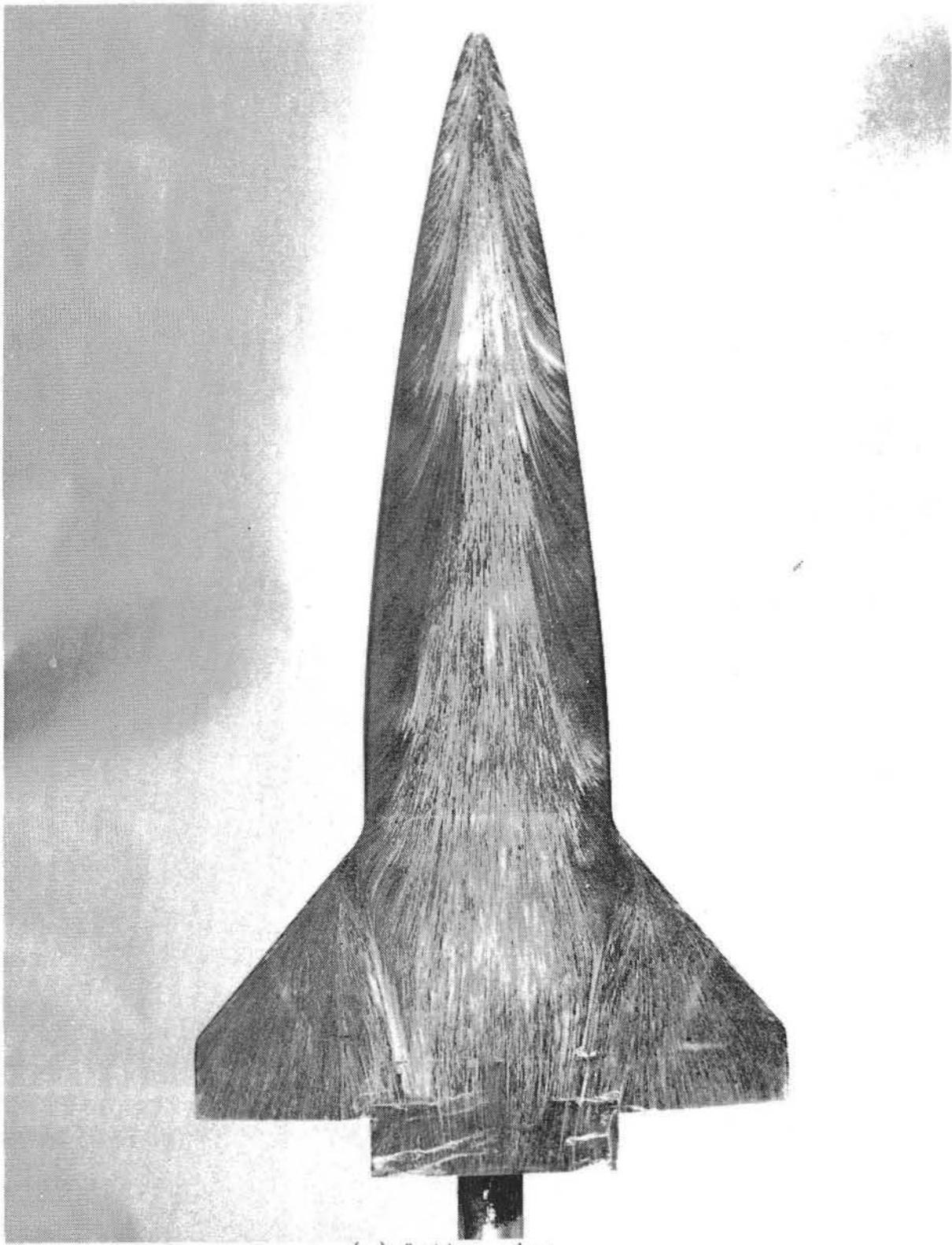
(b) Side view.
Figure 19.- Continued.



(c) Top view.
Figure 19.- Continued.

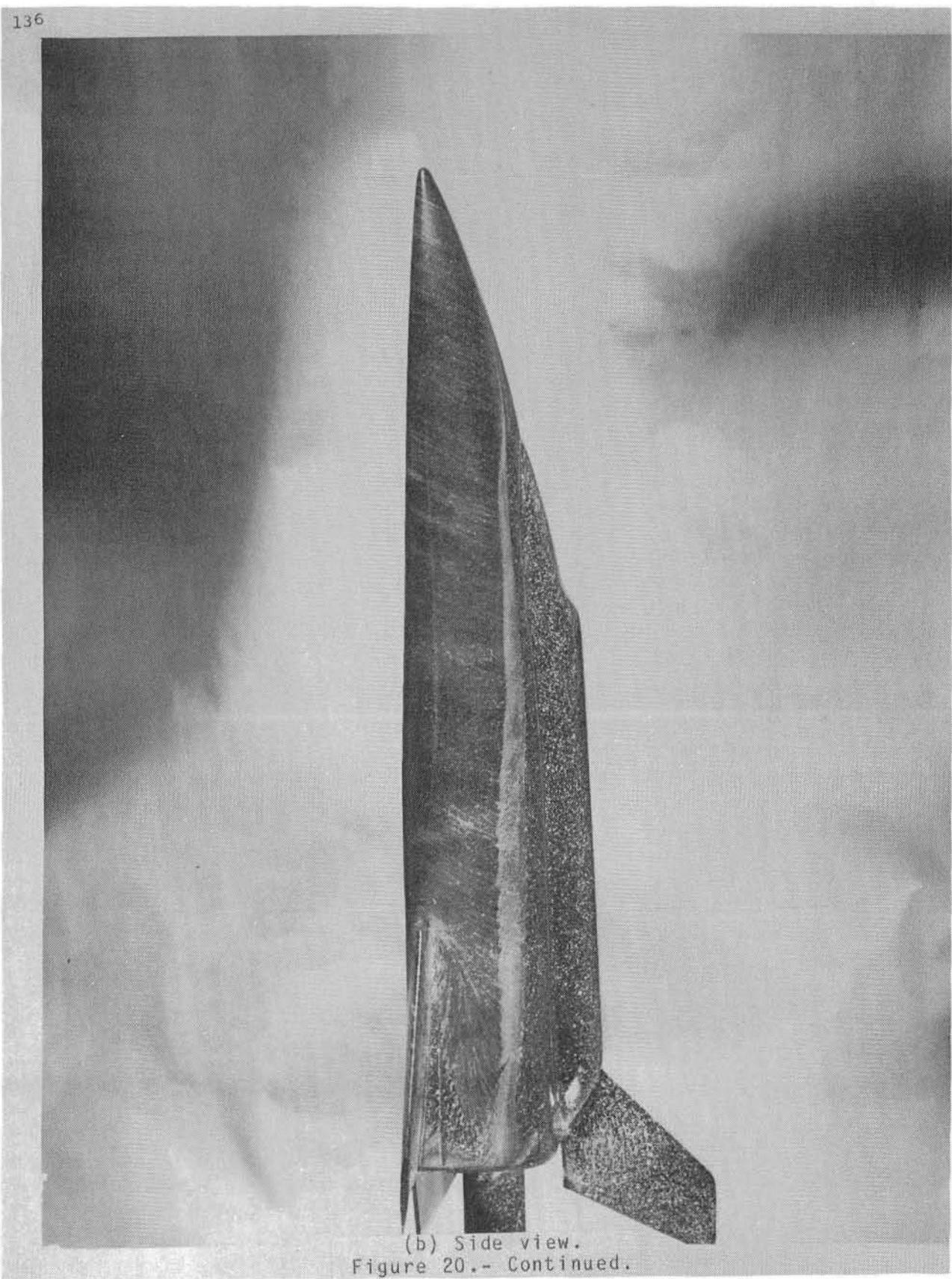


(d) Close-up of wing leeside.
Figure 19.- Concluded.

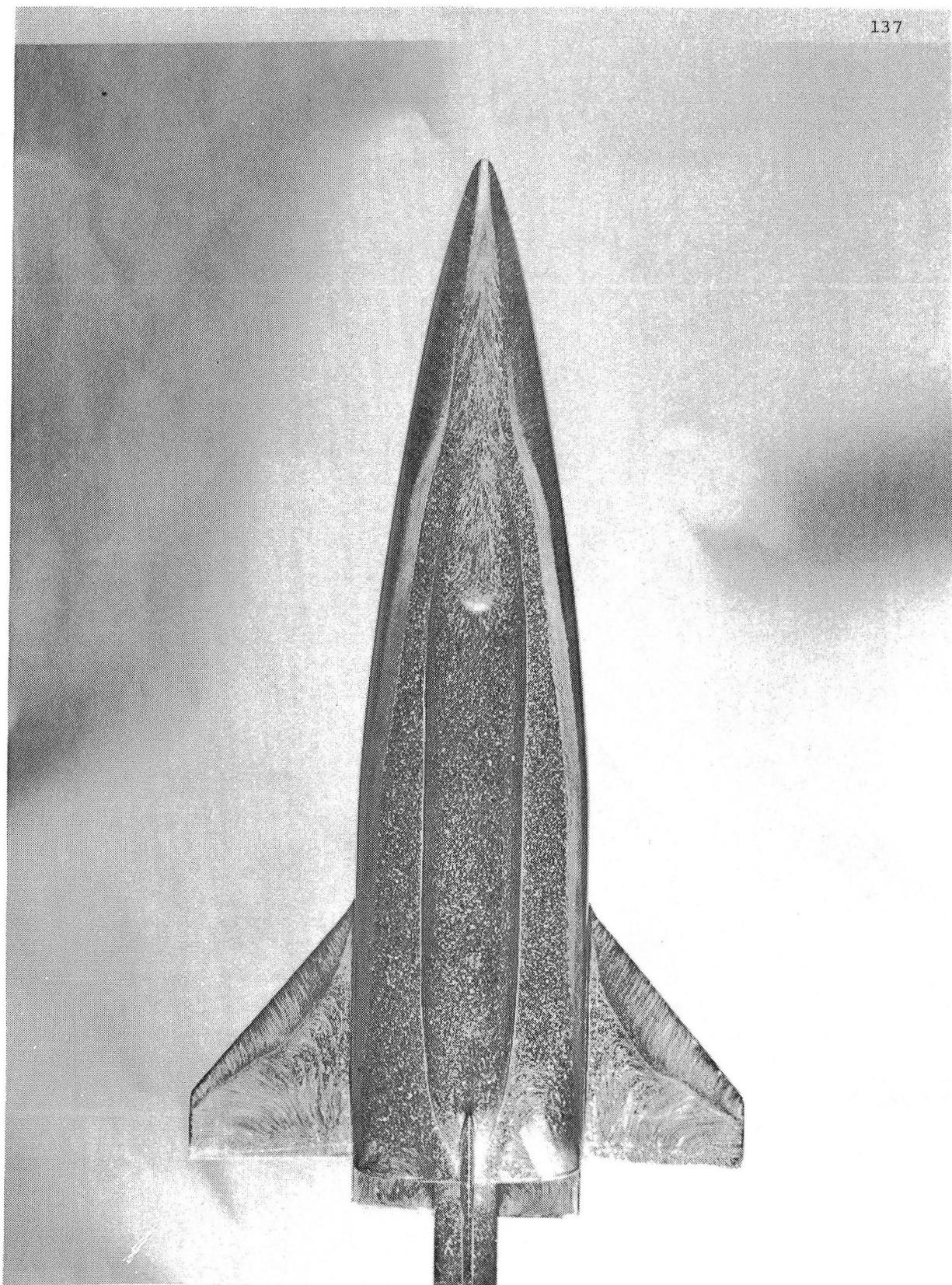


(a) Bottom view.
Figure 20.- Oil flow patterns at $\alpha = 40^\circ$ and
 $Re_\infty = 0.5 \times 10^6$.

136



(b) Side view.
Figure 20.- Continued.



(c) Top view.
Figure 20.- Continued.



(d) Close-up of wing leeside.
Figure 20.- Concluded.

1. Report No. NASA TM-85833	2. Government Accession No.	3. Recipient's Catalog No.	
4. Title and Subtitle Heat Transfer and Oil Flow Studies on a Single-Stage-to-Orbit Control-Configured Winged Entry Vehicle		5. Report Date June 1984	
7. Author(s) V. T. Helms III P. F. Bradley		6. Performing Organization Code 506-51-13-06	
9. Performing Organization Name and Address NASA Langley Research Center Hampton, VA 23665		8. Performing Organization Report No.	
12. Sponsoring Agency Name and Address National Aeronautics and Space Administration Washington, DC 20546		10. Work Unit No.	
		11. Contract or Grant No.	
		13. Type of Report and Period Covered Technical Memorandum	
		14. Sponsoring Agency Code	
15. Supplementary Notes			
16. Abstract Results are presented for oil flow and phase change paint heat-transfer tests conducted on a 0.006-scale model of a proposed single-stage-to-orbit control-configured vehicle. The data were taken at angles of attack up to 40° at a free-stream Mach number of 10 for Reynolds numbers based on model length of 0.5×10^6 , 1.0×10^6 and 2.0×10^6 . The magnitude and distribution of heating are characterized in terms of angle of attack and Reynolds number aided by an analysis of the oil flow data which are used to suggest the presence of various three-dimensional flow structures that produce the observed heating patterns. Of particular interest are streak heating patterns that result in high localized heat-transfer rates on the wing windward surface at low to moderate angles of attack. These streaks are caused by the bow-shock/wing-shock interaction and formation of the wing-shock. Embedded vorticity was found to be associated with these interactions.			
17. Key Words (Suggested by Author(s)) heat transfer, oil flow, winged entry vehicle, streak heating, embedded vorticity		18. Distribution Statement Unclassified - Unlimited Subject Category 15	
19. Security Classif. (of this report) Unclassified	20. Security Classif. (of this page) Unclassified	21. No. of Pages 139	22. Price A07

